Molecular triggers of reactive gliosis and neurodegeneration in proteasome depleted neurons: a role for STAT3 signalling in astrocytes

Anya Snary, BSc

A thesis submission for the
qualification of
doctor in philosophy (PhD)

School of Life Sciences, University of Nottingham,

Derby Road, NG7 2UH

July 2022

Abstract

Neurodegenerative diseases are devastating disorders with a wide social, economic, and environmental impact. These disorders are classified as proteinopathies due to their commonality of exhibiting protein aggregates in late-stage disease and dysfunction in proteolytic mechanisms. In association with protein aggregates, neuroinflammation, the activation of resident astrocytes and microglia, is key in these disorders and has demonstrated pathological roles. However, there is limited research on how neuronal proteotoxicity impacts on glial cells prior to the accumulation of characteristic intraneuronal inclusions. The Psmc1$^{fl/fl}$;CaMKIIα-*cre* mouse model shows a gradual depletion in 26S proteasome in the forebrain and hippocampal neurons resulting in time-dependent proteotoxicity, inflammation, and neurodegeneration. This thesis aimed to examine glial responses in this mouse model during the onset of neuronal dysfunction and neuroinflammation. Firstly, protein expression profiling using SWATH-MS was employed in 2-,3-,4- and 5-week old Psmc1$^{fl/fl}$;CaMKIIα-*cre* mice, which revealed several upregulated neuroinflammatory responses at a molecular level, such as the heat-shock response, necroptosis, neutrophil degradation in association with a downregulation in CaMKIIα-*cre* neuronal components. GFAP, a major astrocyte protein, was consistently upregulated throughout disease progression. Secondly, GFAP, STAT3α and pSTAT3 tyrosine705 expression was quantified to be significantly higher from 3 weeks of age via western blotting and the number of GFAP^{+}/STAT3α^{+} cells was significantly increased in 3 and 4-week Psmc1$^{fl/fl}$;CaMKIIα-*cre* mice, showing a selective increase in astrocytic-STAT3 in the dentate gyrus and CA3 region of these mice. Thirdly, quantitative PCR of astrocytic-STAT3 coupled inflammatory mediators was performed in Psmc1$^{fl/fl}$;CaMKIIα-*cre* mice, whereby TNF-α mRNA expression reported consistent significant results. Finally, astrocytic-STAT3 agonists and inhibitors (ADP/ATP/IL-6/TNF-α/CXCL10 and STATTIC) were applied to 3-week-old acute slices, and astrocytic-STAT3 phosphorylation was confirmed through western blot for the cytokines and chemokines (IL-6/CXCL10/TNF-α) however showed no results for ADP/ATP/STATTIC. Collectively, these results suggest Astrocytic-STAT3 phosphorylation precedes neuron degeneration in the Psmc1$^{fl/fl}$;CaMKIIα-*cre* mice model which warrants further investigation into the role of astrocytes in neurodegenerative disorders.

Acknowledgements

I would like to thank my initial supervisor Dr Lynn Bedford, who sadly is no longer with us. Her spark and passion for her mice model inspired me to carry the project on in her absence. I would also like to thank the fantastic academic staff who stepped in to help me, Dr Tomas Bellamy and Dr Sébastien Serres. I thank them both for their patience with me and their outstanding dedication in supervising a project that was not their speciality. I still cannot decide if continuing the project was idiocy or bravery, but whatever the verdict, it could not have been possible without these two.

I would like to thank the NSG@QMC charity for funding this project, and I have enjoyed my outreach activities with them. I would like to thank Dr Asli Ugun-Klusek from Nottingham Trent University, for her endless cups of coffee and for her help with the SWATH-MS data analysis. Other technical staff to acknowledge include Dr Alex Rathbone and Karen Lawler – two ladies I would be completely lost without. Of course, a major thank-you to all staff in the B.S.U, who were key in making this thesis a reality.

I would like to thank my family, Angela, Alan and Amber. They are continuously supportive, even though I suspect they are not too sure what my work is about. I would like to thank the women at Nottingham's Women Centre, who remind me weekly that life is not all about brains and proteins. Most importantly, I would like to thank the people I work with, for bringing humour and support on dark days. The names are endless, but you know who you are.

Of course, the write-up of this thesis would not have been possible without my unofficial sponsors - Monster Energy Ultra, Cadbury crème eggs, Red bull sugar-free, Café Nero and Mars ice cream bars. I'll finish my acknowledgements with my favourite piece of advice a post-doc gave me:

'I don't think there is a right way to do a PhD… the whole point of a PhD is to keep messing up, being told you are wrong and seeing if you can handle that. At some point, you should become so dead inside that you no longer feel the pain of the rejection... you'll be fine though.'

Table of Figures

Chapter 1

Chapter 2

Chapter 3

Chapter 4

Chapter 5

Chapter 6

Table of Contents

Chapter 1 Introduction

1.1 Proteins: folding and their subsequent degradation

1.1.1 Proteins are key in all of life and fold into their native structure

The first documented use of the word 'protein' has been cited to Mulder, 1838 to describe the common substance of plant albumin, animal albumin, silk, and blood serum. In his seminal paper, he declared that this was the 'foodstuff' of the whole animal kingdom and reasoned that it was only produced by plants. Now, over 200 years on, we know proteins are the key foundation for all life, synthesized from the amino acids encoded by the DNA of every living organism to perform essential roles in molecular biology (Mulder, 1838; Vickery, 1950). Proteins are estimated to comprise ≈55 % of the dry weight of a cell which constitutes all receptors, enzymes and these hold numerous additional roles in structure, transport, and scaffolding (Pal, 2021).

A protein's conformational shape is important for the physiological role they undertake. The amino acid sequence of a protein determines its native structure, with polymers of α-amino acid monomers folding into their secondary structure through hydrogen bonds, to either from an α-helix or β-sheet. After this, polypeptides fold into their 3D structure, the tertiary structure, using hydrophobic and hydrophilic interactions, disulphide bridges and ionic bonds. Multiple polypeptide chains can oligomerize through the interactions of hydrogen bonds and van der Waals forces, forming the quaternary structure of complex proteins (Sun, Foster and Boyington, 2004). This process is extremely quick, with 'slow folding' proteins taking a millisecond to complete (Naganathan et al., 2006; Chong, Im and Ham, 2019).

However, primary amino acid sequence dictating the native structure of protein-folding only accounts for under 50% of all proteins, with 32% of human-protein coding genes dubbed 'intrinsically disordered' and an additional 19% of human protein-coding genes containing 'intrinsic disordered' regions of up to 30 amino acids long (Habchi et al., 2014; Uversky, 2019; Deiana et al., 2019). The evolution of these intrinsically disordered proteins and regions has been proposed as advantageous for their increased flexibility in binding to multiple cellular partners and providing sites for post-translational modification (Wright and Dyson, 2014; Deiana et al., 2019). Protein folding is prone to errors, and so may require assistance

from molecular chaperones (Gidalevitz, Prahlad and Morimoto, 2011; Hartl, Bracher and Hayer-Hartl, 2011).

1.1.2 Proteins are dynamic

Scientists originally believed proteins were simply static unchanging entities in cellular biology. One revolutionary study conducted by Schoenheimer and colleagues showed that mice fed with N-15 labeled amino acids incorporated these into their cellular physiology (Schoenheimer et al., 1938). This led to supporting data, with the scientific community agreeing in 1942 that proteins were dynamic and replaceable (Shemin & Rittenberg, 1942). After this, the question of how proteins were degraded was at the forefront of the scientific community. The first clue came from the examination of a rat liver, whereby phosphatase-enriched fractions were observed. This began the identification and classification of the autophagosome-lysosomal pathway (Novikoff, Beaufay and de Duve, 1956; de Duve, 1963). Lysosomes were shown to degrade cytoplasmic components through the secretion of extracellular proteases, therefore providing a mechanism of action (Ashford and Porter, 1962; de Duve and Wattiaux, 1966).

It was a surprise then when a non-lysosomal proteolytic system was identified, unique in its specificity for individual proteins utilising ATP, a class of cytosolic enzymes and a ‘tagging’ polypeptide (Etlinger and Goldberg, 1977; Ciechanover et al., 1981; Hershko et al., 1983). This process was collectively termed ubiquitin-dependent degradation, carried out by the ubiquitin-proteasome system (UPS).

1.1.3 Ubiquitin and Ubiquitination

Ubiquitin was first identified as a heat-stable polypeptide and has since been confirmed to be evolutionary conserved across species, only varying in 1 and 3 amino acids between yeast and humans (Ciechanover et al., 1981; Zuin, Isasa and Crosas, 2014). The addition of ubiquitin to a substrate is called 'ubiquitination' and is recognized as a post-translational modification. Ubiquitination forms an isopeptide bond between the C-terminal glycine of ubiquitin and the ε-NH2 group of a lysine residue in the protein substrate(Ciechanover and Schwartz, 1998). This ubiquitination can either be singular (monoubiquitination) or contain multiple connecting monomers (polyubiquitination).

1.1.4 Ubiquitin-ligase pathway

Ubiquitination is conducted through the ubiquitin-ligase pathway, which comprises three classes of enzymes: Ubiquitin-activating enzymes (E1), Ubiquitin-conjugating enzymes (E2), Ubiquitin ligase enzymes (E3). To date, a range of these enzymes has been identified in humans and mice (table 1.1).

Table 1.1 Ubiquitin-ligase-related pathway proteins in *homo sapiens* and *mus musculus*
(Semple et al., 2003; Tai et al., 2010).

Class	***Homo sapiens***	***Mus musculus***
E1	16	16
E2	53	61
E3	527	442

The variations of these enzymes show differences in structural, biochemical, and functional properties (Stewart et al., 2016). In brief, ubiquitin is conjugated to the E1 enzyme (ubiquitin-activating enzyme) via ATP hydrolysis. E1 Enzyme transfers ubiquitin to a cysteine residue on the corresponding E2 enzyme (Ubiquitin-conjugating enzyme).

E3 enzyme (Ubiquitin ligase enzyme) transfers the bound ubiquitin molecule on E2 to the amine side chain of a lysine residue on a target protein substrate (figure 1.1). E3 enzymes are the most numerous members of the ubiquitin-ligation pathway, and this is speculated to be due to their specificity in targeting individual proteins. E3 enzymes recognize target protein substrates via N-degrons, phosphodegrons, oxygen and small molecule-dependent degrons, structural motifs and misfolded degrons (Sriram, Kim and Kwon, 2011; Christian Reinhardt and Yaffe, 2013; Lucas and Ciulli, 2016; Zheng and Shabek, 2017; Okoye et al., 2022).

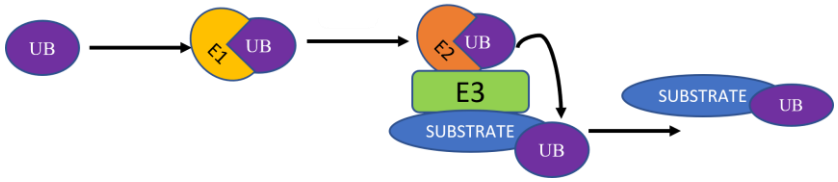

Figure 1.1: Ubiquitin-ligase pathway is responsible for the conjugation of ubiquitin to substrates. A cascade of enzymatic reactions between E1 (ubiquitin-activating enzyme), E2 (ubiquitin-conjugating enzyme) and E3 (ubiquitin ligase enzyme) makes up the ubiquitin-ligase pathway and tags proteins (substrates). *Diagram adapted from Dougherty et al., (2020)* .

Monoubiquitination of proteins has shown extensive roles in DNA repair, gene expression, and endocytosis. This will not be covered in the scope of this thesis however for a full review regarding the roles of monoubiquitination, please refer to the critical review by Sadowski and colleagues (Sadowski et al., 2012). After monoubiquitination, the repeated addition of ubiquitin can be carried out through E3 enzymes to elongate the ubiquitin chain, this occurs through forming isopeptide chains through ubiquitin lysine residues: K6, K11, K27, K29, K33, K48 and K63 (figure 1.2a). The process, collectively termed polyubiquitination, is illustrated in figure 1.2b. The polyubiquitination of the K48 residue is evidenced to have a role in targeting the substrate protein for degradation via the 26S proteasome.

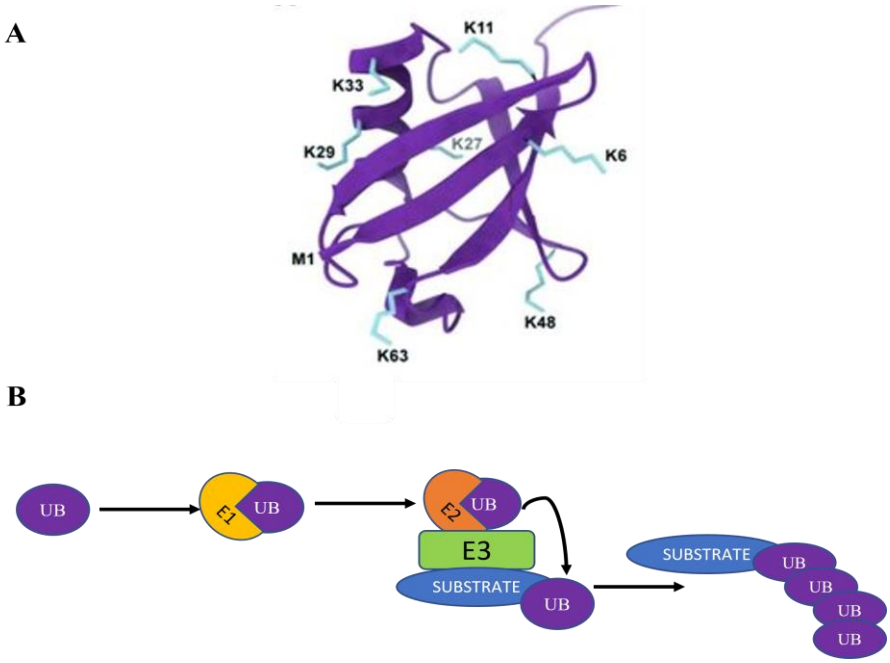

Figure 1.2: Ubiquitin possesses 7 lysine residues which are used for chain extension and responsible for polyubiquitin signaling processes. 1.2A) Structural ubiquitin motif displaying lysine residues, 1.2B) Ubiquitin-ligase pathway is responsible for the polyubiquitination of substrates targeted for proteasomal degradation. *Both diagrams adapted from Dougherty et al.(2020).*

1.1.5 The 26S proteasome

The 26S Proteasome is a multimeric protein complex present in the nucleus and cytosol of eukaryotic cells. It is an essential and abundant complex. The 26S Proteasome is comprised of two subcomplexes: a barrel-shaped 20S proteolytic particle and a 19S regulatory subunit, which recognizes ubiquitinated proteins in the cytosol. The 19S attaches to either end of the 20S barrel to provide ubiquitin-specific degradation. The subunit complex is detailed in figure 1.3.

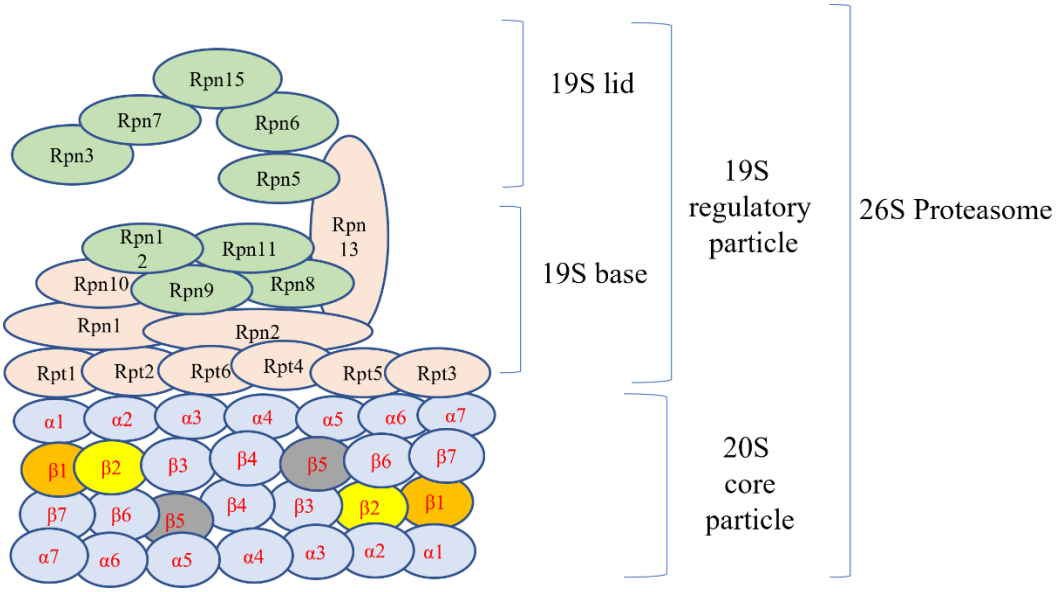

Figure 1.3: 26S proteasome subunit complex of the 20S core particle and the 19S regulatory particle. The 19S regulatory particle is composed of the lid (green subunits) and base (peach subunits). The 20S core particle contains proteolytic subunits which exhibit caspase-like (β1), trypsin-like (β2) and chymotrypsin-like (β5) protease activities. *Figure adapted from Gomes (2013).*

1.1.5.1 The 20S proteasome

The 20S Proteasome is a barrel-shaped complex constituting twenty-eight protein subunits α1/Psma1- α7/Psma7 and β1/Psmb1- β7/Psmb7 (Bedford et al., 2010). The proteins are stacked in 4 heptameric rings, with α1/Psma1- α7/Psma7 as outer rings, and β1/Psmb1- β7/Psmb7 as inner rings. The outer rings contain subunits that are responsible for binding to the regulatory particle, whereas the inner β subunits are proteolytic. β1/Psmb1, β2/Psmb2, and β5/Psmb5 exhibit caspase-like, trypsin-like and chymotrypsin-like activity respectively (Zheng et al., 2012). It is speculated the other subunits are responsible for structural integrity (Baldovino et al., 2006). Proteins are 'threaded' through the toroid structure to enable proteolysis (figure 1.4).

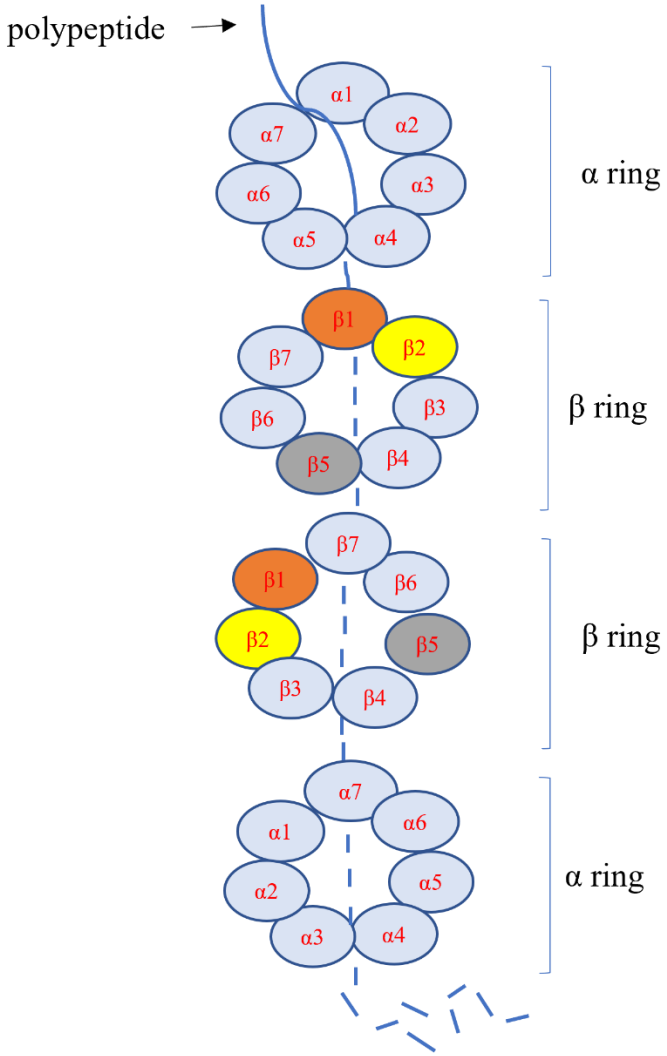

Figure 1.4: Schematic diagram of the 20S proteasome proteolytic activities. The polypeptide is translocated through the core of the 20S proteasome, passing structural α-ring to be digested by in-situ proteases Caspase like (β1), trypsin-like (β2) and chymotrypsin-like (β5). The remaining peptide fragments are cleaved by endogenous cytosolic enzymes.

This proteolysis leads to a generation of peptides 3 to 25 amino acids long, which are digested into their amino acid constituents by cytosolic endopeptidases and aminopeptidases. These amino acids serve as metabolic substrates or are utilized in new protein synthesis (Lecker, Goldberg and Mitch, 2006). The 20S core can act as a proteasome independently of the 19S regulatory caps, degrading hydrophobic oxidized proteins in a ubiquitin-independent fashion (Raynes, Pomatto and Davies, 2016).

1.1.5.2 The 19S regulatory particle

The 19S regulatory subunit is made up of at least eighteen protein subunits, whereby their arrangement has been described as a base and lid mechanism. The base and lid contain a range of subunits responsible for interacting with ubiquitin-tagged substrates. Rpn10/Psmd4 and Rpn13/Adrm1 function as ubiquitin receptors, Rpn1/Psmd2 and Rpn2/Psmd1 direct ubiquitin-tagged substrates into the base of the 19S regulatory particle, whereas Rpn11/Psmd14 removes the ubiquitin from the target protein (Finley, 2009; Liu & Jacobson, 2013; Rosenzweig et al., 2012) (figure 1.5).

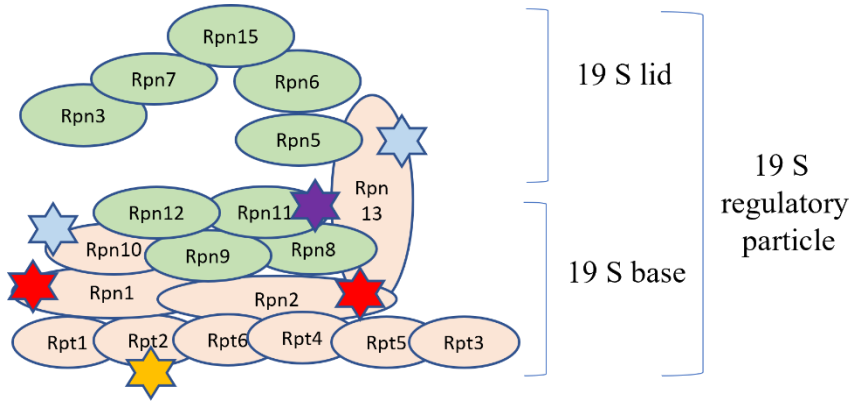

Figure 1.5: 19S regulatory particle is composed of at least 18 protein subunits. Subunits in green are part of the 19S lid complex whereas subunits in pink are part of the 19S base. Coloured stars dictate functions important to note: purple star depicts ubiquitin-deubiquitinating subunit from target protein (Rpn11); blue stars depict ubiquitin receptors (Rpn13/Rpn10), red stars depict subunits responsible for directing the ubiquitin-tagged protein to the 20S core (Rpn1/Rpn2) and yellow star depicts AAA-ATPase subunit responsible for opening the 20S core (Rpt2). *Figure adapted from Gomes et al (2013).*

The base contains a ring of six AAA-ATPase subunits (Rpt1-6) which are responsible for facilitating substrate unfolding and translocation to the 20S core particle. The assembly of these ATPases to form this base has been attributed to three separate dimers comprising of Rpt1 and Rpt2, Rpt 4 with Rpt5, and Rpt 3 with Rpt6, with studies citing deletion of the C-terminal amino acid reporting chronic 19S base assembly defects (Thompson, Hakala and DeMartino, 2009). For this thesis, one of the core ATPases will be highlighted: Rpt2/Psmc1. Rpt2/Psmc1 is responsible for controlling substrate entry into the 20S core particle by opening the pore gated by the 20S α/PSMA subunits (Tanaka, 2009).

1.1.5.3 26S proteasome assembly

The 20S proteasome acts as a platform for the foundation of the 19S regulatory particle. The regulatory particle is assembled base first. Without the base (Rpt1-Rpt6) formation, the lid

cannot bind and thereby the 19S complex is incomplete. The assembly of the 26S Proteasome is achieved through a specific interaction between core particle and regulatory particle subunits: Rpt6/Psmc5 interacts with α2/Psma2, Rpt2/Psmc1 interacts with α7/Psma7 and Rpt5/Psmc3 interacts with α2/Psma4 (Elkharaz, 2013).

1.1.6 26S proteasome in neurons

Neurons are key excitable cells in the central nervous system and the majority of the estimated 100 billion cells in the human CNS are present at birth (Herculano-Houzel, 2009; Aimone et al., 2014). Neurons are post-mitotic cells and therefore unable to divide to escape proteotoxic stress, therefore proteostasis mechanisms in neurons need to be exemplary to ensure cellular survival (Aranda-Anzaldo, 2012).

Proteasome activity in the synaptic terminals is significantly higher than that of the nucleus in mice neurons. The reasons for this have been speculated to be due to the role of the proteasome in neuronal cells. Upon neuron depolarization, proteasomes translocate to neuronal dendritic spines where ubiquitin-proteasome proteolytic activity has been shown to have roles in synaptic plasticity, dendritogenesis and the expression of neurotransmitters receptors (Djakovic et al., 2009; Upadhya et al., 2006; Limanaqi et al., 2019). In support of this principle, injection of Lactacystin, a proteasome inhibitor, into the CA1 region of the hippocampus led to full retrograde amnesia in experimental animals. Furthermore, in untreated animals, avoidance training increased 26S proteasome proteolytic activity, thereby indicating the 26S proteasome's role in memory formation (Lopez-Salon et al., 2001). Overall, it can be summarized that proteasome proteolytic activity is essential in neuronal health and deficiencies in this process are related to nervous system disorders, such as neurodegenerative disease.

1.2 Neurodegenerative disorders

1.2.1 The cost of neurodegenerative disorders – more than money

Throughout life, we spend much of our time forming memories: how to use a knife and fork, our child's name, and the faces of our family. These things may appear trivial, but they are the pieces of the jigsaw that makes up a personality, a person – a self-identity. Many of us are lucky enough to die with our self-identity intact, a knowledge of our life and how we have spent it. However, there is a large proportion of people who do not.

Neurodegenerative disorders, such as Alzheimer's disease (AD), Parkinson's disease (PD), Huntington's disease (HD) and Dementia with Lewy bodies (DLB) share a unifying characteristic of neuronal death. As neurons cannot divide and are therefore irreplaceable; this leads to a declining pathology which leads the patient through a slow onset of disability.

One of the main symptoms of neurodegenerative disorders is dementia, the loss of cognitive faculties. One neurodegenerative disorder that has captured public awareness is AD. One of the major cornerstones is this is the work of William Utermohlen, an exemplary artist, that demonstrated a unique insight into this process. William was diagnosed with Alzheimer's disease in 1995 and drew self-portraits each year until his memory failed him (figure 1.6).

Figure 1.6: William Uttermohlen documents his progression through neurodegeneration (left to right). His paintings are regularly referred to in medical literature and are praised as a unique insight (Harrison, 2013).

William did not die until 2007, highlighting that his health deteriorated for an additional seven years after his final piece. His art demonstrates what many patients deal with – a slow, long progressive illness leading to disability of the brain and body. It is important to note that dementia is not unique to AD, but also manifests in other diseases such as PD, DLB and HD (Davis and Denning, 2021; Weintrab and Irwin, 2022). Due to these conditions being so incapacitating, regularly loved ones step in as full-time carers, forfeiting their jobs and livelihood. From a socioeconomic standpoint, this domino effect leads to a great cost of resources, finance, and a reduction in the workforce.

The financial cost of dementia in the UK is expected to more than double in the next 25 years, from £26bn to £55bn in 2040. Dementia has higher health and social care costs (£11.9bn) than cancer (£5.0bn) and chronic heart disease (£2.5bn) combined. If the onset of dementia could be delayed by 2 years, the savings would be £12.9bn a year by 2050 (£46.5bn from £59.4bm) (Buylova Gola et al., 2020). Emotionally, these times are taxing for patients' families and friends, with many patients committing suicide or opting for assisted dying (Tohid, 2016; Loizeau et al., 2019; Nuebling, Butzhammer and Lorenzl, 2021).

Neurodegenerative disorder onset has displayed a definite link with increasing age with people over 65 being at the greatest risk (Currais et al., 2017; Groh et al., 2017). It has been coined as 'the oncoming wave' with predictions that by 2030, 25% of Europe's population will be over 65 years old, therefore leading to an inevitable increase in these conditions (Foster, 2017). In a more topical approach, a population-based study on COVID-19 positive outpatients revealed these patients were 2-3 times more likely to be diagnosed with neurodegenerative disorders, therefore adding to strain to an already dire situation (Zarifkar et al., 2022).

Despite continued work into potential therapies, in 2020, it was reported that there had been no new approved treatments for neurodegeneration in the UK since 2003 (Yiannopoulou and Papageorgiou, 2020). Even so, all approved treatments for neurodegenerative disorders work at a symptomatic level; in example in Alzheimer's disease, Acetylcholinesterase inhibitors are prescribed to inhibit acetylcholine degradation, therefore restoring synaptic levels to compensate for the death of acetylcholine neurons. In the same vein, Levodopa is prescribed for patients with Parkinson's disease, which is metabolized to dopamine to compensate for the death of dopamine neurons (Rees and Brimijoin, 2003; Poewe et al., 2010). It is important to note that none of these medications slow or stop the loss of neurons. As a remedy for psychiatric symptoms of dementia such as depression, selective serotonin reuptake inhibitors (SSRI's) are used which are typically paired with psycholeptic medications to reduce anxiety (Ruangritchankul et al., 2020). With this polypharmacy at play, current medication regimes are documented to exacerbate the neurodegenerative symptoms leading to patient hospitalization (Renom-Guiteras et al., 2018). Most recently, one new medication, Aducanumab, has been approved in the United States for treatment for early onset Alzheimer's disease, where it has boasted to be "the first ever disease modifying drug for Alzheimer's disease", however the scientific community are dubious about the drug's efficacy (Walsh et al., 2021).

1.2.2 Neurodegenerative disorders are proteinopathies

The classification and diagnosis of neurodegenerative disorders are complex, as whilst patients can be diagnosed throughout their lifetime, validation of this diagnosis is only reached post-mortem through pathological staining. Major neurodegenerative diseases are diagnosed based on neuroanatomical location (as reviewed in Poddar et al., 2021). Despite changes in neuroanatomical location, these diseases share a commonality of protein aggregates found in or around neurons of the neurodegenerative area. One protein for each disease has been a simplifying assumption in the past (table 1.2); however, the current research indicates that the co-existence of different proteins within aggregates across multiple neurodegenerative diseases is observed (Charles et al., 2000; Higashi et al., 2007; Jellinger and Popescu, 2012; Colom-Cadena et al., 2013).

Table 1.2: Neurodegenerative disease is associated with aggregated proteins.

Table adapted from (Tai et al., 2010).

Aggregate protein	Aggregate location	Related disorder
Tau	Intracellular tangles	Alzheimer's disease (AD)
α-Synuclein	Intracellular Lewy bodies	Parkinson's disease (PD), Dementia with Lewy bodies (DLB)
Amyloid β	Extracellular plaque	Alzheimer's disease (AD)

1.2.3 Neurodegenerative disorders are the result of deficient proteostasis

As it has been previously established that 'one protein for one disease' is not a unique driver for neurodegenerative pathology, a more sophisticated argument is needed to explain the aetiology of neurodegenerative disease. A current line of evidence suggests that neurodegenerative disorders are the result of deficient proteostasis; which can be grouped as either an overload of intact proteostasis mechanisms or as a dysfunction of the degradation machinery. The evidence for this is as follows:

1.2.3.1 Familial Parkinson's disease is linked to dysfunctional proteins in the UBL pathway

Mutations in the E3 ligase protein, Parkin, are associated with autosomal-dominant Parkinson's disease (Dawson and Dawson, 2010). To date, there have been up to 130 mutations mapped to the Parkin gene, one of which results in truncation of the protein, which renders it prone to aggregation (Riley et al., 2013; Biran et al., 2017). In addition to this, other mutations have

shown a loss of function of the protein, therefore leading to no functional E2-E3 ubiquitin-ligation pathway. Consequently, ubiquitinated alpha-synuclein is undetected by the 26S proteasome, leading to an accumulation. This combined loss of function is seen as the main contributor to α-synuclein aggregates in Parkinson's disease (Klein and Westenberger, 2012; Fiesel et al., 2015).

1.2.3.2 A spectrum of neurodegenerative disease aggregates share the commonality of poly-ubiquitinated proteins

Under histopathological diagnosis, ubiquitin-positive aggregates are a common feature in Alzheimer's disease, Parkinson's disease and other neurodegenerative diseases (Lowe et al., 1988). As proteins submitted to the 26S proteasome are de-ubiquitinated before translocation, this implicates that the proteasome is defective in these diseases. Alongside poly-ubiquitin, other components of the Ubiquitin-proteasome pathway have been visualised in proteinopathies, such as ubiquitin carboxyl-terminal hydrolase-1 (UCH-L1). However, it must be noted that authors only found this in 10% of cases, suggesting that this protein could be a biomarker implicating the stage of pathological inclusion (Dickson et al., 1994).

1.2.3.3 Proteostasis decreases with old age, a major risk factor for neurodegenerative disease

One of the largest risk factors of non-familial neurodegenerative disease is increasing age. Increasing age is associated with impaired proteostasis in neuronal cells due to the inherent accumulation of misfolded proteins (Klaips, Jayaraj and Hartl, 2018). This is also reflected in the number of the 26S proteasomes – a wide selection of studies have revealed the 20S core particle is the major cellular protease in aged mammals (Fernández-Cruz & Reynaud, 2021; Miller et al., 2005; Sacramento et al., 2020; Saez & Vilchez, 2014; Vernace et al., 2007). Age-related reduction of the 26S proteasome complex thereby limits ubiquitin-mediated degradation via the proteasome, thereby leading to an accumulation of polyubiquitinated proteins. This accumulation of polyubiquitinated proteins can lead to aggregates, whereby aged brains demonstrated inherent protein aggregation (David et al., 2010). In support of this, overexpression of 19S subunit Rpn11 in aged drosophila reduced age-related reduction of the 26S proteasome activity, resulting in the extension of flies with suppression of the age-dependent accumulation of ubiquitinated proteins (Tonoki et al., 2009).

1.2.3.4 Proteasome inhibitor studies replicate neurodegenerative disease pathology

With the above evidence indicating that a decline in proteasome may be responsible for protein aggregation and subsequent neurodegenerative disease, it made great sense to assess proteasome inhibitors in neuronal cell lines. A breakthrough study using Lactacystin, a pharmacological inhibitor of β5 active sites in the 20S core, displayed intracellular Lewy-body inclusion formation and cell death in dopaminergic neuronal culture (McNaught, Mytilin, et al., 2002; Fornai et al., 2003). This was then further supported by the use of a systematic injection of proteasome inhibitor PSI (Z-lle-Glu(OtBu)-Ala-Leu-al), which mirrored pathological defects of human disease in rats (McNaught, Björklund, et al., 2002; McNaught et al., 2004). However, this pathological response from systematic injection was unable to be replicated in other laboratory groups, therefore casting doubt on the construct validity of these findings (Bové et al., 2006; Kordower et al., 2006; Manning-Boğ et al., 2006). Despite this, it has been repeatedly shown that *in-vivo* injection of proteasomal inhibitors to the mesencephalon causes Lewy-like aggregation and dopaminergic death (Xie et al., 2010; Bentea, Verbruggen and Massie, 2017).

1.2.4 Are insoluble aggregates to blame?

Most of the previous work within the neurodegenerative disease field has centered solely on the characteristic insoluble protein deposits to be the root of disease pathology. Amyloid precursor protein aggregates are documented to cause neuronal death, and in addition to this aggregated huntingtin proteins have reported roles in disrupting axonal transport, particularly in mitochondria translocation to synapses (Guo et al., 2020; Morfini et al., 2009; Shearman, 1999). Secondly, aggregated proteins have shown to inhibit the 26S proteasome, due to their inability to be denatured and admitted to the 20S proteolytic cavity, therefore providing additional disruptions to proteostasis attempts (Keck et al., 2003; Menzies et al., 2017; Myeku and Duff, 2018; Thibaudeau, Anderson and Smith, 2018). Thirdly, behavioural studies in animals and clinical trials show that removal of inclusions delays cellular pathology and this reduction in pathology is associated with improved symptoms in behavioural assays, e.g; memory recall and motor-related deficits (Masliah et al., 2005; Asuni et al., 2007; Masliah et al., 2011). Overall, this set of literature supports the hypothesis that inclusions are the main driving force in neurodegenerative pathology.

However, this is only half of the story. If insoluble aggregates are to blame, why are they present in the surviving cells that are seen in histological diagnosis? Amyloid pathology is measurable in Alzheimer's disease years before the cognitive decline, and even so, amyloid pathology is also present in non-demented individuals (Aizenstein et al., 2008; Beason-Held et al., 2013; Farrell et al., 2017). In addition to this, immunisation with AB1-42 antibody in AD patients has resulted in aggregate clearance, however, this clearance did not prevent cognitive decline in clinical trials (Gilman et al., 2005; Holmes et al., 2008). Secondly, examination of inclusions in Huntington's disease has shown aggresome-like morphology and these inclusions have shown to reduce the risk of soluble aggregates and subsequent neuronal death, thereby suggesting this inclusion formation may be a protective mechanism (Arrasate et al., 2004). Thirdly, diffusible aggregates have been found in the brains of patients before Lewy body inclusion formation, therefore supporting the notion that diffusible oligomers may be the culprit of damage rather than aggregates (Bengoa-Vergniory et al., 2017). In support of this, the addition of pre-formed amyloid fibrils plaques to organotypic slices did not reduce long-term potentiation, however, soluble oligomers of the same protein did (Shankar et al., 2007). Confirming this in a pathological setting, the m266 amyloid-beta antibody, an antibody targeted towards soluble αmyloid-β, reversed memory deficits in animal models without the alteration of amyloid-β insoluble plaques (Dodart et al., 2002). Overall, this plethora of data points to small oligomers as the disease initiators in neurodegenerative disease.

In summary, the argument of 'friend or foe' of the insoluble aggregate in neurodegenerative disease pathology is still a matter of debate. However, the evidence listed in the previous section detailing that insoluble aggregate appears to be of beneficial benefit carries great weight, especially with the results from Dodart and colleagues reporting that targeting soluble amyloid-β reversed memory defects. It appears that soluble oligomers appear to be the foe in this situation and can be speculated that insoluble aggregates have been branded to be 'guilty' by association with the consequences of soluble oligomers.

1.3 Neuroinflammation in Neurodegenerative disease

1.3.1 History of neuroimmunology

Neuroimmunology was not formally recognized as a field of research until 1981, however, the experiments that would form the basis of this science started 60 years prior. Japanese scientist Shirai was the first to acknowledge that foreign tissue grafted onto the brain did not produce an immune response, thereby indicating that the brain was not immune competent to the same extent as other tissues. However, in 1948 Medawar replicated this experiment and found that when the same foreign tissue was grafted under the skin of the animal, both tissues were rejected. Medawar deduced that the brain was not devoid of an immune response, but in fact, insensitive to the foreign entity that was detected by the periphery (Murphy & Sturm, 1932.; Medawar, 1948). This led to the term 'immunoprivileged', which is now still used today to describe the brain's unique state (Billingham & Boswell, 1953). Immunoprivileged tissue has a higher threshold for the induction of inflammation than its non-immunoprivileged counterparts. In the case of the brain, the blood-brain barrier (BBB) provides a tight molecular mesh that restricts access of immune cells and immune mediators into the central nervous system (CNS), thereby enabling the brain to be ignorant of peripheral threats (Muldoon et al., 2013). It is now known that the brain consists of resident immune cells, called glia, which have in the last 30 years been found to have a multitude of functions in healthy physiology and disease states.

1.3.2 The resident glia cells in healthy physiology

Virchow was the first scientist to identify glial cells. Under examination, he noticed non-neuronal cells within the brain that he named 'connective cellular elements' from white matter. Due to the differences in connective substance, he named the cells 'Nervenkitt', which translates to 'Nerve glue/Nerve cement' (Somjen, 1988). We now know that "glia" is a class of several different cell types with distinct roles in the brain.

1.3.2.1 Microglia

Rio-Hortega classified a glia cell that mirrored peripheral macrophage qualities, i.e: acting as antigen-presenting cells and as 'scavengers' in the face of pathogenic material. These cells were coined Microglia.

Microglia are CNS-resident macrophages and comprise 10-15% of the brain cells. Microglia are derived from the embryonic yolk sac and colonize the rodent CNS at approximately E10, initially displaying an amoeboid phenotype (Schulz et al., 2012). Microglial undergo rapid proliferation in the first 2 weeks of post-natal development, and within these two weeks transform to a ramified phenotype with multiple cytoplasmic processes. Microglial density decreases in week 3 (Leong and Ling, 1992; Nikodemova et al., 2015). This rapid upregulation is associated with their role in synaptic pruning, and the elimination of synapses, which is supported by age-matched microglia knock-out models reporting increased dendritic spines and immature synapses (Paolicelli et al., 2011). As well as pruning synapses, microglia cells have shown additional neurodevelopmental roles in axonal guidance and the secretion of neurotrophic factors to encourage synaptogenesis (Ueno et al., 2013; Reemst et al., 2016). Within the post-natal rodent brain, microglia occupy individual microdomains within the cortex and continuously survey the surrounding microenvironment for extracellular changes (Nimmerjahn, Kirchhoff and Helmchen, 2005).

Microglia possess a multitude of receptors, with a few of interest to this thesis listed in table 1.3. It must be noted that this table does not represent all microglia receptors, and for a more comprehensive review, the reader is referred to the references listed in the table. In addition to these receptors, microglia can respond to extracellular stimuli by the release of a range of inflammatory/anti-inflammatory mediators, which is reviewed extensively elsewhere (Verkhratsky and Butt, 2013; Domercq, Vazquez-Villoldo and Matute, 2013; Logiacco et al., 2021).

Table 1.3: Microglia possess a range of receptors (Lee, Nagai and Kim, 2002; Verkhratsky and Butt, 2013; Liu, Leak and Hu, 2016)

Receptor name	Receptor ligand
P2Y	ATP, ADP
P2X	ATP
AMPA	Glutamate
Cytokine receptors (IL-1R, IL6-R, TNFR)	IL- 1β, IL-6, TNF-α
Chemokine receptors (CXCR3)	CXCL10
Toll-Like Receptors (TLR1,2,4,5 and 6)	Respective DAMPS/PAMPS

Acronyms: P2 – Purinoreceptors. ATP – Adenosine triphosphate, ADP - Adenosine diphosphate, IL- Interleukin, CXC3R - CXC chemokine receptor 3, CXCL10 – CXC chemokine ligand 10. DAMPS – damage-associated molecular patterns, PAMPS – pathogen-associated molecular patterns.

1.3.2.2 Astrocytes

Ramon y Cajal and Camillo Golgi described an additional subtype of these cells that had close proximity with endothelial cells, now termed as Astrocytes. Astrocytes, or astroglia, are star-shaped cells which make up 40 % of all brain cells (Khakh and Sofroniew, 2015). Astrocytes contain a dense network of intermediate filaments, with the major two being glial fibrillar acidic protein (GFAP) and vimentin (Taft, Vertes and Perry, 2005; Sofroniew and Vinters, 2010). GFAP is regularly used as a gold-standard astrocyte marker for cell identification, however, this intermediate filament is only found in the major branches of the cell and can be absent from fine processes.

Astrocytes are derived from radial glia in the ventricular zone with GFAP being weakly expressed at E18 (Breunig et al., 2012). It has also been reported that subventricular zone progenitor cells can also develop into astrocytes, typically for the first two weeks postnatally (Levison et al., 1993). The glial cell population, in which astrocytes as the most abundant cell type, expands 6-8-fold in the rodent brain during the first three weeks of postnatal development, exhibiting mature gene expression at P17 followed by the blood-brain barrier forming at P20 (Cahoy et al., 2008; Bandeira, Lent and Herculano-Houzel, 2009). Previous experiments have dictated that the average glia-cell cycle is 20 hours and with the use of the GFAP-GFP mice model, the origin of this expansion was shown to be developed from already differentiated astrocytes in the cortex (Korr et al., 1975; Ge et al., 2012). Astrocytes devoid of GFAP show greater sprouting of spinal axons in neighbouring neurons, which supports astrocytes roles in

synapse pruning and forming in neurodevelopment (Bushong, Martone and Ellisman, 2004; Clarke and Barres, 2013). Astrocytes also have established roles in guiding postnatal neuroblasts in the retina, thereby facilitating neuronal differentiation in other areas of the brain (Gengatharan et al., 2016; Li et al., 2019).

A single astrocyte can enwrap on average 4-8 neuronal somata, and single neuron dye fills have revealed that one astrocyte contacts 300–600 neuronal dendrites (Halassa et al., 2007). This close contact with neurons enables them to carry out their functions through responding to and modulating neuronal activity by the release of hormones, cytokines, peptides, growth factors and neurotransmitters at the synaptic cleft (Joe et al., 2018; Upadhya et al., 2020; Verkhratsky et al., 2016; Volterra & Meldolesi, 2005).

To respond to neuronal activity, astrocytes possess a multitude of receptors, with a few of interest to this thesis listed in table 1.4. It must be noted that this table does not represent all astrocyte receptors, and for a more comprehensive review, the reader is referred to the references listed in the table.

Table 1.4: Astrocytes possess a multitude of receptors (Verkhratsky and Butt, 2013; Li et al., 2021)

Receptor name	**Receptor ligand**
P2Y	ATP, ADP
P2X	ATP
AMPA	Glutamate
Toll-Like Receptors (TLR 2 and 4)	DAMPS/PAMPS
Cytokine receptors (IL-1R, IL6-R, TNFR)	IL- 1β, IL-6, TNF-α
Chemokine receptors (CXCR3)	CXCL10

Acronyms: P2 – Purinoreceptors. ATP – Adenosine triphosphate, ADP - Adenosine diphosphate, IL- Interleukin, CXC3R - CXC chemokine receptor 3, CXCL10 – CXC chemokine ligand 10. DAMPS – damage-associated molecular patterns, PAMPS – pathogen-associated molecular patterns

Astrocytes are an extremely heterogenous population of cells, displaying morphological differences in the neocortex and hippocampus (Lanjakornsiripan et al., 2018). This heterogeneity goes beyond morphology, with a wealth of studies citing astrocytes diversity in receptor expression and secreted factors. For instance, fluorescence-activated cell sorting (FACS) in a mouse model has demonstrated five separate astrocyte populations, all with

differential roles in supporting synaptogenesis (John Lin et al., 2017). In support of this, Buosi and colleagues placed neuronal cells in astrocyte-conditioned media from the hippocampus, cortex and cerebellum and reported a significant difference in the expression of synaptic proteins, therefore further solidifying astrocyte-specific roles for supporting neurons (Buosi et al., 2018). In addition to this, other studies have reported that astrocytes from different brain regions are also heterogenous in the release of chemokines, cytokines, and other cellular mediators (Fitting et al., 2010; Khakh and Deneen, 2019). Overall, it can be summarized that astrocytes are tailored for their brain microenvironment.

1.3.3 Neuroinflammation in neurodegenerative disease

Although Alois Alzheimer originally described glia changes in his first paper, it wasn't until over 60 years later this avenue of research resumed, with Ishi and colleagues publishing a paper in 1975, highlighting complement proteins to be associated with amyloid-beta plaques (Ishii et al., 1975; Ste lzma et al., 1995). It was later found that reactive microglia and astrocytes were associated with sites of damage in Alzheimer's disease and Parkinson's disease (McGeer et al., 1988) and since then a plethora of research has centered on the aetiology for this reaction, termed collectively as reactive gliosis.

Reactive gliosis has been classified as a 'non-specific reactive change of glial cells in response to damage to the CNS. In most cases, gliosis involves the proliferation of hypertrophy of several different types of glial cells including astrocytes and microglia (Ko, 2020). Reactive gliosis is not isolated to neurodegenerative disease pathology. It is important to note that many disorders of the central nervous system show reactive gliosis, such as traumatic brain injury (TBI), ischemic stroke, epilepsy, and psychiatric disorders such as depression, schizophrenia and attention deficit hyperactivity disorder (ADHD) (Schimmel, Acosta and Lozano, 2017; Jayaraj et al., 2019; Troubat et al., 2021; Pracucci et al., 2021; Kerekes, Sanchéz-Pérez and Landry, 2021; Vallée, 2022). It has been reported that oligodendrocytes do have an active role in reactive gliosis in neurodegenerative disease; however, this will not be covered in the scope of this thesis and the reader is recommended the following reviews: (Bradl and Lassmann, 2010; McKenzie et al., 2017).

The next two sections will address reactive gliosis found in neurodegenerative models, initially separated by their cell type (microgliosis, astrogliosis). However, it must be noted that astrogliosis and microgliosis can interact with one another, which is covered by recent reviews (Matejuk and Ransohoff, 2020; Han et al., 2021).

1.3.3.1 Microglia and microgliosis polarization

In healthy physiology, microglia have a ramified appearance which consists of a small cell body with long extended thin processes that survey the extracellular space. Upon reacting to extracellular stimuli, microglia change morphology to an amoeboid phenotype, with little to no processes visible (Lull and Block, 2010). This change in morphology has been cited to

encourage microglia motility to the area of damage and causing alterations in signaling pathways, receptor expression and secreted molecules (Fan, Xie and Chung, 2017).

Following from peripheral t-cell axis nomenclature, microglia have been shown to adopt distinct phenotype responses to the stimuli they encounter. These responses have been grouped as either M1, 'proinflammatory' or M2, 'anti-inflammatory', with different stimuli polarising microglia to these phenotypes (Gordon, 2003) (figure 1.7).

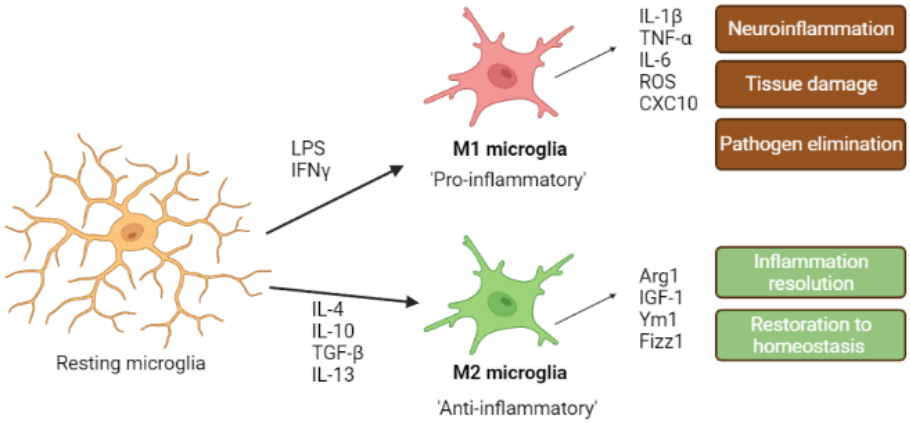

Figure 1.7: Resting microglia undergo polarization to become either 'Pro-inflammatory' or 'Anti-inflammatory'. The figure demonstrates that treatment with liposaccharide (LPS) or interferon gamma (IFN-γ) leads to a 'pro-inflammatory phenotype, leading to the release of chemokines and cytokines IL-1β, TNF-α, IL-6, reactive oxygen species (ROS) and CXCL10 which have subsequent roles in neuroinflammation, tissue damage and pathogen elimination. Treatment with IL-5, IL-10, IL-13 or transforming growth factor beta (TGF-β) leads to an anti-inflammatory phenotype resulting in the release of Arginase 1 (Arg1), Insulin-growth factor 1 (IGF), chitinase-like protein 3 (Ym1), Found in Inflammatory Zone 1 (FIZZ1) which have subsequent roles in inflammation resolution and restoration to homeostasis. *Figure adopted from Salvi et al., (2017)).*

As displayed in the figure, the M1 and M2 phenotypes release factors which are influential on the cellular microenvironment, with M1 microglia resulting in neuroinflammation, tissue damage and pathogen elimination, whereas M2 microglia show inflammation resolution and restoration to brain health homeostasis (Nakagawa and Chiba, 2014; Ghosh, Xu and Pearse, 2016; Orihuela, McPherson and Harry, 2016; Salvi et al., 2017).

The M1/M2 paradigm of microglia polarisation has been extrapolated for use in neurodegenerative disease, with a focus on aggregate-related proteins, such as Tau, Amyloid-Beta and α-synuclein. In Alzheimer's disease, M1 microglia is the common dominator,

reporting increased proliferation, induction of chemotaxis and an increase in inflammatory markers (Heneka, 2017; Sarlus and Heneka, 2017). M2 microglia have been identified to play a role in uptaking and phagocytosing insoluble amyloid-beta plaques, however, microglia in Alzheimer's disease have shown a decrease in this phagocytotic capability (Hickman, Allison and el Khoury, 2008). The literature highlights that microgliosis is initiated by neuronal damage and surpasses its initial neuroinflammatory protective qualities during extensive stimulation, leading to an overproduction of inflammatory mediators, exacerbating neuronal injury.

Upstream polarisation factors have been examined in neurodegenerative disease microglia. Toll-Like Receptors (TLRs), TLR2 and TLR4, have shown to interact with aggregate related proteins such as alpha-synuclein and amyloid-beta oligomers and activate microglia downstream to an M1 phenotype (Kim et al., 2013; Fellner et al., 2013; Doorn et al., 2014; Daniele et al., 2015; Xia et al., 2021). In support of this, TLR2 knockout models shifted microglia from an M1 to M2 phenotype and were associated with an improvement in neuronal function (Liu et al., 2012). In addition, TLR4 has also been implicated the M1 phenotype, with TLR4 inhibitors reporting an improvement in cognitive deficits and a transition to the M2 phenotype in Alzheimer's disease models (Guo et al., 2020; Guo et al., 2022).

The promotion of M2 microglia has been hypothesised as a potential treatment in treating neurodegenerative disorders, with many studies pointing towards the activation of JAK/STAT signaling as the inducer of an M2 phenotype (Zhang et al., 2017; Zhang et al., 2018; Qiao et al., 2020). Missense mutations in the Triggering receptor expressed on myeloid cells 2 (TREM2), a transmembrane receptor in microglia, has been linked to late-onset Alzheimer's disease (Zheng et al., 2018). TREM2 has been reported to be essential for microglial phagocytosis, survival in aggregate deposition and promotion of M2 polarisation (Tanzi, 2015; Walter, 2016; Zhou, Ulland and Colonna, 2018). Overall, this data indicates that microglia have an active role in combating and initiating neurodegenerative disease pathology.

1.3.3.2 Astrogliosis

In healthy physiology, astrocytes present as stellate cells with long processes. Upon activation, collectively termed 'astrogliosis', the cell body undergoes hypertrophy, with astrocytes overexpressing intermediate filaments within a matter of hours (Sofroniew, 2015; Verkhratsky et al., 2019). GFAP elevation, a standard marker for reactive astrogliosis, depends on the proximity to the injury site, type of injury and location in the CNS (Sofroniew, 2015). In mild-moderate gliosis, astrocytes domain extent is relatively unchanged, however, in severe astrogliosis, there is a degree of astrocyte proliferation whereby territorial domains overlap to form a glial scar (Wilhelmsson et al., 2006). Analogous to microglia polarisation, astrocytes have been termed A1 and A2 in relation to their neurotoxicity and neuroprotective qualities (Liddelow et al., 2017). In this model, Liddelow and co simulated microgliosis in a co-culture setting, stimulating astrocytes with Il-1α, TNF and C1q. These astrocytes, termed A1, release pro-inflammatory elements which subsequently damaged synapses and neurons whereas A2 showed beneficial effects in the upregulation of phagocytosis with the release of neurotrophic factors (Liddelow and Barres, 2017). There have been several research papers reporting that astrocytes polarize from one phenotype to another, however, this is now being recognized as an oversimplification of a spectrum of astroglia responses (Ceyzériat et al., 2016; Das et al., 2020).

1.3.3.3 Reactive astrocytes in neurodegeneration

Reactive astrocytes are heavily associated with neurodegenerative disease, with an elevated expression level of GFAP detected in Alzheimer's and Parkinson's disease. Accumulation of α-synuclein aggregates has been associated with astrocyte expansion, thereby supporting the idea that astrocyte proliferation is a response to intracellular aggregate-related proteins (Gu et al., 2010). Reactive astrocytes produce excess GABA and glutamate, with mouse models reporting tonic-inhibition of dentate gyrus neurons and glutamate-excitotoxicity-related neuronal death (Bush et al., 1999; Jo et al., 2014). Overall, this indicates that reactive astrogliosis can contribute to a decline in cognitive performance, highlighting astrogliosis contribution to neurodegenerative disease pathology (Kashon et al., 2004; Li et al., 2011; Phatnani and Maniatis, 2015).

1.3.3.4 Reactive astrogliosis is initiated by JAK/STAT3 signaling in neurodegenerative models

The Janus Kinase (JAK)-Signal transducer and Activator of Transcription (STAT) pathway is a central pathway which has shown roles in controlling astrogliosis. It was discovered in the 1980s, and to date, four JAKs (JAK1, JAK2, JAK3, TYK2) and seven STATs (STAT1,2,3,4,5a,5b,6) have been identified in mammals (Levy et al., 1988; Mitchell and John, 2005). The key pathway investigated in astrocytes is the JAK/STAT3 pathway. To briefly summarise, STAT3 is a transcription factor that controls gene expression in response to extracellular signals. These signals cause STAT3 to be phosphorylated at either tyrosine 705 or serine 727, after which it translocates to the nucleus to bind to STAT responsive elements,enabling the transcription of STAT3-specific genes.

GFAP is well documented to possesses a STAT responsive element and multiple research outputs have supported the necessity of STAT3 activation preceding GFAP upregulation, thereby strongly supporting that STAT3 is a key transcription factor for astrogliosis (O'Callaghan et al., 2014a; O'Callaghan et al., 2014b; Hol and Pekny, 2015; Toral-Rios et al., 2020a; Giannaki et al., 2021).

The JAK/STAT3 pathway in astrocytes has shown multiple roles as an anti-inflammatory pathway effect in gliosis, with roles such as mediation of glia-scar formation, preservation of myelin sheath, and secretion of anti-inflammatory cytokines and reducing leukocyte infiltration (Colombo & Farina, 2016; Giannaki et al., 2021). However, STAT3 activation in primary astrocytes has also been shown in response to a range of neurotoxic stimuli and pro-inflammatory mediators, therefore complicating the question of if STAT3 signaling is neuroprotective or neurotoxic (O'Callaghan et al., 2014a). Many mice models of neurodegenerative disease show an upregulation in astrocytic-specific STAT3 signaling, with STAT3 inhibitors showing an alleviation in disease symptoms and astrocyte hypertrophy (Ceyzériat et al., 2016; Choi et al., 2020; Toral-Rios et al., 2020; Zhang et al., 2021; Abjean et al., 2022).

1.3.3.5 Reactive astrocytes show beneficial roles at the beginning of neurodegeneration

Astrocytes have shown beneficial roles in neurodegenerative disease, including the phagocytosis of intracellular aggregates such as amyloid-beta and α-synuclein (Nielsen et al., 2010; Jones et al., 2013; Booth, Hirst and Wade-Martins, 2017). However, it appears that in the late stages these astrocytes become defective, failing to phagocytosis and remove amyloid-beta plaques in a late-stage Alzheimer's disease model (Pihlaja et al., 2011).Astrocyte phagocytic mechanisms are impaired in neurodegenerative disease, potentially due to the accumulation of reactive oxygen species (Motori et al., 2013). This is supported by studies reporting an initiation in astrocyte-specific autophagy suppressed amyloid beta-induced inflammatory responses (Garwood et al., 2011; Hong et al., 2018).

1.3.3.6 Astrocyte-derived EVs are suggested to spread pathology and exacerbate neurodegeneration

A recent development of interest in the field is Astrocyte Derived Extracellular vesicles (ADEVs). Treatment with A1 initiators such as TNF-α and IL-1β has demonstrated ADEVs enriched in microRNA's related to exacerbation of neurodegeneration (Chaudhuri et al., 2018; Datta Chaudhuri et al., 2020). In addition to this, ADEVs have roles in spreading neurodegenerative pathology, with analysis revealing that ADEVs from Alzheimer's patients contained amyloid-beta and complement proteins, therefore suggesting a pathological role (Goetzl et al., 2016; Winston et al., 2019).

1.3.3.7 The early stages of neurodegeneration are incomplete

It is important to note that most of the research cited in the previous paragraphs focuses on examining reactive gliosis responses to late stages of neurodegeneration, where neuronal death has already occurred. Although it is useful in understanding the mechanism of neuroinflammation in neurodegeneration, this does not inform the scientific community about the initiator of neuroinflammation and thereby, potential treatments to prevent neurotoxicity. There are few studies reporting neuroinflammation before neuron death (Hanzel et al., 2014; Choi et al., 2020), therefore showing a potential literature gap that is important to fill so we are able to investigate the potential contribution of neuroinflammation to neurotoxicity.

1.4 Proteomics and acute slice culture as methods used for studying neurodegenerative disease.

1.4.1 Mass spectrometry and SWATH-MS for proteomics

Mass spectrometry is an analytical- technique based on the ionisation of proteins and subsequent analysis of charged peptides to assess the relative abundance of different proteins in tissue samples. Briefly, the tissue is disrupted, and proteins in the tissue are then proteolytically cleaved into peptides and subjected to separation through liquid chromatography (LC). This separation results in parent molecules, which are separated by their mass to charge (m/z) ratio (MS1) and then further subjected to fragmentation and detection (MS2).

In mass spectrometry, the analysis process can be classified as data-dependent or data-independent (figure 1.8). Data-dependent acquisition (DDA), the most common method, typically performs a 'survey scan' to identify the most abundant ions (called MS1) which are then selected for fragmentation (MS2) (figure 1.8a). DDA has advantages such as the increased dynamic range when profiling over a broad molecular weight range (Stewart, 2015). However, there are disadvantages such as oversampling high-intensity peptides and missing low-intensity peptides, leading to disproportionate proteome representation (Johnson et al., 2013; Kaklamanos, Aprea and Theodoridis, 2016). In contrast, Data-independent acquisition (DIA) selects a predefined m/z charge precursor ion window (from MS1), which is then filtered and fragmented (MS2) (figure 1.8b). This addresses the disadvantages of DDA's selection bias in protein coverage. For example, in triple quadruple mass spectroscopy, selected precursor ions are filtered through the quadrupoles and provides high resolution and specificity in the selection of ion fragments. Despite total coverage of the window selected, windows are predetermined and therefore this does not cover the entire proteome.

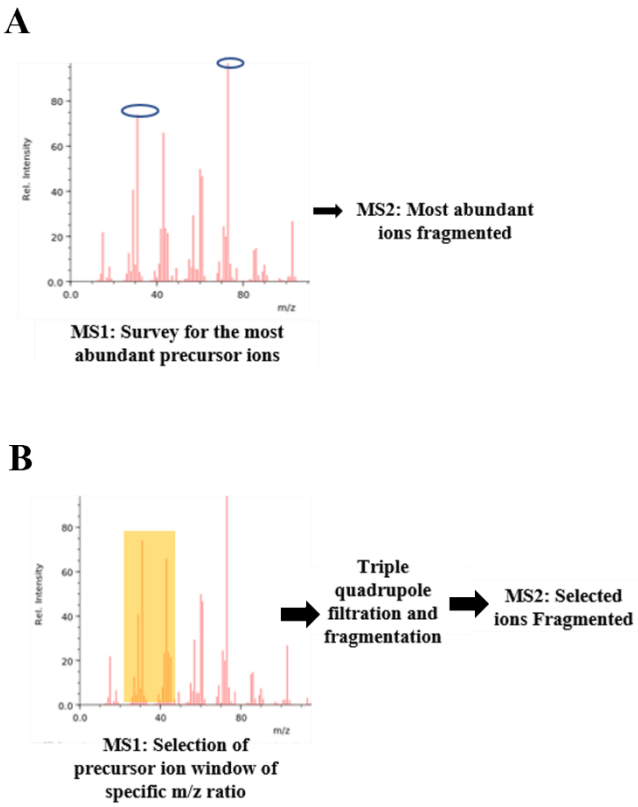

Figure 1.8: Mass spectrometry can be operated in either data dependent acquisition or data independent acquisition mode. 1.8A) Peaks in the relative intensity (Y axis) of the precursor parents ions separated by m/z ratio (X axis) are regarded as the most abundant. In DDA, the most abundant ions are fragments, typical of Time of Flight (TOF) mass analyzer. 1.8B) The peaks in the relative intensity (Y axis) of the precursor parents ions separated by m/z ratio (X axis) does not matter in DIA, as a specific window of m/z is selected (highlighted) and this selection is subjected to fragmentation. It is only the selected ions within that range that are fragmented. *Image adapted from Ciborowski and Silberring (2016)*

Sequential window acquisition of all theoretical mass spectra (SWATH-MS) is a quantitative MS proteomic technique, which utilizes both data independent and data dependent acquisition (Gillet et al., 2012). Individual samples undergo SWATH-MS – a series of 32 sequential overlapping scans at pre-determined windows of 25 m/z throughout the m/z range, covering 400 – 1200 m/z. Before this, a spectral library needs to be created where a selection of pooled samples are running in DDA mode which is subsequently made into a spectral library (figure 1.9A) which is used to mine data from subsequent scans of individual samples (figure 1.9B). This spectral-library extracts results in an extract ion chromatogram, where the quantitative value of the peptide is calculated using the area under the peak (Ciborowski and Silberring, 2013).

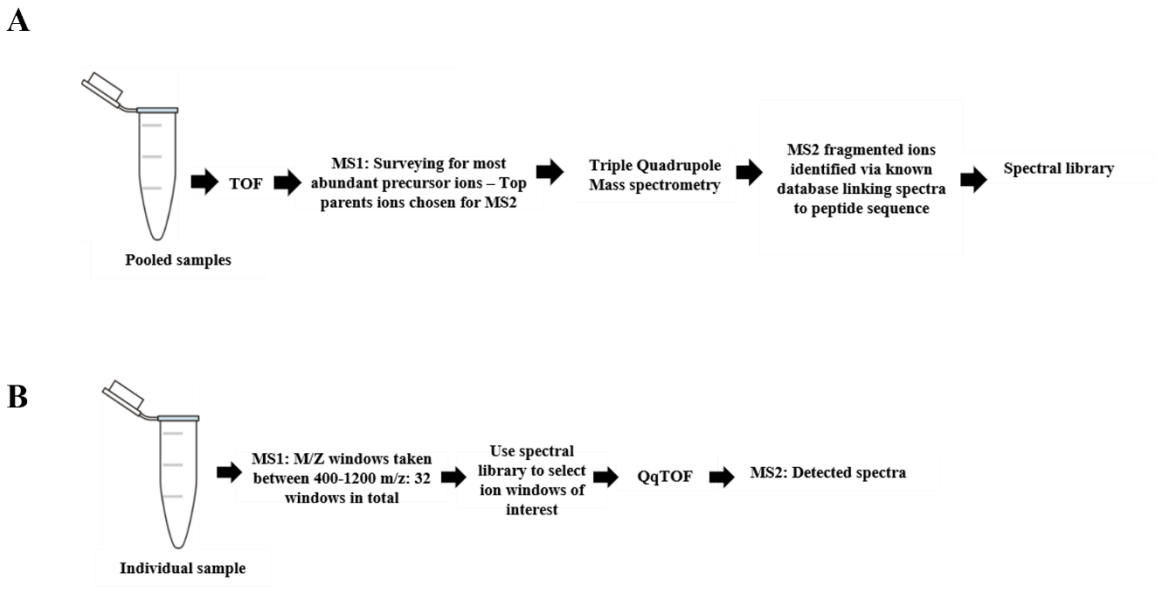

Figure 1.9: SWATH-MS requires a spectral library for data independent acquisition. 1.9A) A spectral library is created from a selection of pooled samples from each condition, typically run in DDA mode such as Time Of Flight (TOF). Top parent ions are chosen to be subject to quadrupole mass spectrometry where resulting fragmented ions are identified via a known database. This is the creation of the spectral library. 1.9B) Individual samples undergo continuous MS1 overlapping scans which is saved individually. The spectral library 'mines' the data by identifying identical ions from the sample. These parent ions are subject to QqTOF which then results in the detected spectra (MS2). *Image adapted from Ciborowski and Silberring,(2013)*

Using many consecutive isolation windows, the entire mass range is covered continuously during each scan cycle, allowing the identification and quantification of a range of peptides regardless of their abundance. SWATH spectral libraries can be updated and mapped onto the MS1 scan, therefore creating an abundance of data that can be referred to for several experiments (Carlyle, Trombetta and Arnold, 2018).

SWATH-MS shows high accuracy compared to other mass spectrometry methods (Jylhä et al., 2018) and has shown utility in neurodegenerative disease proteomic research, particularly in identifying non-invasive biomarkers for the diagnosis of diseases through blood, cerebral spinal fluid and urine (Jylhä et al., 2018; Park et al., 2020). It is also a robust screening technique to identify novel proteins that may have vital roles in pathologies but have traditionally been missed due to the lack of sensitivity in other analytical methods.

1.4.2 Acute slices and organotypic culture

Immunohistochemistry and Immunofluorescence staining of fixed brain tissue is a common wet-lab principle to visualize glia cells and their reactivity status in neurodegenerative disorders and has been used successfully in a multitude of research outputs and disease classification (Lowe, Hand and Mayer, 2005; Serrano-Pozo et al., 2011; Deture and Dickson, 2019). Although these techniques are useful in understanding the reactivity status in these disorders, the study of inherent glia mechanisms underlying their reactivity is difficult to capture in a snapshot of tissue.

The study of isolated glia *in vitro* has shown beneficial effects, namely understanding glia responses to aggregated proteins in neurodegenerative disease (Ransohoff and Perry, 2009; Jones et al., 2013; Sobue et al., 2021). However, research has shown that these experiments show poor translational scope in applying these results to *in-vivo* models, presenting the argument that isolated glia experiments do not truly reflect the complexities at play (Parviainen et al., 2017; Belle et al., 2018; di Lucente et al., 2018). In addition, the study of glia is particularly hard due to the isolation process changing gene expression and morphology of the cells and thereby consequently, does not reflect gliotransmission with neurons in an *in-vivo* setting, therefore supporting a lack of construct validity (Ransohoff and Perry, 2009; Lull and Block, 2010; Butovsky et al., 2014).

Pioneer Henry McIlwain reported the first use of acute brain slices in the late 1950s, and his basic technique continues to be used today (Li and McIlwain, 1957; Wellbourne-Wood and Chatton, 2018). Brain slices are cut at 350 µM to 400 µM thickness and maintained in an artificial cerebral spinal fluid (aCSF) supplemented with carbogen (O_2-CO_2) at 32-33 ºC to avoid temperature sensitivity changes (Teyler, 1980; Fujii, Baumgärtl and Lübbers, 1982; Reid et al., 1988). The use of acute slices has been praised for translational relevance in the field, with many studies reporting reproducible *in-vivo* results (Cho et al., 2004; Sherer et al., 2003). This is partly attributed to the acute slice maintaining its inherent structure, thereby the study of neurons and glia functional relationships is more valid.

Acute slices have the potential to undergo pharmaceutical manipulation and therefore can assess clinical candidates before phase 1 trials (Cho, Wood and Bowlby, 2007; Malla et al., 2022). One of the disadvantages of acute slices is their short life span, reporting a maximum of 6-12

hours of cell viability, however, this is aimed to be remedied by organotypic culture where slices can be maintained for multiple weeks. Organotypic culture has already shown promise as a testing platform in neurodegenerative mice model brain slices (Humpel, 2015; Croft et al., 2017; Croft et al., 2019; Malla et al., 2022).

1.5 Psmc1$^{fl/fl}$;CaMKII*α-cre* mouse as a model for studying neurodegenerative disease

1.5.1 Cre-LoxP

The use of genetic manipulation in animal models has been utilized for the study of human pathological conditions, with manipulation of the 'CreLoxP system' one of the first to be reported. The CreLoxP system is a vital part of the P1 bacteriophage life cycle and reproduction (Adams, Bliska and Cozzarelli, 1992; Łobocka et al., 2004; Yarmolinsky and Hoess, 2015). Cre Recombinase (named cyclization recombinase) is a site-specific enzyme that catalyses genetic recombination of DNA between two Locus over X P (LoxP) sites, comprising of 13 palindromic base pairs separated by an 8 base paired spacer.

In brief, Cre recombinase acts as two separate subunits on each LoxP site, cleaving the DNA backbone, leading the two partnered subunits to form a tetramer, circling the DNA 'floxed' between these two points. Depending on the LoxP site orientation, this can lead to specific recombination leading to DNA insertion (for replication in daughter cells) or deletion (removing the formation of dimers) from the plasmid. This technique was first discovered to be applicable for genetic deletion or insertion in mammalian cells by Sauer and Henderson (Sauer & Henderson, 1988). Later, LoxP flanked selection cassettes were inserted into introns of the chosen gene in mice embryonic stem cells to produce genetic knock-out animal models (McHugh et al., 1996). Although knock out models has gained success in the past, many genes have shown to be vital in embryonic development and thus, complete deletion of genes of interest that have these roles renders unviable offspring (Capecchi, 1989; Beglopoulos and Shen, 2004; Mak, 2007). The CreLoxP system offers a functionality whereby the position of cre recombinase under a postnatal development-specific promoter enables the examination of the depletion of a protein in an animal model, therefore bypassing this caveat. This functionality has been exploited for the manipulation of gene expression in mouse models of neurodegeneration.

1.5.2 CaMKIIα-cre

Calcium signaling is crucial for several aspects of plasticity at glutamatergic synapses. Intracellular free calcium changes induce phosphorylation and activity of target proteins involved in neurotransmitter synthesis and release, neuronal plasticity and gene expression. These processes are mediated by the Ca^{2+}/calmodulin-dependent protein kinase (CaMKII)

family (Mayford et al., 1996; Hudmon and Schulman, 2002; Merrill et al., 2005; Whitlock et al., 2006).

This holoenzyme is composed of four different chains: α, β, γ and δ, encoded by genes camk2a,camk2b,camk2d, and camkdg, respectively. The subunit composition varies in areas of the brain -for instance, CaMKIIβ presence is enriched within the cerebellum, whereas CaMKIIα is enriched within the adult forebrain and hippocampal regions (McGuinness, Lai and Greengard, 1985; Miller and Kennedy, 1985; Shonesy et al., 2014; Zalcman, Federman and Romano, 2018).

CaMKIIα expression is localised within the CA1 and CA3 pyramidal glutamatergic neurons in the hippocampus and the dentate gyrus, comprising 2% of the total protein level (Hudmon & Schulman, 2002; Wang et al., 2013). CaMKIIα translocates from the cytosol to associated neuronal membranes and post-synaptic junctions in dendritic spines, initiated by elevated synaptic activity during the second and third week of development (Burgin et al., 1990; Mayford et al., 1996; Ahmed and Frey, 2005). Pharmaceutical inhibition of CaMKIIα activity results in long- and short-term memory impairment, suggesting this isoform has a key role in learning (Zalcman, Federman and Romano, 2018).

Placing the Cre recombinase enzyme under the control of the CaMKIIα promoter allows for various transgenic models to target individual proteins roles within neurons central to memory formation, such as the NMDA receptor (McHugh et al., 1996). CaMKIIα-cre mice studies have shown that the Cre protein is expressed at P3, however, Cre LoxP reporter mice show the initial recombination in Lacz/GFP reporter mice at days P18-P19 (Kelly and Vernon, 1985; Casanova et al., 2001; Tsien, 2016).

1.5.3 Psmc1$^{fl/fl}$;CaMKIIα-cre mirrors human pathology

With strong evidence based on proteasome disruption in neurodegenerative disorders alongside conflicting evidence of proteasome inhibitor studies, a new approach was needed to investigate the role of the proteasome in neurodegenerative mechanisms. Bedford and colleagues generated the Psmc1$^{fl/fl}$;CaMKIIα-*cre* mice strain (Bedford et al., 2008).

This mouse model placed the Psmc1 gene, which encodes the rpt2 subunit of the 19S regulatory particle, under spatial control of the CaMKIIα promoter. A chronological table of the pathological events is shown in table 1.5. As the CaMKIIα promoter is activated at p18-19, Psmc1 gene deletion was initiated at this time in CaMKIIα expressing cells; namely neurons in the dentate gyrus, CA1, CA3 region and the forebrain. The 26S proteasome is depleted over 10 days, whereby at 3 weeks mice have an increase in the accumulation of ubiquitin tagged proteins, alongside an induction of autophagy. At 4 weeks, the 26S proteasome is completely depleted, with pyknotic nuclei and intraneuronal inclusions present. At 5 weeks old, CaMKIIα-*cre* neurons show signs of apoptosis. Intraneuronal inclusions resembling human pale bodies appeared at 6 weeks old, alongside impaired autophagy-lysosomal function (figure 1.10). At this point, animals also demonstrated severe anxiety and memory deficits in field tests compared to control littermates. In addition to this, the Psmc1$^{fl/fl}$;CaMKIIα-*cre* mice also report an upregulation in neuroinflammation markers Iba1 and GFAP across the cortex, which increase in association with disease pathology (Geiszler et al., 2018). However, it must be noted that the aetiology of this neuroinflammation cascade, and its potential consequences, have not been accounted for.

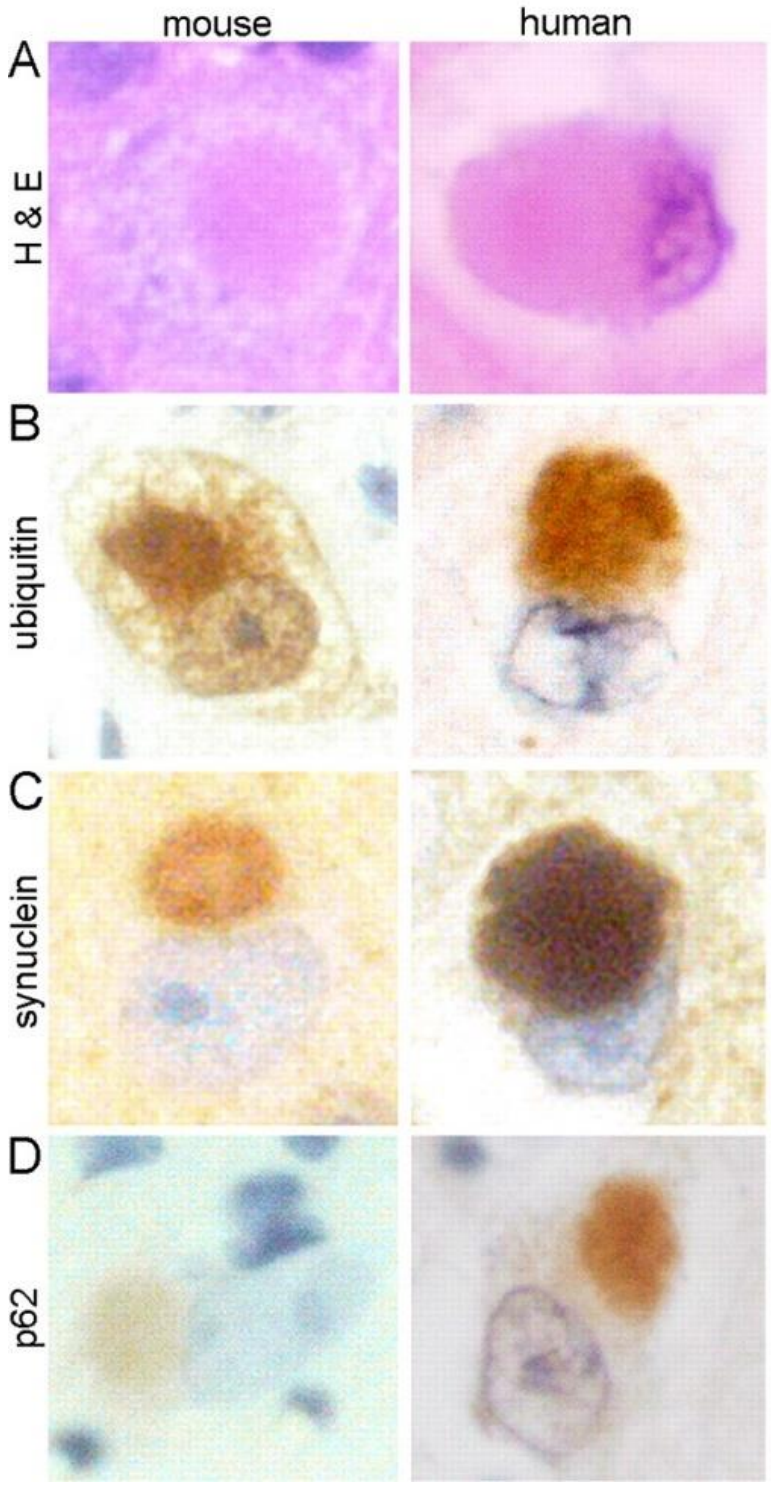

Figure 1.10: Psmc1 $^{fl/fl}$;CaMKII*α*-*cre* mice resemble human-like pathology at 6-weeks of age, resembling pale-body inclusions in CaMKII*α*-*cre* neurons. Panels reflect the staining method used: A) Haemotoxylin and Eosin (H&E) B) Ubiquitin, C) alpha-synuclein, and D) P62. The figure is taken from Bedford et al. (2008).

Table 1.5: Overview of Psmc1$^{fl/fl}$;CaMKIIα-*cre* pathology from published peer-reviewed research papers

Descriptor		Age (weeks)				
		3	4	5	6	8
Phenotype	Anxiety				↑	
	Spatial learning				↓	
	Memory				↓	
	Body weight				↓	
CaMKIIα neurons	26S proteasome	decrease in 26S proteasome complex	20S predominate complex			
	Neuronal death/aggregate formation		Pyknotic nuclei Intraneuronal inclusions	Neuronal death	Pale bodies	ND
	Ubiquitin-tagged proteins	↑				
	Autophagy	↑	↓			
Microglia	Iba1 area	↑				
	Iba1 soma size	↑				
Astrocytes	GFAP fold change*	↑				
	Oxidative defence via PRDX6		↑ Inverse relationship with ROS			
Mitochondria	Mitochondria location	Paranuclear				
	Mitochondria mitophagy	↑	↓			
	Mitochondria dysfunction	↑				

Key: ↑ - upregulated compared to age-matched control littermates. ↓ - downregulated compared to age-matched control littermates. **Acronyms:** ND – Neurodegeneration; ROS – reactive oxygen species. Boxes highlighted in red are particular to neuroinflammation. Boxes with no text represent a lack of peer-reviewed data for this descriptor * - measured via western blot. *Data extracted from the following papers: Bedford et al., 2008; Elkharaz et al., 2013; Ugun-Klusek et al., 2017; Geiszler et al., 2018).*

1.6 Aims of this thesis

1.6.1 Rationale

The Psmc1$^{fl/fl}$;CaMKIIα-*cre* transgenic mice model is the first *in vivo* model which demonstrates time-dependent 26S proteasome depletion resulting in neurodegenerative disease, comparable with human pathology. Since the CaMKIIα protein has only been visualised in neurons, the Psmc1$^{fl/fl}$;CaMKIIα-*cre* transgenic mice provides an opportunity to investigate the mechanisms of direct neuronal proteotoxicity effect on the brain's microenvironment throughout neurodegenerative disease (Garwood et al., 2013; Ouimet et al., 1984; Scholz et al., 1988). As this model displayed intraneuronal inclusions at 4 weeks old, followed by neuronal death at 5-weeks old then neurological defects at 6 weeks old, this gives a 3-week period to investigate glia responses before disease pathology. The next section will briefly outline the rationale and aims for each data chapter, intending to further clarify glia-responses to neuronal-26S proteasome depletion.

1.6.2 Proteomic profiling using SWATH-MS

Protein expression profiling will be employed in 2,3,4-5 weeks of Psmc1$^{fl/fl}$;CaMKIIα-*cre* mice and their age-matched litter mates, to report quantitative protein differences in correlation with progressive disease pathology. These protein changes will be uploaded to a bioinformatics analysis programme to derive and evaluate potential pathways enriched before neurodegenerative disease pathology is present.

1.6.3 GFAP upregulation and subsequential Astrocytic-STAT3 reactivity

Based on SWATH-MS data, GFAP immunoreactivity and expression will be explored in the mouse model prior to the onset of extensive neuronal death. 2,3-and 4 week old Psmc1$^{fl/fl}$;CaMKIIα-*cre* mice and their age-matched control controls will be subjected to western blot for key markers; GFAP, STAT3α and phosphorylated-STAT3 tyrosine 705. These markers will also be explored in immunofluorescence staining to provide the number of GFAP^{+}/STAT3α^{+} astrocytes and localised astrocytic-STAT3.

1.6.4 Pharmacological treatment of acute slices to investigate potential STAT3-agonists

Quantitative PCR will be used to assess potential astrocytic-STAT3 agonists in Psmc1$^{fl/fl}$;CaMKIIα-*cre* mice, and then pharmacological treatment of acute slices will be performed to investigate direct astrocytic-STAT3 Tyrosine 705 phosphorylation in situ. STAT3 Tyrosine 705 phosphorylation will be assessed by immunohistochemistry and western blot analysis.

Chapter 2 Materials and Methods

The following chapter describes the materials and experimental methods used throughout this thesis. In addition to this chapter, a brief overview of the relevant techniques will be given at the beginning of each experimental chapter.

2.1 Animal model

2.1.1 Ethics and animal husbandry

The mice were from a C57BL/6 background and housed in the Biomedical Services Unit, Queens Medical Centre, the University of Nottingham, in line with the UK Animals Scientific Procedures Act (ASPA) 2012. Mice were housed in a specific pathogen-free environment in identical isolator cages. These cages occupied appropriate environmental enrichment, underwent 12-hour light and 12-hour dark cycles, and allowed mice to have free access to food and water. Animals were reviewed daily by staff members, and animal welfare concerns were reported to the Named Animal Care and Welfare Officer (NACWO). Mice in moderate to severe distress were culled. All procedures were carried out with ethical approval from the University of Nottingham Ethical Review Committee and conducted under personal and project licenses granted by the UK Home Office in accordance with the Animals (Scientific Procedures) Act 1986 (P3/75A76/FE).

2.1.2 Generation of animal model

The generation and breeding of the Psmc1$^{fl/fl}$;CaMKIIα-*cre* mouse model was in place prior to the thesis project beginning, and have been housed in the Biomedical Services Unit at the University of the Nottingham for approximately 10 years. The paper 'Depletion of 26S proteasome in mice forebrain neurons' detailed the generation of the Psmc1$^{fl/fl}$;CaMKIIα-*cre* mouse model (Bedford et al., 2008). A LoxP flanked neomycin-thymidine kinase selection cassette and a loxP site was inserted into introns 1 and 3, respectively, of the Psmc1 gene (Gene ID 19179) in mouse 129/Sv embryonic stem (ES) cells. Cre was transiently expressed *in vitro* to excise the Psmc1 gene. PCR amplification identified the correct Psmc1 $^{fl/fl}$ clones.

Identified correct Psmc1 $^{fl/fl}$ clones in ES cells underwent chimeric aggregation: the correct Psmc1-$^{fl/fl}$ clones were aggregated with a CD-1 morula (early-stage embryo) to produce male

Psmc1 $^{fl/wt}$ mice. These were bred with CD-1 females to produce homozygous female Psmc1 $^{fl/fl}$ mice. The details of the origin of these CD-1 females are unknown.

Neuron-specific ablation of Psmc1 was achieved by crossing the Psmc1$^{fl/fl}$ mice with CaMKIIα-*cre* mice (Lindeberg, Mattsson and Ebendal, 2002) to produce Psmc1 $^{fl/wt}$;CaMKIIα-*cre* and Psmc1$^{fl/wt}$;CaMKIIα-WT mice. CaMKIIα is strongly expressed in hippocampal neurons, particularly granule and pyramidal neurons (≈ 70%), and to a lesser context in the neocortex (≈35%) (Wang et al., 2013). Female Psmc1 $^{fl/wt}$;CaMKIIα-*cre* mice mated with Psmc1$^{fl/fl}$;CaMKIIα-WT mice to produce the mutant mouse model, Psmc1$^{fl/fl}$; CaMKIIα-*cre*. This was the final breeding scheme for the colony. As Psmc1 $^{fl/wt}$;CaMKIIα-*cre and* Psmc1$^{fl/fl}$;CaMKIIα-WT mice displayed no detectable alterations compared to the mutant phenotype, they were used as control mice for the colony (Paine, 2013).

2.1.3 Rederivation attempts

Rederivation, for the removal of inherited pathogens common to the mice strain, was attempted many times with the Psmc1$^{fl/fl}$;CaMKIIα-*cre* colony prior to this beginning of this thesis project; however, it was deemed unsuccessful. The colony tested positive for *Mouse Norovirus, Helicobacter hepaticus* and *Tritrichomonas sp*. Due to this, several experimental constraints are sign-posted in each affected method.

2.1.4 Genotyping

2.1.4.1 gDNA extraction

Genotyping of the colony was conducted in-house and throughout this thesis project. Ear notches (2 mm diameter) were taken from mice after weaning (P21 onwards) and collected in 1.5 mL Eppendorf labelled with the corresponding pedigree number. 500 µL of Lysis Buffer (100 mM Tris-HCl pH 8.5, 5 mM Sodium Chloride, 2mM EDTA, 0.2 % SDS and 200 mM NaCl) with 25 µL of Proteinase K (#P2308, Sigma-Aldrich) was added to ear notches and incubated at 56 °C overnight. After overnight incubation, the ear notch was vortexed for 10 seconds and centrifuged at 9300 g for 10 minutes to pool debris. The supernatant was removed and an equal volume proportional to the isopropanol volume was added with end-over-end mixing to encourage precipitation of genomic DNA (gDNA).

The DNA pellet was washed with 500 µL of 70% sterile ethanol (vol/vol) and then subjected to centrifugation at 16,100 g for an additional 10 min. The 70% ethanol was removed and the pellet was left to air dry. Upon confirmation that all ethanol was successfully removed, pellets were resuspended in 50 µL of HyClone™ water (#10307052, Fisher Scientific). The gDNA quantity (ng/µL) was assessed with the NanoDrop™ spectrophotometer (#ND-2000, Fisher Scientific).

2.1.4.2 PCR reaction

100 ng/µL of gDNA from each pedigree was used in 10 µL Polymerase Chain Reactions (PCRs). Primers were synthesised by Sigma Aldrich to detect the Psmc1 floxed allele and cre are detailed in table 2.1.

Table 2.1: PCR primers used for genotyping Psmc1$^{fl/fl}$;CaMKIIα-*cre* colony

Target	Sequence	Base pairs (BP)
Cre (sense)	GGTAGCACCGCAGGTGTAG	380
Cre (antisense);	CTAATCGCCATCTTCCAGCAG	380
Psmc1 (control and floxed sense (LB3))	TACGAACCTCCTGTCCCAAC	395
Psmc1 (knock-out sense (D1360))	CAGAAATACAGCCAGTGACC	216
Psmc1 (common antisense (X316)).	CTGGAACTCAGTGGATTGAG	349

Cre sense and antisense were utilised in the same reaction, and Psmc1 alleles were utilised separately, leading to two separate PCRs per pedigree. Each 10 µL reaction was made up in sterile 0.2 mL eppendorfs in the following manner (table 2.2)

Table 2.2:PCR reaction composition (per one gene)

Volume (µL)	Ingredient
1.00	10X DreamTaq™ Buffer (#B65, Fisher Scientific)
1.00	1mM dNTPs
0.5	Forward Primer (4µM)
0.5	Reverse Primer (4µM)
0.05	DreamTaq™ DNA polymerase (#EP0702, Fisher Scientific)
100 ng as determined by nanodrop	Template gDNA
to final volume (10)	HyClone™ water

After making up the PCR reaction, eppendorfs were centrifuged briefly to ensure DNA was at the bottom of the tube. Eppendorf caps were fitted securely to avoid evaporation of the PCR

product and placed in the Mastercycler gradient PCR machine (#950000023, Eppendorf), running the programme listed in table 2.3.

Table 2.3:PCR programme for amplification of Psmc1-wt/Psmc1-floxed and Cre positive genes

Temperature	Duration (mins)
94	3.0
94	0.5
65	0.5
72	0.5
	35 cycles
72	3.0

2.1.4.3 Visualising PCR products

3 % (w/v) Seakem agarose in Tris-acetate-EDTA (TAE buffer) was heated for 5 min to create an acrylamide gel mixture. The gel mixture was left to cool to room temperature then 5% (vol/vol) SYBR™ Safe DNA Gel Stain (#S33102, Fisher Scientific) was added and mixed thoroughly. This gel mixture was poured into an agarose tank mold with combs and left to set for 30 min. After setting the gel and removing the combs, the 3% agarose gel was submerged in TAE buffer (0.04M Tris, 0.001M Na-EDTA and 0.02M acetic acid, pH 8.0) in a gel-electrophoresis tank (#FB58120, Fisher Scientific). 5 µL of 100 bp DNA ladder (#N3231L, New England Biolabs) and 10 µL PCR products were added to the gel. The gel was run at 100 V, 300 mA for 30 min. For visualisation, the gel was transferred to an ultra-violet light imaging cabinet (Gene Genuis Bioimaging System, SynGene), where PCR products were visualised and captured using the GeneSnap software (figure 2.1).

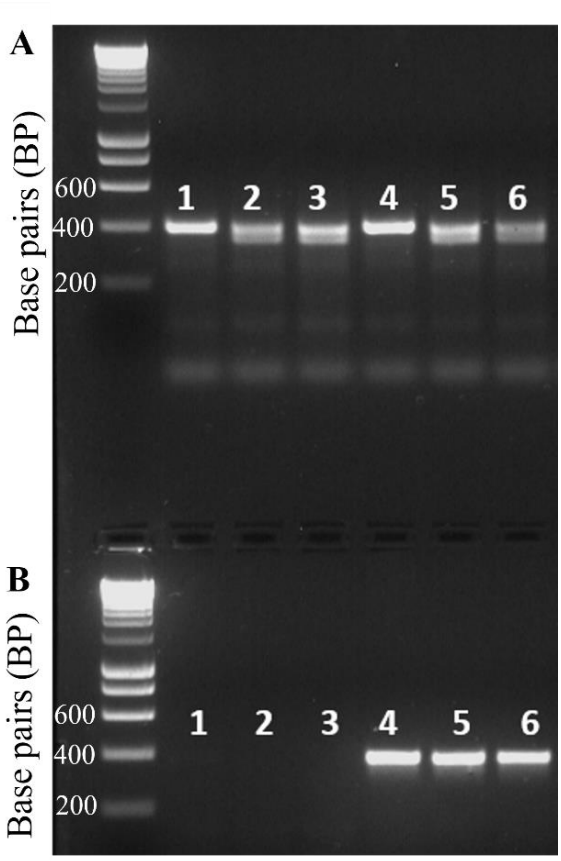

Figure 2.1: Genotype experiment performed as part of the project for maintenance and breeding of the Psmc1$^{fl/fl}$;CaMKIIα-*cre* colony. 2.1A) Psmc1 gene present as floxed (band at 395bp), Psmc1 gene control (band at 350bp). 2.1B) Cre band either present or absent (band at 380bp). Mice genotype as follows: Mouse 1: Psmc1$^{fl/fl}$;CaMKIIα-wt (Control),Mouse 2: Psmc1$^{fl/wt}$;CaMKIIα-wt (Control), Mouse 3: Psmc1 $^{fl/wt}$;CaMKIIα-wt (Control),Mouse 4: Psmc1$^{fl/fl}$;CaMKIIα-*cre* (Mutant),Mouse 5: Psmc1$^{fl/wt}$;CaMKIIα-*cre* (Control),Mouse 6: Psmc1$^{fl/wt}$;CaMKIIα-*cre* (Control).

2.2 Sequential Window Acquisition of all Theoretical Mass Spectra (SWATH-MS)

2.2.1 SWATH-MS sample preparation

2,3-,4- and 5-week old mouse brains (Psmc1$^{fl/fl}$;CaMKIIα-*cre* (n= 6), control (n= 6)) were used for these experiments. Brains were separated by midline hemisphere, and one hemisphere was utilised for mass spectrometry analysis and the remaining hemisphere was used for wet-lab experiments to validate the mass-spectrometry data set. Sample preparation was undertaken by Dr Jamal Ibrahim Elkharaz.

One hemisphere per each experimental animal was homogenised in 200 µL of Lysis Buffer (9.5 M Urea, 2 % Dithiothreitol (DTT) and 1% n-octyl-β-D-glucoside (βOG)). The samples were centrifuged at 16,000 g, then frozen at -80 °C for 15 mins then thawed at room temperature for 15 mins twice to encourage cell lysis. The samples were placed on ice and sonicated with three pulses for 5 secs, followed by centrifugation at 9300 g for 5 min at a temperature of 4 °C. These pellets contained insoluble debris, and supernatants were removed to clean pre-cooled eppendorf tubes, and proteins were quantified using a Bradford Assay (Bradford, 1976).

After protein concentrations had been determined, 50 µg of protein was made in a volume of up to 20 µL using double distilled water, then 1 µL of 0.5 M dithiothreitol was added to each sample and incubated at 52 °C for 20 min. 2.7 µL of 0.55 M iodoacetamide was added to each sample and incubated for 15 min in the dark at room temperature. Samples were dried in an Eppendorf ™ concentrator at 45 °C for 60 minutes, then pellets were resuspended in 100 µL of 50 mM triethyl ammonium bicarbonate. 2 µg of trypsin in 1 mM HCl was added to the sample and incubated in a 37 °C shaker block overnight. The sample was dried in an Eppendorf ™ concentrator at 45 °C for 90 minutes. Pellets were resuspended in 50 µL of 5 % acetonitrile in 0.1% formic acid solution. Samples were centrifuged at 8 °C for 10 min at 9300 g. The supernatants were transferred to mass spectrometry vials for further analysis. Mass spectrometry analysis was performed on the SWATH acquisition feature, AbSciex TripleTOF® 6600 Mass Spectrometer at Nottingham Trent University and performed by Dr David Boocock.

2.2.2 Sample analysis

The resulting data was uploaded and analysed with the 'Protein Workflow expression' application hosted by Basespace Illumina. The protein workflow expression application has in-house statistical testing which controls for multiple comparisons and the removal of false

positive and negative results. The raw data was downloaded at 0% confidence with single peptides removed. In this context, confidence refers to the positive assurance that the abundance of ions matches the assigned peptide by using in-programme algorithms to check databases of similar samples(Keller et al., 2002). Two-week-old control and Psmc1$^{fl/fl}$;CaMKIIα-*cre* mice show no significant differences in neuroanatomy (Bedford et al., 2008) therefore representing a reference to base level for confidence changes.

Proteins detected in this group showed a maximum of 54% confidence; therefore, this was the lower limit for subsequent studies. Protein lists were separated via experimental groups filtered to 54% and above confidence. In-programme student *t*-test results from SWATH-MS data comparing Psmc1$^{fl/fl}$;CaMKIIα-*cre* mice (n=6) vs age-matched control mice (n=6) for each age group (3, 4 and 5 weeks), therefore providing three experimental groups, and were presented as an expression of protein upregulation/downregulation vs the Psmc1$^{fl/fl}$;CaMKIIα-*cre* mice model. The results of these were used to select significant data (probability ≤ 0.05) for subsequent analysis.

2.2.3 Search Tool for the Retrieval of Interacting Genes/Proteins (STRING) data analysis

Selected proteins over 54% in confidence were assigned their corresponding gene name from Uni-Prot (https://unitprot.com) and submitted for network analysis in Search Tool for the Retrieval of Interacting Genes/Proteins (STRING) version 11(https://string-db.org/)(Szklarczyk et al., 2019). Network analysis displayed molecular interactions in various data sources such as text mining, experiments, databases, co-expression, neighbourhood, gene fusion and co-occurrence. The minimum required interaction score was set at 40 % and above. for protein pathways to be considered. PPI (Protein-Protein Interaction) map was exported displaying the strength of interaction, and the enrichment p-value and FDR (False Discovery Rate) were recorded.

2.3 Immunohistochemistry – paraffin-embedded.

2.3.1 Tissue retrieval

Transcardial perfusion was performed on mice to remove contaminating blood from the brain. This was undertaken under PIL number: I9D138A1A, under project license: P3/75A76/FE for this project. 100 µL of pentobarbital was injected intraperitoneally into mice. On confirmation of deep anaesthesia via loss of pinch reflex, mice underwent transcranial perfusion with approximately 20 mL of saline solution (0.9% NaCl, 1% Heparin Sulphate (w/v) in PBS) to flush contaminating blood from tissue. Due to rederivation issues, paraformaldehyde (PFA) was unable to be flushed via the circulatory system due to a lack of safe disposal. To remedy this, brains were quickly removed intact and submerged in 4% PFA (w/v) in PBS and left overnight at 4 °C.

2.3.2 Tissue processing

After overnight fixation, brains were washed with PBS (#18912014, Fisher Scientific) three times for 5 min intervals. Tissues were processed in paraffin in a TP1050 tissue processor (Leica) at the School of Life Science Imaging Facility (SLIM), University of Nottingham. Brain tissues were subjected to the following process: Ethanol was used to dehydrate the tissue whilst chloroform was used as a clearing agent to remove excess ethanol before embedding it in paraffin, following a 10-step protocol (table 2.4).

Table 2.4: Tissue processing steps utilised by TP1050 tissue processor

Step	Station	Time (mins)
1	70%Ethanol	90
2	80% Ethanol	90
3	96 % Ethanol	90
4	100% Ethanol	60
5	100% Ethanol	60
6	100% Ethanol	60
7	100% Chloroform	180
8	100% Chloroform	180
9	Paraffin wax	120
10	Paraffin wax	120

Paraffin wax, heated to 60 °C, was added to brain tissue in a metal mould, and the treated tissue was placed on ice to prevent the formation of large crystals using a Leica EG1160 Embedding Centre. Once paraffin wax cooled and solidified, the block was removed from the mould and kept at 4 °C until cutting with a microtome. Leica RM2155 rotary microtome was used to take 10 µm sections with the brain in a horizontal orientation to match the Mouse Brain Atlas (Franklin and Paxinos, 2008). Paraffin sections were smoothed out in a heated water bath and then applied to 3-Aminopropyltriethoxysilane (APES) covered slides (#42763006-1, Glycomatrix). Excess water was removed using filter paper to apply slight pressure on the section. Slides were dried at 40 °C and kept in slide boxes at room temperature.

2.3.3 Immunofluorescence staining

Formalin Fixed Parrafin Embedded (FFPE) slides created using the procedure in section 2.3.2 were used for Immunofluorescence staining for the examination of GFAP and STAT3 reactivity in 2-,3- and 4-week old mice. All slides for this staining were chosen so age-matched controls were closely aligned to the horizontal map co-ordinates (Interaural:4.36mm Bregma: -5.64 mm) in the mouse brain atlas mentioned previously. These slides were taken through dehydration stages of xylene, 100% ethanol,95% ethanol, 70% ethanol and running water for ten mins each. After this, antigen retrieval was performed with Tris-EDTA (pH 9.0) for 20 min at 95-100 °C. The slides were left in antigen retrieval buffer at room temperature for 20 min to cool, then washed in running tap water for 10 mins to remove excess salt. Slides were then treated with 0.1% sodium borohydride solution (w/v) in Phosphate Buffered Saline (PBS) (#003002, for 30 min to remove endogenous fluorescence. After this, slides were washed with 0.9% (w/v) saline solution six times for 5 min, using a new solution each time. Slides were washed with PBS thrice for 5 mins. Slides were dried, taking care to avoid the tissue sections.

An ImmEdge® Hydrophobic Barrier pen (H-4000, Vector Laboratories) was used to draw around the brain to create a hydrophobic barrier to keep following solutions localised. Blocking of non-specific staining was achieved using 5% goat serum in Mouse On Mouse (M.O.M) blocking solution (v/v in TBS-T) (#MKB-2213-1, Vector Labs) for 1 hr at room temperature. This solution was removed, and sections were incubated in M.O.M reagent (v/v in TBS-T) for 5 minutes. This was then removed, followed by incubation with primary antibodies (STAT3α-Rabbit, 1:100, Cell Signaling #8768); (GFAP-Mouse, 1:500, #ab4648, Abcam) in 5% Goat Serum in M.O.M reagent overnight at 4 ºC. Following incubation, slides were washed in PBS for 20 minutes thrice to remove excess primary antibodies. Fluorescent secondary antibodies

and nuclear stain were mixed in 5% goat serum in M.O.M reagent (Alexafluor 488 donkey anti-mouse; (#R37114, Thermofisher) 1:500, Alexafluor 568 goat anti-rabbit;(#A-11011, Thermofisher) 1:500, 4′,6-diamidino-2-phenylindole (DAPI) (#62248, Thermofisher) (1:1000) and incubated in the dark for 1 hour. Slides were washed in PBS thrice and mounted with DAKO mounting media. These were sealed with nail varnish and left to dry.

2.3.4 Analysis

Zeiss Axio Vert.A1 Microscope was used to take images at x20 magnification using Zen 2.5 software (www.zeiss.com). Regions of interest (ROI) were identified in each hemisphere: Cerebral cortex (2), Hippocampus (CA1 (2), CA3 (3), DG (4)) whereby the number represents the number of individual images captured to cover the region of interested. The cerebral cortex images were taken in layers 1-4, focusing on the somatosensory cortex. The images were taken in the following fashion at the following light intensity (%) and time exposure (ms - milliseconds) (table 2.5).

Table 2.5:Immunofluorescence channels, secondary antibody imaged, intensity percentage and exposure times used for the image taken and further image analysis

Channel	Secondary antibody	Intensity (%)	Exposure (ms)
DAPI	DAPI	100	20
FITC	Alexafluor donkey-anti mouse 488	100	150
TRITC	Alexafluor goat-anti rabbit 568	100	600

Images were saved as multichannel images then imported to Microsoft PowerPoint and assigned an experimental number per each image (I.E: n1, n2, n3…) which corresponded to the slide number, genotype, age and region of interest in a separate excel document. The image scale bar was removed for analysis to avoid visual obstruction of potential positive cells. To establish that the criteria for the number of positive cells was consistent, a sample stack of images were analysed by three independent researchers with the criteria listed in section 2.3.4.1, all blinded to age and genotype to ensure a non-biased analysis. After validation of this criteria showing consistency across three independent researchers, future analysis was carried out by myself with the knowledge that the criteria was replicable, ensuring I was blinded to age and genotype also. After the analysis was complete, the excel sheet was used to regroup the data for statistical analysis.

2.3.4.1 Number of GFAP$^+$/STAT3α^+ & STAT3α^+/DAPI$^+$ cells

For both analyses, to establish the number of positive cells per area (I.E: CA1, CA3, DG, Frontal cortex), images were imported to Microsoft PowerPoint, and gridlines were imposed. The number of cells was counted in each photograph, using the gridlines as reference. The number of cells was divided by the number of images per area. If the average resulted in one

decimal places, the count was either rounded up or down depending on the decimal place (E.g 11.3 would be rounded down to 11, 13.7 would be rounded up to 14).

Example: GFAP$^+$/STAT3α $^+$/DAPI$^+$ cells in the CA1 region

3 images

Photograph 1: 13 Photograph 2: 14 Photograph 3: 11

$$\frac{13 + 14 + 11}{3} = 12.6$$

12.6 rounded up = 13 positive cells

For a cell to be defined as GFAP$^+$/STAT3α$^+$/DAPI$^+$, the criteria were:

- STAT3α$^+$ was localised to a DAPI$^+$ nucleus
- STAT3α$^+$ and DAPI$^+$ positive nucleus was surrounded by a GFAP positive cell body which included a minimum of one process.
- GFAP$^+$ positive processes overlap with STAT3α$^+$ positive process, minimum of one process.

The number of cells conforming to these criteria was counted visually and numbers were collated in a Microsoft Excel document under the assigned experimental number (figure 2.2). For labelling purposes, these cells were named GFAP$^+$/STAT3α$^+$ cells in subsequent data reporting. For STAT3α$^+$/ DAPI$^+$ cell count, the channels were split using image J and DAPI and TRITC channels were merged for analysis. For a cell to be defined as STAT3α$^+$/DAPI$^+$; the criteria were:

- STAT3α$^+$ was localised to a DAPI$^+$ nucleus

The number of cells confirming these criteria was counted visually and numbers were collated in a Microsoft Excel document under the assigned experimental number (figure 2.3).

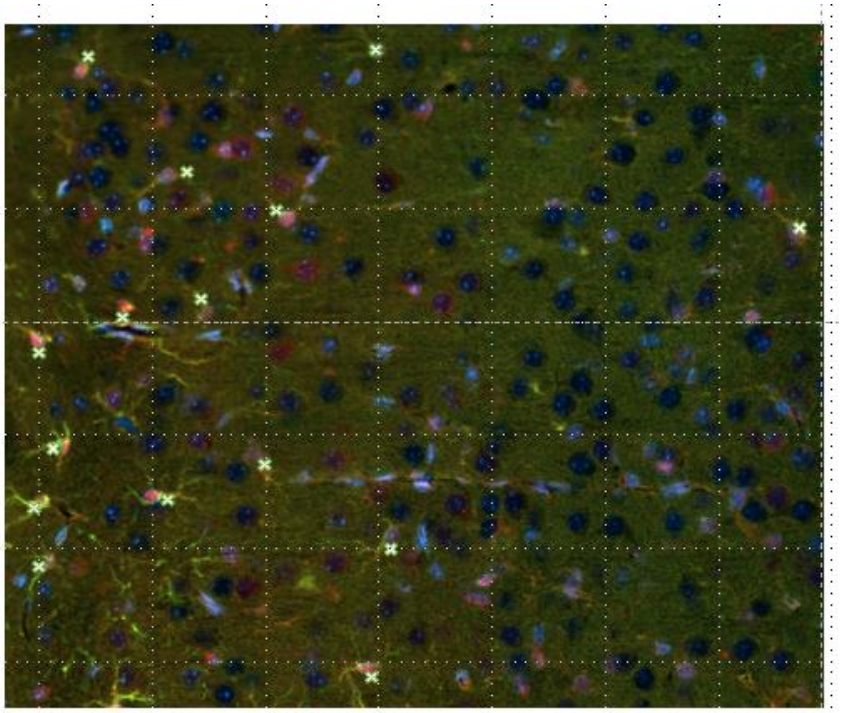

Figure 2.2:Example of GFAP^{+}/STAT3α^{+}/DAPI^{+} counting technique and positive cells in the frontal cortex. Cells were counted using the criteria and an X was marked adjacent to cells that matched the criteria. This field of view illustrates 15 positive cells.

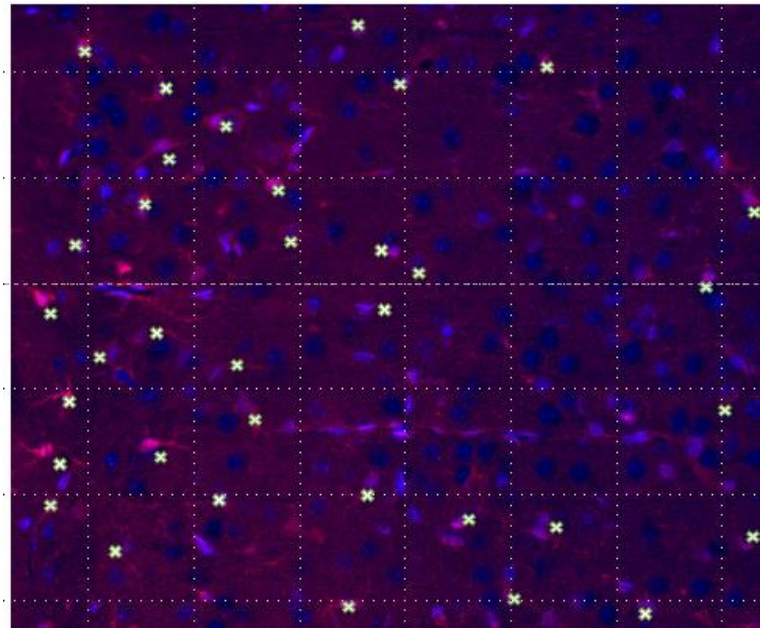

Figure 2.3:Example of STAT3α^{+}/DAPI^{+} counting technique and positive cells in the frontal cortex. Cells were counted using the criteria and an X was marked adjacent to cells that matched the criteria. This field of view illustrates 34 positive cells.

Results for each replicate of genotype (n=4) were grouped for each region of interest by experimental group. The resultant numbers were used for a two-way ANOVA (analysis of

variance) to assess statistical significance between age (IV), genotype (IV) and number of positive cells (DV).

2.3.4.2 Percentage of STAT3α$^+$/DAPI$^+$ cells associated with GFAP

From each picture, STAT3α$^+$/DAPI$^+$ positive cells were counted and the number of GFAP$^+$/STAT3α$^+$/DAPI$^+$ positive cells was divided to assess the percentage of cells associated with GFAP in each experimental condition. The resultant percentage was subtracted from 100% to assess the percentage of STAT3α$^+$/DAPI$^+$ only cells. The result for each replicate of each genotype (n=4) was grouped for each region of interest by experimental group. No statistical test was performed on this data set.

Example:

GFAP$^+$/STAT3α$^+$/DAPI$^+$ cells in the frontal cortex = 15

STAT3α$^+$/DAPI$^+$ cells in the frontal cortex = 34

$$\frac{15}{34} \times 100 = 44.11\%$$ **GFAP$^+$/STAT3α$^+$/DAPI$^+$ cells**

$$100 - 44.11 = 55.89\%$$ **STAT3α$^+$/DAPI$^+$ cells**

2.3.4.3 Region of interest for GFAP$^+$ area analysis

A representative section of that image was selected by cropping the image to a 3 x 3 cm box and saving the resultant image under its experimental number in TIFF format (figure 2.4) Images were analysed subsequently with ImageJ (NIH, US (https://imagej.nih.gov/ij/)).

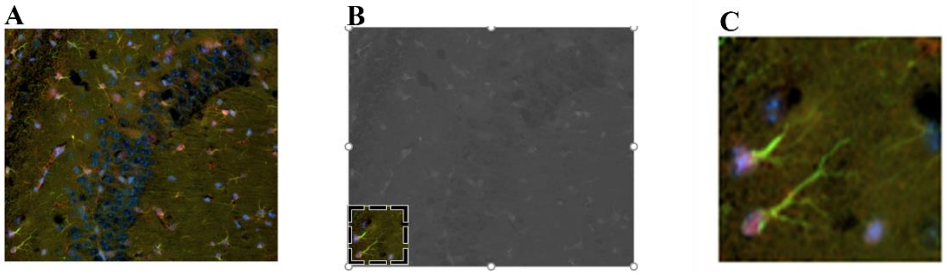

Figure 2.4*:* Images were imported to Microsoft Powerpoint, and a representative section of that image (3 x 3) was used to assess the GFAP$^+$/STAT3α$^+$ area. 2.4A) Image (CA3) was cropped to 3x3cm square (2.4B) to produce a resultant image (2.4C) that was used for image J analysis.

2.3.4.4 GFAP$^+$ area measurement

Channels were separated using the 'split channel' feature, and the FITC channel (GFAP) underwent manual thresholding to carefully include all areas of GFAP, minimising background

interference, to create a binary image. The total area of GFAP was measured using the measure function to provide GFAP area measurement (measured in pixels/255) (figure 2.5). The result for each replicate (n=4) was grouped for each region of interest. The resultant numbers were used for a two-way ANOVA to assess statistical significance.

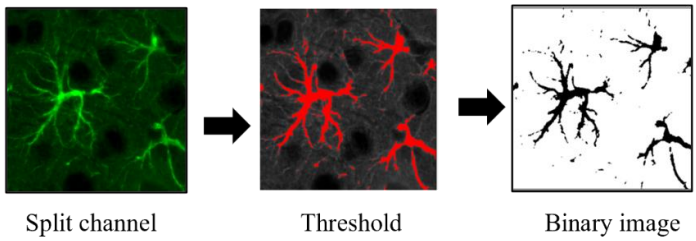

Figure 2.5: GFAP area was measured in the region of interest (ROI): Image was split into individual resultant channels (DAPI/FITC/TRITC). The DAPI and TRITC channel was discarded. Image underwent thresholding to include all visible GFAP signal, minimising background interferences. The resultant binary image was analysed using the 'measure' function in ImageJ, counting the number of pixels positive for STAT3α^{+} area measurement

Channels were separated using the 'split channel' feature, and the TRITC channel (STAT3α) underwent thresholding to carefully include all areas of STAT3α, minimizing background interference, to create a binary image. The total area of STAT3α was measured using the measure function to provide STAT3α area measurement (measured in pixels/255) (figure 2.6). The result for each replicate of each genotype (n=4) was grouped for each region of interest. The resultant numbers were used for a two-way ANOVA to assess statistical significance between age (IV), genotype (IV) and number of positive cells (DV).

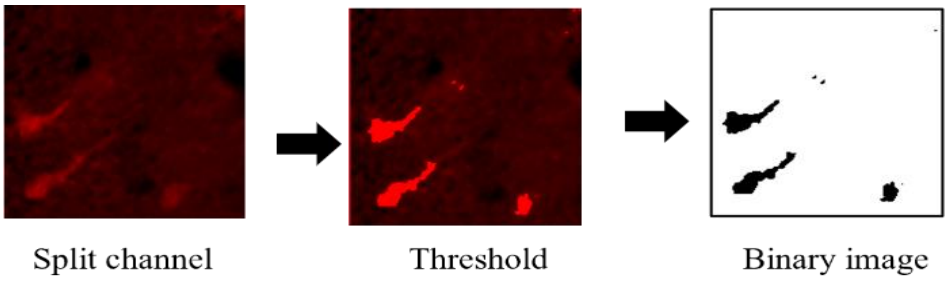

Figure 2.6:STAT3α area was measured in the region of interest (ROI). Image was split into individual resultant channels (DAPI/FITC/TRITC). The DAPI and FITC channel was discarded. Image underwent thresholding to include all visible STAT3α signal, minimising background interferences. The resultant binary image was analysed using the 'measure' function in ImageJ, counting the number of pixels positive for the thresholded signal**.**

2.3.4.5 Astrocytic-STAT3 measurement

To assess Astrocytic-STAT3α, the image channels were split to DAPI/TRITC/FITC once again. The TRITC channel was thresholded as described previously to create a binary image. The select tool was used to select STAT3α localized within a chosen $GFAP^+/STAT3\alpha^+$ cell. The measure function was then used to measure the area of Astrocytic-STAT3α (figure 2.7). The result for each replicate (n=4) was grouped for each region of interest. The resultant numbers were used for a two-way ANOVA to assess statistical significance.

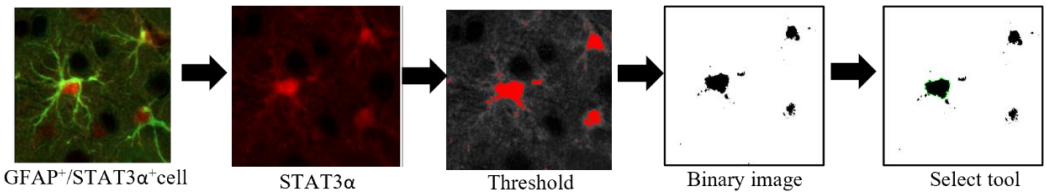

Figure 2.7:Astrocytic-STAT3α area was investigated by using the threshold, select and measure tool in ImageJ software. Figure illustrates process of investigating Astrocytic-STAT3α area. Region of Interest (ROI) was selected, which was then thresholded to become a binary image. The select tool was then used to select astrocytic-STAT3α and the measure function was used to express astrocytic-STAT3α area (/255 pixels)

2.4 Western blot

Western blotting was used to estimate total protein quantity levels for the following targets: GFAP, STAT3α, Phosphorylated-STAT3 (Tyrosine 705) and GAPDH.

2.4.1 Tissue processing

In this project, animals were culled via the Schedule 1 method of cervical dislocation aligning with home office animal regulations (see section 2.1.1). The mouse was decapitated, the skin was removed from the head and brains were rapidly removed from the skull. The brain was separated via the fissure line and separate hemispheres were placed in 1.5 mL cryotubes. The tissue was flash-frozen via dropping in liquid nitrogen. Liquid nitrogen was removed, and tubes containing the brain pieces sections were stored at -80 ºC until the tissue lysis procedure.

To lyse the tissue, tissues were placed on dry ice and radioimmunoprecipitation assay buffer (RIPA buffer) buffer was prepared: 50 mM Tris hydrochloride, 150 mM sodium chloride, 1.0% (v/v) NP-40, 0.5% (w/v) sodium deoxycholate, 1.0 mM EDTA, 0.1% (w/v) SDS and 0.01% (w/v) sodium azide at a pH of 7.4. Protease inhibitor cocktail (1:500, #ab271306,Abcam) and

phosphatase inhibitor cocktail (1:500, # P2850, Sigma Aldrich) were added immediately before use.

Small plastic beads were added (10 approx.) to each brain section, and 500 µL of RIPA buffer was added to each halved cortice. Tissue was carried on ice to the Beadbeater BP, mixed for 20 secs twice with 10 secs rest. After this, the tissue was centrifuged at 16,100 g for 10 minutes. The supernatants were removed and collected in a new Eppendorf tube. These supernatants were assessed for protein concentration using the Pierce ™ Bicinchoninic acid (BCA) assay kit (#23225, Thermofisher).

2.4.2 BCA assay

BCA assay was conducted according to the manufacturer's instructions, with adaptations. BSA standards of varying concentrations from 0 to 0.05 mg/mL were made from 1 mg/mL stock and diluted with RIPA buffer. 2 µL of the sample was diluted with 48 µL of RIPA buffer and three replicates of each standard were undertaken. BCA reagent A and BCA reagent B were mixed per the manufacturer's instructions, and 150 µL was added to each well of 96 well plates with clear bottom. This reaction was heated to 37 ºC for 30 minutes. A spectrometer (SPECTROstar Nano, BMG Labtech) was used to read the absorbance of the samples at 562 nm. Known standards were plotted on a graph to create a standard curve, which was used to estimate protein concentration in unknown samples (figure 2.8).

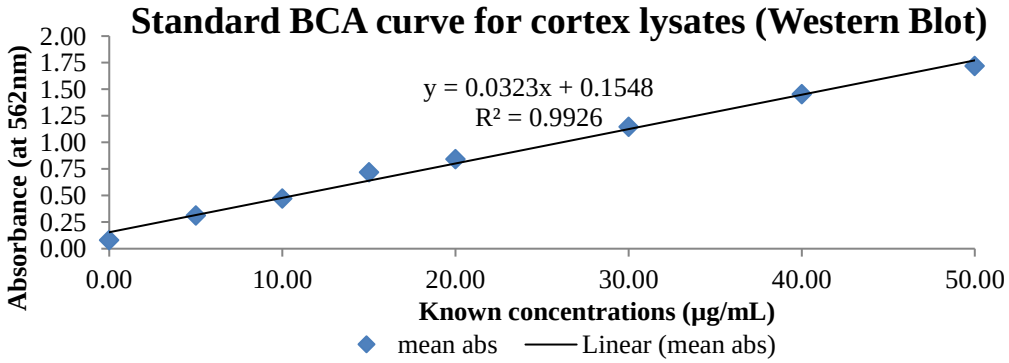

Figure 2.8:Standard BCA curve for cortex lysates for estimating protein concentration for western blot lysates. The predetermined concentration of BSA (0-50µg/mL) was plotted and measured against absorbance values (measured at 562nm). The line of best fit was used to create intercept and slope values.

In this example, the protein concentration is estimated using the intercept value (0.1548) and slope value (0.0323) of the curve. For example, A triplicate of unknown lysates reporting an

absorbance value of 0.77, 0.74, and 0.79 would undergo this calculation to estimate protein concentration:

$$\text{Replicate 1: } 0.77 \quad \frac{0.77-0.1548}{0.0323} = 19.07\ \mu g$$

$$\text{Replicate 2: } 0.74 \quad \frac{0.74-0.1548}{0.0323} = 18.11\ \mu g$$

$$\text{Replicate 3: } 0.79 \quad \frac{0.79-0.1548}{0.0323} = 19.07\ \mu g$$

These replicates were averaged to find the mean concentration of the lysate:

$$\frac{19.07+18.11+19.07}{3} = 18.75\ \mu g$$

The resultant number is divided by 2 (the number of microlitres added to the sample) to establish µg/µL

$$\frac{18.75}{2} = 9.375\ \mu g/\mu L$$

To establish the volume of the lysate to add to establish 100 µg of protein, the following calculation is undertaken:

$$\frac{100}{9.375} = 10.66\ \mu L$$

Due to the low concentration of phosphorylated proteins, 100 µg of protein was used as a standard for all western blots in this thesis.

2.4.3 Sample preparation

100 µg of lysate was mixed in equal volume with 2 x Gel Application Buffer (0.15M Tris, 8M Urea, 2.5% (w/v) SDS, 20% glycerol, 10% 2-mercaptoethanol, 3% DTT) (i.e. 2 x GAB) in 1.5 mL Eppendorf tubes. These tubes were then heated to 95 ºC for 5 min and centrifuged at 16,100 g for 10 min.

2.4.4 Sodium-dodecyl sulfate-polyacrylamide gel electrophoresis (SDS-PAGE)

A 5-20 % Tris-Glycine gradient gel was utilised for separating proteins via molecular size for western blotting analysis. Prior, gel plates were cleaned with 70 % ethanol and assembled using large bulldog clips to secure a gasket between the large and smaller plate. A spirit level was used to ensure the plate alignment was straight. 5% and 20% resolving gels were made as in

table 2.6, adding ammonium persulphate (APS) and tetramethylethylenediamine (TEMED) just before use. A gradient-gel pourer was used to make the gradient gel. Water-layered butanol was then overlaid on the top of the gel to eliminate air bubbles. The gel was left to set for 10 min, then water-saturated butanol was washed off with distilled water and blotted thoroughly. Stacking gel was then made and poured onto the resolving gel, a 14-well comb was put in and left for 10 min. The comb was removed under deionised water washes to remove excess acrylamide and then assembled into the gel tank. The inner chamber of the gel tank was filled with electrode buffer (25mM Tris, 186 mM Glycine, 0.1% (w/v) SDS). 3µL of BLUeye Prestained Protein Ladder (#PM007-0500, Bio Helix) was inserted alongside the samples to estimate protein size. The gel tank was run at 40V per gel (Max 500 mA) for 90 minutes, or until the dye front was no longer visible.

Table 2.6: Gel compositions (5% resolving gel, 20% resolving gel, 4% stacking gel) for SDS-PAGE

5% Resolving Gel

Volume (mL)	Reagent
3.33	Buffer B (1.1 M Tris, 0.1% (w/v) SDS, pH 8.8)
5.00	Water
0.1	10% w/v APS
1.67	Acrylamide
0.0.1	TEMED
0.10	0.1% w/v SDS

20% Resolving Gel

Volume (mL)	Reagent
3.33	Buffer A (1.1 M Tris, 0.1% (w/v) SDS, 30% Glycerol, pH 8.8)
6.67	Acrylamide
0.10	10% w/v APS
0.01	TEMED
0.10	0.1% w/v SDS

4% Stacking gel

Volume (mL)	Reagent
5.00	Stacking gel (0.14 M Tris, 0.1% (w/v) SDS)
1.00	Acrylamide
0.10	10% w/v APS
0.01	TEMED

2.4.5 Western blot transfer

One piece of 11 cm x 15 cm 0.45 µm-pore size nitrocellulose membrane (#1620115, Biorad) and two 12 cm x 16 cm blotting papers per gel were submerged in Western Transfer Buffer and then assembled in the cassette: Positive Anode (Red), Blotting Paper, Nitrocellulose, gel, Blotting Paper (Negative Anode). Air bubbles were removed by using a rolling motion over the sandwich. The cassette was inserted into a western blot transfer tank, submerged in western transfer buffer (0.025 M Tris, 0.192 M glycine, 20% (v/v) Methanol) and ran at 8 V (max 40 mA) overnight. As GAB and the SDS denaturation of the protein give the protein an overall negative charge, this causes the proteins from the gel to transfer onto the paper.

2.4.6 Visualising protein transfer

After overnight transfer, the quality of protein transfer to the membrane was assessed. The membrane was removed from the cassette and placed in Ponceau stain (0.1% Ponceau S, 100 mL glacial acetic acid, 900 mL deionised water) for 5 min. Ponceau is a reversible stain which is used to visual protein bands in red or pink colour (Sander et al., 2019).After this, the ponceau stain was removed and the membrane was placed in Tris Buffer Saline solution (10mM Tris, 150 mM sodium chloride, pH 7.5) (TBS) to wash off excess ponceau. The blot was scanned using University scanner software for future reference (figure 2.9).

Figure 2.9: Example of Ponceau stain used to visualise protein transfer after overnight transfer. Ponceau was added to the membrane for 5 mins then washed with TBS to remove excess ponceau then scanned for future reference. This membrane was discarded due to air bubble formation at the MW kDa region of interest.

If the ponceau stain highlighted uneven loading of proteins, poor transfer, or trapped air bubbles in regions of interest, the membrane was discarded. The membrane was washed for 10 min thrice in TBS to remove excess ponceau stain.

2.4.7 Blocking, primary and secondary antibody treatment of membrane

After the ponceau stain was completely removed, the membrane was blocked against non-specific binding proteins in 5% Marvel® powder in TBS with 0.05% tween (TBS-T) for one hour, then incubated with the following antibodies diluted in 5% Marvel® in TBS-T: GFAP, Phospho-STAT3 Tyrosine 705 (pSTAT3 Tyrosine 705),STAT3α and Glyceraldehyde 3-phosphate dehydrogenase (GAPDH) at 4 ºC overnight at differing concentrations (table 2.7).

Table 2.7: Primary antibodies used for Western Blot in control and Psmc1$^{fl/fl}$;CaMKIIα-*cre* cortices

Antibody target	Raised in	Product number	Concentration
GAPDH	Rabbit	#ab128915, Abcam	1:10,000
GFAP	Mouse	#ab4648, Abcam	1:4000
STAT3α	Rabbit	#8768, Cell signaling	1:1000
Phospho-STAT3 (Tyrosine 705)	Rabbit	#ab76315, Abcam	1:500

After overnight incubation, membranes were washed with TBS-T for 20 min three times to remove excess primary antibodies. Horseradish Peroxidase (HRP) tagged secondary antibodies (table 2.8) were diluted in 5% Marvel® in TBS-T and the membranes were incubated with the species-appropriate solution for 1 hr at room temperature. After this, membranes were washed in TBS-T for 5 min thrice to remove excess secondary antibodies.

Table 2.8: HRP secondary antibodies used for the western blot of control and Psmc1$^{fl/fl}$;CaMKIIα-*cre* cortices

Antibody target	Raised in	Product number	Concentration
Rabbit	Swine	P0399, DAKO	1;1000-1:4000
Mouse	Rabbit	P0260,DAKO	1:4000

2.4.8 Visualising blot

The membranes were transferred to a clean container. Equal volumes of the Pierce™ ECL Western Blotting Substrate detection agent (#32106, Thermofisher) were mixed in a universal and added to the blot for approximately 2 min. The excess detection agent was removed, and the blots were wrapped in cellophane and secured in a developing cassette. Under UV light, transfer film was added, and the cassette was closed. After a fixed time, the transfer film was submerged in Ilford 2150XL developer to visualise protein bands and placed in ILFORD 2150XL fixative solution (#1992182, Ilford) for 2 min minimum. The films were washed in water and left to dry. The film was scanned using University scanner software for analysis.

2.4.9 Analysis

The scanned film was analysed using ImageJ software (NIH, US,(https://imagej.nih.gov/ij/)). The rectangle tool was used to draw around the protein band of interest, keeping a standard region of interest size for each protein band (area: 0.020) (figure 2.10). The measure function

was then used, and the mean value of the resultant measurement was used for further quantitative analysis.

Figure 2.10:Image J analysis of western blot to assess the quantitative value of protein bands Region of interest was drawn using the rectangle box around protein bands, the measure function was then used to give a quantitative number which was used for subsequent analysis.

The mean value was then subtracted from 255 (number of pixels) to give the overall value. This was repeated with each lane. The background value was also calculated by using the same sized region of interest to measure just below the band (figure 2.11). This mean value was also subtracted from 255 (number of pixels) to give the overall value. This was also repeated with each lane.

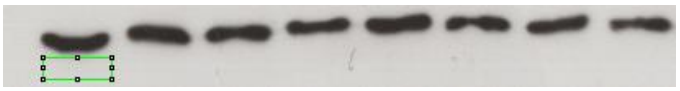

Figure 2.11:Background measurement in Image J was calculated to remove potential background from the protein band. The same region of interest was used and selected underneath the protein band; the measure function was then used to give a quantitative number of background measurements which was used for subsequent analysis.

The background value was subtracted from the signal value to give the final mean value. This was repeated for each protein of interest (GFAP, Phospho-STAT3 Tyrosine 705 (pSTAT3 Tyrosine 705), STAT3α) and its corresponding loading control (GAPDH) on each blot. A calculation was undertaken where each replicate protein signal was normalised to the corresponding control replicate to create a fold change:

$$\frac{\text{Signal of chosen protein (113)}}{\text{Loading control (95)}} = 1.19 \text{ fold change}$$

The fold change ratios were calculated for each replicate (4 = control) (4 = Psmc1 $^{fl/fl}$;CaMKIIα-*cre*) in each experimental condition (2 weeks, 3 weeks, 4 weeks) for each protein of interest. The fold change ratios were analysed in Prism (Graphpad, version 9) software, where an unpaired-t-test was conducted to assess statistical significance.

2.5 Quantitative real-time polymerase chain reaction (qRT-PCR)

2.5.1 RNA extraction

Before starting, all surfaces were sprayed with RNAzap to prevent potential contamination. RNA extraction is per the manufacturer's protocol (#74134, RNeasy Plus Mini Kit, Qiagen). For sample extraction, flash-frozen hippocampi from 3,4 and 5 weeks-old Psmc1 $^{fl/fl}$;CaMKIIα-*cre* mice and age-matched control littermates were used. Hippocampi were weighed before RNA processing to ensure the RNeasy spin column was not overloaded.

Tissues were kept on dry ice in 1.5 mL Eppendorf tubes, and 1 mL of QIAzol Lysis Reagent (#79306, QIAGEN) was added to the hippocampi on ice and homogenised using a rotator stator homogeniser for 20 seconds. The sample was left to stand at room temperature for 5 minutes. 100 µL of gDNA eliminator solution was added and samples were shaken vigorously for 15 seconds.180 µL of chloroform was added to each tube and the sample was shaken vigorously for 15 seconds. The sample was left to stand at room temperature for an additional 3 minutes. The lysates were centrifuged at 12,000 g for 15 minutes at 4 ºC. This led to a 3-layered gradient, containing an aqueous phase (RNA),white interphase and a red organic phase. 600 µL of the aqueous phase was added to an RNA-free tube and mixed with an equal volume of 70% ethanol through pipetting.600 µL of the sample was transferred to a RNeasy mini spin columns placed in a 2 mL collection tube and centrifuged for 15 secs at 8000 x g at room temperature. This flow-through was then discarded. This was repeated with the remainder of the sample, again discarding the flow through. 700 µL of Buffer RWT was added to the RNeasy spin column and centrifuged for 15 secs at 8000 g, and the flow through was discarded. 500 µL of Buffer RPE was added to the RNeasy spin column and centrifuged for 15 secs at 8000 g, and the flow through was discarded.

A final 500 µL of Buffer RPE was added to the RNeasy spin column and centrifuged for 2 min secs at 8000 g, and the flow through was discarded. 30 µL of RNAse-free water was added to the RNeasy spin column and centrifuged for 1 min at 8000 x g to elute RNA. The resulting RNA concentration per µL was assessed by pipetting using Nanodrop 2000c UV/IV Spectrophotometer (#ND2000CLAPTOP, Thermofisher) and 260/230 ratios were checked for quality.

2.5.2 cDNA synthesis

cDNA synthesis is carried out using reverse transcriptase enzyme, using the RNA template to create complementary DNA. The following materials were combined in a 200 µL sterile eppendorf for cDNA synthesis, with the same total volume for each reaction (table 2.9).

Table 2.9: Volumes of reagents used for cDNA synthesis of isolated RNA from mice hippocampi

Volume (µL)	Reagent
1	50 µM random hexamers
1	10 mM dNTP mix (A/T/C/G)
Up to 11	Template mRNA (100 ng)
Up to 13	HyClone Water

The materials were briefly mixed and then centrifuged (1000, g for 10 secs) to ensure the RNA was at the bottom of the tube. This mixture was heated at 60 °C for 5 min and then placed on ice for one min to allow the random hexamers and dNTPs to anneal to the RNA.

To synthesise double-stranded cDNA, a reverse transcriptase (RT) reaction is needed. Again, the following materials were combined in 200 µL sterile eppendorf tubes (table 2.10).

Table 2.10: Reverse Transcription Reaction for double-stranded cDNA synthesis

Volume (µL)	Reagent
4	5 x SuperScript™ IV RT Reaction Buffer (#18090050B, Thermofisher)
1	100 mM dithiothreitol (#R0861, Thermofisher)
1	RNaseOUT™ Recombinant RNase Inhibitor (#10777019, Thermofisher)
1	SuperScript® IV Reverse Transcriptase (200 U/µL (#18090010, Thermofisher)

The 7 µL RT reaction mix was added to the annealed RNA then incubated at 23 °C for 10 min,50–55 °C for 10 min, then inactivated the reaction by incubating at 80 °C for 10 min. The resultant cDNA was quantified using the Nanodrop 2000c UV/IV Spectrophotometer (#ND2000CLAPTOP, Thermofisher) and stored at -20 ºC until use.

2.5.3 qRT-PCR

10-25 ng of cDNA was used in each PCR reaction depending on the quantity of DNA needed for specific target gene expression. As DNA template concentration was variable between each replicate, the amount of cDNA was variable (table 2.11, table 2.12). A no template control (NTC) was also included. The qPCR plate was centrifuged and checked for bubbles before running on the Agilent Step One Plus thermocycler using the standard cycling program (table

2.13). A melt curve was also performed to assess the purity and specificity of each product (table 2.14).

Table 2.11: cDNA quantity, primer targets and forward and reverse primers for qRT-PCR in hippocampi

cDNA (ng/µL)	Target	Reverse	Forward
25	TNF-α	GCTACGACGTGGGCTACAG	CCCTCACACTCAGATCATCTTCT
10	IL-6	TTGGTCCTTAGCCACTCCTTC	TAGTCCTTCCTACCCCAATTTCC
25/10	GAPDH	TGCTGTTGAAGTCGCAGGAG	TGGTGAAGCAGGCATCTGAG
10	CXCL10	GGCTTGACATATACTCCATGTAGGG	AGCAAGGAAAGGTCTAAAAGATCTCC
10	STAT3α	CAGACTGGTTGTTTCCATTCAGAT	ACCCAACAGCCGCCGTAG

Table 2.12: qRT-PCR SYBR™ Green Master Mix composition

Volume (µL)	**Reagent**
10	PowerUp™ SYBR™ Green Master Mix (2X) (#15350929, fisher scientific)
Variable	Forward and reverse primers 400nM
Variable	DNA template + Nuclease-Free Water (10 ng / 25 ng cDNA for each reaction)

Table 2.13: Standard Cycling Mode PCR programme for qRT-PCR

Temperature (°C)	**Duration (secs)**
50	120
	1 cycle
95	120
	1 cycle
60	30
	40 cycles
60	30

Table 2.14: Melt curve cycling mode to assess purity and specificity of target

Step	Ramp rate	Temperature	Duration
1	1.6°C/second	95°C	15 sec
2	1.6°C/second	60°C	1 min
3	0.15°C/second	95°C	15 sec

2.5.4 qRT-PCR data analysis and statistical testing

For qRT-PCR analysis, the threshold value was set in the exponential phase. NTC samples were checked for no or minimal signal to ensure there were no contaminants present. Melt curves were checked for a sharp specific peak to indicate specificity to the target. Multiple plates were used and the thresholds were set at the same value for each gene on each plate. The comparative Ct method was used to compare test samples to a calibrator (control) sample, and by also normalising to housekeeper gene, GAPDH. All the Ct values of test genes were normalised to housekeeper gene GAPDH for both control and Psmc1$^{fl/fl}$;CaMKIIα-*cre* mice samples:

Difference between Ct values of target gene (e.g TNF-α) and housekeeping (GAPDH) = ΔCt

This value was normalised to the average of the control samples at each time point.

ΔCt sample - ΔCt control average = ΔΔCt

Results were expressed as fold change compared to control which assumes there is double the amount of product. $2^{-\Delta\Delta Ct}$

The fold change of the qRT-PCR target compared to the housekeeper compared to control sample value ($2^{-\Delta\Delta Ct}$) was used for this analysis. GraphPad Prism software was used to undertake unpaired t-tests between each target in each experimental group (i.e: CXCL10 in 3-week control and 3-week Psmc1$^{fl/fl}$; CaMKIIα-*cre* mice). Two-way ANOVA's were conducted on Astrocytic-STAT3 initiators and Astrocytic-STAT3 markers (DV) between age (IV) and genotype (IV).

2.6 Acute slice experiments

2.6.1 Experimental setup

A 1L stock solution of standard Krebs buffer was prepared: 126 mM sodium chloride, 3 mM potassium chloride, 1.2 mM sodium dihydrogen phosphate, 25 mM sodium bicarbonate, 15 mM glucose w/v deionised water. Before the experiment started, 3mM magnesium sulfate was added to 250 mL to create the 'cutting buffer' and then placed at - 20°C for 1 h. The remaining solution was supplemented with 2 mM magnesium sulphate and 2 mM calcium chloride and bubbled with carbogen (95% O_2, 5% CO_2) in a 32 °C heated water bath.

In this project, a C57BL mouse pup (p21) was culled by cervical dislocation, followed by decapitation to confirm death. The brain was rapidly removed and placed in pre-cooled carbogenated cutting buffer, on ice.

Brains were dissected by the removal of the cerebellum and occipital lobes, then a scalpel was used to cut down the midline to separate the hemispheres. This dissection ensured that portions of the frontal, parietal, temporal and occipital lobes and underlying subcortical regions were available for slicing. The block was mounted on a vibratome cutting plate, secured with superglue on the cut surface with the sagittal plane uppermost. The cutting plate was mounted in the vibratome bath, which was filled with ice-cold cutting buffer, which was continuously bubbled with carbogen. The vibratome (VT1000 S vibratome, Leica) was used to cut 400 µm slices in the sagittal plane (figure 2.12).

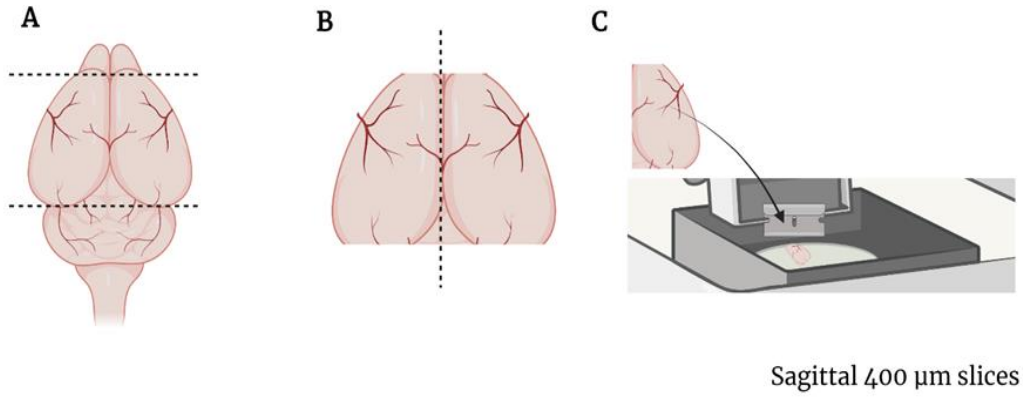

Figure 2.12:Brain dissection and mounting to retrieve sagittal slices 2.12A) Occipital lobes and cerebellum were removed from the brain and discarded. 2.12B) A scalpel was used to cut down the midline to separate the two hemispheres. 2.12C) Each hemisphere was mounted on the vibratome stage with the sagittal plane uppermost, cutting 400µm sagittal orientation slices.

2.6.2 Recovery and experimental chambers

Using a cut Pasteur pipette, slices were transferred to the nylon mesh in a hand-made designed recovery chamber in a water bath at 32 ºC, which was situated alongside 3 experimental chambers. These chambers were filled with Krebs buffer supplemented with magnesium sulphate and calcium chloride (Krebs 2 mM $MgSO_4$, 2 mM $CaCl_2$) ensuring the buffer covered the nylon mesh which would contain the brain slices. The inlet line supplied a continuous source of carbogenation, to provide sufficient oxygenation and slices were left in the recovery chamber in the heated water bath for 1 hr to recover from the slicing procedure (figure 2.13).

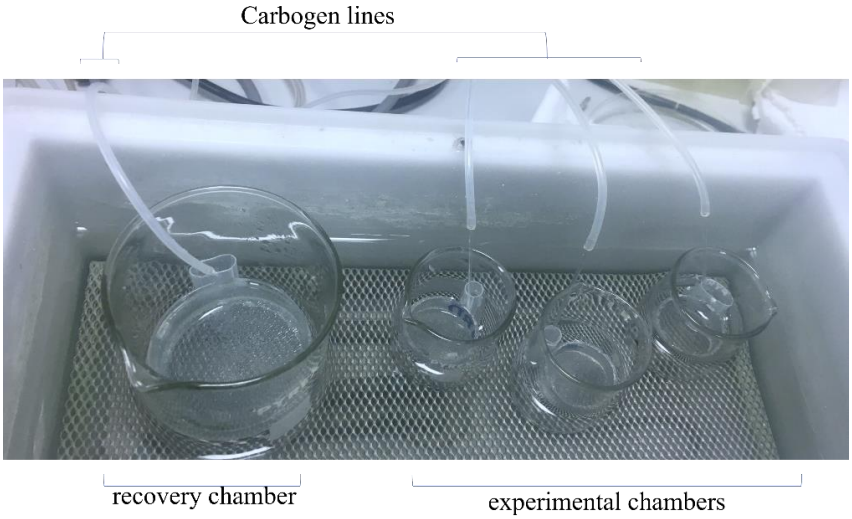

Figure 2.13:Recovery and experimental chambers used for acute slices. The recovery chamber and experimental chambers are shown in the diagram with carbogen inlets featured. Slices were placed in the recovery chamber for 1hr before pharmacological treatment.

2.6.3 Pharmacological treatment

After 1 hr, 50 mL of heated Krebs 2 mM $MgSO_4$, 2 mM $CaCl_2$ buffer was poured into experimental chambers with each carbogen line set up. 3 slices were transferred from the recovery chamber to each experimental chamber. The pharmacological agent (CXCL10, #500-P129, Peprotech; IL-6, #216-16; Peprotech; TNF-α #510-RT, R&D Systems; Bz-ATP, #A-385, Alome; 2-MeS-ADP, #1624, Tocris; STATTIC, #2798, Tocris,) was diluted to desired concentration in total bath volume via direct pipetting into the experimental chamber. For control slices, an equal volume of Krebs (2 mM $MgSO_4$, 2 mM $CaCl_2$) was added, represented by the term 'NULL'. A timer for 2 minutes was set in between multiple conditions to ensure all slices had equal time in the pharmacological reagent and ensure there was enough time for inactivating the slices in tandem. Slices were incubated in the reagent for 30 min.

2.6.4 Inactivation of slices

After 30 min, a 2 min timer was set in which within this period slices were inactivated. As 3 slices were present in each experimental chamber, 2 slices were processed for immunofluorescence staining and 1 slice was used for western blot. It was ensured that the slice number for each replicate matched, and each condition had a common approximate brain region to standardise analysis. The slices that were for immunofluorescence staining were fixed in 4% paraformaldehyde and 5% sucrose in 0.1M phosphate buffer solution (pH 7.4) for 3 hrs at 4 °C. The slice that was for western blot was collected in an eppendorf and flash frozen in liquid nitrogen and stored at -80 °C until tissue lysis was needed. Due to the limited number of slices available for each experiment, pharmacological tests were separated into separate runs (table 2.15).

Table 2.15: Experimental time course of pharmacological treatments in acute slices

Run	Pharmacological agent	Reagent concentration
1	CXCL10	100 ng/µL
	IL-6	100 ng/µL
	TNF-α	200 ng/µL
	Null	N/A
2	2-MeS-ADP	100 µM
	Bz-ATP	100 µM
	STATTIC	10 µM
	Null	N/A

2.6.5 Immunohistochemistry of acute slices

2.6.5.1 Tissue slice fixing and sectioning

After fixation, tissue slices were submerged in 20% sucrose (w/v PBS) overnight at 4 °C. Slices were then placed in a cryomold using a fine paintbrush and submerged in an embedding medium (Tissue-Tek OCT; Raymond Lamb, London, UK) for 30 min. These were left to solidify in the freezer for 30 min. These were then mounted onto a cryostat chuck. A Leica cryostat 3050 S model was equilibrated to the block temperature of -12 °C and the chamber temperature of -20 °C. This cryostat was then used to cut 12 µM slices, which were mounted on Epredia™ SuperFrost Plus™ Adhesion slides (#10149870, Fisher Scientific). Slides were kept in a slide box at - 20 °C.

2.6.5.2 Immunofluorescence on frozen tissue

For full details of the source of the reagents used, please refer to section 2.3.3

Slides were returned to room temperature and washed in PBS for 5 min. Slides were treated with 0.1% sodium borohydride for 10 min thrice, then washed with 0.9% (w/v) saline for 40 min then washed with PBS for 40 min. The non-specific background was blocked using a 10% goat serum v/v M.O.M blocking agent (as directed) for one hour at room temperature. The blocking agent was removed, and primary antibodies (pSTAT3 Tyrosine 705: 1:50; GFAP 1:200) in 10% goat serum and 10% M.O.M concentrate was added and incubated for 48 hours at 4 °C. Slides were washed with PBS for one hour, then secondary antibody (1:500 AF568 Rabbit, 1:500 AF488 Mouse) in 10% goat serum and 10% M.O.M concentrate for one hour in the dark. Slides were washed in PBS then DAPI (1:1000) was applied for 5 mins. Slides were washed in PBS and then mounted with 5 µL of DAKO media, using nail varnish to seal the edges.

2.6.5.3 Analysis

Zeiss Axio Vert.A1 Microscope was used to take images at x10 and x20 magnification using Zen 2.5 software (www.Zeiss.com). Unfortunately, due to tissue degradation, in-depth analysis as performed in section 2.3.4 was unable to be replicated.

2.6.6 *Western blotting of acute slices*

Please see section 2.4.7 for details on how the tissue was lysed, protein quantity was estimated, SDS-PAGE electrophoresis, western blot transfer and visualising of protein transfer was conducted. The blocking and primary incubation of Phospho-STAT3 Tyrosine 705 with 5% Marvel in TBS-T was kept the same for all conditions. For these experiments, 100 µL of RIPA buffer with associated protein and phosphatase inhibitors was added, instead of 500 µL.

2.6.6.1 Detection of pSTAT3 Tyrosine 705

For fluorescence secondary antibody, IRDye® 680RD Goat anti-Rabbit IgG Secondary Antibody (# 926-68071, LI-COR) was diluted to a 1:5000 dilution in TBS and used for detection of Phospho-STAT3 Tyrosine 705. Membranes were incubated in this solution in a light-proof container for one hour, then washed with TBS-T twice for 10 min, with a final wash

of TBS for 10 min. The image was then scanned in a LI-COR Odyssey® 9120 Imaging system to visualise protein bands. The results image was exported into a TIFF file and subsequently analysed in Image J.

2.6.6.2 Analysis

All membranes, LI-COR and HRP underwent the same protein band measurements as listed in section 2.4.9. As immunofluorescence showed endogenous phospho-STAT3 Tyrosine 705 activation at the cut edge in control slices, the calculation was changed to normalise to membrane-specific control phosphoSTAT3 tyrosine instead of a housekeeping gene.

$$\frac{\text{Signal of pharmacological reagent } (172)}{\text{Signal of control slice } (104)} = 1.65 \text{ fold change}$$

The fold change ratios were calculated for each replicate per condition (4 replicates). The fold change ratios were submitted to Prism GraphPad where an unpaired t-test was conducted to assess statistical significance.

Chapter 3 Protein expression profiling in Psmc1$^{fl/fl}$;CaMKIIα-*cre* mice across disease progression using SWATH-MS.

3.1 Introduction

3.1.1 Protein expression profiling by proteomics

Genetic mutations are widely accepted as risk factors for familial inherited neurodegenerative disease; however, this only accounts for 5 % of all neurodegenerative diseases (NDs), suggesting sporadic cases have unclear etiopathogenesis (Julio-César and Rosa-Helena, 2018). Therefore, our current knowledge of the molecular pathogenesis involved in neurodegenerative disease is currently incomplete. As these diseases are complex, a broad investigative approach is needed to unravel the molecular pathways underlying these conditions.

Humans are estimated to have 19,969 genes potentially which after transcription, translation, alternative RNA splicing and post-translational modification (PTM) can potentially represent 400,000 different types of proteins (Kozak, 2007). This range of proteins presents an analysis problem when trying to understand the key changes that occur during neurodegenerative diseases, as they are taking place after the transcription of genes and post-translationally. The field of proteomics, the study of protein expression by the cell, may be able to enlighten this situation.

Mass spectrometry analysis of patient and animal model samples shows high accuracy in the identification of proteins and has shown utility in identifying non-invasive biomarkers for the diagnosis of diseases through blood, cerebral spinal fluid, and urine (Diamandis, 2004; Meyer and Schilling, 2017; Carlyle, Trombetta and Arnold, 2018). One of the limitations of current literature in the field is that it is mainly focused on proteomics of known neurodegenerative diagnosis, therefore fails to address pre-pathological states before neurodegenerative onset. As Psmc1$^{fl/fl}$;CaMKIIα-*cre* mice display the early and pathological stages of the lewy-body dementia disease process, from healthy to neurodegenerative pathology, proteomic analysis of this model allows the opportunity for protein expression profiling to be mapped across disease progression.

3.1.2 STRING analysis to highlight dysregulated pathways in neurodegenerative disease

STRING – (Search Tool for the Retrieval of Interacting Genes/Proteins) is a bioinformatic database that contains information on known and predicted protein-protein interactions (PPI). STRING analyses groups of user-selected proteins to display the physical, functional, spatial, and co-regulatory protein interactions, with the ability to co-select for physical subcomplexes (Szklarczyk et al., 2019).

Three distinct large categories of proteins have been defined, such as cellular components, molecular function, and biological processes. This, coupled with KEGG and Reactome pathways makes STRING a popular database for highlighting functional enrichments in proteome data. STRING represents data as a diagram, dictated by nodes and edges (table 3.1), helping to illustrate the functional connectivity of the proteome.

Table 3.1: STRING analyses user-entered protein-protein interactions which are represented as a protein interaction map, defined by tabled labels

Label	**Explanation**
Nodes	Number of proteins selected analysis
Edges	Number of proteins that have shown an interaction
Average node degree	The number of how many interactions (at the score threshold) that a protein has on the average in the network.
Expected number of edges:	how many edges are to be expected if the nodes were to be selected at random
Average local clustering coefficient	the measure of how connected the nodes in the network are
PPI enrichment value	Protein-Protein Interaction (PPI) enrichment value

3.1.3 Aims of this chapter

This chapter provides proteomic profiling of the ongoing disease process of 3,4- and 5-week-old Psmc1$^{fl/fl}$;CaMKIIα-*cre* mice to age-matched controls. Protein-fold change level was analysed via STRING cluster map analysis to identify both individual proteins and potential proteome interactions in key molecular pathways, which could be responsible for the initiation and progression of neurodegenerative diseases.

3.2 Materials and methods

A schematic diagram of the methods used for this chapter is displayed in figure 3.1. For full details on SWATH-MS sample preparation and subsequent analysis, please see section 2.2. Confidence, the assurance that peptides detected were related to the protein assigned, was used as a cut-off point for further STRING analysis.

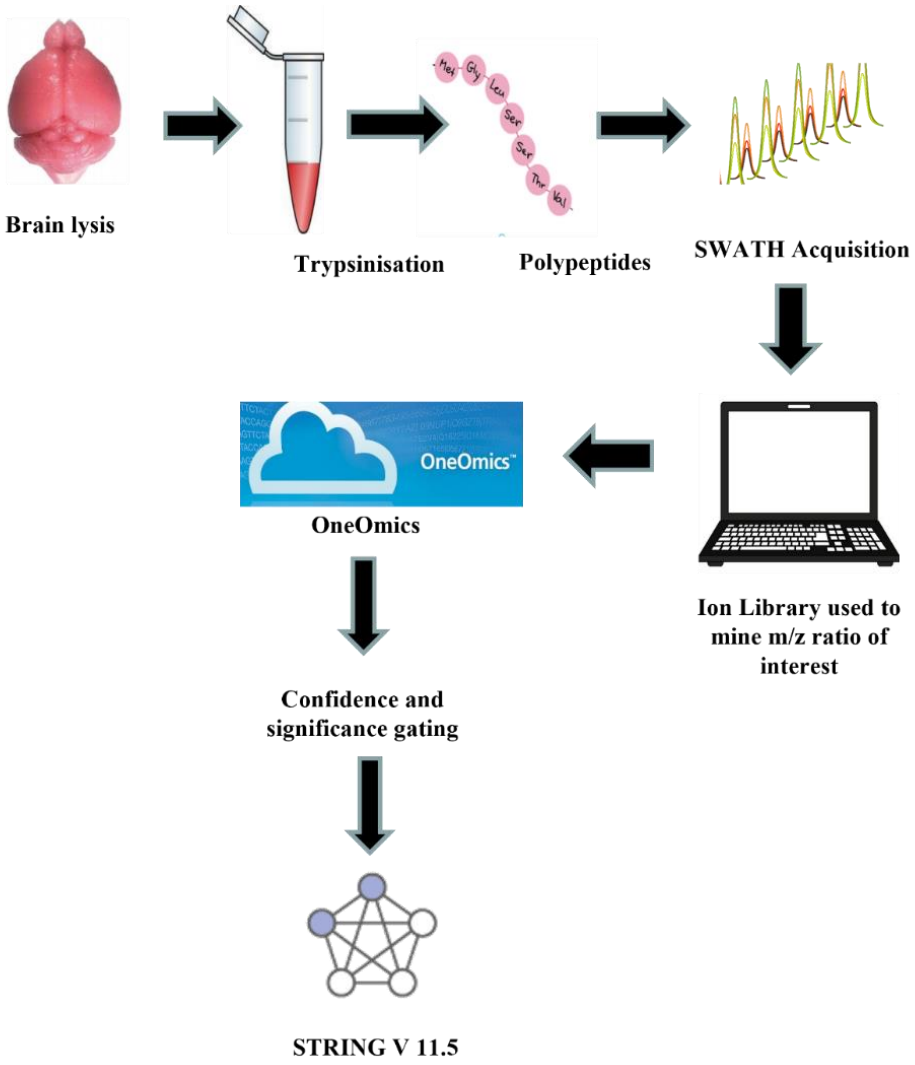

Figure 3.1:Overview of SWATH-MS method. In brief, six mice cortices from each condition (Control and Psmc1$^{fl/fl}$;CaMKIIα-*cre* of each age group (2 weeks, 3 weeks, 4 weeks, 5 weeks old)) were subjected to brain lysis and subsequent trypsinisation. Samples were subjected to SWATH acquisition, where a predefined ion library was used to mine the m/z ratio of interest. All data was uploaded and assessed using the AbSciex OneOmics package. After this, single polypeptides were removed, and proteins deemed significant via an in-programme performed t-test were put forward for STRING analysis.

3.3 Results

3.3.1 The confidence threshold for 3-,4- and 5-week samples were determined by the confidence value of 2-week-old samples

In the first instance, we analysed expression levels of proteins in control versus Psmc1 $^{fl/fl}$;CaMKIIα-*cre* mice for 2-week samples, before the activation of the transgene had occurred. This was used to identify a cut-off level for confidence value that would need to be exceeded for a meaningful change in expression pattern due to the onset of pathology to be accepted. Taking this into consideration, the uppermost confidence value detected in these samples was 54%, therefore samples with a confidence value of 54% and over were included in the following data analysis (figure 3.2).

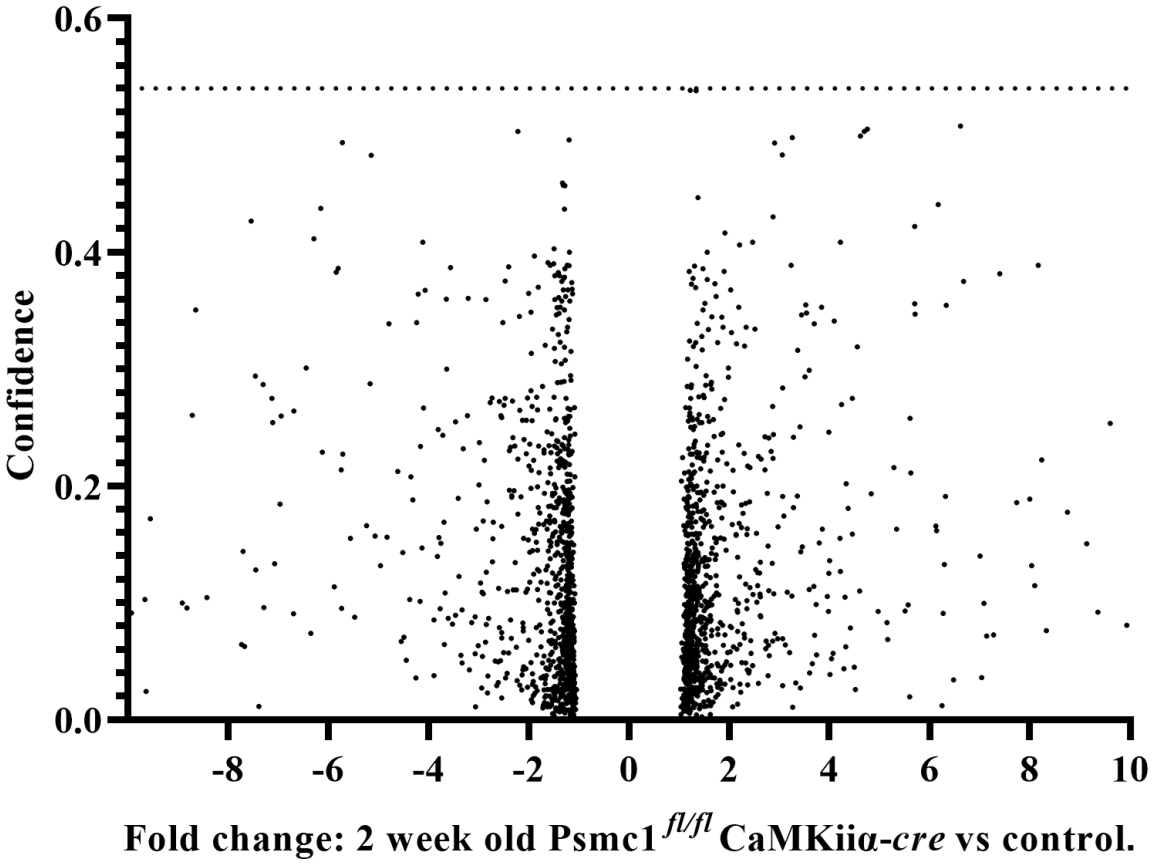

Figure 3.2:Confidence threshold was determined by analysing upper confidence value in both Psmc1$^{fl/fl}$;CaMKIIα-*cre* and aged matched control littermates at 2-weeks of age. Previous data indicates that there is no change between Psmc1 $^{fl/fl}$;CaMKIIα-*cre* mice and control littermates control at 2 weeks old. Proteins at 54% confidence and over were included for the following data analysis

3.3.2 Confidence gating 3-week-old mice

In a total of 2092 differentially expressed proteins, 1071 were upregulated and 1021 downregulated in 3-week-old Psmc1$^{fl/fl}$;CaMKIIα-*cre* mice cortices at 0 % confidence (figure 3.3A). Confidence gating at 54% reduced the number to 14 upregulated proteins and 9 downregulated proteins, whereby 8 and 7 reached statistical significance, respectively (figure 3.3B).

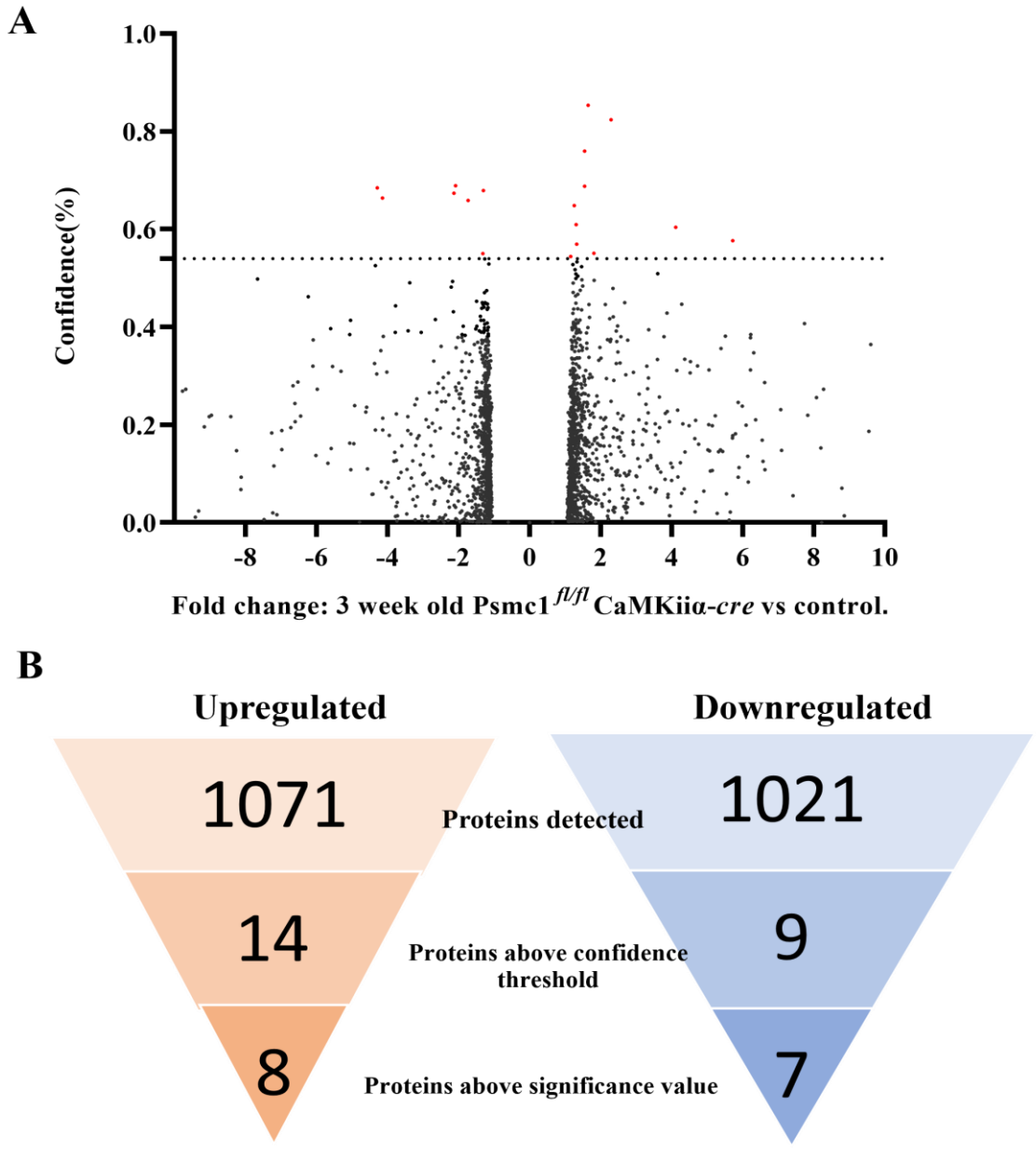

Figure 3.3:SWATH-MS proteins detected 2092 differently expressed proteins in 3-week old Psmc1 $^{fl/fl}$;CaMKIIα-*cre* mice versus age-matched controls. 3.3A) Total proteins detected in SWATH-MS data in 3-week old Psmc1$^{fl/fl}$;CaMKIIα-*cre* mice versus age-matched control, dotted line indicates confidence cut-off point. 3.3B) Schematic diagram displaying the number of final proteins from SWATH-MS data set submitted for STRING analysis.

3.3.2.1 Upregulated pathways

8 proteins which surpassed confidence and significance conditions from the SWATH-MS data were inputted to STRING for protein-protein interaction analysis (table 3.2). The protein interactome map was deemed significant, with a significant PPI value below p<0.05 (figure 3.4). STRING analysis reported enrichment of the ubiquitin-ligase protein binding process and the SCF-ubiquitin-protein complex. An upregulation in the ubiquitin-ligase pathway has previously been validated in this model at 3 weeks of age (figure 3.5).

Table 3.2: Upregulated proteins detected via mass spec in 3-week old Psmc1 $^{fl/fl}$;CaMKIIα-*cre* cortices versus age-matched control.

STRING	Protein	FC	SD	C	Sig	
RBX1	E3 ubiquitin-protein ligase RBX1	1.81	0.10	0.55	0.04	*
FBXO2	F-box only protein 2	1.55	0.02	0.69	0.05	*
PSMC4	26S proteasome regulatory subunit 6B	1.33	0.00	0.54	0.01	***
GFAP	Glial fibrillary acidic protein	2.30	0.00	0.82	0.00	***
UCHL1	Ubiquitin carboxyl-terminal hydrolase isozyme L1	1.26	0.00	0.65	0.00	***
GSTA4	Glutathione S-transferase A4	1.31	0.01	0.61	0.00	****
RPS27A	Ubiquitin-40S ribosomal protein S27a	1.65	0.01	0.85	0.00	***
CACYBP	Calcyclin-binding protein	1.55	0.01	0.76	0.00	****

Key: *STRING – String Label, FC = Fold change detected by SWATH-MS, SD – standard deviation, C – confidence, Sig = Significance value of FC, (* = P<0.05 , ** = P<0.01, *** = P<0.001, **** = P<0.0001).*

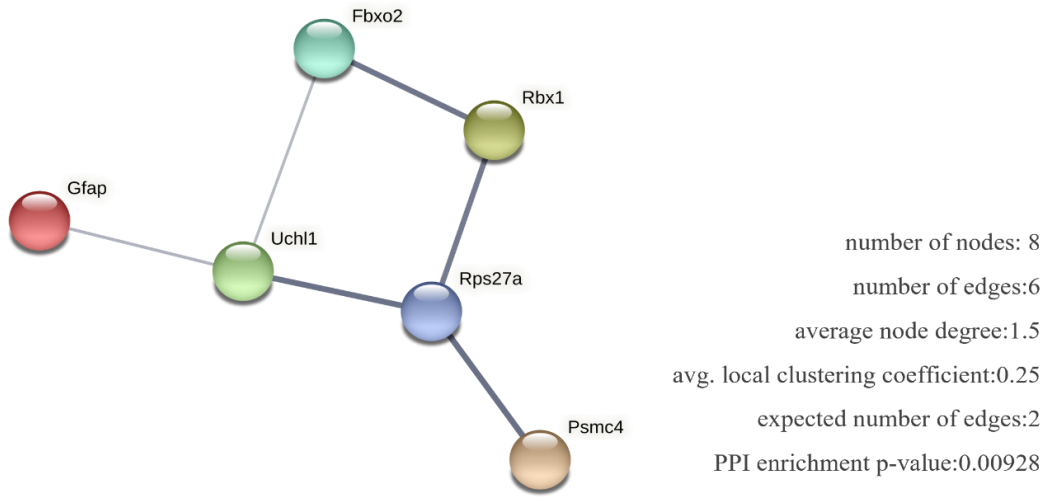

Figure 3.4:Upregulated proteins in 3-week-old Psmc1$^{fl/fl}$;CaMKIIα-*cre* mice show a significant protein-protein interaction value, indicating pathway enrichment. STRING diagram showing the interaction of proteins via 'strength' – thicker and darker lines indicate stronger interaction.

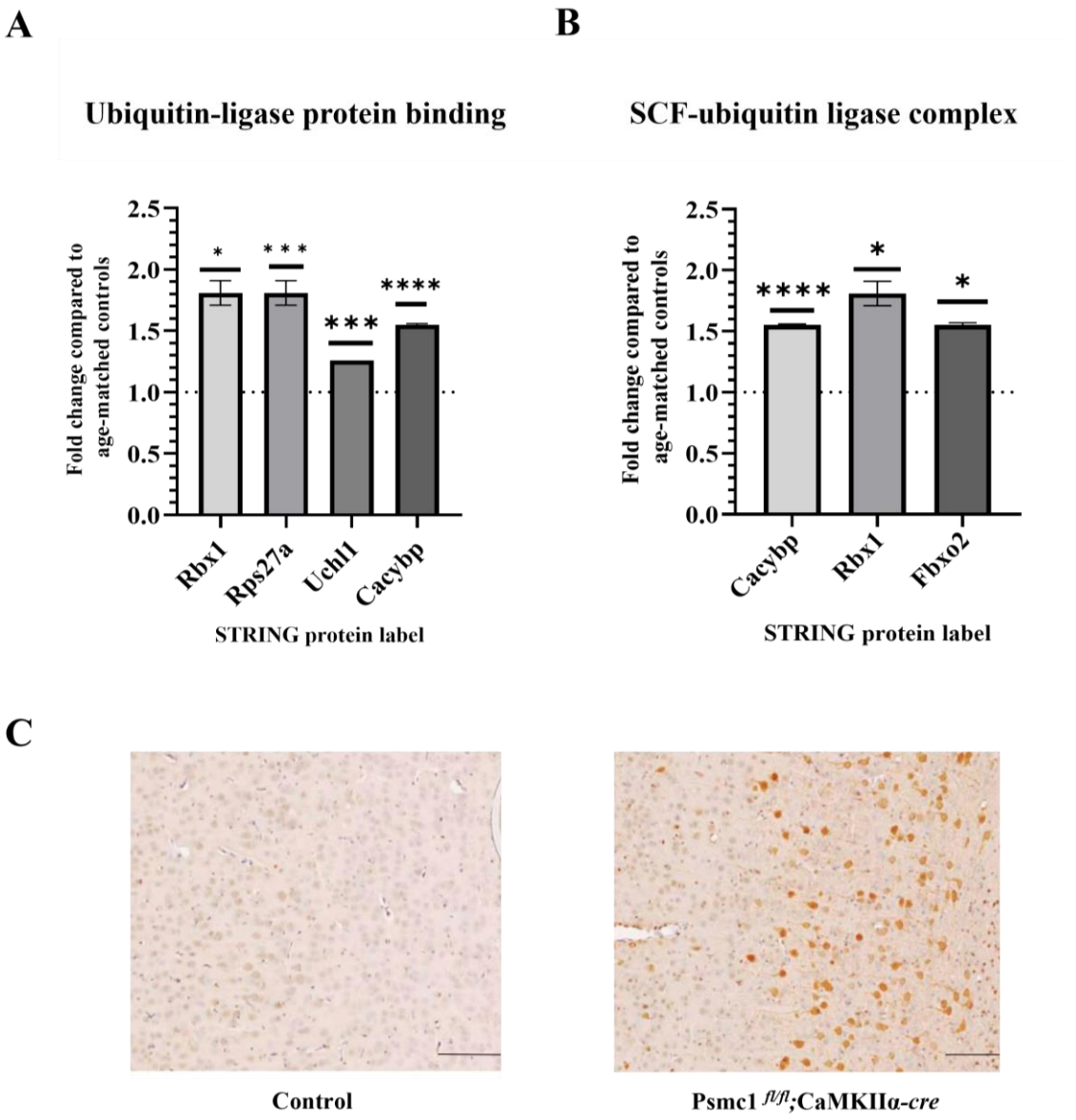

Figure 3.5:Ubiquitin-protein ligase binding proteins are upregulated in 3-week-old Psmc1 $^{fl/fl}$;CaMKIIα-*cre* mice. 3.5A) SWATH-MS quantitative mass spectrometry fold change values for 4 key proteins enriched in Ubiquitin ligase binding (1.56, FDR: 0.0080) and 3.5B) the SCF-Ubiquitin Ligase Complex (Strength, 2.14 FDR: 0.0045) as determined by STRING analysis. 3.5C) Ubiquitin-staining in the frontal cortex is visibly localised to neuronal cells in 3-week old Psmc1$^{fl/fl}$;CaMKIIα-*cre* mice (Geiszler et al., 2018) (Scale Bar = 100 µm).

3.3.2.2 Downregulated pathways

Despite these changes in expression level, STRING database analysis showed no significant protein-protein interactions amongst these candidates (table 3.3). Despite these changes in expression level, STRING database analysis showed no significant protein-protein interactions amongst these candidates.

Table 3.3: Downregulated proteins detected via SWATH-MS in 3-week old Psmc1 $^{fl/fl}$CaMKIIα-*cre* cortices versus age-matched control.

STRING	Protein	FC	SD	C	Sig	**
LYPLA1	Acyl-protein thioesterase 1	-1.30	0.01	0.68	0.00	***
STOML2	Stomatin-like protein 2, mitochondrial	-1.26	0.01	0.54	0.00	***
SRRT	Serrate RNA effector molecule homolog	-4.29	0.26	0.68	0.01	***
ADAP2	Arf-GAP with dual PH domain-containing protein 2	-1.32	0.00	0.55	0.01	*
KRT77	Keratin, type II cytoskeletal 1b	-1.73	0.00	0.66	0.02	*
SLC27A1	Long-chain fatty acid transport protein 1	-4.14	0.51	0.66	0.03	*
MRPL13	39S ribosomal protein L13, mitochondrial	-2.09	0.06	0.69	0.04	*

Key: *STRING – String Label, FC = Fold change detected by SWATH-MS, SD – standard deviation, C – confidence, Sig = Significance value of FC, (* = P<0.05 , ** = P<0.01, *** = P<0.001, **** = P<0.0001).*

3.3.3 Confidence gating in 4-week-old mice

In a total of 1919 differentially expressed proteins, 1098 were upregulated and 821 downregulated in 4-week-old Psmc1$^{fl/fl}$;CaMKIIα-*cre* mice cortices at 0 % confidence (figure 3.6A). Confidence gating reduced the number to 61 upregulated proteins and 13 downregulated proteins, from which 39 and 9 reached statistical significance ($p<0.05$) (figure 3.6B).

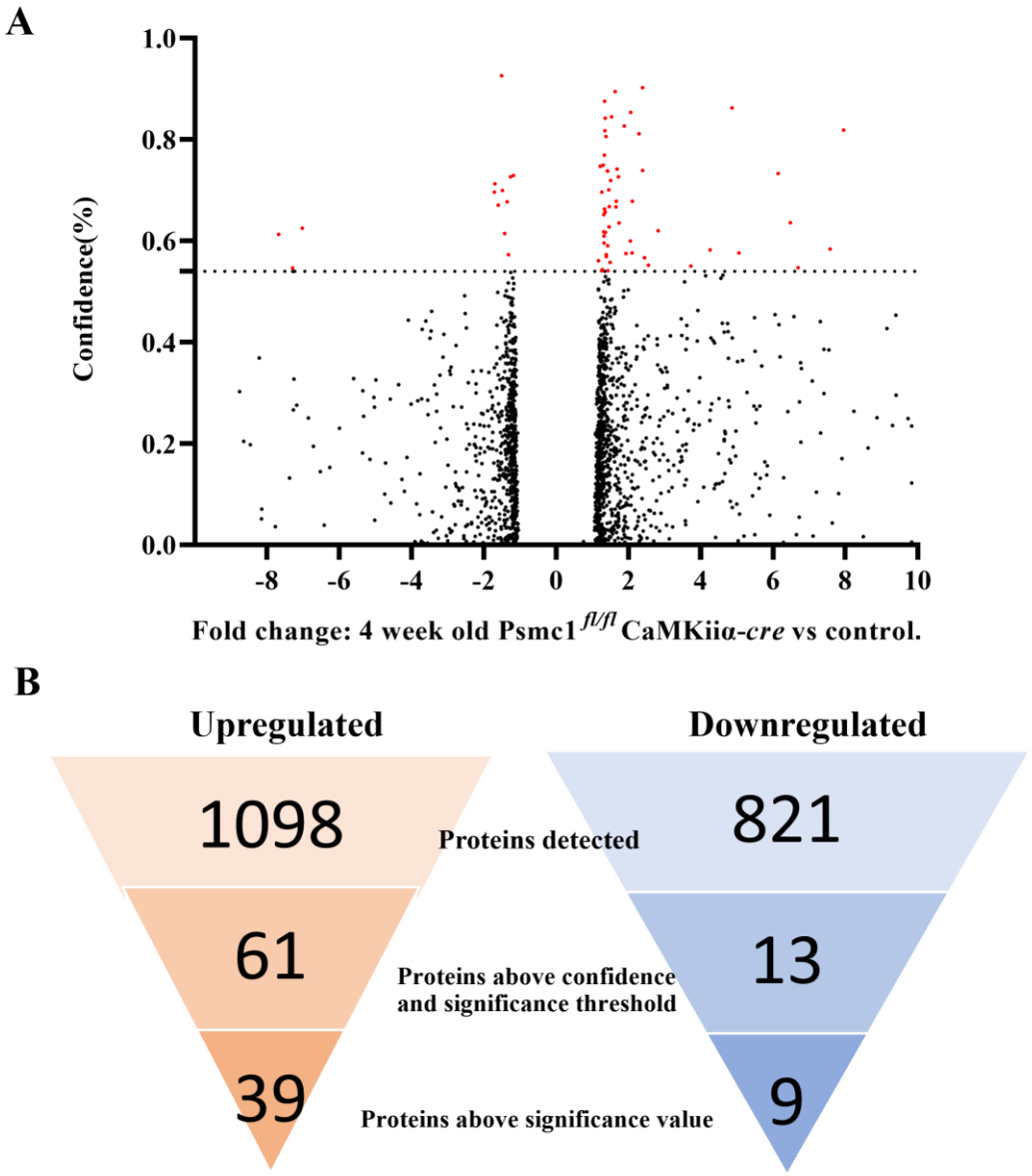

Figure 3.6:SWATH-MS proteins detected 1919 differently expressed proteins in 4-week old Psmc1 $^{fl/fl}$;CaMKIIα-*cre* mice versus age-matched control. 3.6A) Total proteins detected in SWATH-MS data in 4-week old Psmc1$^{fl/fl}$;CaMKIIα-*cre* mice versus age-matched control, dotted line indicates confidence cut-off points. 3.6B) Schematic diagram displaying the number of final proteins from SWATH-MS data set submitted for STRING analysis.

3.3.3.1 Upregulated proteins

39 proteins which surpassed confidence and significance conditions were inputted to STRING for protein-protein interaction analysis. 35 proteins were detected to be upregulated that were not present in 3-week analysis, highlighted in table 3.4. The protein interactome map was deemed significant, with a significant PPI value below $p<0.05$ (figure 3.7).

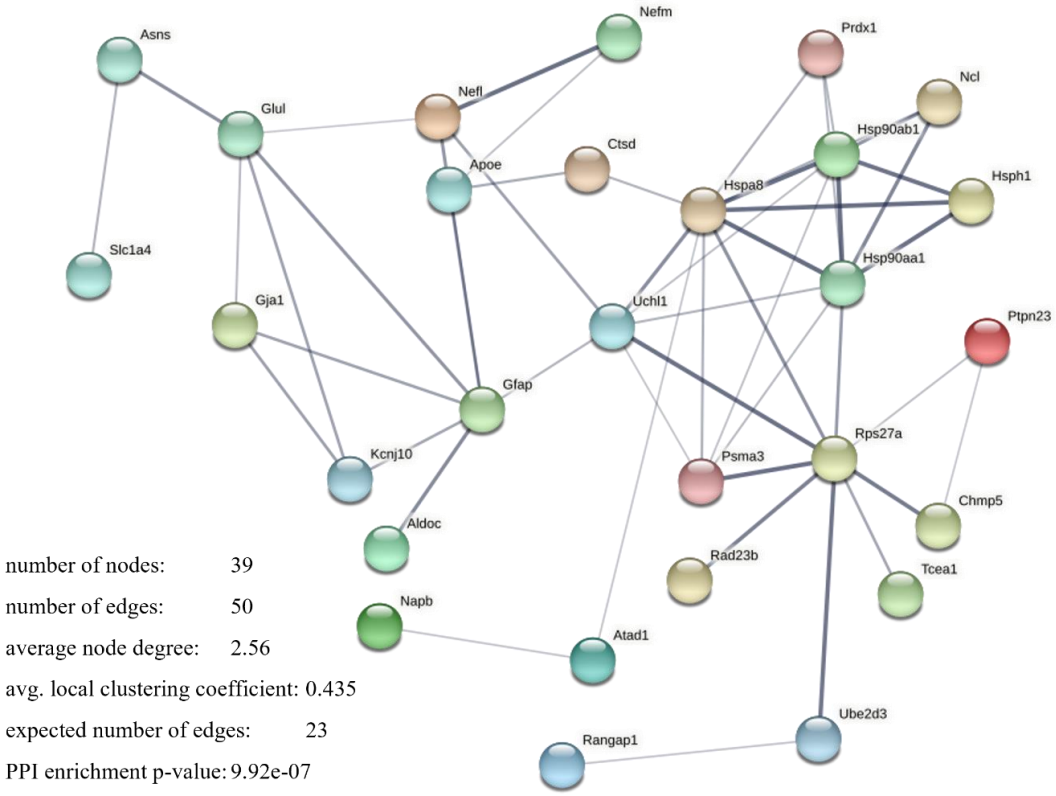

Figure 3.7:Upregulated proteins in 4-week-old Psmc1$^{fl/fl}$;CaMKIIα-*cre* mice show a significant protein-protein interaction value, indicating pathway enrichment. STRING diagram showing interaction via 'strength' – thicker and darker lines indicate stronger association.

Table 3.4: Upregulated proteins detected via mass spec in 4-week old Psmc1$^{fl/fl}$;CaMKIIα-*cre* cortices versus age-matched control littermates (1/2)

STRING label	Protein	FC	SD	C	Sig	**
FBXO2	F-box 2	2.06	0.07	0.85	0.00	****
RPS27A	Ubiquitin-40S ribosomal protein S27a	2.39	0.01	0.90	0.00	****
UCHL1	Ubiquitin carboxyl-terminal hydrolase isozyme L1	1.35	0.00	0.82	0.00	****
GFAP	Glial Fibrillary Acidic Protein	4.86	0.12	0.86	0.00	***
CHP1	Calcineurin B homologous protein 1	1.74	0.03	0.63	0.00	****
PCLO	Protein piccolo	2.29	0.02	0.81	0.00	****
CPNE5	Copine-5	1.48	0.00	0.70	0.00	****
PRDX1	Peroxiredoxin-1	1.43	0.01	0.74	0.00	****
HSP90AA1	Heat shock protein HSP 90-alpha	1.63	0.00	0.89	0.00	****
ALDOC	Fructose-bisphosphate aldolase C	1.36	0.00	0.84	0.00	****
TCEA1	Transcription elongation factor A protein 1	1.72	0.00	0.73	0.00	****
RANGAP1	Ran GTPase-activating protein 1	2.82	0.22	0.62	0.00	****
PTPN23	Tyrosine-protein phosphatase non-receptor type 23	1.33	0.00	0.77	0.00	****
HSP90AB1	Heat shock protein HSP 90-beta	1.53	0.00	0.84	0.00	****
HSPH1	Heat shock protein 105 kDa	1.42	0.00	0.74	0.00	****
ATAD1	ATPase family AAA domain-containing protein 1	1.39	0.00	0.57	0.00	****
ASNS	Asparagine synthetase [glutamine-hydrolyzing]	1.68	0.03	0.74	0.00	****
PSMA3	Proteasome subunit alpha type-3	1.32	0.00	0.61	0.00	****
ARCN1	Coatomer subunit delta	1.31	0.04	0.65	0.00	****

Key: *STRING – String Label, FC = Fold change detected by SWATH-MS, SD – standard deviation, C – confidence, Sig = Significance value of FC, (* = P<0.05 , ** = P<0.01, *** = P<0.001, **** = P<0.0001*

Table 3.4: Upregulated proteins detected via mass spec in 4-week old Psmc1$^{fl/fl}$;CaMKIIα-*cre* cortices versus age-matched control littermates continued(2/2)

STRING	Protein	FC	SD	C	Sig	**
GJA1	Gap junction alpha-1 protein	2.39	0.02	0.74	0.00	****
UBE2D3	Ubiquitin-conjugating enzyme E2 D3	1.22	0.00	0.75	0.00	****
HSPA8	Heat shock cognate 71 kDa protein	1.34	0.00	0.88	0.00	****
NDRG2	Protein NDRG2	1.38	0.01	0.81	0.00	***
PREPL	Prolyl endopeptidase-like	1.93	0.13	0.57	0.00	***
NUDCD3	NudC domain-containing protein 3	1.49	0.02	0.56	0.00	***
GLUL	Glutamine synthetase	1.26	0.00	0.70	0.00	***
CHMP5	Charged multivesicular body protein 5	6.14	2.09	0.73	0.00	***
TAGLN2	Transgelin-2	3.73	0.11	0.55	0.00	***
CTSD	Cathepsin D	1.89	0.07	0.83	0.00	***
RAD23B	UV excision repair protein RAD23 homolog B	1.42	0.01	0.59	0.01	***
SLC1A4	Neutral amino acid transporter A	1.45	0.03	0.70	0.01	***
APOE	Apolipoprotein E	2.11	0.04	0.68	0.01	***
NAPB	Beta-soluble NSF attachment protein	1.31	0.02	0.62	0.01	**
SUB1	Activated RNA polymerase II transcriptional coactivator p15	1.66	0.02	0.67	0.01	**
KCNJ10	ATP-sensitive inward rectifier potassium channel 10	6.48	1.18	0.64	0.01	**
NEFM	Neurofilament medium polypeptide	1.47	0.01	0.63	0.02	**
NEFL	Neurofilament light polypeptide	1.34	0.00	0.66	0.02	**
NCL	Nucleolin	1.47	0.02	0.67	0.05	*
COX7C	Cytochrome c oxidase subunit 7C, mitochondrial	7.96	2.79	0.82	0.00	****

Key: *STRING – String Label, FC = Fold change detected by SWATH-MS, SD – standard deviation, C – confidence, Sig = Significance value of FC, (* = P<0.05 , ** = P<0.01, *** = P<0.001, **** = P<0.0001*

3.3.3.1 Upregulated pathways

STRING analysis reported an additional set of upregulated pathways linked to defined cellular processes, with four of interest that were specific to 4-week Psmc1$^{fl/fl}$;CaMKIIα-*cre* mice: unfolded protein binding (Strength: 1.44, FDR 0.0086 (figure 3.8A), microtubule based transport (Strength: 1.19, FDR: 0.0081) (figure 3.8B), negative regulation of MAPK pathway (Strength: 1.12, FDR = 0.0346) (figure 3.8C), and negative regulation of apoptotic pathways (Strength:1.09,FDR = 0.038) (figure 3.8D).

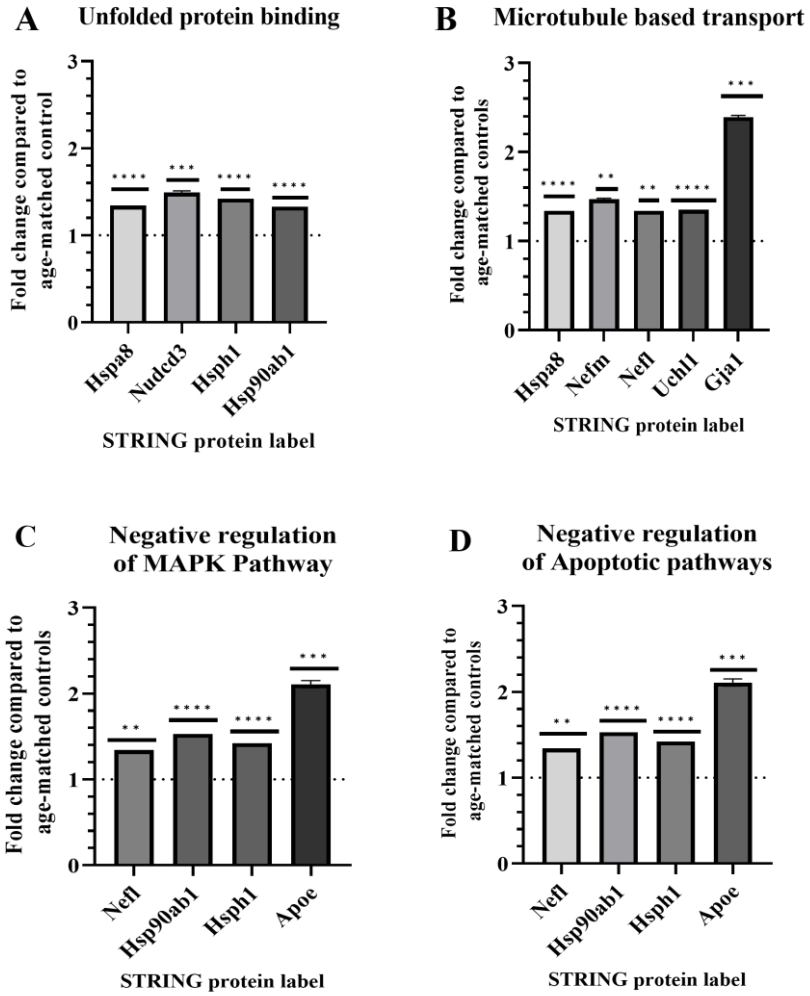

Figure 3.8:Unfolded protein binding, negative regulation of the MAPK cascade, microtubule-based transport, and negative regulation of apoptotic pathways are enriched processes in 4-week old Psmc1$^{fl/fl}$;CaMKIIα-*cre* mice. 3.8A) Unfolded protein binding (Strength: 1.44, FDR 0.0086), 3.8B)Microtubule based transport (Strength: 1.19, FDR: 0.0081), 3.8C) Negative regulation of MAPK pathway (Strength: 1.12, FDR = 0.0346), 3.8D)Negative regulation of Apoptotic pathways (Strength:1.09, FDR = 0.038) are enriched pathways from SWATH-MS data as determined by the STRING analysis. *Fold change expressed compared to age-matched controls. Dotted line indicates baseline, in programme t-test was conducted (* = P<0.05, ** = P<0.01, *** = P<0.001, **** = P<0.0001).*

3.3.3.2 Post-translational modification is a shared process in 3 and 4-week-old Psmc1$^{fl/fl}$;CaMKIIα-*cre* mice

To further examine the meaning of functional clustering of upregulated proteins, we tested for process-level associations in the results from 3- and 4-week samples. Post-translational modification, a process which involves the covalent modification of a protein, was shown to be a highly enriched process in both 3 weeks (Strength 1.04, FDR: 0.018) and 4 weeks (strength 0.65, FDR: 0.016) Psmc1$^{fl/fl}$;CaMKIIα-*cre* mice (figure 3.9). The SWATH-MS fold change values of proteins enriched in this pathway is displayed in figure 3.10.

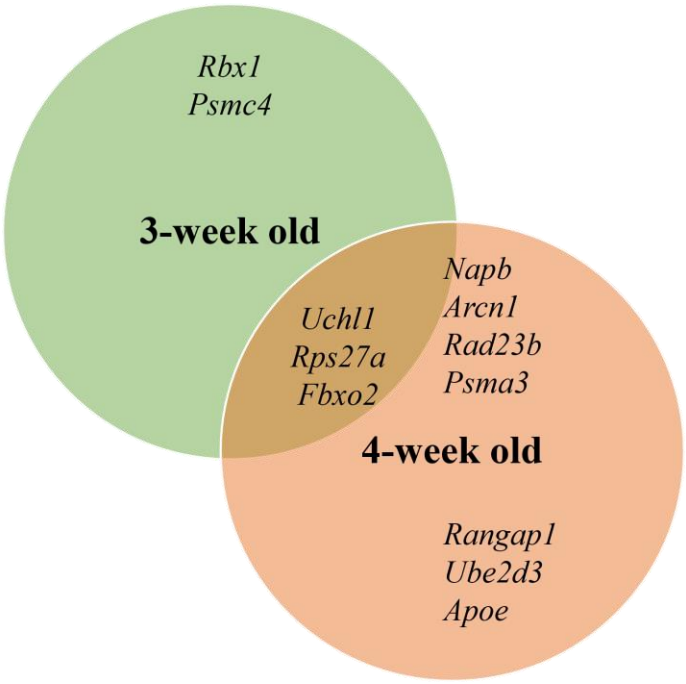

Figure 3.9:Upregulated proteins in 3 and 4-week-old Psmc1$^{fl/fl}$;CaMKIIα-*cre* mice show a significant pathway enrichment in post-translational modification proteins. Venn Diagram shows unique proteins as derived from SWATH-MS data that are present in the STRING enrichment that are present in 3 weeks, 4 weeks, and their shared proteins

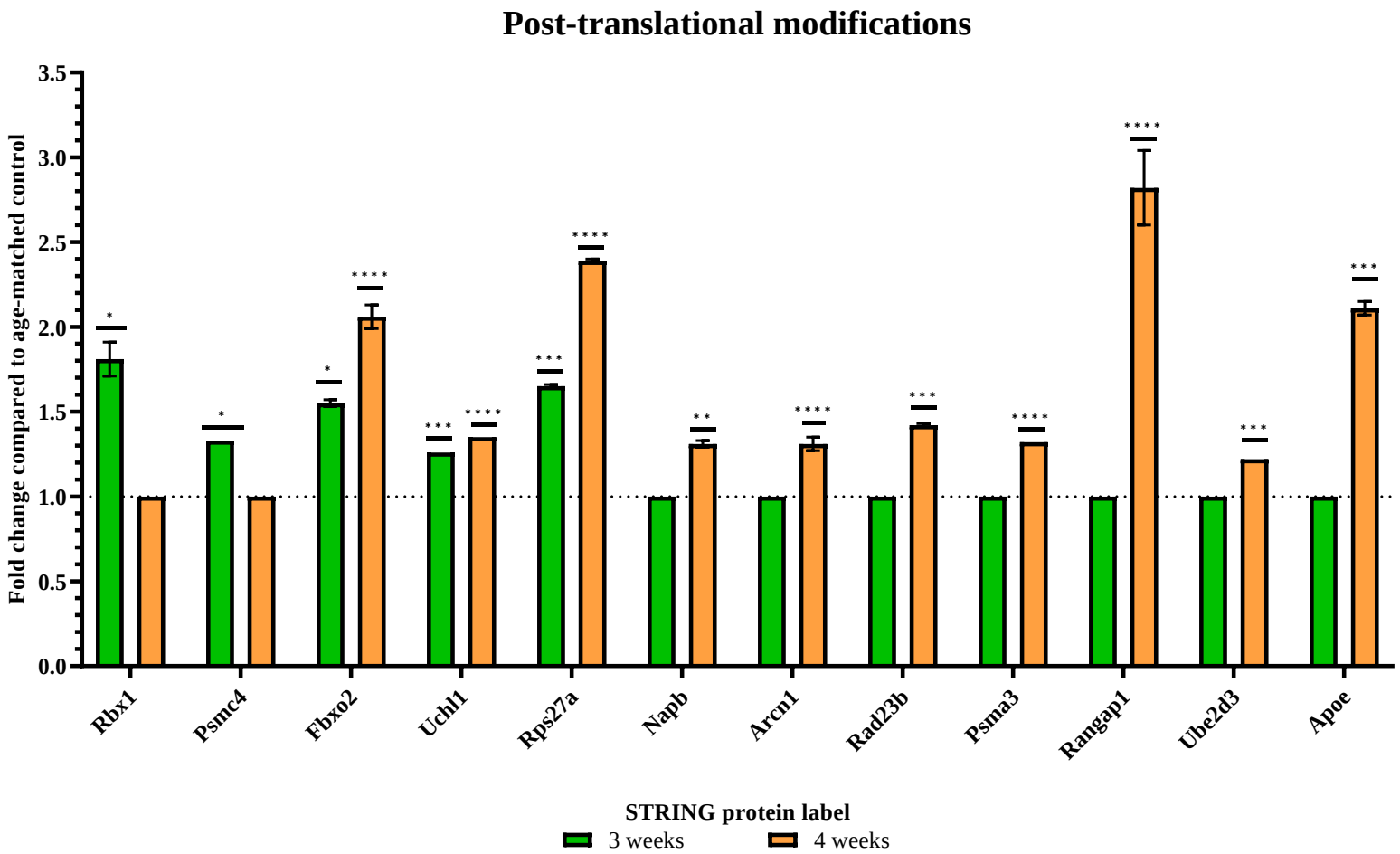

Figure 3.10:3 and 4-week-old Psmc1$^{fl/fl}$;CaMKII*α-cre* mice show a significant upregulation in proteins related to the post-translational modification pathway. Graph displays alterations in fold change of enriched proteins compared to age-matched controls. Dotted line indicates baseline, t-test was conducted (* = P<0.05 , ** = P<0.01, *** = P<0.001, **** = P<0.0001).

3.3.3.3 Downregulated pathways

9 proteins which surpassed confidence and significance conditions were inputted to STRING for protein-protein interaction analysis (table 3.5). There was no overlap between 3 and 4-week downregulated proteins, therefore all proteins detected were unique to each age. The protein interactome map was deemed insignificant, with a PPI value of 0.477 ($p>0.05$) (figure 3.8).

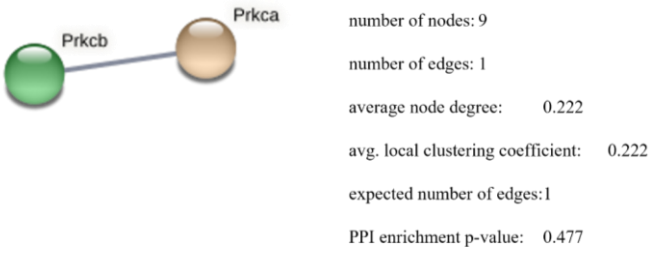

Figure 3.11:Downregulated proteins in 4-week-old Psmc1$^{fl/fl}$;CaMKIIα-*cre* mice show an insignificant protein-protein interaction value. STRING diagram showing interaction via 'strength' – thicker and darker lines indicate stronger interaction

Table 3.5: Downregulated proteins detected via SWATH-MS in 4-week old Psmc1$^{fl/fl}$;CaMKIIα-*cre* cortices versus age-matched control

STRING	Protein	FC	SD	C	Sig	**
CACNA1B	N-type calcium channel subunit alpha-1B	-7.68	0.59	0.61	0.00	****
PRKCA	Protein kinase C alpha type	-1.51	0.01	0.93	0.00	****
FGF12	Fibroblast growth factor 12	-1.25	0.01	0.54	0.00	****
NPTXR	Neuronal pentraxin receptor	-1.69	0.02	0.71	0.00	****
NECAB2	N-terminal EF-hand calcium-binding protein 2	-1.60	0.02	0.67	0.00	***
SYT5	Synaptotagmin-5	-1.18	0.01	0.73	0.00	**
PRKCB	Protein kinase C beta type	-1.36	0.01	0.68	0.02	*
SLC2A3	Solute carrier family 2, facilitated glucose transporter member 3	-1.31	0.01	0.57	0.02	*
TRFC	Transferrin receptor protein 1	-1.71	0.02	0.70	0.00	****

***Key**: STRING – String Label, FC = Fold change detected by SWATH-MS, SD – standard deviation, C – confidence, Sig = Significance value of FC (* = P<0.05 , ** = P<0.01, *** = P<0.001, **** = P<0.0001*

Protein kinase C alpha (Prkca) and Protein Kinase C Beta (Prkcb) are key calcium-dependent enzymes responsible for a range of cellular pathways. Upon further analysis through KEGG pathways, Cacna1b, N-type calcium channel subunit alpha-1B, is strongly associated with Prkca and Prkcb interaction in the MAPK/ERK neuroinflammatory pathways. This is of

particular interest, seeing as proteins associated with negative regulation of MAPK/ERK signaling are upregulated at 4 weeks old.

3.3.4 Confidence gating in 5-week-old mice

In a total of 1614 differentially expressed proteins, 851 were upregulated and 763 downregulated in 5-week-old Psmc1 $^{fl/fl}$;CaMKIIα-*cre* mice cortices at 0 % confidence (Figure 3.12A). Confidence gating reduced the number to 67 upregulated proteins and 40 downregulated proteins, whereby 44 and 23 were featured in STRING diagrams, respectively. (Figure 3.12B).

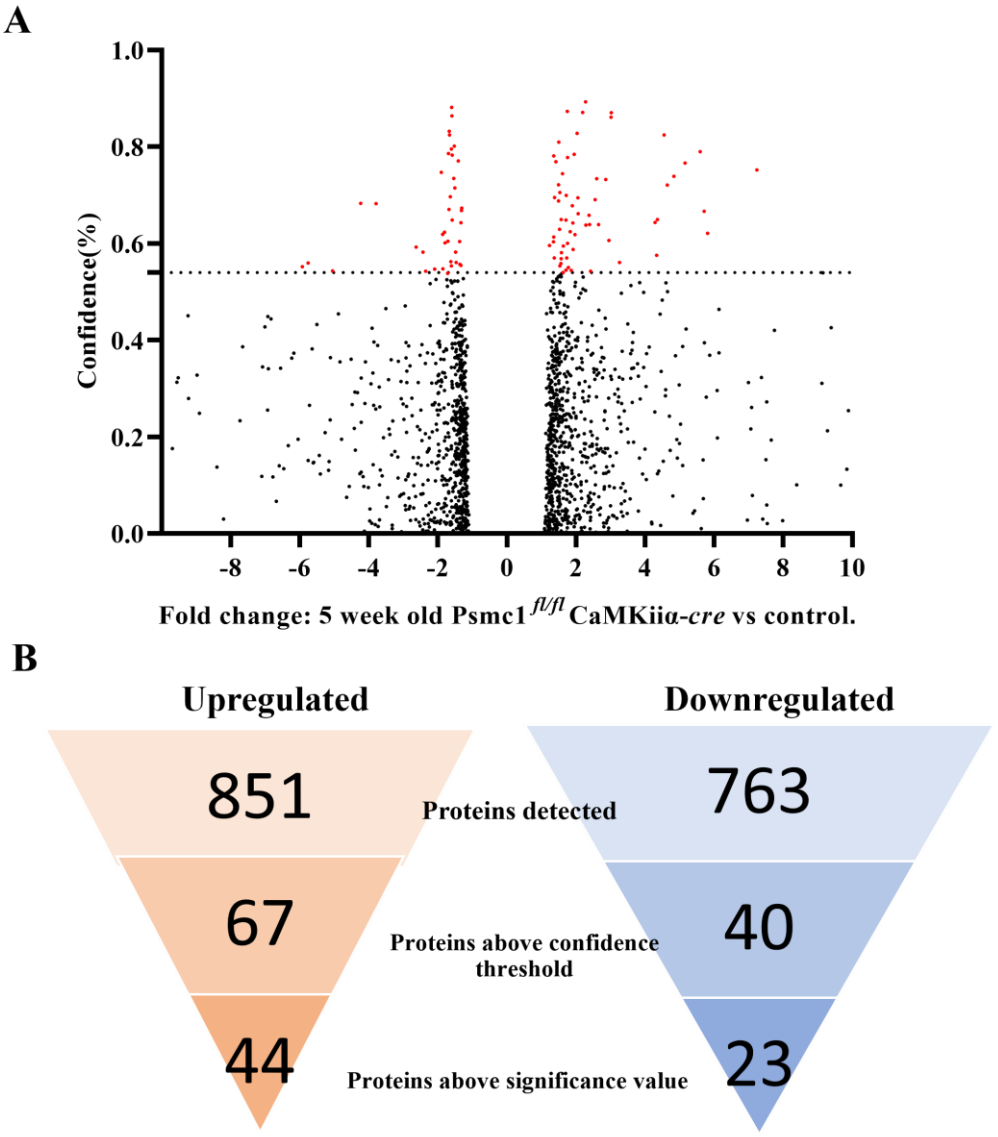

Figure 3.12:SWATH-MS proteins detected 1614 differently expressed proteins in 5-week-old Psmc1 $^{fl/fl}$;CaMKIIα-*cre* mice versus age-matched control. 3.12A) Total proteins detected in SWATH-MS data in 5-week old Psmc1$^{fl/fl}$;CaMKIIα-*cre* mice versus age-matched control, dotted line indicates confidence cut-off points 3.12B) Schematic diagram displaying the number of final proteins from SWATH-MS data set submitted for STRING analysis

3.3.4.1 Upregulated proteins

Forty-three proteins were submitted for STRING for analysis, which reported a significant protein-protein interaction value ($p<0.001$) (figure 3.13). 30 proteins were detected that were not present in 4-week upregulated data, highlighted in table 3.6.

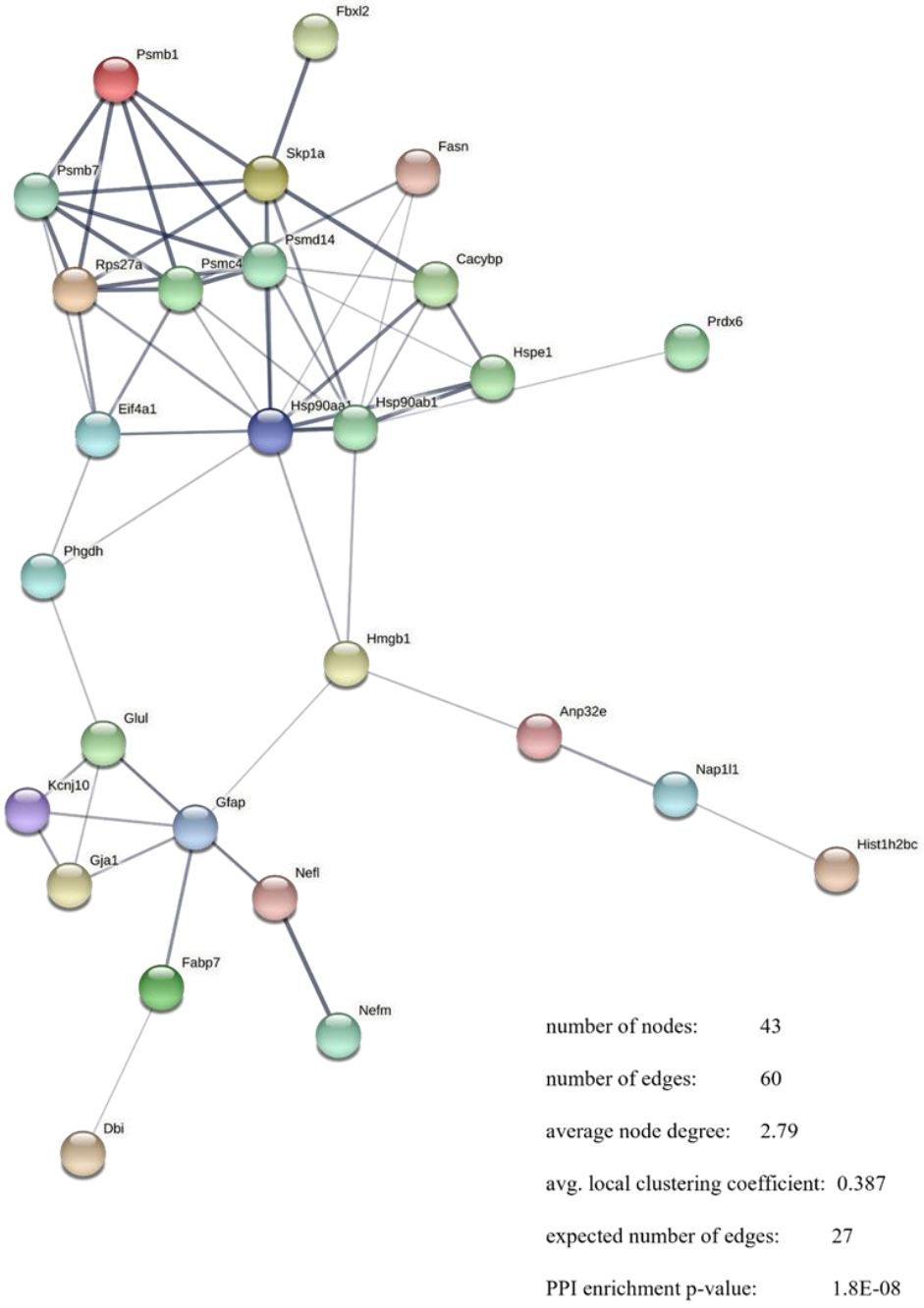

Figure 3.13:Upregulated proteins in 5-week-old Psmc1$^{fl/fl}$;CaMKII*α-cre* mice show a significant protein-protein interaction value, indicating pathway enrichment. STRING diagram showing interaction via 'strength' – thicker and darker lines indicate stronger reaction.

Table 3.6: Upregulated proteins detected via SWATH-MS detection in 5-week-old Psmc1$^{fl/fl}$;CaMKII*α-cre* cortices versus age-matched control (1/2)

STRING	Protein	FC	SD	C	Sig	
RPS27A	Ubiquitin-40S ribosomal protein S27a	2.28	0.11	0.89	0.00	**
HSD17B4	Peroxisomal multifunctional enzyme type 2	1.75	0.09	0.87	0.00	****
HSP90AA1	Heat shock protein HSP 90-alpha	2.19	0.01	0.87	0.00	****
FBXO2	F box only protein 2	3.02	0.14	0.87	0.00	**
GFAP	Glial Fibrillary Acidic Protein	12.78	0.20	0.87	0.02	*
CTSD	Cathepsin D	3.01	0.08	0.86	0.00	**
HSP90AB1	Heat shock protein HSP 90-beta	2.03	0.05	0.83	0.00	****
GLUL	Glutamine synthetase Gf	1.50	0.00	0.81	0.01	*
PSMC4	26S proteasome regulatory subunit 6B	1.36	0.01	0.78	0.00	****
SOD1	Superoxide Dismutase	1.42	0.04	0.77	0.00	****
KCNJ10	ATP-sensitive inward rectifier potassium channel 10	5.16	1.40	0.77	0.00	**
C1QB1	Complement C1q subcomponent subunit B	7.24	1.60	0.75	0.00	****
NEFL	Neurofilament Light Polypeptide	1.61	0.08	0.74	0.05	*
GJA1	Gap junction alpha-1 protein	4.83	0.94	0.74	0.02	*
CST3	Cystatin-C	2.86	0.36	0.73	0.01	**
PSMD14	26S proteasome non-ATPase regulatory subunit 14	1.50	0.00	0.72	0.00	****
RTN3	Reticulon-3	1.72	0.03	0.70	0.02	*
AHCYL1	S-adenosylhomocysteine hydrolase-like protein 1	1.38	0.01	0.69	0.01	**
CYB5R3	NADH-cytochrome b5 reductase 3	2.55	0.20	0.69	0.00	****
HMGB1	High mobility group protein B1	1.50	0.00	0.69	0.00	**
FABP7	Fatty acid-binding protein, brain	1.89	0.02	0.68	0.00	****
SUB1	Activated RNA polymerase II transcriptional coactivator p15	2.06	0.03	0.66	0.03	*
CACYBP	Calcyclin-binding protein	2.38	0.09	0.66	0.00	****

Table 3.6: Upregulated proteins detected via SWATH-MS detection in 5-week-old Psmc1$^{fl/fl}$;CaMKIIα-*cre* cortices versus age-matched control continued. (2/2)

STRING	Protein	FC	SD	C	Sig	
PRDX6	Peroxiredoxin-6	1.57	0.05	0.65	0.05	*
NT5C3B	7-methylguanosine phosphate-specific 5'-nucleotidase	1.71	0.05	0.65	0.01	*
ANP32E	Acidic leucine-rich nuclear phosphoprotein 32 family member E	4.29	0.73	0.64	0.00	**
DBI	Acyl-CoA-binding protein	1.90	0.06	0.64	0.02	*
HEXB	Beta-hexosaminidase subunit beta	2.39	0.05	0.64	0.00	****
ASAH1	Acid ceramidase	2.65	0.17	0.64	0.02	*
EIF4A1	Eukaryotic initiation factor 4A-I	2.29	0.70	0.64	0.00	**
NEFM	Neurofilament Medium Polypeptide	1.83	0.16	0.62	0.01	**
DHRS1	Dehydrogenase/reductase SDR family member 1	5.81	1.90	0.62	0.00	**
PREPL	Prolyl endopeptidase-like	2.95	0.07	0.61	0.03	*
HIST2H2BB	Histone H2B	1.35	0.01	0.60	0.02	*
HSPE1	10 kDa heat shock protein, mitochondrial	1.24	0.01	0.60	0.00	****
PHGDH	D-3-phosphoglycerate dehydrogenase	1.63	0.02	0.59	0.00	****
PSMB1	Proteasome subunit beta type-1	1.58	0.01	0.58	0.02	*
NAP1L1	Nucleosome assembly protein 1-like 1	4.34	0.26	0.58	0.03	*
PSMB7	Proteasome subunit beta type-7	1.73	0.06	0.57	0.00	**
ARF2	ADP-ribosylation factor 2	3.26	0.22	0.56	0.00	**
SKP1A	S-phase kinase-associated protein 1	1.56	0.01	0.56	0.00	****
FASN	Fatty acid synthase	1.54	0.03	0.55	0.00	**
TSR2	Pre-rRNA-processing protein TSR2 homolog	1.78	0.20	0.55	0.00	****

***Key**: STRING – String Label, FC = Fold change detected by SWATH-MS, SD = standard deviation, C = confidence, Sig = Significance value of FC, (* = P<0.05 , ** = P<0.01, *** = P<0.001, **** = P<0.0001)*

3.3.4.1 The proteome of cortices of 4- and 5-week old Psmc1$^{fl/fl;}$CaMKIIα-*cre* share upregulated processes

STRING analysis of 4 and 5-week old Psmc1$^{fl/fl}$;CaMKIIα-*cre* mice interactomes share cellular pathways related to necroptosis, innate immunity and cellular stress response (figure 3.14 – 3.18). Table 3.7 illustrates the commons processes, the number of proteins in each interactome and its corresponding false discovery rate (FDR).

Table 3.7: Shared enriched processes between 4- and 5-week-old interactomes show the number of proteins and corresponding false discovery

	4-weeks old			5-weeks old		
Process	**# nb**	**PPI**	**FDR**	**# nb**	**PPI**	**FDR**
Cellular response to stress	8	1.06	<0.001	9	1.07	<0.0001
Innate immunity	8	0.68	<0.05	15	0.91	<0.0001
Necroptosis	4	1.17	<0.05	4	1.13	<0.05

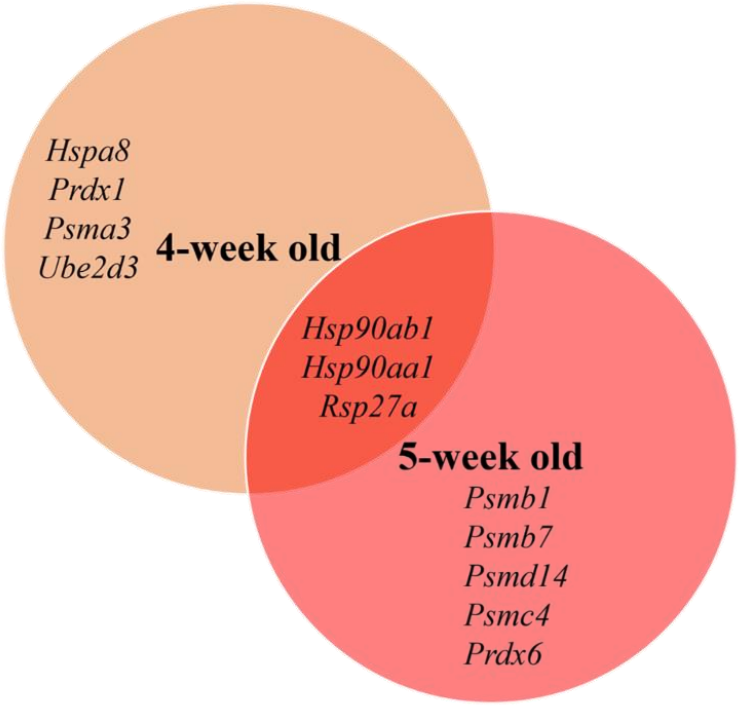

Figure 3.14:Upregulated proteins in 4 and 5-week-old Psmc1$^{fl/fl}$;CaMKIIα-*cre* mice show a significant pathway enrichment in the cellular response to stress. Venn Diagram shows unique proteins present in 4 weeks, and 5 weeks and their shared proteins.

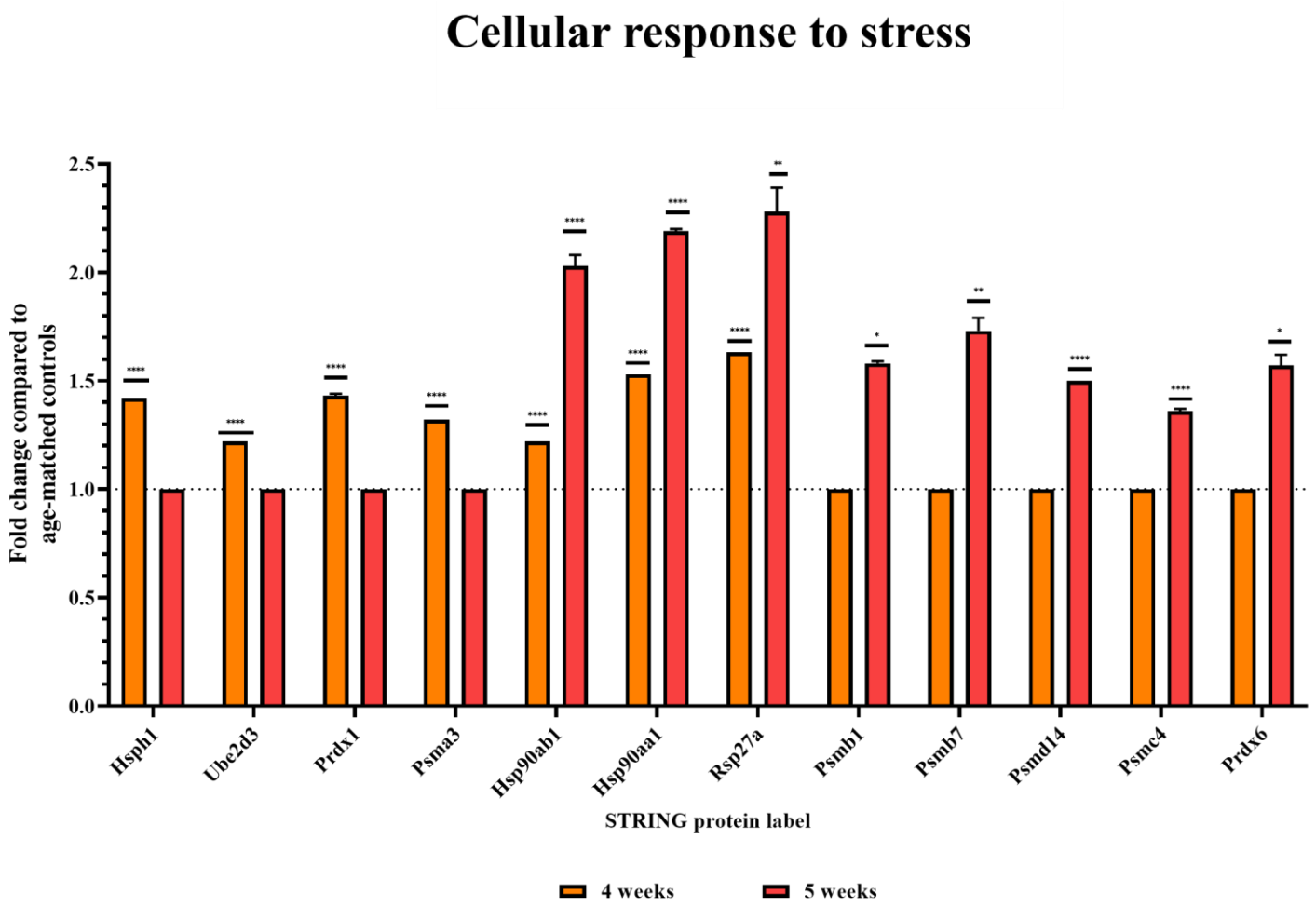

Figure 3.15:4 and 5-week-old Psmc1$^{fl/fl}$;CaMKII*α-cre* mice show a significant upregulation in proteins related to cellular response to stress. Graph displays alterations in fold change of enriched proteins compared to age-matched controls**.** Dotted line indicates baseline, a t-test was conducted (* = P<0.05 , ** = P<0.01, *** = P<0.001, **** = P<0.0001)

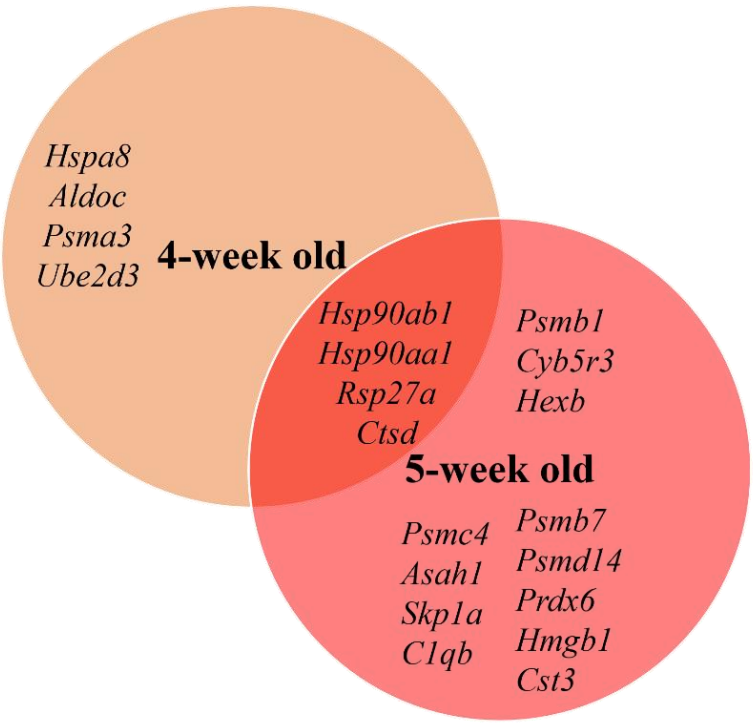

Figure 3. 16:Upregulated proteins in 4 and 5-week-old Psmc1$^{fl/fl}$;CaMKIIα-*cre* mice show a significant pathway enrichment in innate immunity. Venn Diagram shows unique proteins present in 4 weeks, and 5 weeks and their shared proteins.

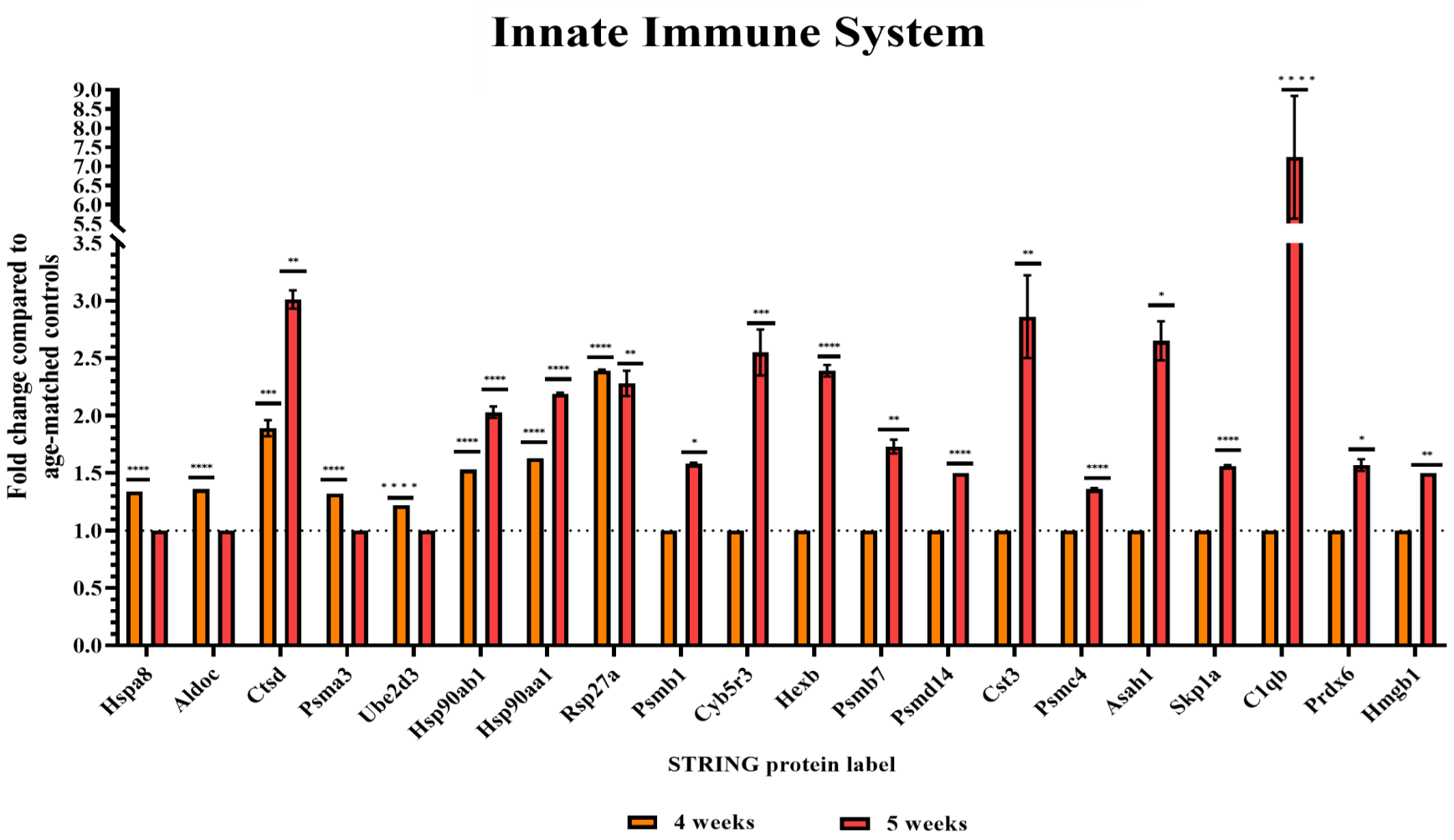

Figure 3. 17:4 and 5-week-old Psmc1$^{fl/fl}$;CaMKII*α-cre* mice show a significant upregulation in proteins related to Innate immune system. Graph displays alterations in fold change of enriched proteins compared to age-matched controls. Dotted line indicates baseline, a t-test was conducted (* = P<0.05 , ** = P<0.01, *** = P<0.001, **** = P<0.0001)

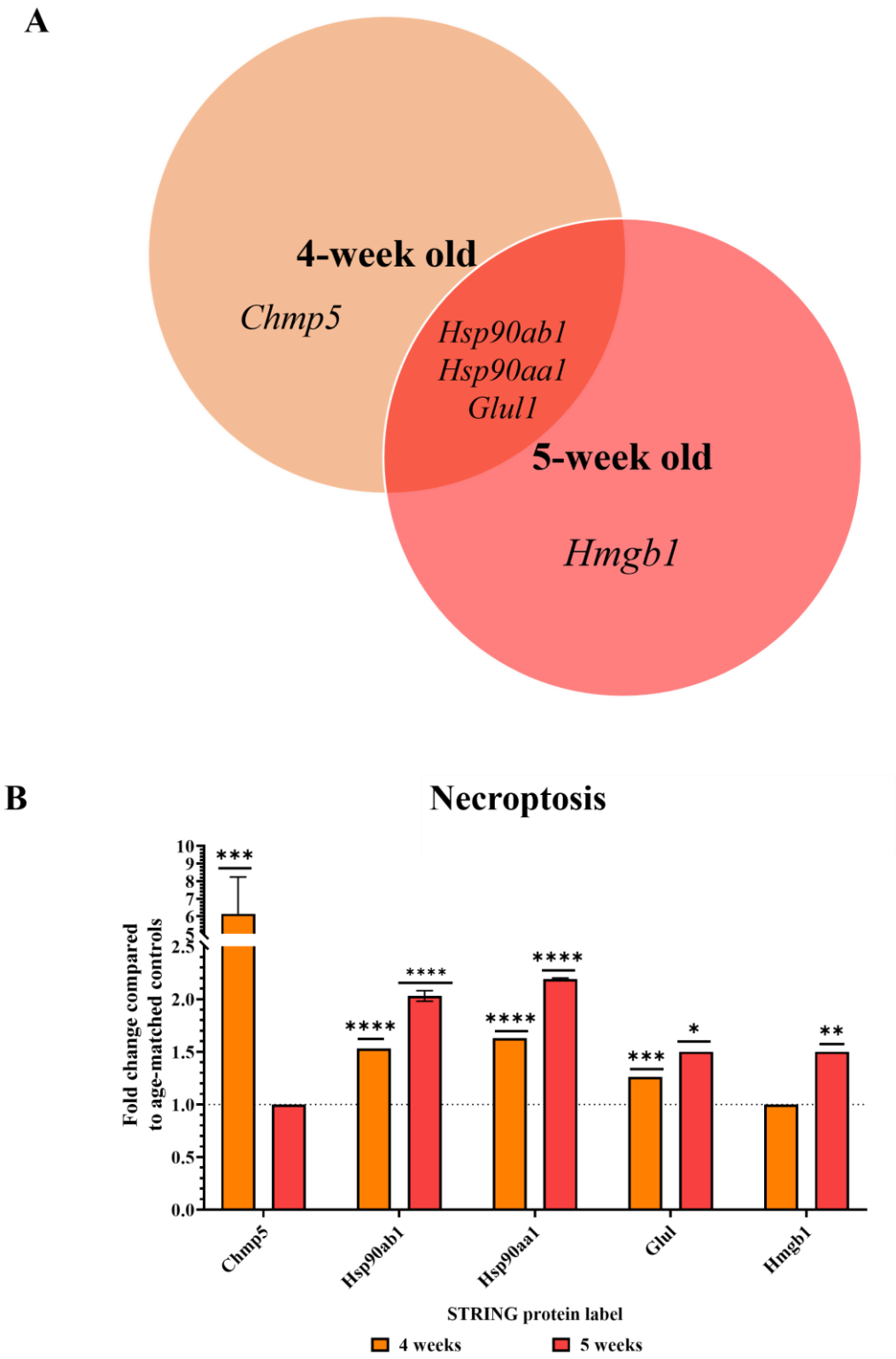

Figure 3.18:Upregulated proteins in 4 and 5-week-old Psmc1$^{fl/fl}$;CaMKIIα-*cre* mice show a significant pathway enrichment in necroptosis.3.18A) Venn Diagram shows unique proteins present in 4 weeks, and 5 weeks and their shared proteins. 3.18B) Fold change expressed compared to age-matched controls. Dotted line indicates baseline, students a t-test was conducted (* = P<0.05, ** = P<0.01, *** = P<0.001, **** = P<0.0001**)**

3.3.4.1 Upregulated pathways

STRING pathways analysis reported that IL-1 signaling (Strength: 1.58; FDR = 0.000591) and Neutrophil degranulation (Strength: 1.04; FDR = 0.006) are key enriched pathways (Figure 3.19) in 5-week-old mice.

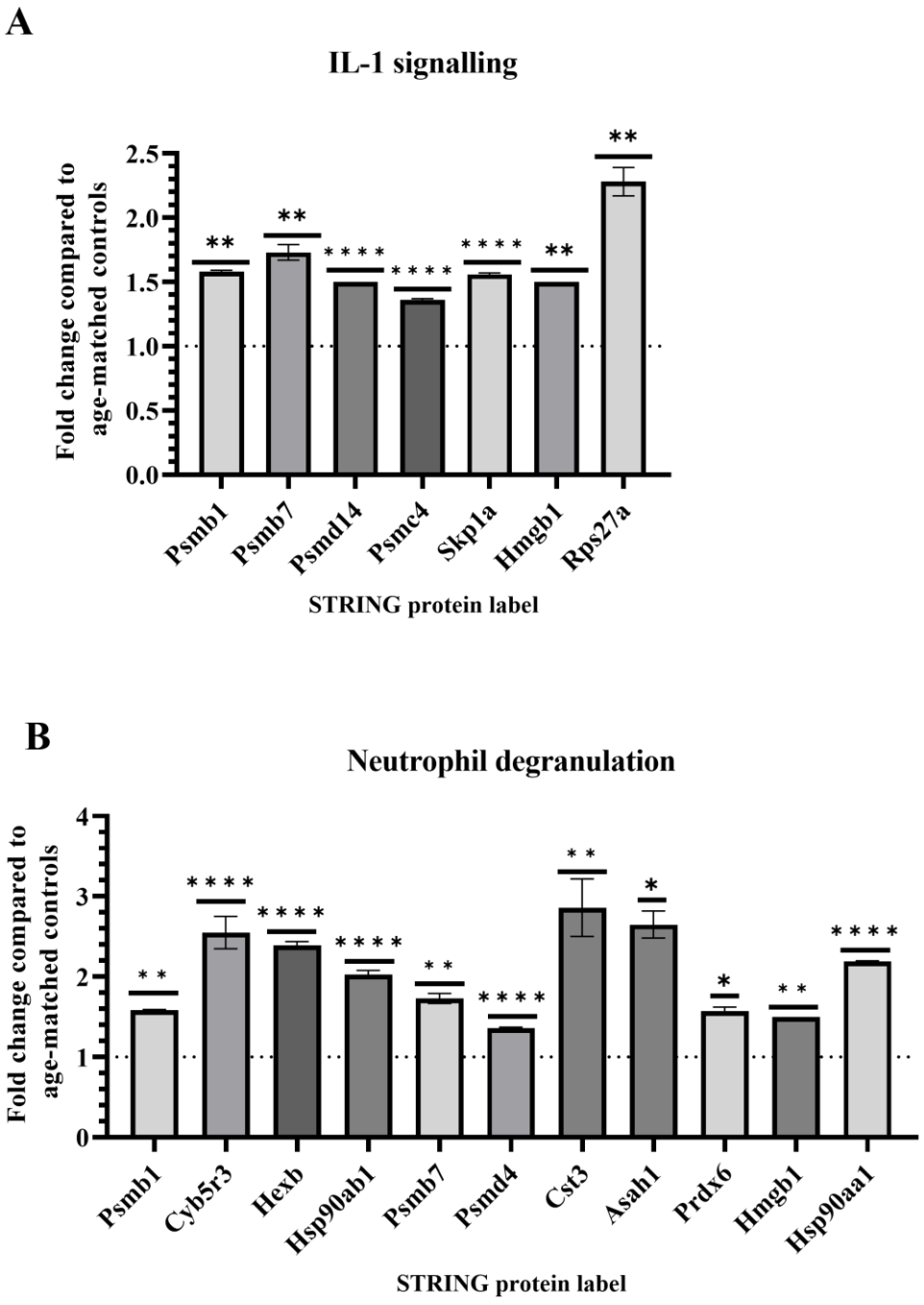

Figure 3.19:STRING pathways enrichment reports upregulation in proteins associated with IL-1 signaling and neutrophil degranulation. Dotted line indicates baseline, students t-test conducted (* = P<0.05, ** = P<0.01, *** = P<0.001, **** = P<0.0001).

3.3.4.2 Downregulated proteins

The 23 proteins downregulated proteins which surpassed confidence and significance conditions were inputted to STRING for protein-protein interaction analysis. The protein interactome map was deemed significant, with a PPI value below $p<0.05$ (figure 3.20).20 of the proteins that were detected that were not present in 4-week downregulated data, highlighted in table 3.6.

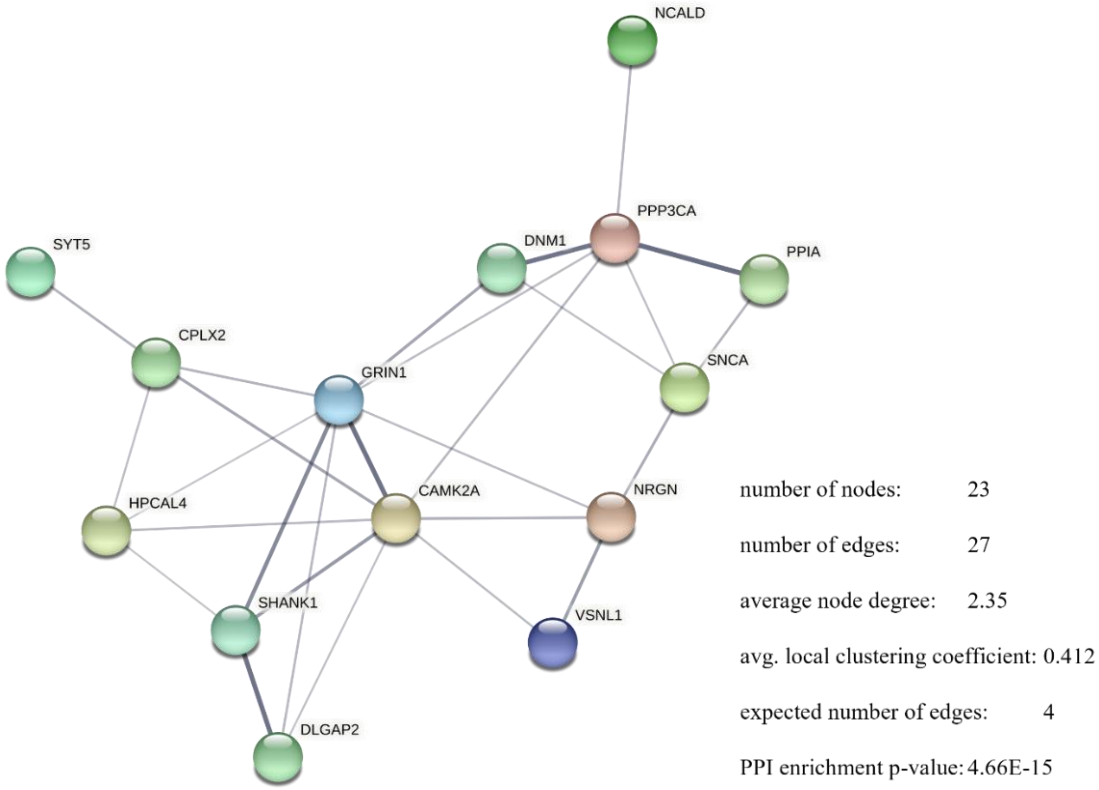

Figure 3.20:Downregulated proteins in 5-week-old Psmc1 $^{fl/fl}$;CaMKIIα-*cre* mice show a significant protein-protein interaction value, indicating pathway enrichment. STRING diagram showing interaction via 'strength' – thicker and darker lines indicate a stronger reaction.

Table 3.8 Downregulated proteins detected via mass spec in 5-week old Psmc1$^{fl/fl}$;CaMKIIα-*cre* cortices versus age-matched control

STRING	Protein	FC	SD	C	Sig	**
CAMK2A	Calcium/calmodulin-dependent protein kinase type II subunit alpha	-1.66	0.01	0.82	0.00	****
KCTD16	TB/POZ domain-containing protein KCTD16	-1.52	0.03	0.80	0.00	****
AGPS	Alkyldihydroxyacetonephosphate synthase, peroxisomal	-1.86	0.00	0.62	0.00	****
BRSK1	Serine/threonine-protein kinase BRSK1	-1.37	0.01	0.60	0.00	****
SHANK1	SH3 and multiple ankyrin repeat domains protein 1	-2.35	0.36	0.54	0.00	****
DCLK1	Serine/threonine-protein kinase DCLK1	-1.51	0.00	0.71	0.00	**
GRIN1	Glutamate receptor ionotropic, NMDA 1	-1.37	0.01	0.56	0.00	**
HPCAL4	Hippocalcin-like protein 4	-1.81	0.04	0.62	0.00	**
DNM1	Dynamin 1	-1.60	0.01	0.86	0.00	**
NRGN	Neurogranin	-2.43	0.05	0.58	0.00	**
NCALD	Neurocalcin-delta	-1.61	0.02	0.80	0.00	**
VSNL1	Visinin-like protein 1	-1.54	0.05	0.73	0.01	**
SNCA	Alpha-Synuclein	-1.90	0.09	0.75	0.01	**
PPIA	Peptidyl-prolyl cis-trans isomerase A	-1.58	0.03	0.78	0.01	*
DLGAP2	Disks large-associated protein 2	-1.47	0.03	0.56	0.01	*
MRPL13	39S ribosomal protein L13, mitochondrial	-1.31	0.01	0.67	0.02	*
SYT5	Synaptotagmin-5	-1.60	0.00	0.88	0.02	*
AGFG1	Arf-GAP domain and FG repeat-containing protein 1	-1.49	0.01	0.58	0.02	*
PPP3CA	Serine/threonine-protein phosphatase 2B catalytic subunit alpha isoform	-1.70	0.00	0.79	0.04	*
FGF12	Fibroblast growth factor 12	-1.71	0.06	0.60	0.04	*
NPTXR	Neuronal Pentraxin Receptor	-1.86	0.12	0.55	0.04	*
ABRACL	Costars family protein ABRACL	-1.59	0.00	0.65	0.05	*
CPLX2	Complexin 2	-1.72	0.07	0.51	0.00	**

***Key**: STRING – String Label, FC = Fold change detected by SWATH-MS, SD – standard deviation, C – confidence, Sig = Significance value (* = P<0.05 , ** = P<0.01, *** = P<0.001, **** = P<0.0001*

3.3.4.3 The somatodendritic compartment in neurons are downregulated in 4 and 5-week Psmc1$^{fl/fl}$;CaMKIIα-*cre* mice

Proteins that are assigned as enriched in the somatodendritic region were downregulated over 4 weeks (Strength: 1.05; FDR = 0.0084) and 5 weeks (Strength: 0.95, FDR: 0.000425) (figure 3.21,3.22).

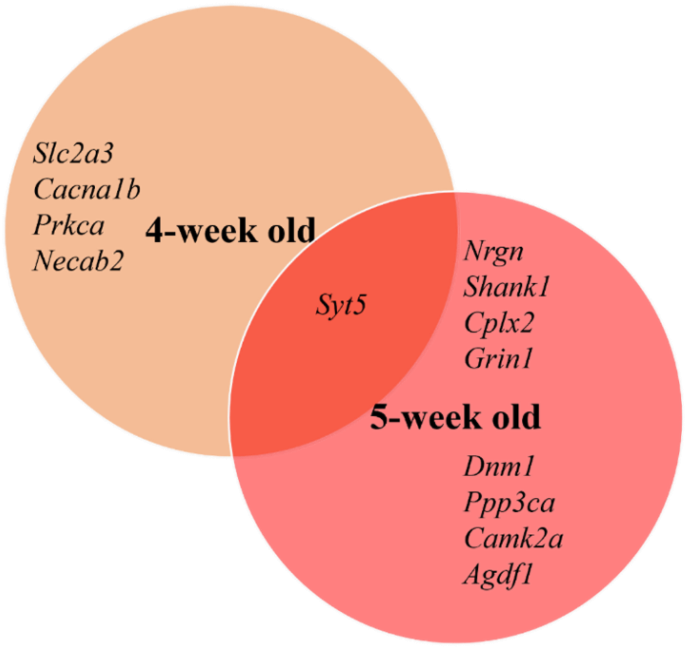

Figure 3.21:Downregulated proteins in 4 and 5-week-old Psmc1$^{fl/fl}$;CaMKIIα-*cre* mice show a significant pathway enrichment in the somatodendritic compartments of neurons. Venn Diagram shows unique proteins present in 4 weeks, and 5 weeks and their shared proteins.

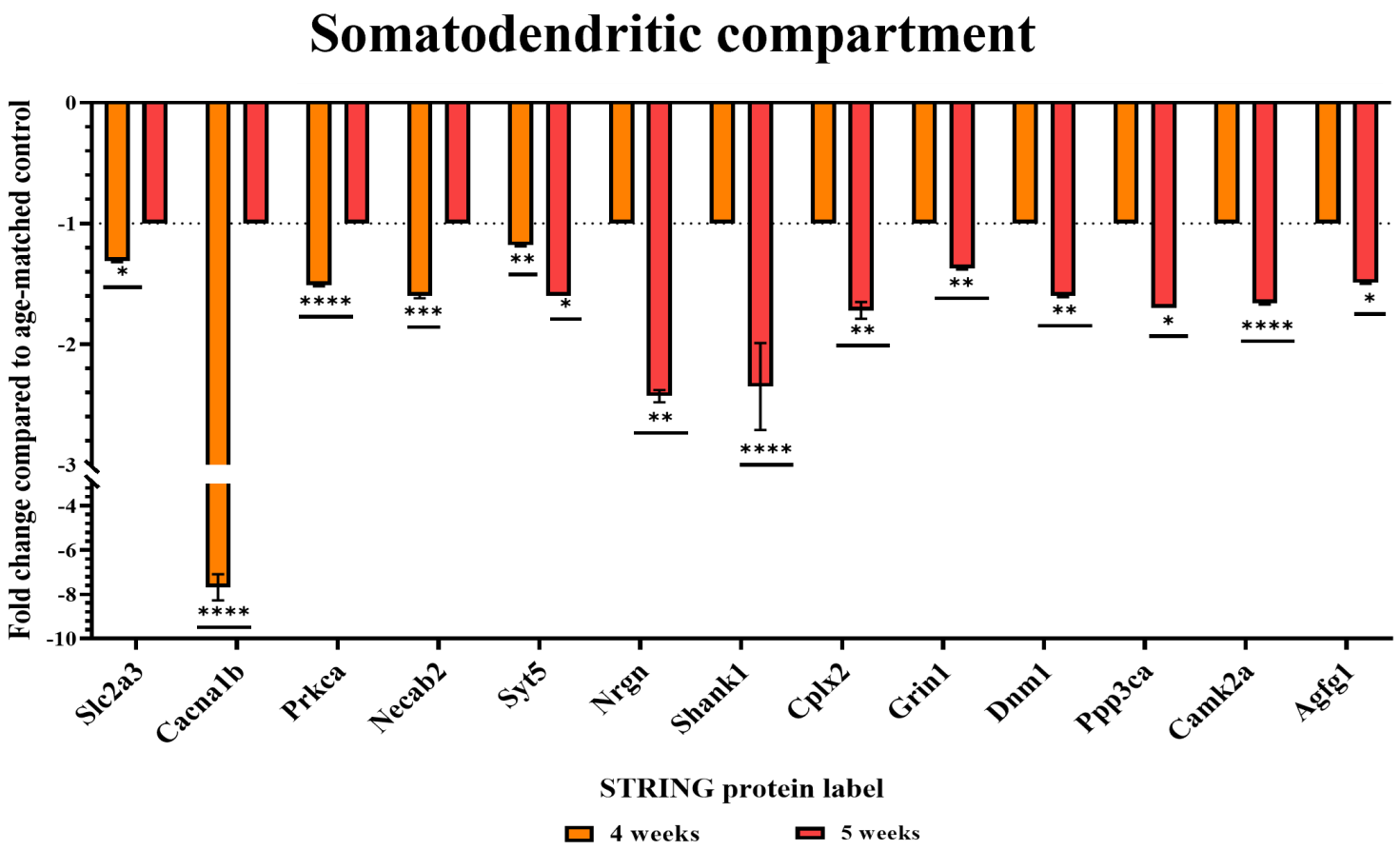

Figure 3.22:4 and 5-week-old Psmc1$^{fl/fl}$;CaMKIIα-*cre* mice show a significant upregulation in proteins related to Innate immune system. Graph displays alterations in fold change of enriched proteins compared to age-matched controls. Dotted line indicates baseline, a t-test was conducted (* = P<0.05 , ** = P<0.01, *** = P<0.001, **** = P<0.0001).

3.3.4.4 Downregulated cellular components

STRING pathways reported additional neuronal cellular components to be downregulated in 5-week old Psmc1$^{fl/fl}$;CaMKIIα-*cre* mice such as neuron projection (strength: 0.79; FDR: 0.00020) (figure 3.23) and glutamatergic synapses (strength: 1.22; FDR: 0.000035) (figure 3.24).

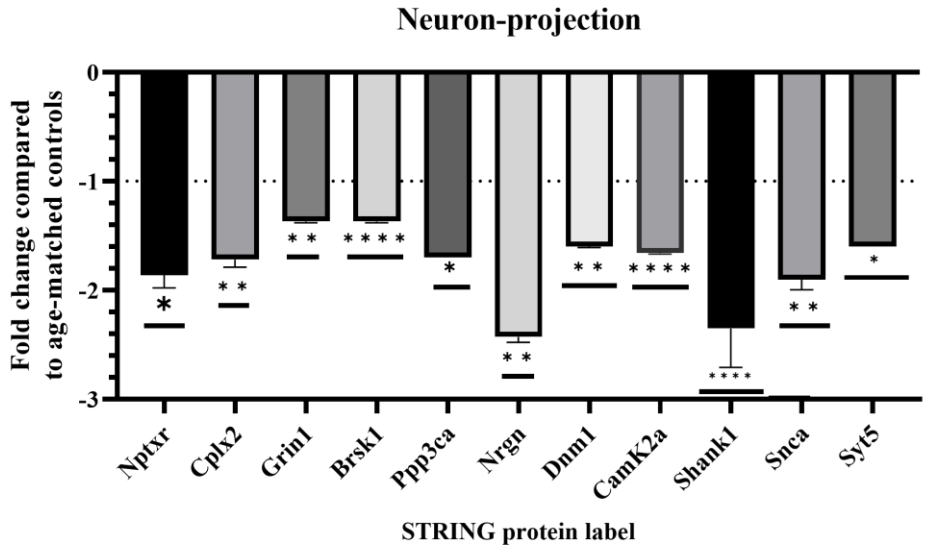

Figure 3. 23:Proteins associated with neuron-projection was significantly downregulated in 5-week-old Psmc1 $^{fl/fl}$;CaMKIIα-*cre* mice compared to age-matched control. (Strength: 0.79; FDR: 0.00020) Dotted line indicates baseline, students t-test conducted (* = P<0.05 , ** = P<0.01, *** = P<0.001, **** = P<0.0001).

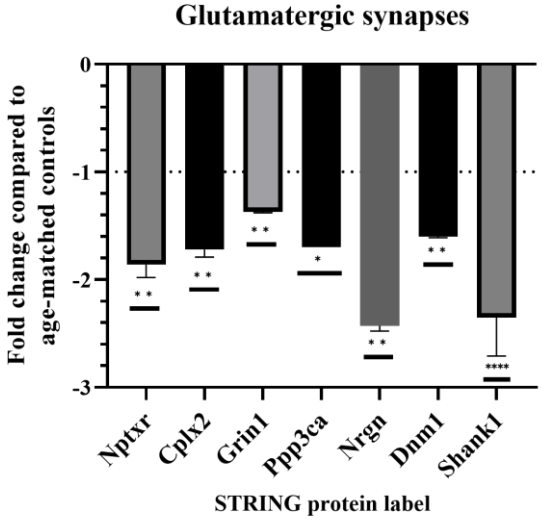

Figure 3. 24:Proteins associated with glutamatergic synapses was significantly downregulated in 5-week-old Psmc1$^{fl/fl}$;CaMKIIα-*cre* mice compared to age-matched control. (Strength: 1.22; FDR: 0.000035) Dotted line indicates baseline, students t-test conducted (* = P<0.05, ** = P<0.01, *** = P<0.001, **** = P<0.0001).

3.3.5 Shared protein enrichment over disease progression implicates a strong astroglial response

The Venn diagram below demonstrates proteins unique and shared proteins identified between 3,4 and 5-week-old Psmc1$^{fl/fl}$;CaMKIIα-*cre* mice (figure 3.25***).*** Three proteins were consistently detected to be upregulated in Psmc1$^{fl/fl}$;CaMKIIα-*cre* mice; Glial Fibrillary Acidic Protein (GFAP), Ubiquitin-40S ribosomal protein S27a (RPS27A) and F box only protein 2 (FBXO2).

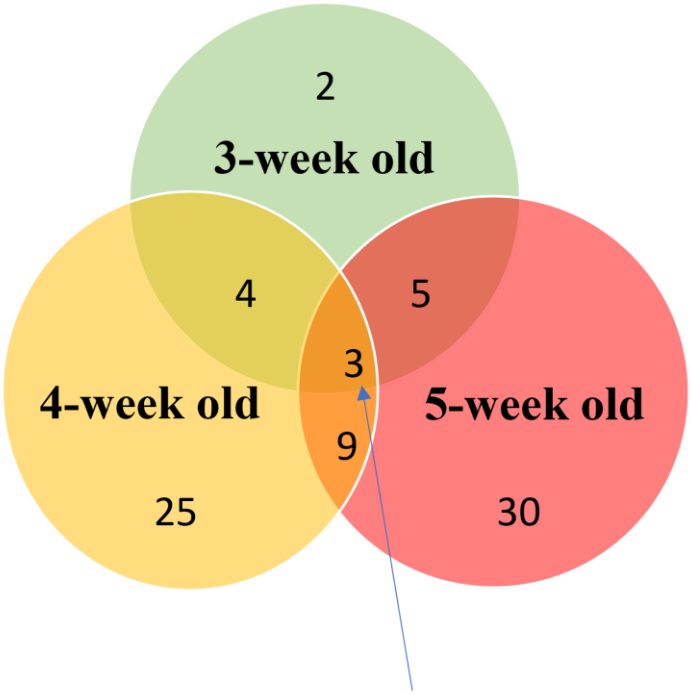

STRING	Protein	3 wks	sig	4 wks	sig	5 wks	sig
GFAP	Glial fibrillary Acidic Protein	2.30	***	4.86	***	12.78	*
RPS27A	Ubiquitin-40S ribosomal protein S27a	1.65	***	2.39	****	2.28	****
FBX02	F box only protein 2	1.55	*	2.06	****	3.02	**

Key: STRING – string label, WKs – weeks, Sig – significance value as reported by SWATH-MS compared to age-matched littermates

Figure 3. 25: Shared and unique identified upregulated proteins in 3, 4 and 5-week-old Psmc1$^{fl/fl}$; CaMKIIα-*cre* mice, with three proteins showing consistent upregulation across disease progression. Venn Diagram shows unique proteins present in 3, 4 weeks, 5 weeks and shared proteins GFAP, RPS27A and FBX02 fold change values and their resulting significance is shown.

STRING pathway analysis of SWATH-MS data reported enrichment in astroglial projection (figure 3.26) and myelin sheath components (figure 3.27,figure 3.28) indicating an astroglial response to neuronal proteasome depletion.

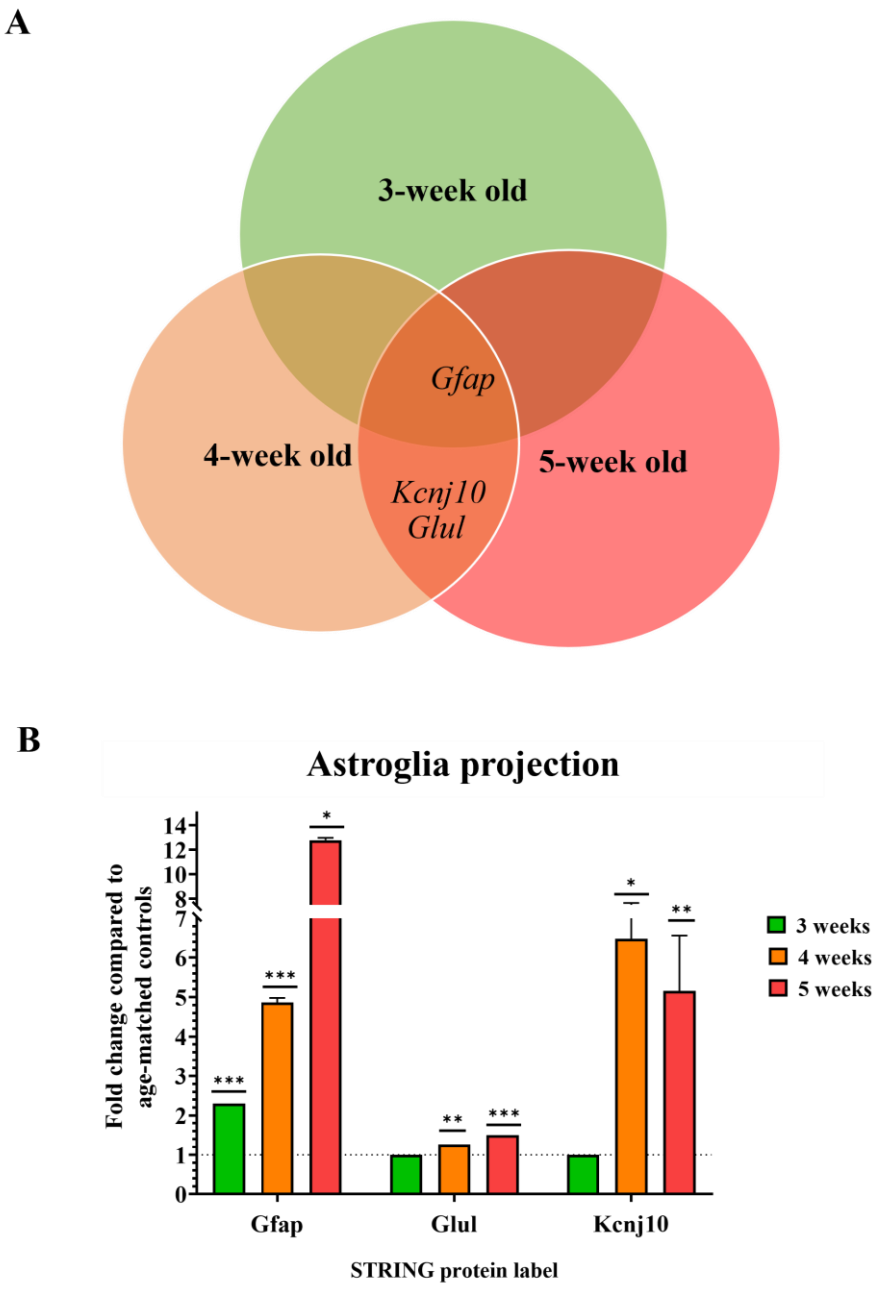

Figure 3. 26: Upregulated proteins in 3, 4 and 5-week-old Psmc1$^{fl/fl}$;CaMKIIα-*cre* mice show a significant pathway enrichment in the Astroglia projection. 3.26A) Venn Diagram shows unique proteins present in 3, 4 weeks, 5 weeks and their shared proteins. 3.26B) Fold change expressed compared to age-matched controls. Dotted line indicates baseline, a t-test was conducted (* = P<0.05 , ** = P<0.01, *** = P<0.001, **** = P<0.0001).

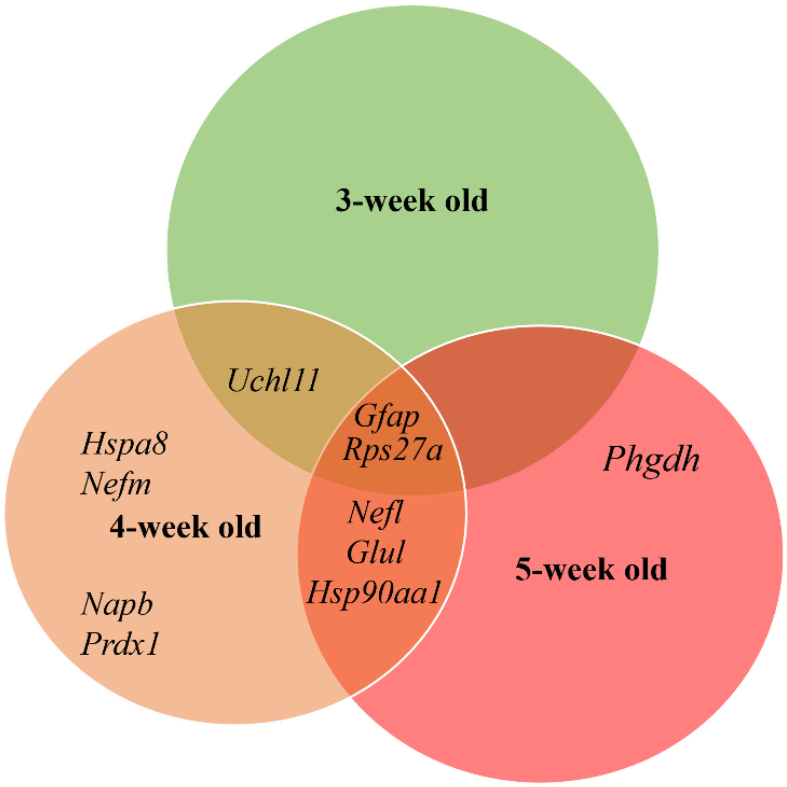

Figure 3. 27: Upregulated proteins in 3, 4 and 5-week-old Psmc1 $^{fl/fl}$;CaMKIIα-*cre* mice show a significant pathway enrichment in the myelin sheath. Venn Diagram shows unique proteins present in 3, 4 weeks, and 5 weeks and their shared proteins.

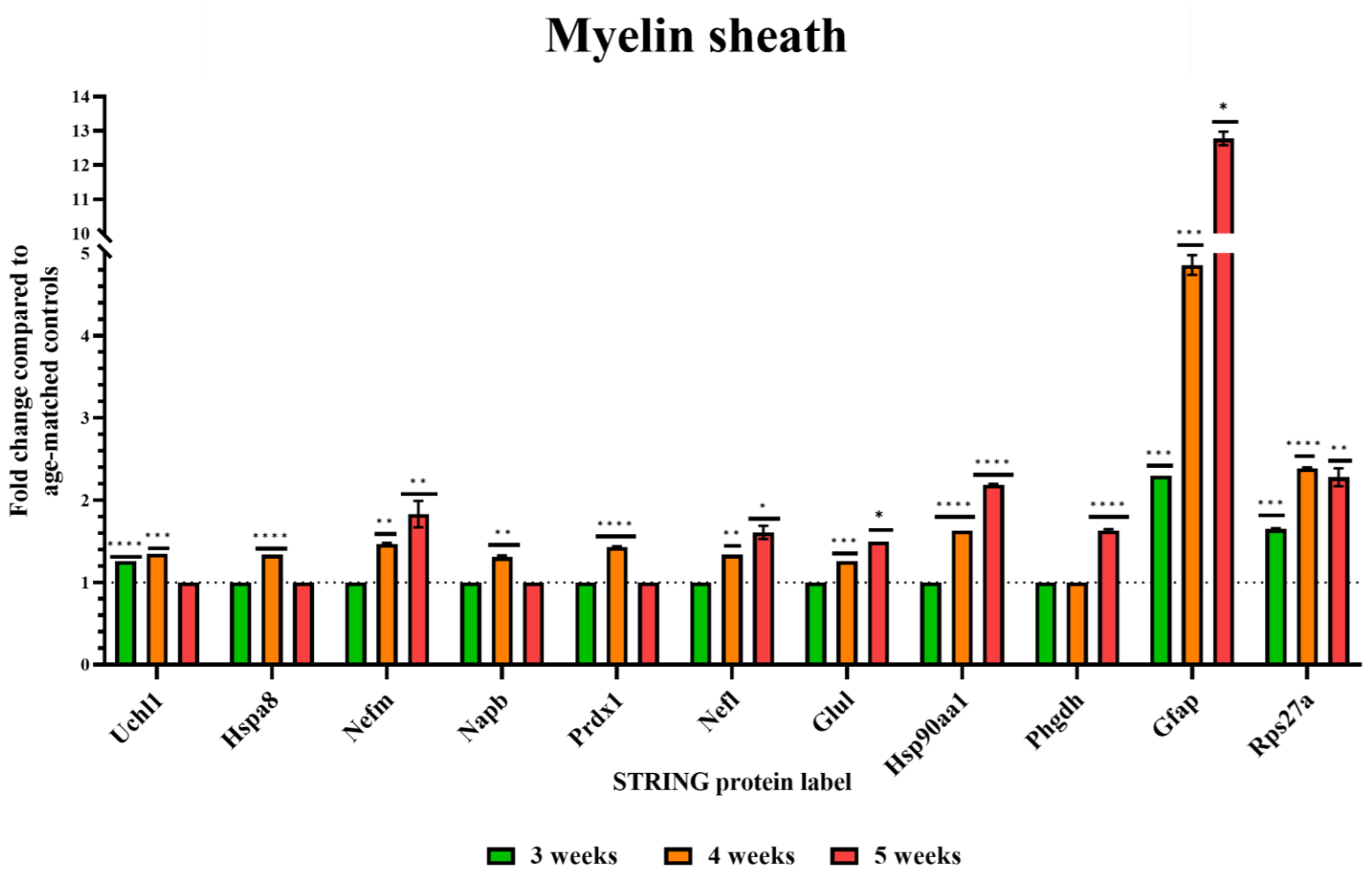

Figure 3. 28: 3, 4 and 5-week-old Psmc1$^{fl/fl}$;CaMKII*α-cre* mice show a significant upregulation in proteins related to the myelin sheath component. Graph displays alterations in fold change of enriched proteins compared to age-matched controls. Dotted line indicates baseline, a t-test was conducted (* = P<0.05, ** = P<0.01, *** = P<0.001, **** = P<0.0001)

3.4 Discussion

3.4.1 SWATH-MS reveal key pathways in the progression of neurodegenerative disease

SWATH-MS was used to perform a proteomic analysis of 3, 4 and 5-week Psmc1$^{fl/fl}$;CaMKIIα-*cre* mice alongside aged-matched controls, to identify key biochemical processes that are disrupted in response to 26S proteasomal depletion in forebrain neurons. In summary, the bioinformatic package, STRING, revealed several defined cellular processes and specific signaling pathways that were significantly altered, based on interactome analysis of SWATH-MS protein levels at progressive points from the onset of the disease.

This analysis shows a progressive disruption of cellular processes caused by the loss of Psmc1. Early changes in key astroglial markers and post-translational modification processes are followed by an intermediate disruption of microtubules, MAPK signaling, cell stress and apoptosis, leading ultimately to the appearance of immune markers and loss of neuron-specific proteins. These results help identify the key changes at the molecular level that underlie previous anatomical evidence for the progressive onset of neurodegeneration in this mouse model.

3.4.2 3-week upregulated pathways

One of the earliest identified changes due to loss of Psmc1 and proteasome dysfunction was in ubiquitin ligase proteins. The SCF-ubiquitin ligase complex is a ubiquitin ligase with multiple subunits that transfers activated ubiquitin to target-protein substrates. The SKP1-CUL1-F-box protein (SCF) Ubiquitin Ligase Complex reported a strength of 2.14 (FDR: <0.01), Rbx1 (E3 ubiquitin-protein ligase RBX1) and Fbxo2 (F-Box only Protein 2) are shown to be part of the cellular complex, whereas Cacybp (Calcyclin-binding protein) has shown interaction with SKP1.

In addition to this, ubiquitin-ligase protein binding was also reported as an enriched upregulated process in 3-week Psmc1$^{fl/fl}$;CaMKIIα-*cre*. The four proteins; Uchl1, Rbx1, Rsp27a,Cacybp reported a strength of 1.56 (FDR <0.01). Ubiquitin C-Terminal Hydrolase L1 (Uchl1) has been determined as a neuron-specific biomarker and is associated with neuronal inclusions in neurodegenerative disease (Day and Thompson, 2010; Reinicke et al., 2019).Rps27a, Ubiquitin-40S ribosomal protein S27a, is a specific ribosomal protein responsible for the synthesis of ubiquitin, indicating an increase in ubiquitin translation and production. Previous

immunohistology experiments display a strong increase in neuronal-centric ubiquitin-staining at 3-weeks of age. The reduction in 26S proteasome complexes caused by *cre* activation impairs ubiquitin-mediated protein degradation, so the upregulation of these proteins would be consistent with an attempt to compensate for this loss and sustain proteolysis (Bedford et al., 2010).

3.4.3 Post-translational modification is upregulated in 3 and 4-week-old Psmc1 $^{fl/fl}$;CaMKIIα-cre mice

The process of post-translational modification is upregulated in 3- and 4-week-old Psmc1 $^{fl/fl;}$ CaMKIIα-*cre* mice, with unique and common proteins in both conditions, with a strength of 1.04 (FDR: 0.018) and a strength of 0.65 (FDR: 0.016), respectively. E3 ubiquitin-protein ligase RBX1(Rbx1) and 26S proteasome regulatory subunit 6B (Psmc4) are unique to three weeks, with Ubiquitin carboxyl-terminal hydrolase isozyme L1 (Uchl1), Ubiquitin-40S ribosomal protein S27a (Rsp27a) and F-box only protein 2 (Fbxo2) shared between 3 and 4 weeks old. Proteins unique to 4-week-old Psmc1 $^{fl/fl}$;CaMKIIα-*cre* mice include Beta-soluble NSF attachment protein (Napb), Coatomer subunit delta (Arcn1), UV excision repair protein RAD23 homolog B (Rad23b), Ran GTPase-activating protein 1 (Rangap1), UV excision repair protein RAD23 homolog B (Ube2d3) and Apolipoprotein E (APOE).

It is worth noting that the proteins shared between 3 and 4 weeks old did show an increase in fold change between the two conditions, however as statistical testing was carried out by SCIEX software, the raw data was unable to be accessed for in-house statistical testing. Post-translational modifications have been demonstrated to be vital in supporting or hindering protein aggregation of neurodegenerative-related proteins.

For instance, the acetylation of the N-terminus in alpha-synuclein was demonstrated to decrease the ability of α-synuclein protein aggregation whereas phosphorylation of serine residues increases the formation of oligomers and the formation of fibrillar aggregates ((Samuel et al., 2016; Schaffert & Carter, 2020). Furthermore, APOE O-glycosylation is associated with increased solubility and potential to aggregate compared to other APOE with post-translational modifications (DiBattista, Sierra and Masliah, 2020).

Of interest, two proteins unique to 4-week-old post-translation modification, Ruvb1 and Rad23b, are associated with a response to double-strand DNA breaks (DSBs). The cause of

DSBs is attributed to chemical and oxidative damage, with most recent studies reporting an early neuronal accumulation of DSBs in neurodegenerative diseases (Shanbhag et al., 2019). Upregulation of these proteins indicates the initiation of a repair mechanism at this stage of the pathology.

3.4.4 4-week upregulated pathways

3.4.4.1 Microtubule transport

Microtubule transport in neurons is vital for their survival, as they oversee many cell movements, including intracellular transport and positioning of membrane vesicles and organelles.

Microtubule transport enriched proteins reported from STRING analysis of 4-week Psmc1$^{fl/fl}$; CaMKIIα-*cre* mice showed a strength of 1.19 (FDR: 0.0081). Proteins enriched in this process include Neurofilament Light Polypeptide (Nefl), Neurofilament medium polypeptide (Nefm), Heat shock cognate 71 kDa protein (Hspa8), Connexin 43 (Gja1) and Ubiquitin carboxyl-terminal hydrolase isozyme L1 (Uchl1).

In particular, Nefl, has shown a prominent role in neurodegeneration. An increase in Nefl has been characterised as a marker of axonal damage, which can be detected via CSF or blood depending on the extent of the injury (Khalil, 2018). CSF-derived Nefl has shown to increase in association with declining cognitive states (normal – AD, PD, ALS) in human studies (Ollson, 2018). In support of this, the increase of Nefl is associated with increased brain atrophy in Alzheimer's disease, therefore illustrating a causal relationship and making it a promising biomarker (Mattson, 2016).

Neurofilament expression, such as Nefl and Nefm, in the Psmc1$^{fl/fl}$;CaMKIIα-*cre* model has previously been characterised by the lab, demonstrating a significant upregulation in Nefl and Nefm proteins from 4-weeks old via western blot and immunohistology analysis (Mohamed, 2018). This is useful confirmation of the consistency of changes identified using different analysis techniques.

Connexin 43 (Gja1) is a gap junction protein, localised to astrocytes, that has shown to be regulated by microtubules. Gja1 has shown roles in neuron-glia interaction in

neurodegeneration. Gja1 KO Astrocytes showed reduced amyloid-beta phagocytosis and a neuroprotective phenotype (Kajiwara et al., 2018) and an increase in Gja1 is associated with a neurotoxic astrocyte in ALS (Spitale et al., 2020). Overall, this increase in connexin 43 may have a role in neuronal death (Yi et al., 2016).

Uchl1 and Hspa8 have also shown roles in axonal transport on synaptic proteins. This upregulation in microtubule processes can be hypothesised to be a mechanism from the neuron to enable the formation of intraneuronal inclusions that are present at 4-weeks of age (Robinson et al., 2005; Bheda et al., 2010; Stricher et al., 2013; Bishop, Rocca and Henley, 2016; Ganguly et al., 2017; Lyon and Milligan, 2019).

3.4.4.2 Negative regulation of the apoptotic pathway

Negative regulation of apoptotic pathways (Strength:1.09, FDR = 0.038) included proteins such as Neurofilament protein light (Nefl), Heat shock protein 90 β (Hs90ab1), Heat shock protein 105 kDa (Hsph1) and Apolipoprotein E (APOE).

Neurofilament light peptide has shown to have roles of negative regulating apoptosis by default, with knock-out studies displaying upregulated apoptosis in both the brain and spinal cord(Wang et al., 2021). Heat shock protein 105 is also implicated in the negative regulation of apoptosis, with overexpression of HSP105 in PC12 cells displaying a strong protective effect against various apoptotic stimulating treatments (Hatayama *et al,* 2001; Kennedy *et al,* 2014).

Apolipoprotein E (APOE) is well known for its role in the pathogenesis of Alzheimer's Disease but has also shown a role in the negative regulation of apoptosis. Hayashi and colleagues report found that APOE-containing lipoproteins, secreted from glial cells, protect neurons from apoptosis (Hayashi et al., 2007). This is supported by more recent studies detailing that specific isoform effects of APOE, such as APOE2 and APOE3, alleviates hydrogen-peroxide-induced neuronal apoptosis(Gao et al., 2021). Overall, from these studies it can be concluded that APOE does have a negative regulatory effect on apoptosis, suggesting that this disruption of regulated cell death may be a feature of progressive neurodegeneration in our model.

3.4.4.3 MAPK pathway and negative regulation of MAPK-pathway

The MAPK/ERK pathway is a key inflammatory pathway which has shown deleterious effects on brain health, particularly in neurodegenerative disorders such as Parkinson's disease, Alzheimer's disease, and Amyotrophic lateral sclerosis (Albert-Gascó et al., 2020). In 4-week-old Psmc1$^{fl/fl}$;CaMKIIα-*cre* mice, downregulated proteins (Cacnb1, Prkca, Prkcb) detected via STRING analysis indicate a downregulation in the MAPK pathway (Strength: 1.41; FDR=0.0075).

Cacanb1 (N-type calcium channel subunit alpha-1B) is a component of a neuronal voltage-gated calcium channel that has a multitude of roles such as neurotransmitter release. ERK-phosphorylation of the calcium subunit alpha-1 has shown to be important in modulating these channels (Martin et al., 2006). Protein kinase C has shown strong evidence in coupling with downstream MAPK/ERK effectors to elucidate a range of cellular processes such as TNF-α release (Song et al., 2017).

Overall, it can appear here that there is a downregulation of MAPK signaling in 4-week Psmc1 $^{fl/fl}$;CaMKIIα-*cre* mice. However, it must be taken into consideration that 26S proteasome depletion may not necessarily lead to a direct downregulation in MAPK signaling. One reason for this is the MAPK protein was found to be upregulated in 4-week Psmc1$^{fl/fl}$;CaMKIIα-*cre* mice compared to age-matched control controls (2.1 increase in Log_2 fold change), however, this change did not reach statistical significance (p-value = 0.941).

In addition to this, proteins associated with the negative regulation of the MAPK pathway (Nrdg2, Uchl1, Hsph1 and Apoe) were upregulated in 4-week-old Psmc1$^{fl/f}$;CaMKIIα-*cre* mice (Strength: 1.12, FDR = 0.0346). NRDG2, N-myc downstream-regulated gene 2, is a multifunctional protein associated with cellular proliferation and transmembrane transport. NDRG2 expression has been shown to negatively regulate the MAPK pathway via disrupting phosphorylation of the ERK protein (Huang et al., 2020). In the central nervous system, NDRG2 is strongly associated with Astrocytes, with several papers indicating co-localisation with other astrocyte markers such as GFAP and S100β (Okuda, Kokame and Miyata, 2008; Flügge et al., 2014; Lin et al., 2015). The changes observed may therefore vary between different cell types.

Elevated NDGR2 expression has been cited in popular neurodegenerative disease models such as APP/PS1 transgenic mice and mice treated with MPTP (Takeichi et al., 2011; Wang et al., 2014). Interventional NDGR2-reduction studies in these models report a downregulation in GFAP and NDGR2, alongside diminishing behavioral deficits (Wang et al., 2014.). Overall, it can be concluded that elevated NDGR2 expression in the Psmc1$^{fl/fl}$;CaMKIIα-*cre* model may be related to reactive astrogliosis, which could potentially drive a neurotoxic phenotype.

In summary, it can be argued that negative regulation of MAPK signaling through NDRG2 overexpression is potentially a neurotoxic mechanism employed by astrocytes in response to 26S-proteasome depletion.

3.4.5 4- and 5-week old Psmc1$^{fl/fl}$;CaMKIIα-cre mice shared upregulated pathways

3.4.5.1 Cellular stress response

The cellular stress response was a STRING-enriched process in 4 and 5-week-old Psmc1 $^{fl/fl}$;CaMKIIα-*cre* mice, with four proteins unique to 4 weeks, three shared proteins, and five proteins unique to 5 weeks old.

Heat shock protein 71, Heat Shock Protein 90α and Heat-shock protein 90β are molecular chaperones which are part of the Heat Shock Response, a cellular response mounted in response to proteotoxicity. Proteasome inhibition has previously shown an upregulation in the heat shock proteins (Bush, Goldberg and Nigam, 1997) and shows molecular action in suppressing the aggregation of misfolded proteins through binding through hydrophobic regions (van Noort, Bugiani and Amor, 2017; Raghunath et al., 2018; Lang et al., 2021). Furthermore, the overexpression of heat shock proteins in neurodegenerative models has been shown to rescue disease pathology (Hoshino et al., 2011; Jiang et al., 2013; Cox, Carver and Ecroyd, 2014).

PSMA3, a 20S proteasomal subunit, was also significantly upregulated. PSMA3 also has roles in binding intrinsically disordered proteins, therefore contributing to a reduction in proteotoxic stress (Biran et al., 2017). Together, an upregulation in these proteins indicates a neuronal-centric response to ubiquitin-aggregates.

A group of peroxiredoxins were also significantly upregulated in 4- and 5-week mice. Peroxiredoxins are antioxidant proteins that have a role in the oxidative stress response (Szeliga, 2020). PRDX1 was significantly upregulated at 4 weeks old. PRDX1 overexpression has shown roles in Alzheimer's disease and is associated with protection against amyloid-β toxicity (Cumming et al., 2007).

PRDX6 was significantly upregulated at 5 weeks old. PRDX6 overexpression in astrocytes is associated with decreased amyloid-β plaques in association with activated microglia (Pankiewicz et al., 2020). The PRDX6-astrocyte expression has already been demonstrated in Psmc1$^{fl/fl}$;CaMKIIα-*cre* mice, thereby supporting the reliability of SWATH-MS data (Elkharaz et al., 2013). Although seen as typically neuroprotective, excessive PRDX6 activity has been shown to inhibit neurogenesis, thereby obstructing neuronal repair (Yun et al., 2015; Yeo et al., 2019).

At 5 weeks of age, there was a significant increase in proteasomal subunits Psmb1, Psmb7, Psmd14 and Psmc4. Psmb1 and Psmb7 form the 20S proteasome complex, whilst Psmd14 and Psmc4 form the 19S regulatory cap. Upregulation in proteasomal subunits in response to proteotoxicity is a predictable and well-documented phenomenon.

3.4.5.2 Necroptosis

At 4 and 5-week, STRING analysis showed upregulation of several key proteins associated with "necroptosis".

Typically known as 'inflammation-induced cell death', necroptosis is induced by activation of a Toll-Like Receptor (TLR), Death Receptor (DR) or interferon or Tumour Necrosis Factor activation (Dhuriya and Sharma, 2018). Necroptosis is a hybrid of necrosis and apoptosis and regulates cell death through key morphological features such as swelling, which leads to the rupture of the plasma membrane. This membrane disruption leads to the extracellular release of Damage Associated Molecular Patterns (DAMPS), such as HMGB1, which in turn, activates downstream innate and adaptive immune components(Riegler et al., 2019). Excitotoxicity, oxidative stress and mitochondrial dysfunction are all shown to trigger neuronal necroptosis in neurodegenerative disorders (Vandenabeele et al., 2010). Incidentally, these three features are

evidenced in the Psmc1$^{fl/fl}$;CaMKIIα-*cre* model at 5 weeks (Elkharaz et al., 2013; Geiszler et al., 2018).

Necroptosis in CaMKIIα-*cre* neurons is a reasonable prediction. 4-week-old Psmc1 $^{fl/fl}$;CaMKIIα-*cre* mice showed a significant upregulation in the Charged Multibody Vesicle Binding Protein 5 (Chmp5). Chmp5 is a key protein in the endoplasmic reticulum and its upregulation indicates an increased sorting-cargo responsibility and is a major constituent of necroptotic exosomes (Shlomovitz et al., 2021). Upon cellular stress response to misfolded proteins (indicated by upregulated in heat shock response proteins Hsp90β and Hsp90α), the final resolution is conducted through the necroptotic process. The necroptotic mechanism involves caspase-8 regulated RIP3 cleavage which further leads to the activation of Glutamine synthetase (Zhang et al., 2009), a protein present both in 4 and 5 week Psmc1 $^{fl/fl}$;CaMKIIα-*cre* SWATH-MS data.

High mobility group box 1 protein, HMGB1, is uniquely upregulated in 5-week-old mice. HMGB1 is a unique DAMP which is released from necroptotic cells and interacts with TLR2/TLR4 pathways, promoting NF-κB P65 translocation and leading to IL-1 signaling (Paudel et al., 2018). Necroptosis is also implicated in astrocytes, showing active roles in reactive astrogliosis with necroptotic astrocytes inducing neuronal apoptosis through ADEVs (Chen et al., 2021; Re et al., 2014; Zhu et al., 2020; Zhu et al., 2021).

3.4.5.3 Innate immunity and IL-1 signaling

KEGG pathway analysis indicated that innate immunity was upregulated in 4-week and 5-week mice. 5 proteins were uniquely expressed at 4 weeks, whilst 12 were uniquely expressed at 5 weeks old. 3 proteins were in the overlap. Many proteins in the ‘cellular response to stress’ pathway are also found in this enrichment. At 4 weeks old, an upregulation in HSP71 (HSPA8) with HSP90 indicates a mounting of the unfolded protein response.

Additionally, upregulation of lysosomal proteins, cathepsin D (Ctsd), Beta-hexosaminidase subunit beta (Hexb) and acid ceramidase (Asha1) was reported at 4- and 5 weeks old. Lysosomal protein degradation has been reported to be upregulated in neurodegenerative disease, including loss of function mutations in cathepsin D have been shown to be linked to familial neurodegenerative pathology (Suire et al., 2020; Bunk et al., 2021).

Proteins in glycolysis were also upregulated across 4 -5 week Psmc1$^{fl/fl}$;CaMKIIα-*cre* mice such as Fructose-biphosphate aldolase (Aldoc) and Cytochrome B5 Reductase (Cyb5r3). Aldoc is localised to astrocytes, and its expression is linked to STAT3 activation(Levine et al., 2016).

Ubiquitin-conjugating enzyme E2 D3 (Ube23d), also present in the cellular stress response pathway, is a ubiquitin-ligase conjugating enzyme responsible for conduction of the autophagy-lysosomal pathway through P62/SQSTM1(Wang et al., 2021). This specific ubiquitin-ligase is also responsible for the degradation of ikkb1, a NF-κb inhibitory protein, thereby initiating NF-κb phosphorylation and translocation to the nucleus. In addition to this, S-phase kinase-associated protein 1 (Skp1a) was also upregulated at 5 weeks, which forms part of the SCF-ubiquitin-ligase complex. This, in addition to an upregulation in proteasomal subunits, Psmb1, Psmc4, and Psmb7, indicates an increased efficiency in proteolysis.

Complement protein C1qb is significantly upregulated in 5-week-old Psmc1$^{fl/fl}$;CaMKIIα-*cre* mice. C1qb has been cited to be localised to microglia and upregulation has been detected in neurodegenerative diseases (Holtman et al., 2015).

3.4.5.4 Neutrophil degranulation

Neutrophil degranulation is activated by oxidative stress, amyloid-β aggregates and cytokines. This degranulation is reported to have either beneficial or detrimental effects in neurodegenerative disease pathology and has shown deleterious effects on the blood-brain barrier (Manda-Handzlik and Demkow, 2019). In support of this, pharmacological inhibition of neutrophils proteases in models of neurodegenerative disease has shown a reduction in disease phenotype (Pietronigro et al., 2017).

3.4.6 Downregulation in neuronal components at 5 weeks of age

There is a downregulation in glutamate signaling detected in 5-week-old Psmc1$^{fl/fl}$;CaMKIIα-*cre*, with many proteins being cited to be localised to glutamate-neurons. Glutamatergic synapses in neurodegenerative diseases are well-documented, and for their role in excitotoxicity, with glutamate antagonists having potential therapeutic benefits (Sheldon and Robinson, 2007). The loss of glutamatergic synapses in neurons is reported in human studies (Crabbé et al., 2019). Glutamatergic synapses are also regulated by astrocytes, with astrocyte

dysfunction also leading to the loss of glutamatergic synapses (Mahmoud et al., 2019). In conclusion, the downregulation of glutamatergic synapses indicates a likely excitotoxic cause of neuronal death at 5 weeks.

In addition to this, proteins associated with a downregulation in neuron-projection were additionally found, such as alpha-synuclein, synaptotagmin 5 and CamK2A were also reported to be significantly downregulated. These proteins have a multitude of roles such as synaptic-vesicle release and long term-potentiation. As CAMKIIα neurons were targeted, their downregulation is expected.

3.4.7 Upregulation in Astroglia-associated proteins coincides with downregulation of neuronal components.

An overview of all proteins shared across disease pathways reported 3 key proteins to be upregulated in each disease stage: GFAP, FBXO2 and RSP27A. As these are present before intraneuronal inclusions and neuronal death, it can be assumed that these proteins have an active role in the initiation of pathology. STRING pathway analysis reported that these proteins are constituent components of the myelin sheath and astroglia-cell projection, therefore supporting a role for astrocytes in the progression of disease pathology. In addition to this, several upregulated pathways presented in this chapter have shown to be associated with astroglia including MAPK-pathway, cellular stress response, innate immunity, necroptosis and neutrophil degranulation (Yi et al., 2016; Spitale et al., 2020; Zhu et al., 2020; Zhu et al., 2021; Chen et al., 2021).

3.5 Conclusions and further work

Overall, this proteome analysis has effectively mapped the trajectory of changes in molecular signaling in the brains of mice with progressive neurodegeneration induced by loss of Psmc1. Despite the loss of Psmc1 being present in previous work by the group, SWATH-MS data failed to detect Psmc1, even in raw data sets, suggesting that key proteins maybe overseen using this method. In addition to this, although a range of proteins were identified through SWATH-MS data, this chapter is limited by the caveats of STRING network analysis. STRING does not consider the significance value noted in SWATH-MS data, therefore only providing a simple-overlap of protein function, and thereby reducing the biological significance of fold change and its significance to the control. In addition to this, STRING is not localized to brain specific proteins, thereby enriched pathways that have shown significance elsewhere may not be present in the brain. Thirdly, this proteomic dataset has not been validated by immunofluorescence in fixed-tissue to confirm the cellular localization of SWATH-MS proteins, therefore leaving questions on cellular pathways specific to each cell type unanswered.

Despite these caveats, one of the noteworthy results that raises new questions is the early onset of protein enrichment in the astroglia projection and myelin sheath. This is clearly an enriched cellular component in Psmc1$^{fl/fl}$;CaMKIIα-*cre* mice, suggesting that gliosis is one of the earliest indicators of pathology in the mouse model. Astrocytes have shown a prominent role in the SWATH-MS data with the key marker, GFAP, reporting an increased protein fold change associated with progressive neurotoxicity. To progress this, I will investigate GFAP expression across the early stages of neurodegenerative disease (2-,3-, 4 weeks) in my next chapter.

Chapter 4 JAK/STAT3 signaling in Psmc1$^{fl/fl}$;CaMKIIα-*cre* cortex

4.1 Introduction

4.1.1 STAT3 is a key regulator of astrogliosis

In the previous chapter, Glial Fibrillary Acidic Protein (GFAP) was shown to be a key upregulated protein, which exhibited an increasing fold change in association with a depletion in 26S proteasome complexes in CaMKIIα neurons. The significant elevation of GFAP at three weeks, a mere four days after the initial proteasome depletion occurs in CaMKIIα neurons, strongly indicates a transcellular mechanism, where changes in the neurons are being rapidly detected by glia (Bedford et al., 2008). This suggests that the disruption in proteostasis is modulating neuron-astrocyte crosstalk.

The elevation of GFAP is a marker for astrocyte reactivity. Astrogliosis presents as hypertrophy of cellular processes, cell proliferation, and functional changes that lead to the formation of the glial scar. Astrogliosis is a multi-graded process, and has shown to be injury specific - reporting distinct transcriptomic signatures (e.g. in acute CNS injury versus neurodegeneration) (Das et al., 2020). Overall, this complex collection of phenotypic changes has been hypothesised to be regulated by JAK/STAT3-mediated gene expression (Ceyzériat et al., 2016).

The JAK/STAT3 pathway in astrocytes has shown multiple effects in gliosis, with roles such as mediation of glia-scar formation, preservation of myelin sheath, secretion of anti-inflammatory cytokines and the reduction of leukocyte infiltration (Colombo and Farina, 2016; Giannaki,2020). STAT3 activation in primary astrocytes has been shown in response to a range of neurotoxic stimuli and pro-inflammatory mediators (O'Callaghan et al., 2014).

Many mice models of neurodegenerative disease show an upregulation in Astrocytic-specific STAT3 signaling, with STAT3 inhibitors showing an alleviation in disease symptoms and astrocyte hypertrophy (Ceyzériat et al., 2016; Ceyzériat, ben Haim, Denizot, Pommier, Matos, Guillemaud, M. A. Palomares, et al., 2018; Abjean et al., 2021). Collectively, this evidence suggests the hypothesis that the early increase in GFAP observed in our mouse model results from the activation of STAT3 signaling pathways in astroglia.

4.1.2 Aims of this chapter

This chapter aims to determine whether STAT3 activation is associated with upregulation of GFAP in Psmc1$^{fl/fl}$;CaMKIIα-*cre* mice and disease progression. To this end, we have used Western Blot and Immunofluorescence methods to examine the expression of STAT3, p-STAT3 Tyrosine 705 and GFAP in cortical regions across the progression of 26S Proteasome depletion.

4.2 Materials & Methods

Western blotting of cortex lysates will be used to investigate the protein quantity of STAT3, GAPDH, GFAP and p-STAT3 Tyrosine 705. Immunofluorescence histological staining will be used to visualize GFAP, STAT3α and its subsequent co-localisation in areas enriched with CaMKIIα neurons, such as the dentate gyrus, CA1, CA3 and cortex. For full details please refer to sections 2.3 and section 2.4.

4.2.1 Western blotting

2-,3-,4-week old Psmc1 $^{fl/fl}$;CaMKIIα-*cre* mice (n=4) and age-matched control littermates (n=4) were culled by S1, and the brain was rapidly removed and snap frozen in liquid nitrogen. Brains were kept at -80 until the lysis procedure. Cortex was lysed in RIPA buffer and further homogenized using the BeadBeater BP. Tissue was centrifuged to pellet debris and the supernatant was collected for subsequent protein quantification using a BCA assay. 100 µg of each sample was loaded to SDS page gels and transferred overnight.

The resultant membrane was checked for protein transfer using ponceau staining and the membrane was blocked in 5% Marvel® in TBS-T for one hour. Primary antibodies (GAPDH/pSTAT3/STAT3α/GAPDH/GFAP) were added at the required dilution and incubated overnight. Secondary antibodies (HRP) were added to 5% Marvel ® in TBS-T and membranes were incubated for one hour. ECL was used to visualize protein bands.

4.2.2 Immunofluorescence of FFPE brain tissue

2-,3-,4-week old Psmc1 $^{fl/fl}$;CaMKIIα-*cre* mice (n=4) and age-matched control littermates (n=4) were culled by PIL procedure and brains were submerged in 4% PFA and processed to formalin-fixed paraffin embedded (FFPE) slides. Slides were rehydrated followed by antigen-retrieval. Endogenous fluorescence was blocked using several washes of 0.1% Sodium borohydride in PBS, then washed with saline and PBS. M.O.M blocking reagent supplemented with goat serum was used as a blocking solution and primary antibodies (GFAP/STAT3α) were incubated on tissues overnight at 4ºC. Secondary fluorescent antibodies with DAPI were incubated for 1 hr in the dark at room temperature. Slides were mounted with DAKO mounting media. Several images of each brain region were taken for each sample (DG – 4, CA1 – 2, CA3 – 3, FC – 2).

4.3 Results

4.3.1 An increase in astrocyte reactivity is observed in the cortex

Firstly, western blotting for GFAP was undertaken to validate the mass spectrometry results shown in the previous chapter. Western blot results supported SWATH-MS data, reporting no significant fold change at two weeks (1.06 $p > 0.5$) to a significant fold change of 1.56 ($p < 0.0001$) at 3 weeks old, increasing to 2.18 ($p < 0.0001$) at 4 weeks old compared to age-matched control littermates (figure 4.1A; 4.1C). It is noteworthy that in the Psmc1$^{fl/fl}$;CaMKIIα-*cre* mice model there are additional isoforms present, marked by detection under the 50 kDa band. This has previously been reported in this model (Elkharaz et al., 2013).

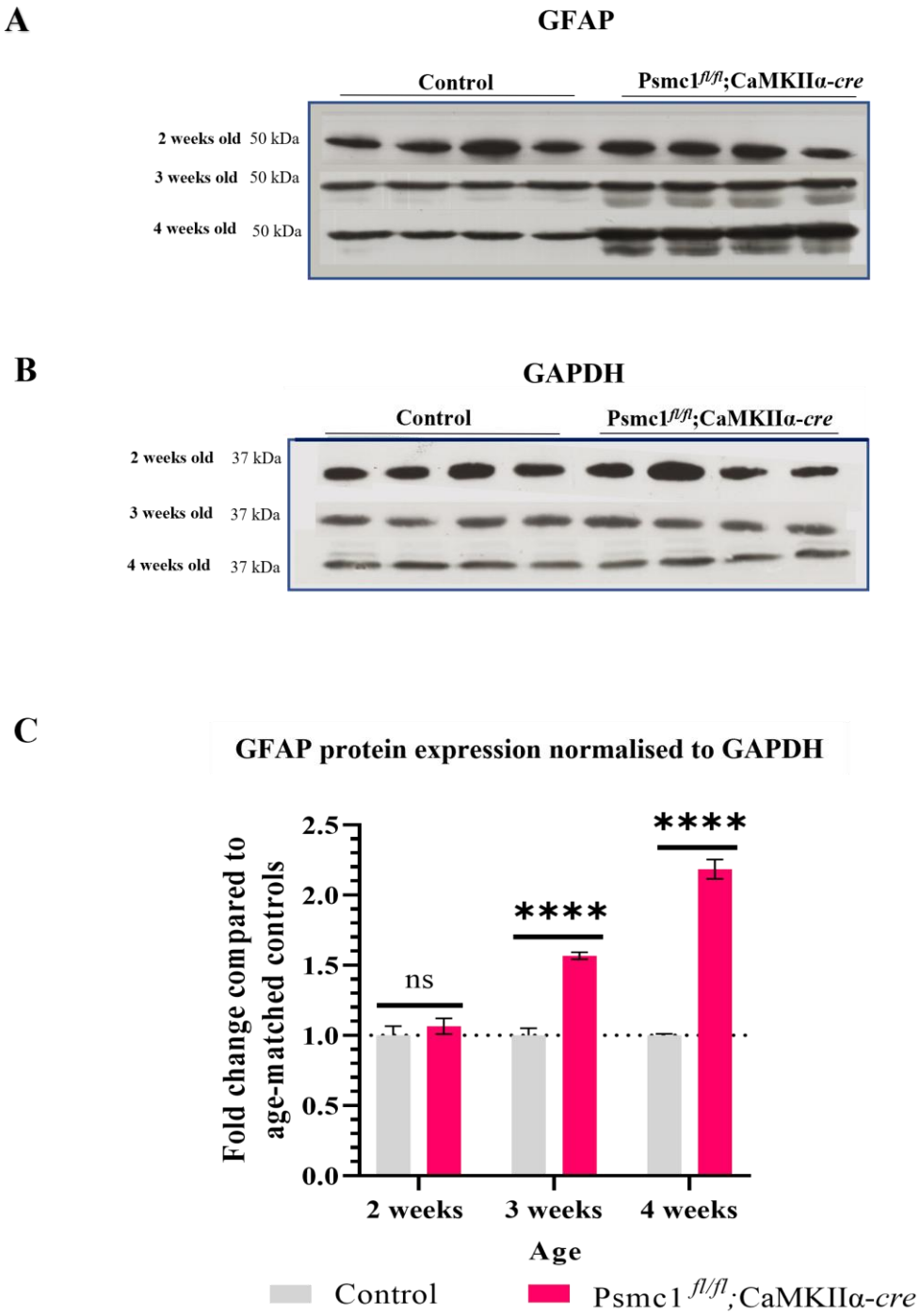

Figure 4.1:Immunoblotting demonstrates GFAP protein expression is significantly increased in Psmc1$^{fl/fl}$;CaMKIIα-*cre* mice in 3 and 4-week cortex. 4.1A) 100 µg protein lysate was loaded (Psmc1$^{fl/fl;}$CaMKIIα-cre mice – n=4, age-matched control- n=4) in 2, 3, and 4-week old mice. 4.1B) GAPDH of corresponding 2-, 3- and 4-week. 4.1C) Unpaired t-test shows significant increase of GFAP in Psmc1$^{fl/fl}$;CaMKIIα-*cre* mice at 3 and 4 weeks old (**** = P <0.0001).

4.3.2 Immunofluorescence demonstrates an increase in astrocyte-hypertrophy in CaMKIIα areas

After western blot demonstrated a significant upregulation of GFAP, it was then decided to assess astrocyte morphology in brain areas containing CaMKIIα neurons. Brain regions were identified from the previous mapping of the CaMKIIα-GFP model (Wang et al., 2013). In brief, it was reported that CaMKIIα was strongly expressed in the Dentate Gyrus, followed by the CA3 and then CA1 regions of the hippocampus. The cortex (somatosensory and auditory cortex) was also examined due to its loss manifesting in neurodegenerative symptoms. By analysing these regions, it can be inferred that astrocyte morphology, thereby reactivity can be attributed to the progressing neuronal proteotoxicity.

A two-way ANOVA was performed to analyse the effect of age and genotype on GFAP area expression. Four separate two-way ANOVAs were conducted for each region of interest (Cortex, CA1, CA3, DG).

In the cortex, the two-way ANOVA revealed that there was a statistically significant interaction between the effects of age and genotype ($F(2,18=6.656)$, $p=0.0069$).Tukeys multiple comparison analysis reported that GFAP area in the cerebral cortex showed no significant difference at 2 weeks old (10.73 vs 10.28, $p>0.05$),but increased in 3-week Psmc1$^{fl/fl}$;CaMKIIα-*cre* mice compared to control (14.70 vs 22.02, $p<0.05$) and in 4-week Psmc1$^{fl/fl}$;CaMKIIα-*cre* mice (20.76 vs 29.50, $p <0.01$) and also a statistically significant increase in GFAP area between 3-week and 4-week-old Psmc1 $^{fl/fl}$;CaMKIIα-*cre* mice (22.02 vs 29.50, $p <0.05$) (figure 4.2).

In analysis of the CA1 region, the two-way ANOVA revealed that there was a statistically significant interaction between the effects of age and genotype ($F(2,18=35.62)$, $p=0.00234$).
Tukeys multiple comparison analysis reported that GFAP area in the CA1 region of the hippocampus showed no significant difference at 2 weeks old (7.30 vs 7.53 $p >0.05$), or 3 weeks old (20.10 vs 22.93) however the area increased in 4-week Psmc1 $^{fl/fl}$;CaMKIIα-*cre* mice compared to control (13.57 vs 28.76, $p <0.01$).In addition to this, there was no significant increase in GFAP area between 3-week and 4-week-old Psmc1 $^{fl/fl}$;CaMKIIα-*cre* mice (22.02 vs 28.76, $p >0.05$) (figure 4.3).

In analysis of the CA3 region, the two-way ANOVA revealed that there was a statistically significant interaction between the effects of age and genotype ($F(2,18=25.62)$, $p= <0.0001$). Tukeys multiple comparison analysis reported that the CA3 region showed no significant difference at 2 weeks old (6.88 vs 6.82 $p >0.05$), however, there was a significant increase in area at 3 weeks old (12.91 vs 25.57 $p<0.004$) and 4-week old Psmc1$^{fl/fl}$;CaMKIIα-*cre* mice (10.06 vs 38.30, $p<0.003$). In addition to this, there was a significant difference between 3 and 4-week-old Psmc1$^{fl/fl}$;CaMKIIα-*cre* GFAP area (25.57 vs 38.30, $p <0.003$) (figure 4.4).

In analysis of the DG region, the two-way ANOVA revealed that there was a statistically significant interaction between the effects of age and genotype ($F(2,18=38.75)$, $p= <0.0001$). Tukeys multiple comparison analysis reported that GFAP area in the DG region showed no significant difference at 2 weeks old (9.24 vs 9.30 $p >0.05$) but showed a significant increase in area at 3 weeks old (14.45 vs 32.71, $p<0.0001$) and 4-week old Psmc1$^{fl/fl}$;CaMKIIα-*cre* mice (10.06 vs 38.30, $p<0.003$), in addition to this there was no significant difference between GFAP area in 3 and 4-week-old Psmc1$^{fl/fl}$;CaMKIIα-*cre* mice (32.71 vs 38.30, $P >0.05$) (figure 4.5).

Overall, this data shows a significant increase in GFAP area at 3 weeks old, prior to intraneuronal inclusions and pyknotic nuclei at 4 weeks.

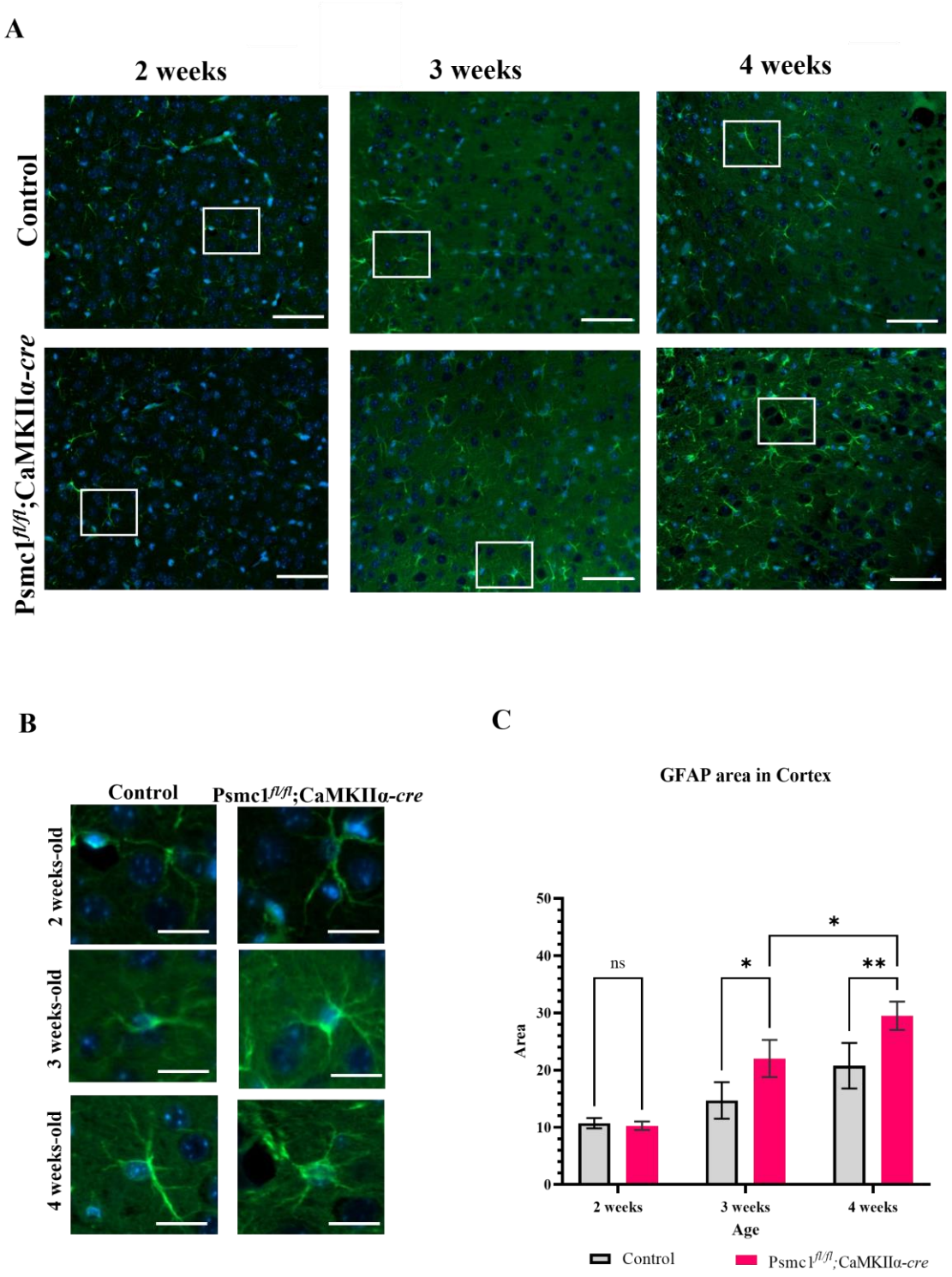

Figure 4.2:GFAP area is significantly increased in 3- and 4-week Psmc1$^{fl/fl}$;CaMKIIα-*cre* mice cerebral cortex. 4.2A) 20x images of GFAP (green) and nuclei (blue) in 2,3,4 week Psmc1$^{fl/fl}$;CaMKIIα-*cre* mice and aged-matched control, scale bar: 100µm White box indicates the region of interest (3 x 3) which was used for GFAP area (%) analysis. 4.2B) GFAP ROI identified, scale bar 25 µm. 4.2C) Post-hoc Tukeys multiple comparison test reported a significant difference between age-matched conditions across age groups (* = P<0.05, ** =P<0.01).

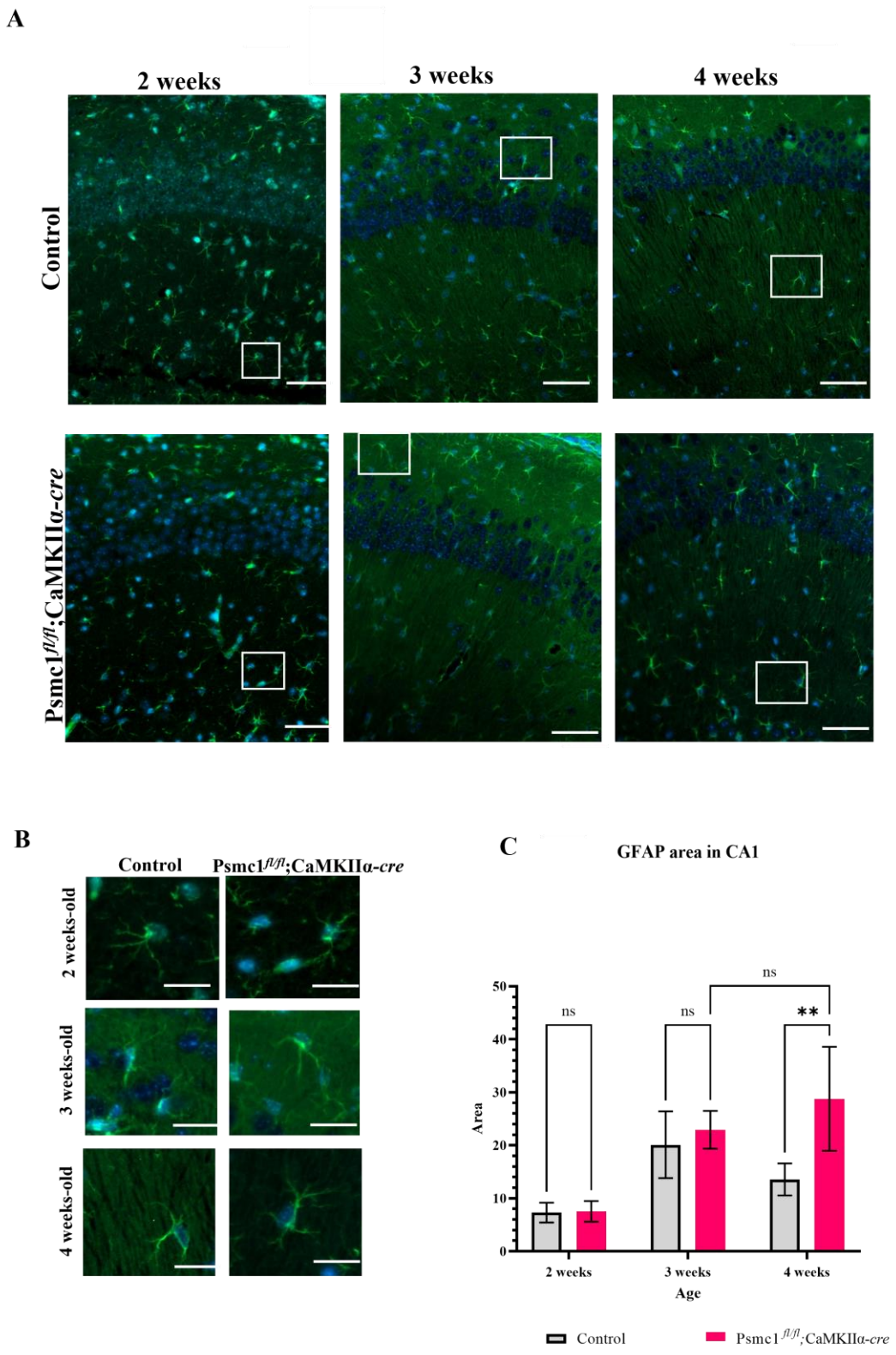

Figure 4.3:GFAP area is significantly increased 4-week Psmc1$^{fl/fl}$;CaMKIIα-cre mice CA1 region. 4.3A) 20x images of GFAP (green) and nuclei (blue) in 2,3,4 week Psmc1$^{fl/fl}$;CaMKIIα-*cre* mice and aged-matched control, scale bar: 100µm. 4.3B) GFAP ROI identified, scale bar 25 µm.4.3C) Post-hoc Tukeys multiple comparison test reported a significant difference between 4-week control and Psmc1$^{fl/fl}$;CaMKIIα-*cre* mice (** =P<0.01).

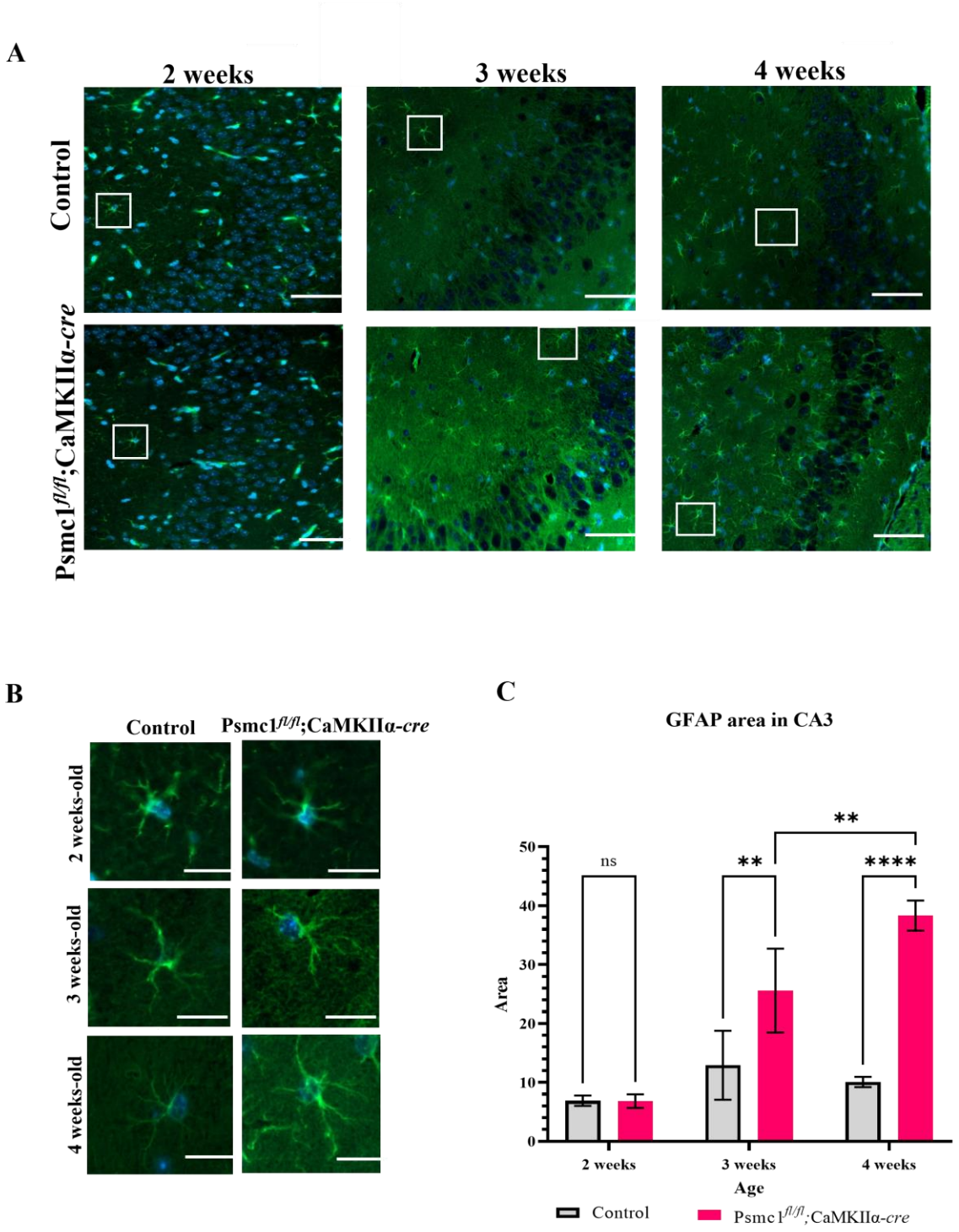

Figure 4.4: GFAP area is significantly increased in 3 and 4-week Psmc1 $^{fl/fl}$;CaMKIIα-*cre* mice CA3 region

4.4A) 20x images of GFAP (green) and nuclei (blue) in 2,3,4 week Psmc1$^{fl/fl}$;CaMKIIα-*cre* mice and aged-matched control, scale bar: 100µm. 4.4B) GFAP ROI identified, scale bar 25 µm. 4.4C) Post-hoc Tukeys multiple comparison test reported a significant difference in GFAP area between 3 and 4-week control and Psmc1 $^{fl/fl}$;CaMKIIα-*cre* mice (** =P<0.01,****=P<0.0001).

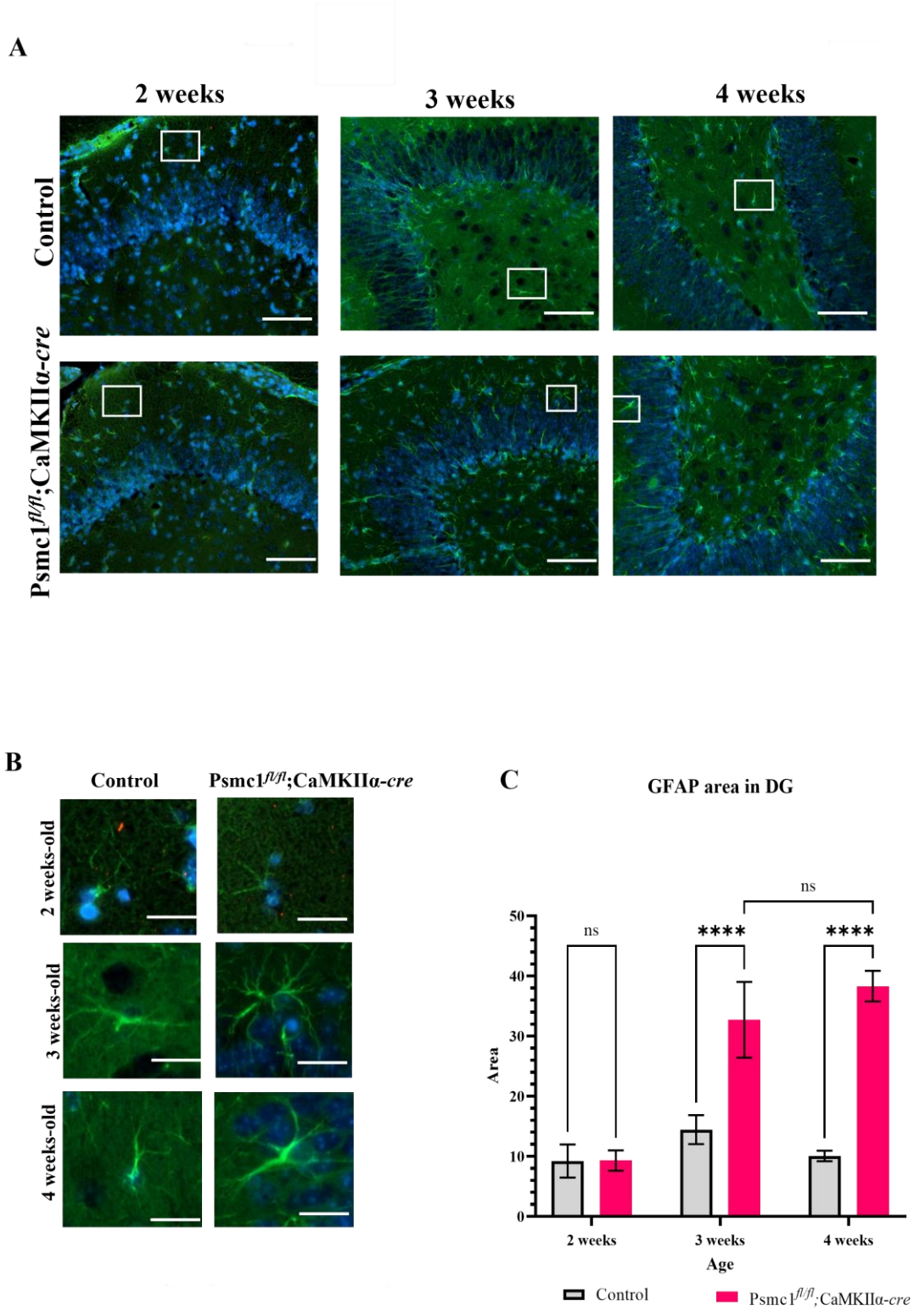

Figure 4.5: GFAP area is significantly increased in 3 and 4-week Psmc1$^{fl/fl}$;CaMKIIα-*cre* mice in the Dentate Gyrus (DG). 4.5A)20x images of GFAP (green) and nuclei (blue) in 2,3,4 week Psmc1$^{fl/fl}$;CaMKIIα-*cre* mice and aged-matched control, scale bar: 100 µm. The white box indicates the region of interest (3 x 3) which was used for GFAP area analysis. 4.5B) GFAP ROI identified, scale bar 25 µm. 4.5C) Post-hoc Tukeys multiple comparison test reported a significant difference between 4-week control and Psmc1$^{fl/fl}$;CaMKIIα-*cre* mice (**** =P<0.0001).

4.3.3 JAK/STAT3 signaling is significantly increased in Psmc1 $^{fl/fl}$;CaMKIIα-cre mice

JAK/STAT signaling has been cited as a key regulator of astrogliosis (Hong and Song, 2014). Therefore, immunoblotting for STAT3α and phosphorylated STAT3 (Tyrosine 705) was performed in 2,3 and 4-week-old cortex in both control and Psmc1$^{fl/fl}$;CaMKIIα-*cre* mice (n = 4). Western blots probing for STAT3α in Psmc1$^{fl/fl}$;CaMKIIα-*cre* mice demonstrated no significant fold change at two weeks (1.06,$p>0.5$) but a significant fold change of 1.70 ($p <0.0001$) at 3 weeks old, increasing to 1.90 ($p <0.0001$) at 4 weeks old compared to age-matched control littermates (figure 4.6). In line with this, there was no detection of phosphorylated-STAT3 tyrosine 705 at 2 weeks, however, there was a significant fold change of 1.94 at 3 weeks ($p <0.0001$) and 1.77 at 4 weeks old ($p <0.0001$) in Psmc1$^{fl/fl}$;CaMKIIα-*cre* mice compared to age-matched-control littermates (figure 4.7).

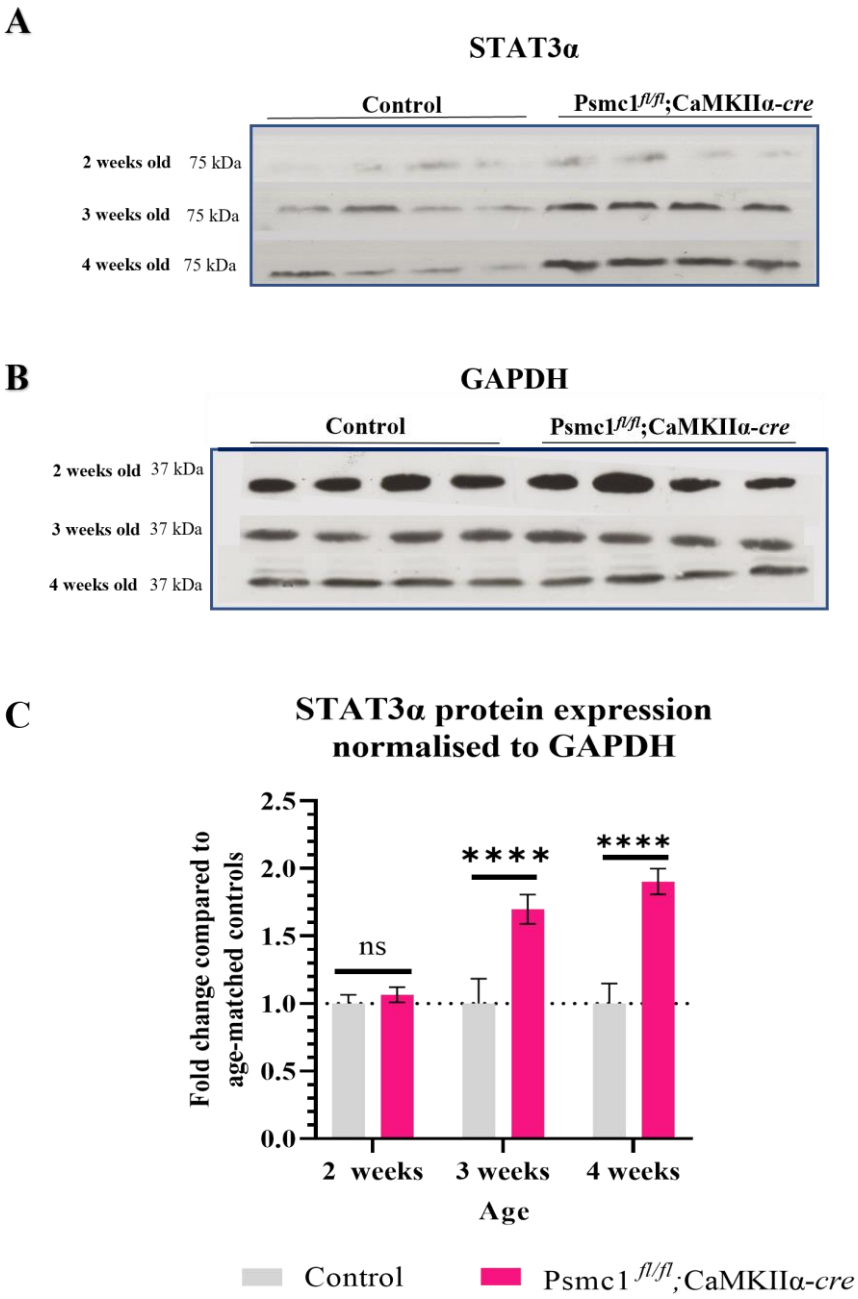

Figure 4.6:Immunoblotting demonstrates STAT3α protein expression is significantly increased in Psmc1 $^{fl/fl}$;CaMKIIα-*cre* mice in 3 and 4-week cortex. 4.6A) 100 µg protein lysate was loaded (Psmc1$^{fl/fl}$;CaMKIIα-*cre* mice – n=4, age-matched control n=4) in 2, 3, and 4-week old mice. 4.6B) GAPDH of corresponding 2-, 3- and 4-week proteins. 4.6C) Unpaired t-test shows significant increase of STAT3α in Psmc1$^{fl/fl}$;CaMKIIα-*cre* mice at 3 and 4 weeks old (**** = P <0.0001).

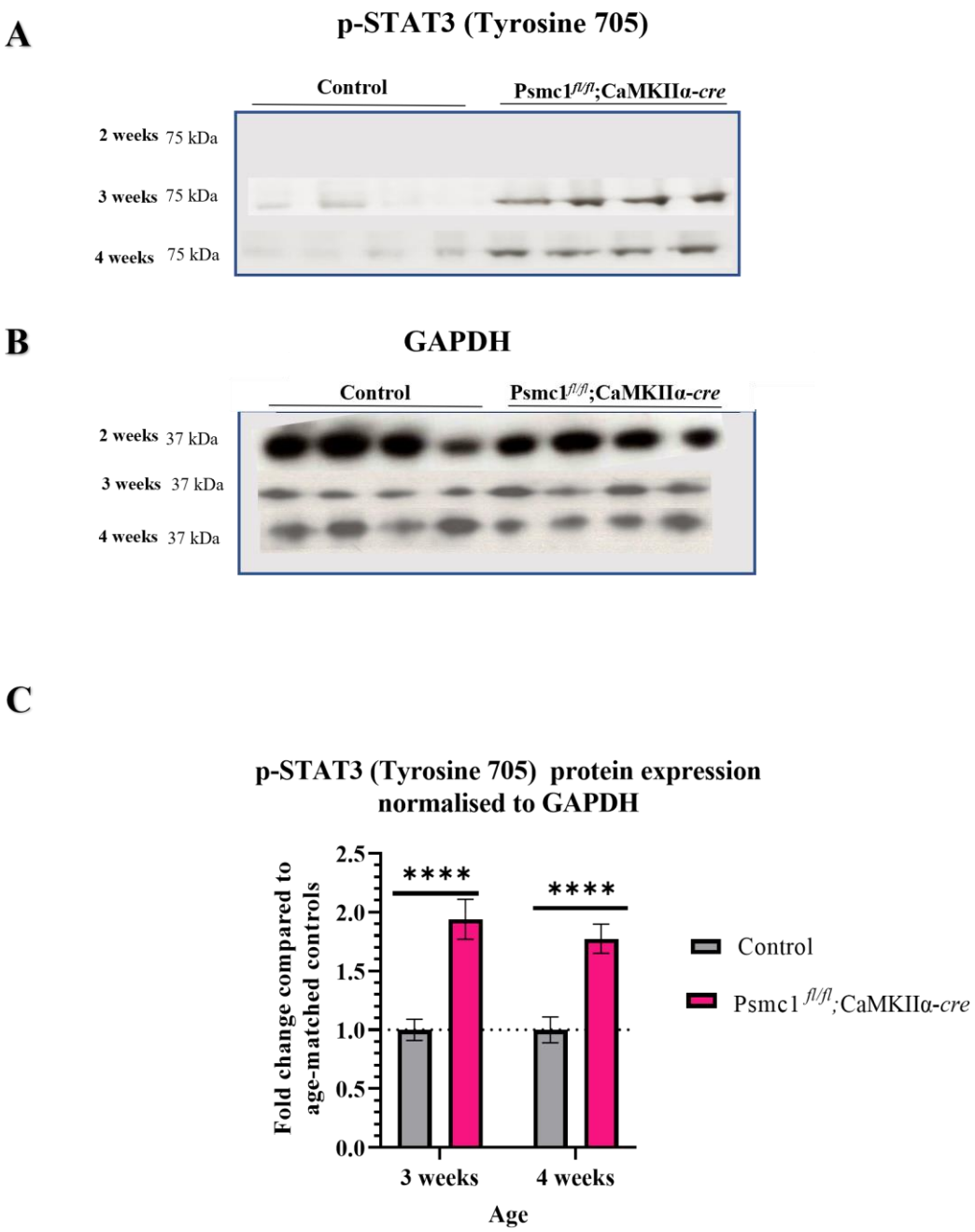

Figure 4.7:Immunoblotting demonstrates that p-STAT3 (Tyrosine 705) protein expression is significantly increased in Psmc1$^{fl/fl}$;CaMKIIα-*cre* mice. 4.7A) 100 µg protein lysate was loaded (Psmc1$^{fl/fl}$;CaMKIIα-*cre* mice – n=4, age-matched control- n=4) in 2-, 3-, and 4-week-old mice. 4.7B) GAPDH of corresponding 2, 3 and 4-week proteins. 4.7C) Unpaired t-test shows significant increase of p-STAT3(Tyrosine 705) in Psmc1 $^{fl/fl}$;CaMKIIα-*cre* mice at 3 and 4 weeks old (**** = P <0.0001).

4.3.4 The number of STAT3/DAPI colocalized cells is significantly increased in Psmc1 $^{fl/fl}$; CaMKIIα-cre mice

Immunoblotting data indicates that there is an upregulation in STAT3α and p-STAT3 (Tyrosine 705) protein expression in Psmc1$^{fl/fl}$;CaMKIIα-*cre* mice compared to control mice. Unfortunately, direct immunofluorescence staining of p-STAT3(Tyrosine 705) antibody in histology preparations was unsuccessful in our hands. As STAT3α dimerises and translocates to the nucleus as part of its activation mechanism after phosphorylation, it was deemed reasonable to use this as a proxy measure of potential p-STAT3 formation, by examining colocalised STAT3α^{+}/DAPI^{+} cells. This same method has been used by many other groups as a marker of phosphorylated-STAT3 (Lucile et al., 2015; Haim et al., 2015; Ceyzériat et al., 2016; Ceyzériat, ben Haim, Denizot, Pommier, Matos, Guillemaud, M. A. Palomares, et al., 2018; Guillemaud et al., 2020).

A two-way ANOVA was performed to analyse the effect of age and genotype on the number of STAT3α^{+}/DAPI^{+} cells. Four separate two-way ANOVAs were conducted for each region of interest (Cortex, CA1, CA3, DG).

In the cortex, the two-way ANOVA revealed that there was a statistically significant interaction between the effects of age and genotype ($F(2,18=4.532)$, $p=0.025$) on the number of STAT3α^{+}/DAPI^{+} cells. Tukeys multiple comparison analysis reported a significant difference in the cerebral cortex (+12 cells, $p < 0.05$) at 3-weeks of age and a significant increase at 4-weeks old (+13, < 0.05) in Psmc1$^{fl/fl}$;CaMKIIα-*cre* mice vs controls. There was no significant difference between 3 and 4-week old Psmc1$^{fl/fl}$;CaMKIIα-*cre* mice (-0.5, $p>0.05$) (figure 4.8).

In the CA1 region, the two-way ANOVA revealed that there was a statistically significant interaction between the effects of age and genotype ($F(2,18=7.411)$, $p=0.0045$) on the number of STAT3α^{+}/DAPI^{+} cells. Tukeys multiple comparison analysis reported that a significant difference in the CA1 region (+10, $p <0.001$) at 3-weeks of age however there was no significant difference 4-weeks old (+3, $p>0.05$) in Psmc1$^{fl/fl}$;CaMKIIα-*cre* mice vs controls. There was no significant difference between 3 and 4-week old Psmc1$^{fl/fl}$;CaMKIIα-*cre* mice (+ 1.25, $p>0.05$) (figure 4.9).

In the CA3 region, the two-way ANOVA revealed that there was no statistically significant interaction between the effects of age and genotype ($F(2,18=3.307)$, $p=0.0598$) on the number

of STAT3α^{+}/DAPI^{+} cells. Tukeys multiple comparison analysis reported that there is no significant difference in the CA3 region (+5, $p > 0.05$) at 3-weeks of age however there was a significant difference at 4-weeks old (+12, $p < 0.05$) in Psmc1$^{fl/fl}$;CaMKIIα-*cre* mice vs controls. There was no significant difference between 3 and 4-week old Psmc1$^{fl/fl}$;CaMKIIα-*cre* mice (+10, $p > 0.05$) (figure 4.10).

In the DG region, the two-way ANOVA revealed that there was a statistically significant interaction between the effects of age and genotype ($F(2,18=8.098)$, $p=0.0031$) on the number of STAT3α^{+}/DAPI^{+} cells. Tukeys multiple comparison analysis reported that there is no significant difference in the DG region (+16, $p<0.01$) at 3-weeks of age however there was a significant difference at 4-weeks old (+22, $p < 0.05$) in Psmc1$^{fl/fl}$;CaMKIIα-*cre* mice vs controls. There was no significant difference between 3 and 4-week old Psmc1$^{fl/fl}$;CaMKIIα-*cre* mice (+9, $p > 0.05$) (figure 4.11).

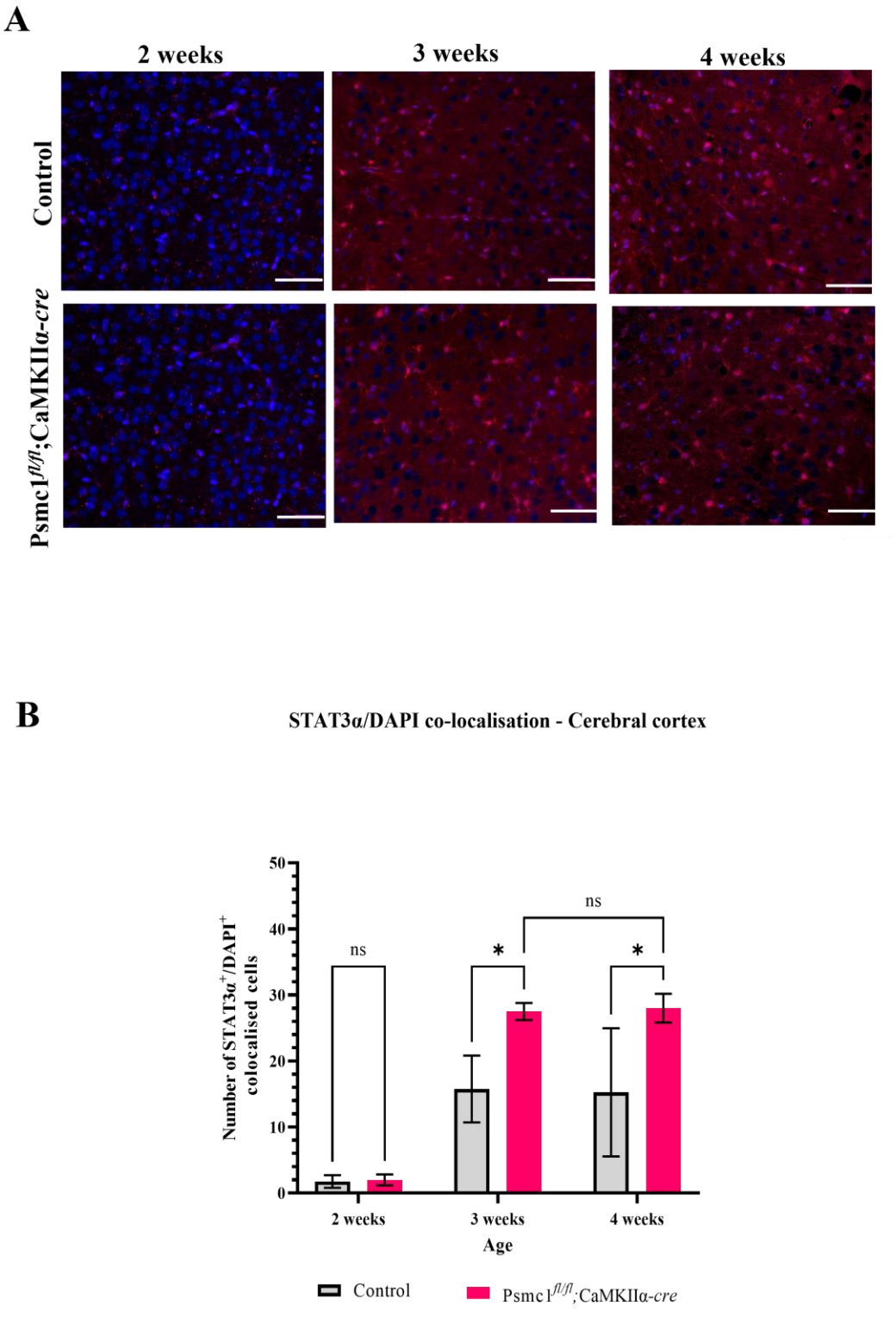

Figure 4.8: Number of STAT3α^{+}/DAPI^{+} colocalised cells is significantly increased in 3 and 4-week Psmc1 $^{fl/fl}$;CaMKIIα-*cre* mice cerebral cortex. 4.8A)20x images of STAT3α (red) and nuclei (blue) in 2,3,4 week Psmc1 $^{fl/fl}$;CaMKIIα-*cre* mice and aged-matched control, scale bar: 100µm. 4.8B) Post-hoc Tukeys multiple comparison reported a significant difference between 3 and 4 week Psmc1$^{fl/fl}$;CaMKIIα-*cre* mice versus age-matched control (* =p<0.05).

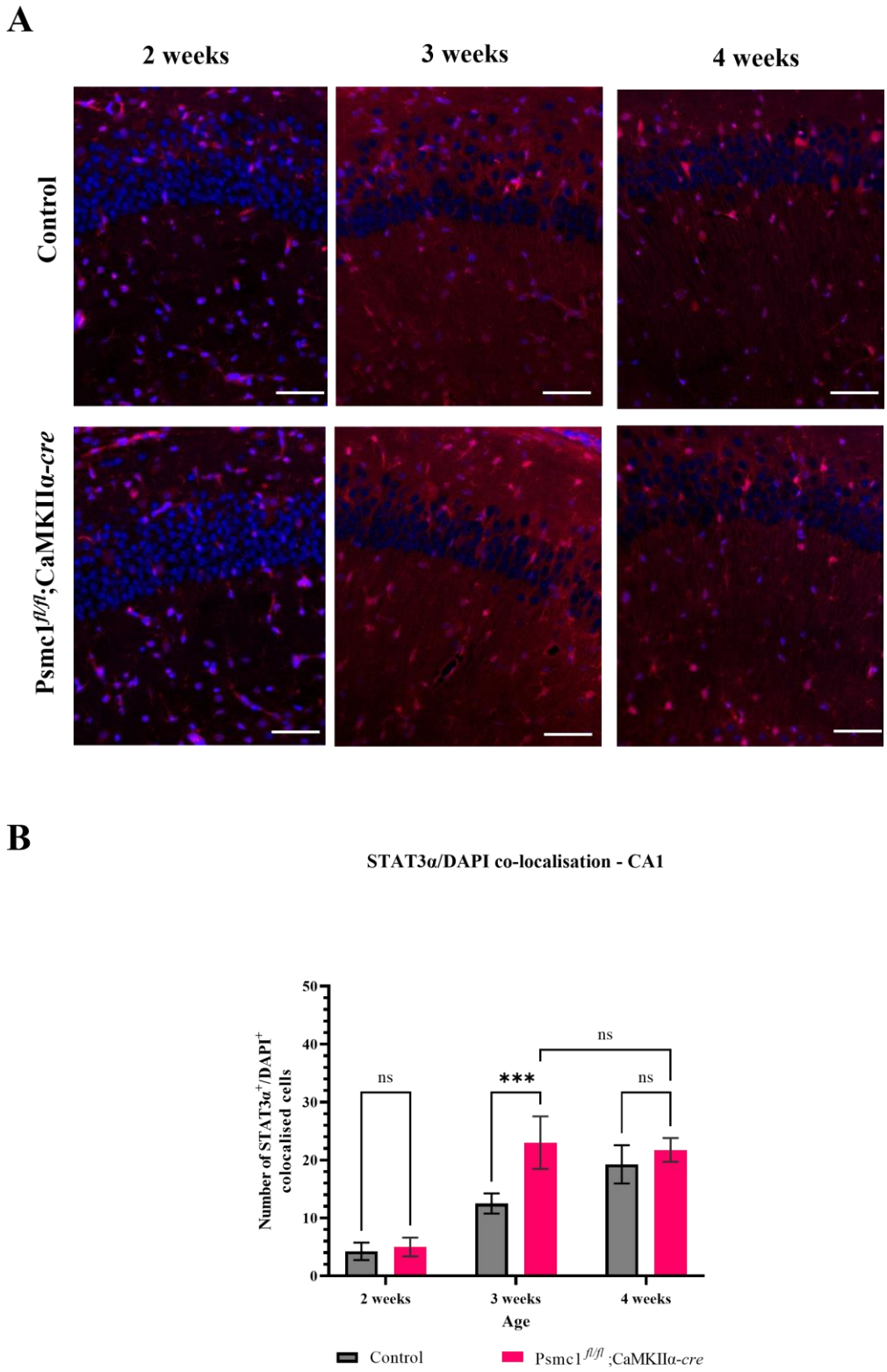

Figure 4.9:Number of STAT3α^{+}/DAPI^{+} colocalised cells is significantly increased in 3-week Psmc1 $^{fl/fl}$;CaMKIIα-*cre* mice in the CA1 region. 4.9A)20x images of STAT3α (red) and nuclei (blue) in 2,3,4 week Psmc1$^{fl/fl}$;CaMKIIα-*cre* mice and aged-matched control, scale bar: 100µm. 4.9B) Post-hoc Tukeys multiple comparison reported a significant difference between 3-week-old Psmc1$^{fl/fl}$;CaMKIIα-*cre* mice versus age-matched control (***=p<0.001), however, showed no significant difference at 4-weeks old.

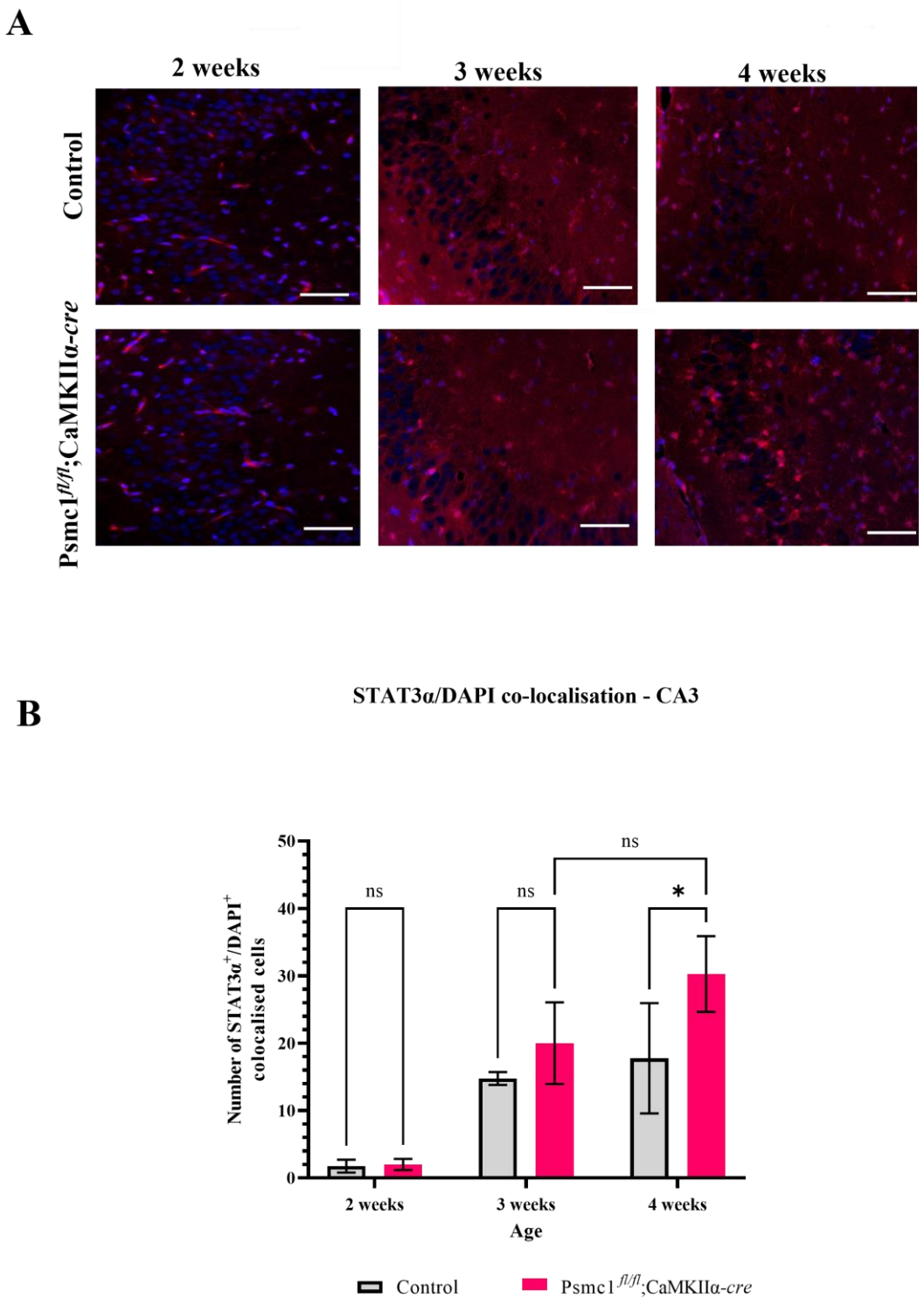

Figure 4.10:Number of STAT3α^{+}/DAPI^{+} colocalised cells is significantly increased in 4-week Psmc1 $^{fl/fl}$;CaMKIIα-*cre* mice in the CA3 region. 4.10A)20x images of STAT3α (red) and nuclei (blue) in 2,3,4 week Psmc1$^{fl/fl}$;CaMKIIα-*cre* mice and aged-matched control, scale bar: 100µm. 4.10B) Post-hoc Tukeys multiple comparison reported a significant difference between 4 week old Psmc1$^{fl/fl}$;CaMKIIα-*cre* mice versus age-matched control (*** =p<0.001), however no significant difference at 3-weeks old.

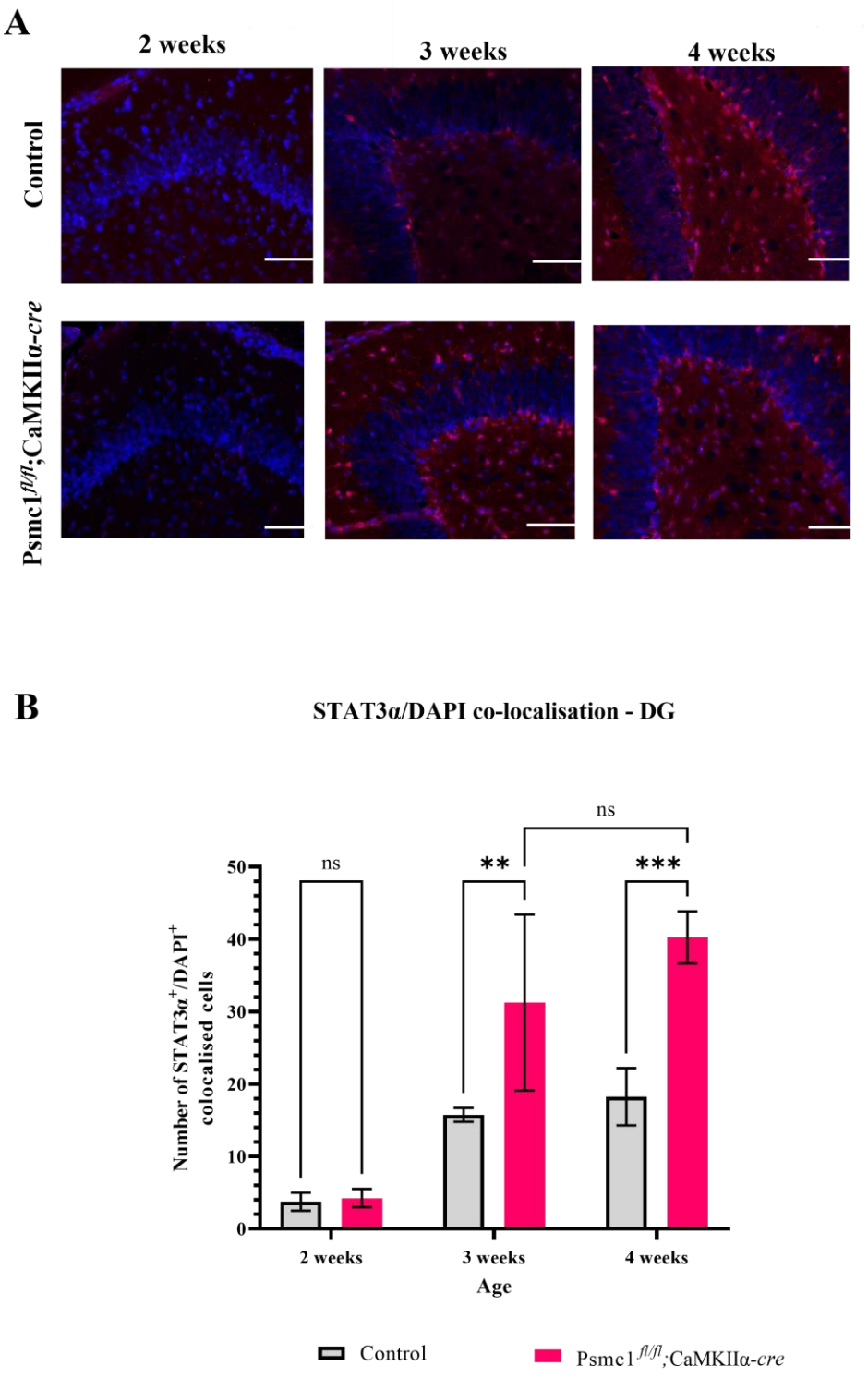

Figure 4.11:The number of STAT3α^{+}/DAPI^{+} colocalised cells is significantly increased in 3 and 4-week Psmc1$^{fl/fl}$;CaMKIIα-*cre* mice in the DG region. 4.11A)20x images of STAT3α (red) and nuclei (blue) in 2,3,4 week Psmc1$^{fl/fl}$;CaMKIIα-*cre* mice and aged-matched control, scale bar: 100µm. 4.11B) Post-hoc Tukeys multiple comparison reported a significant difference between 3 and 4-week-old Psmc1$^{fl/fl}$;CaMKIIα-*cre* mice versus age-matched control (*** =p<0.001), (** =p<0.01).

4.3.5 The number of GFAP$^+$/STAT3α$^+$ cells is increased in Psmc1$^{fl/fl}$;CaMKIIα-cre mice

As STAT3 is a key regulatory of astrogliosis, dual immunofluorescence staining of GFAP and STAT3α was used to assess astrocyte-specific reactivity in the cortex. It must be noted that for GFAP$^+$/STAT3α$^+$ cells to be counted, they must have both a STAT3α positive nucleus and closely associated GFAP labelling.

A two-way ANOVA was performed to analyse the effect of age and genotype on the number of GFAP$^+$/STAT3α$^+$ cells. Four separate two-way ANOVAs were conducted for each region of interest (Cortex, CA1, CA3, DG).

In the cortex, the two-way ANOVA revealed that there was a statistically significant interaction between the effects of age and genotype ($F(2,18=73.93)$, $p=<0.0001$) on the number of GFAP$^+$/STAT3α$^+$ cells. Tukeys multiple comparison analysis reported a significant difference in GFAP$^+$/STAT3α$^+$ positive cells at 3-weeks old (+19, $p < 0.0001$) and 4-weeks old (+20, $p<0.0001$) in Psmc1$^{fl/fl}$;CaMKIIα-*cre* mice vs control mice. There was no significant difference between the number of GFAP$^+$/STAT3α$^+$ positive cells at 3-week and 4-week old Psmc1$^{fl/fl}$;CaMKIIα-*cre* mice (+1, $p>0.05$) (figure 4.12,4.13, 4.14).

In the CA1 region, the two-way ANOVA revealed that there was a statistically significant interaction between the effects of age and genotype ($F(2,18=17.61)$, $p=<0.0001$) on the number of GFAP$^+$/STAT3α$^+$ cells. Tukeys multiple comparison analysis reported a significant difference in GFAP$^+$/STAT3α$^+$ positive cells at 3 weeks-old (+12, $p < 0.0001$) and 4-weeks old (+6, $p <0.01$). There was no significant difference between the number of GFAP$^+$/STAT3α$^+$ positive cells at 3-week and 4-week old Psmc1$^{fl/fl}$;CaMKIIα-*cre* mice (+1, $p>0.05$)(figure 4.15,4.16,4.17).

In the CA3 region, the two-way ANOVA revealed that there was a statistically significant interaction between the effects of age and genotype ($F(2,18=12.79)$, $p=<0.0004$) on the number of GFAP$^+$/STAT3α$^+$ cells. Tukeys multiple comparison analysis reported a significant difference in GFAP$^+$/STAT3α$^+$ positive cells in the CA3 region at 3-weeks old (+10, $p<0.05$) and 4-weeks old (+19, $p<0.001$). There was a significant difference between the number of GFAP$^+$/STAT3α$^+$ positive cells at 3-week and 4-week old Psmc1$^{fl/fl}$;CaMKIIα-*cre* mice (+9, $p<0.05$)(figures 4.18,4.19,4.20).

In the DG region, the two-way ANOVA revealed that there was a statistically significant interaction between the effects of age and genotype ($F(2,18=10.66)$, $p=0.0009$) on the number of $GFAP^+/STAT3\alpha^+$ cells. Tukeys multiple comparison analysis reported a significant difference in the number of $GFAP^+/STAT3\alpha^+$ positive cells at 3 weeks old and 4-weeks old (+19, $p<0.001$) (+25, $p < 0.0001$). There was no significant difference in $GFAP^+/STAT3\alpha^+$ cells between 3-week and 4-week old $Psmc1^{fl/fl}$;CaMKIIα-*cre* mice (+8,$p>0.05$)(figures 4.21,4.22,4.23).

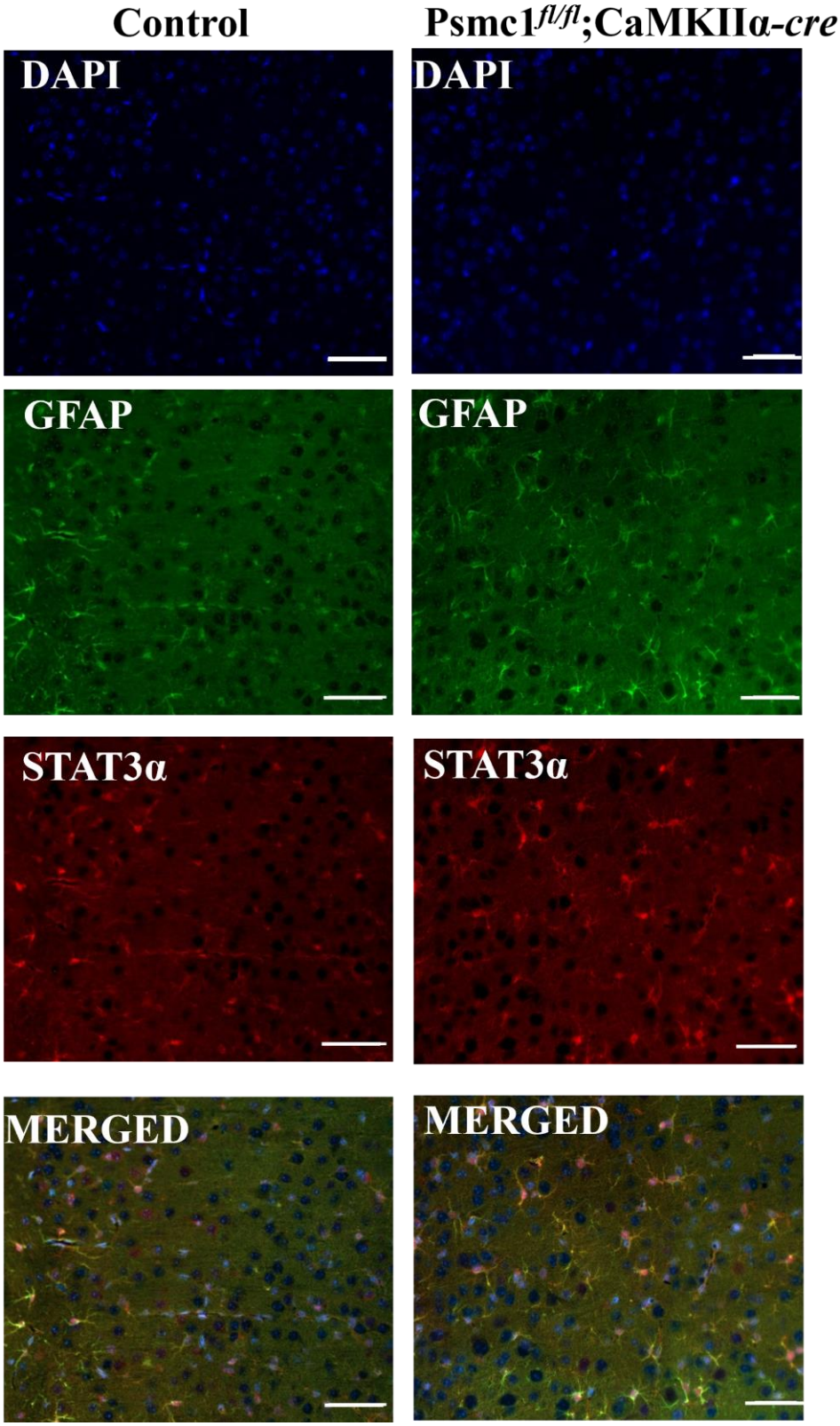

Figure 4.12: DAPI, GFAP and STAT3α staining in the 3-week-old cerebral cortex in control and Psmc1 *fl/fl*;CaMKIIα-*cre* mice. 20x images of DAPI (blue),.GFAP (green) and STAT3α (red) – scale bar: 100 µm.

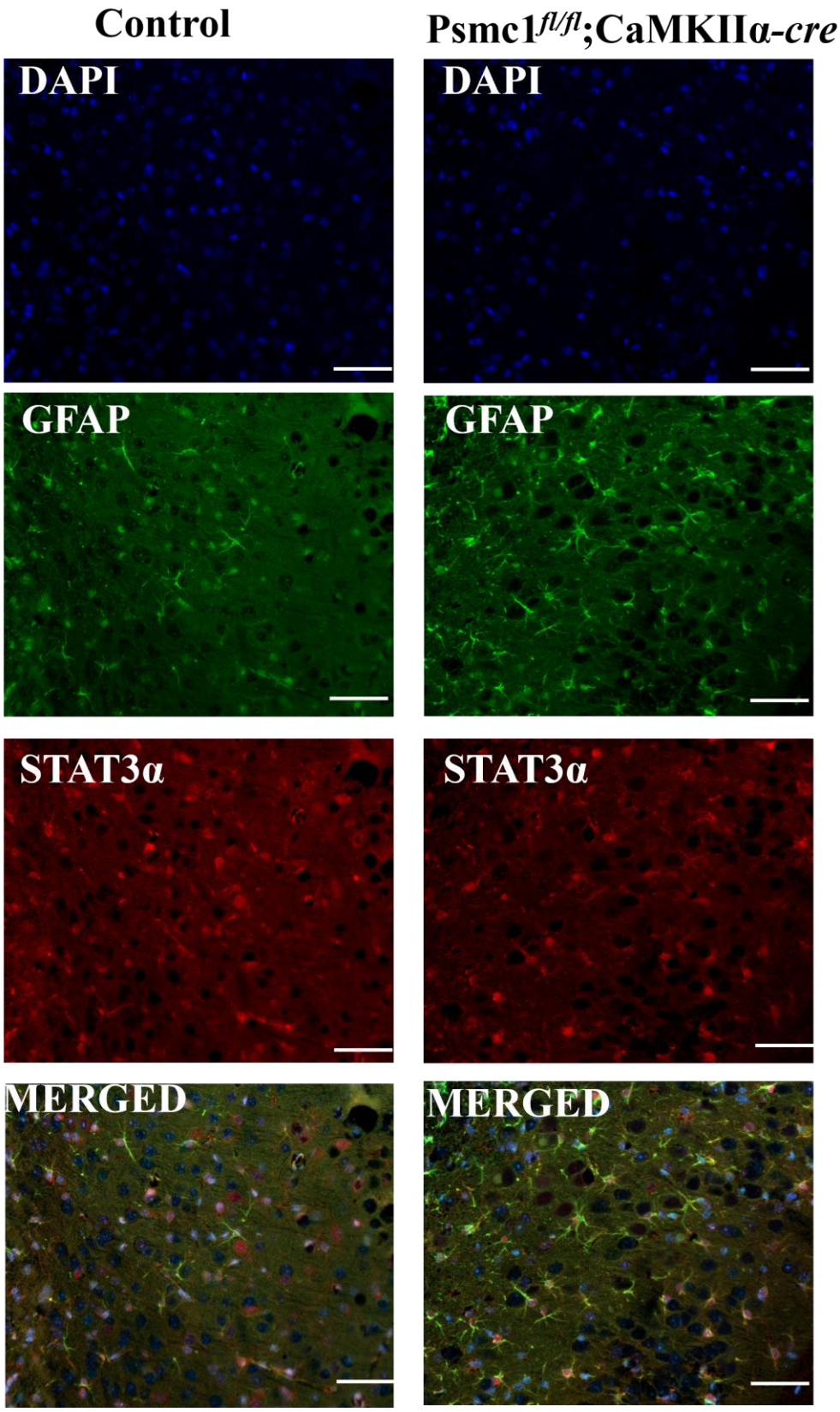

Figure 4.13: DAPI, GFAP and STAT3α staining in the 4-week-old cerebral cortex in control and Psmc1 *fl/fl*;CaMKIIα-*cre* mice. 20x images of DAPI (blue).GFAP (green) and STAT3α (Red) –scale bar: 100 µm.

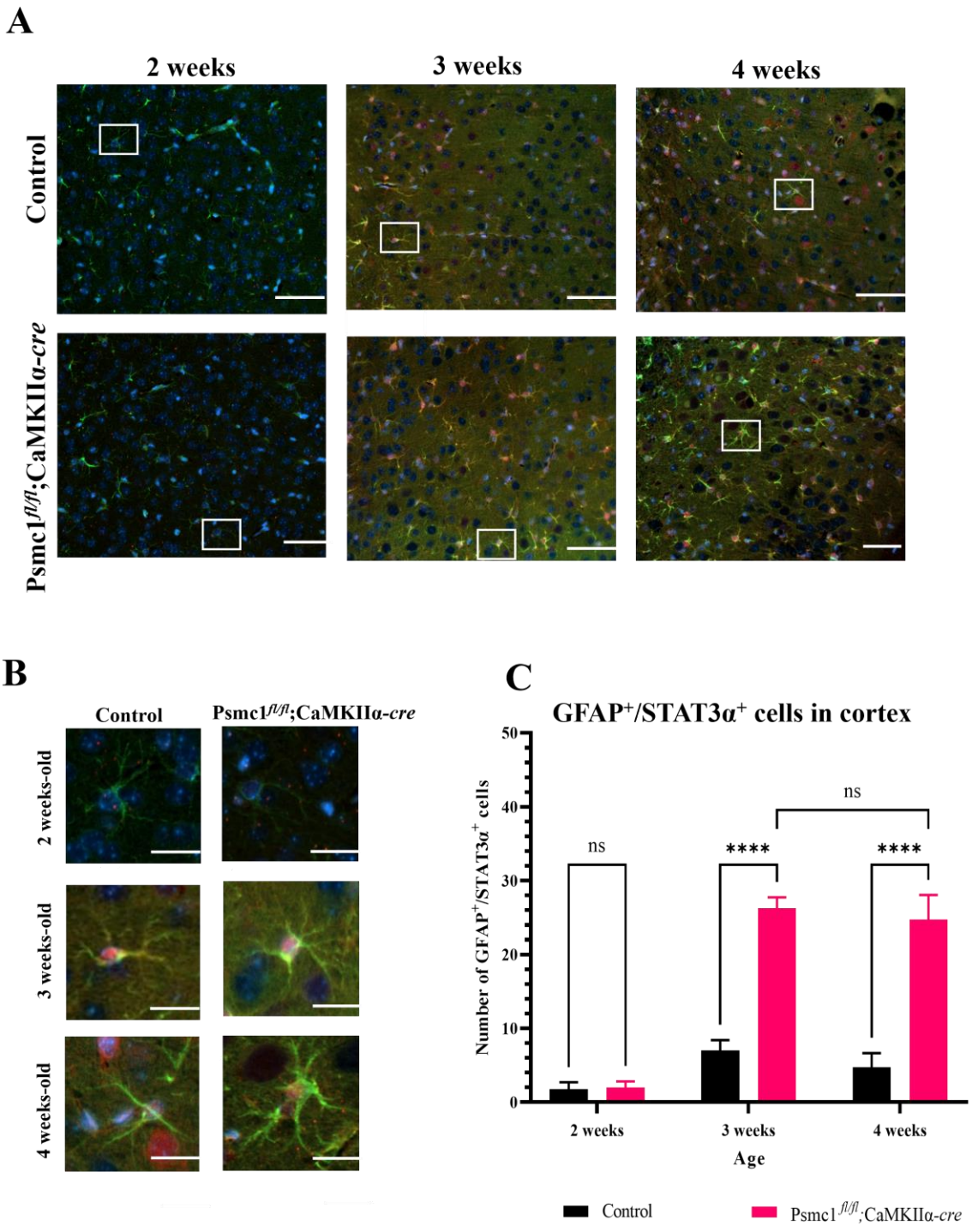

Figure 4.14:GFAP^{+}/STAT3α^{+} cells are significantly increased in 3 and 4-week Psmc1$^{fl/fl}$;CaMKIIα-*cre* mice in the cerebral cortex. 4.14A)20x images of STAT3α, GFAP and DAPI (merged) in 2,3,4 week Psmc1 $^{fl/fl}$;CaMKIIα-*cre* mice and aged-matched control, scale bar: 100 µm. The white box indicates the region of interest (3 x 3) which was used for GFAP area analysis. 4.14B) ROI identified, scale bar: 25 µm. 4.14C) Post-hoc Tukeys multiple comparison reported a significant difference in the number of GFAP^{+}/STAT3α^{+} cells between 3 and 4 weeks Psmc1$^{fl/fl}$;CaMKIIα-*cre* and their aged-matched litter mates (**** P=<0.0001).

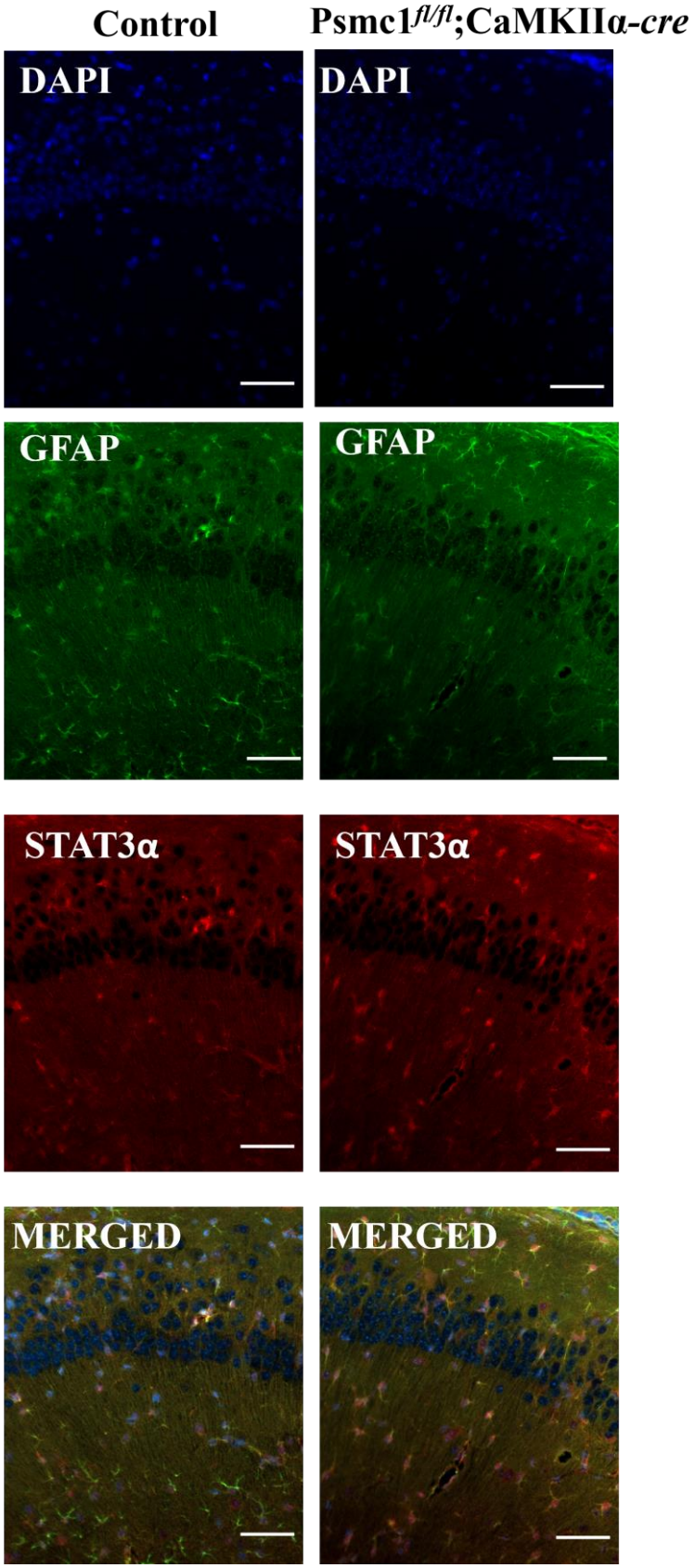

Figure 4.15:DAPI, GFAP and STAT3α staining in the 3-week-old CA1 region in control and Psmc1 *fl/fl*;CaMKIIα-*cre* mice. 20x images of DAPI (blue), GFAP (green) and STAT3α (red) –scale bar: 100µm.

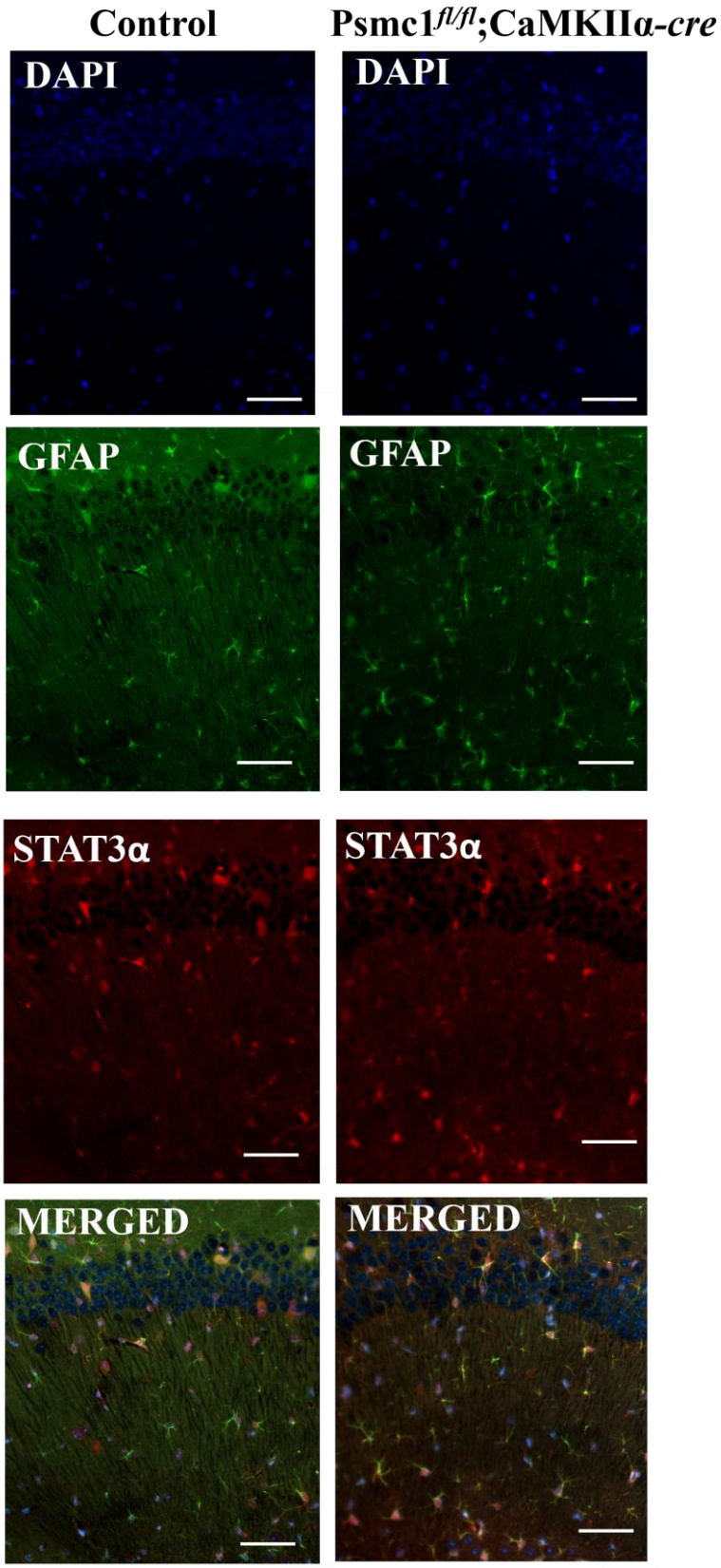

Figure 4.16:DAPI, GFAP and STAT3α staining in the 4-week-old CA1 region in control and Psmc1 *fl/fl*;CaMKIIα-*cre* mice. 20x images of DAPI (blue).GFAP (green) and STAT3α (red) –scale bar: 100 µm.

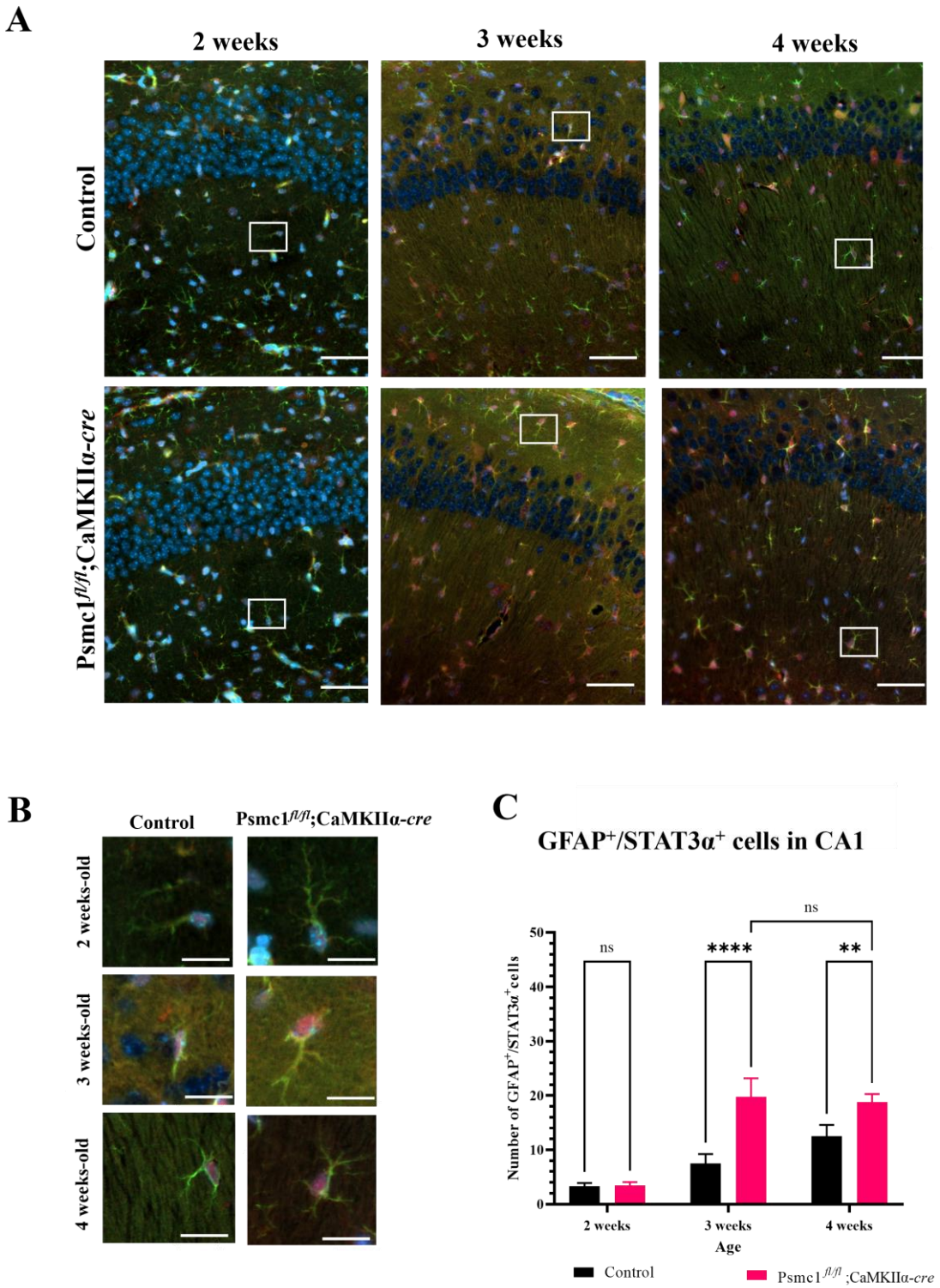

Figure 4.17:GFAP$^+$/STAT3α$^+$ cells are significantly increased in 3 and 4-week Psmc1$^{fl/fl}$;CaMKIIα-*cre* mice in the CA1 region. 4.17A)20 x images of STAT3α, GFAP and DAPI (merged) in 2,3,4 week Psmc1 $^{fl/fl}$;CaMKIIα-*cre* mice and aged-matched control, scale bar: 100µm. The white box indicates the region of interest (3 x 3) which was used for GFAP area analysis. 4.17B) ROI identified, scale bar 25 µm. 4.17C) Post-hoc Tukeys multiple comparison reported a significant difference in the number of GFAP$^+$/STAT3α$^+$ cells between 3 and 4 week Psmc1 $^{fl/fl}$;CaMKIIα-*cre* mice and their age-matched litter mates (****p =<0.0001, *** p = <0.001).

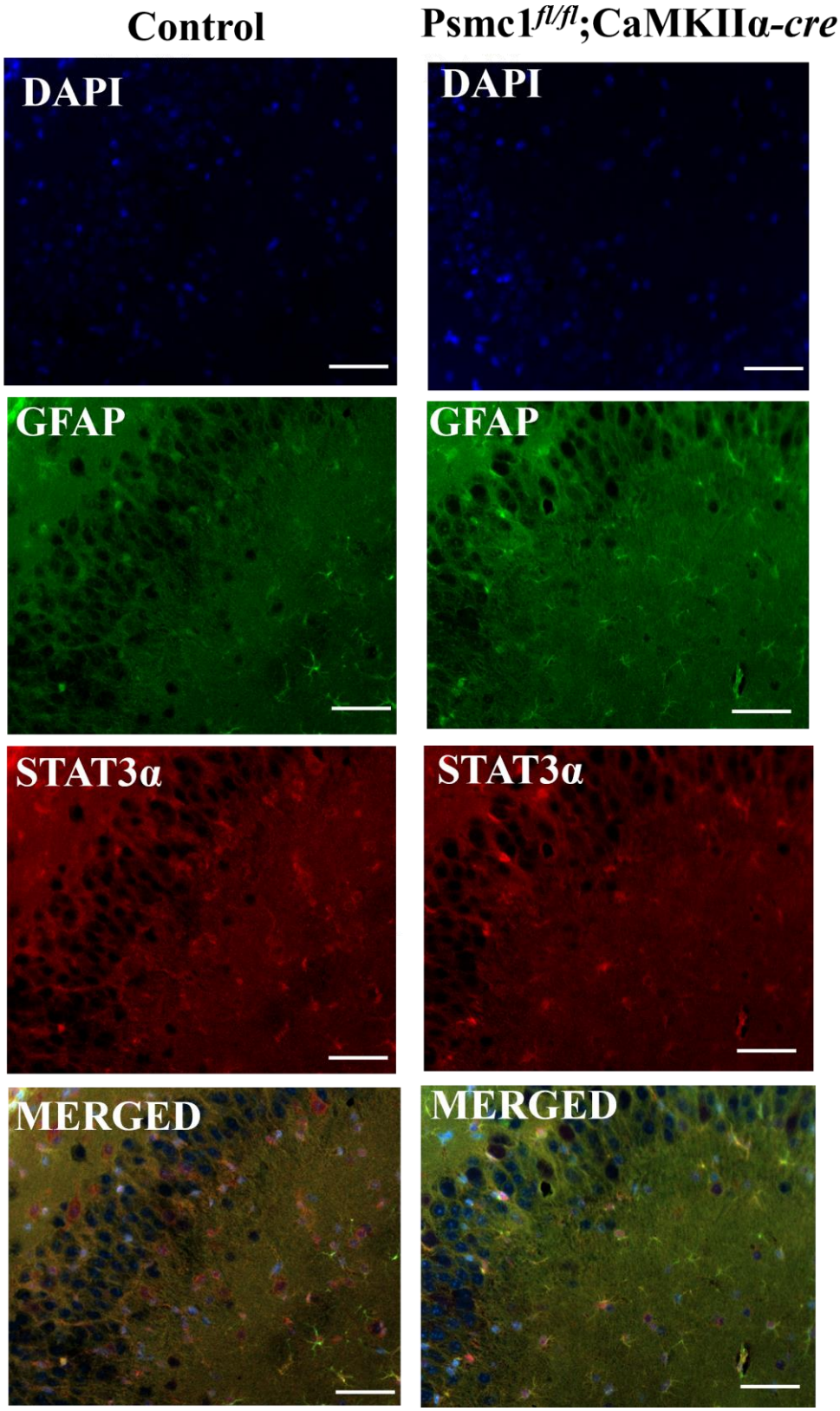

Figure 4.18:DAPI, GFAP and STAT3α staining in the 3-week-old CA3 region in control and Psmc1 *fl/fl*;CaMKIIα-*cre* mice. 20x images of DAPI (blue),GFAP (green) and STAT3α (red) –scale bar: 100 µm

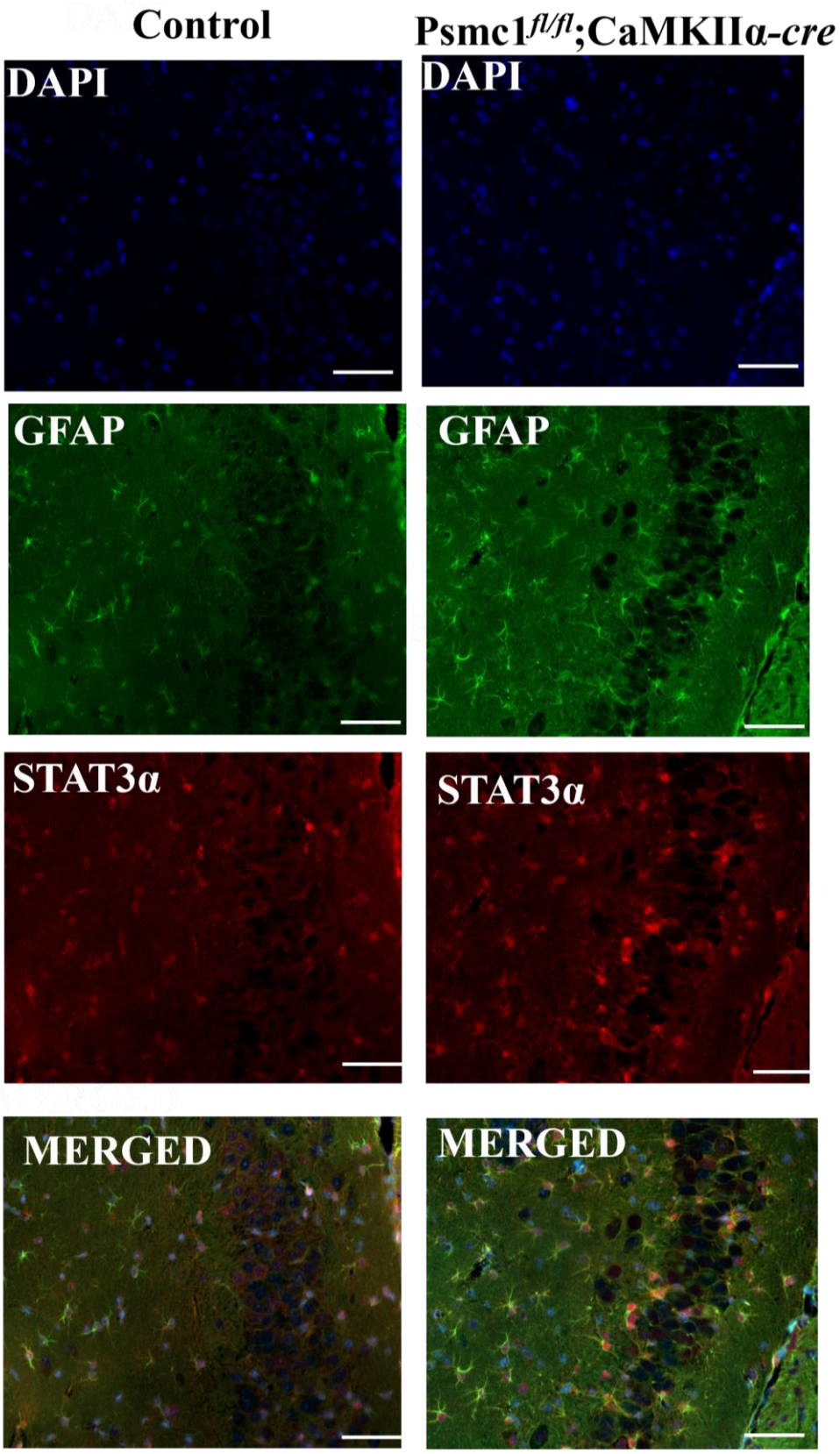

Figure 4.19:DAPI, GFAP and STAT3α staining in 4-week-old in the CA3 region in control and Psmc1 *fl/fl*;CaMKIIα-*cre* mice. 20x images of DAPI (blue), GFAP (green) and STAT3α (red) – scale bar: 100 µm

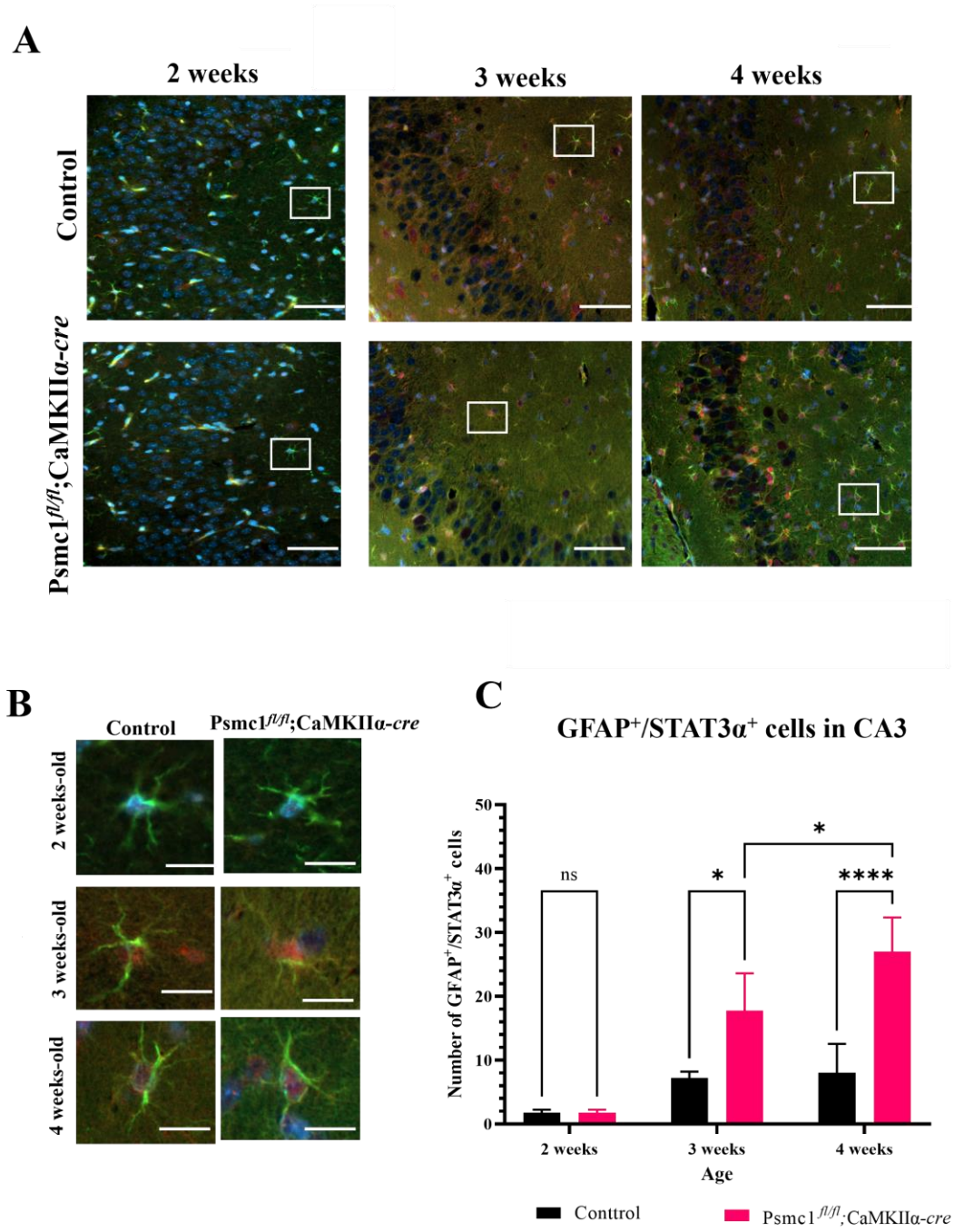

Figure 4.20:GFAP$^+$/STAT3α$^+$ cells are significantly increased in 3 and 4-week Psmc1$^{fl/fl}$;CaMKIIα-*cre* mice in the CA3 region. 4.20A)20 x images of STAT3α, GFAP and DAPI (merged) in 2,3,4 week Psmc1$^{fl/fl}$;CaMKIIα-*cre* mice and aged-matched control, scale bar: 100µm. The white box indicates the region of interest (3 x 3) which was used for GFAP area analysis. 4.20B) ROI identified, scale bar 25 µm. 4.20C) Post-hoc Tukeys multiple comparison T reported a significant difference in the number of GFAP$^+$/STAT3α$^+$ cells between 3 and 4 week Psmc1 $^{fl/fl}$;CaMKIIα-*cre* mice and their age-matched littermates (****p =<0.0001, *** p = <0.001) and a significant increase from 3 to 4 weeks old ($p<0.05$).

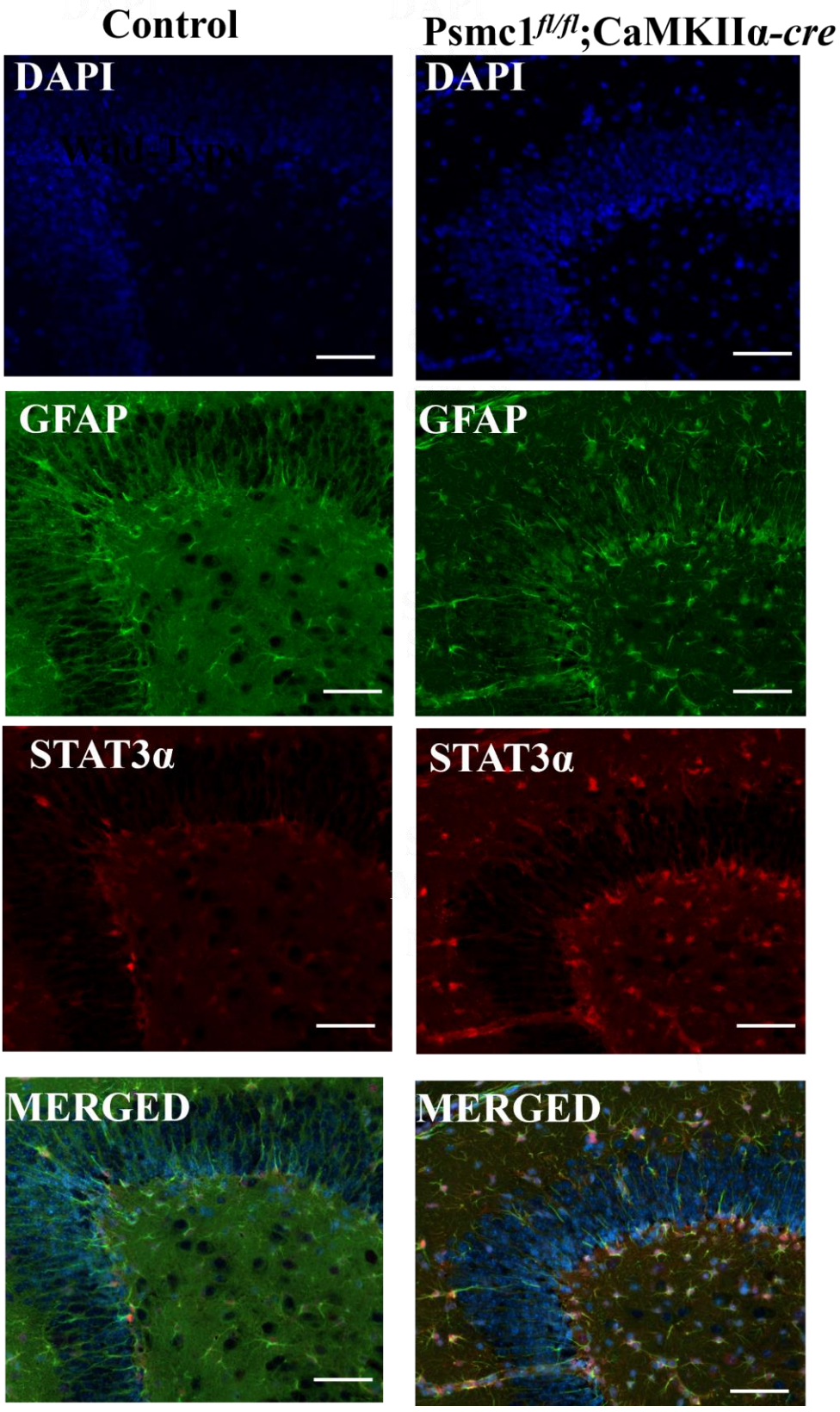

Figure 4. 21: DAPI, GFAP and STAT3α staining in 3-week-old DG region in control and Psmc1 $^{fl/fl}$; CaMKIIα-*cre* mice. 20x images of DAPI (blue).GFAP (green) and STAT3α (red) –scale bar: 100µm.

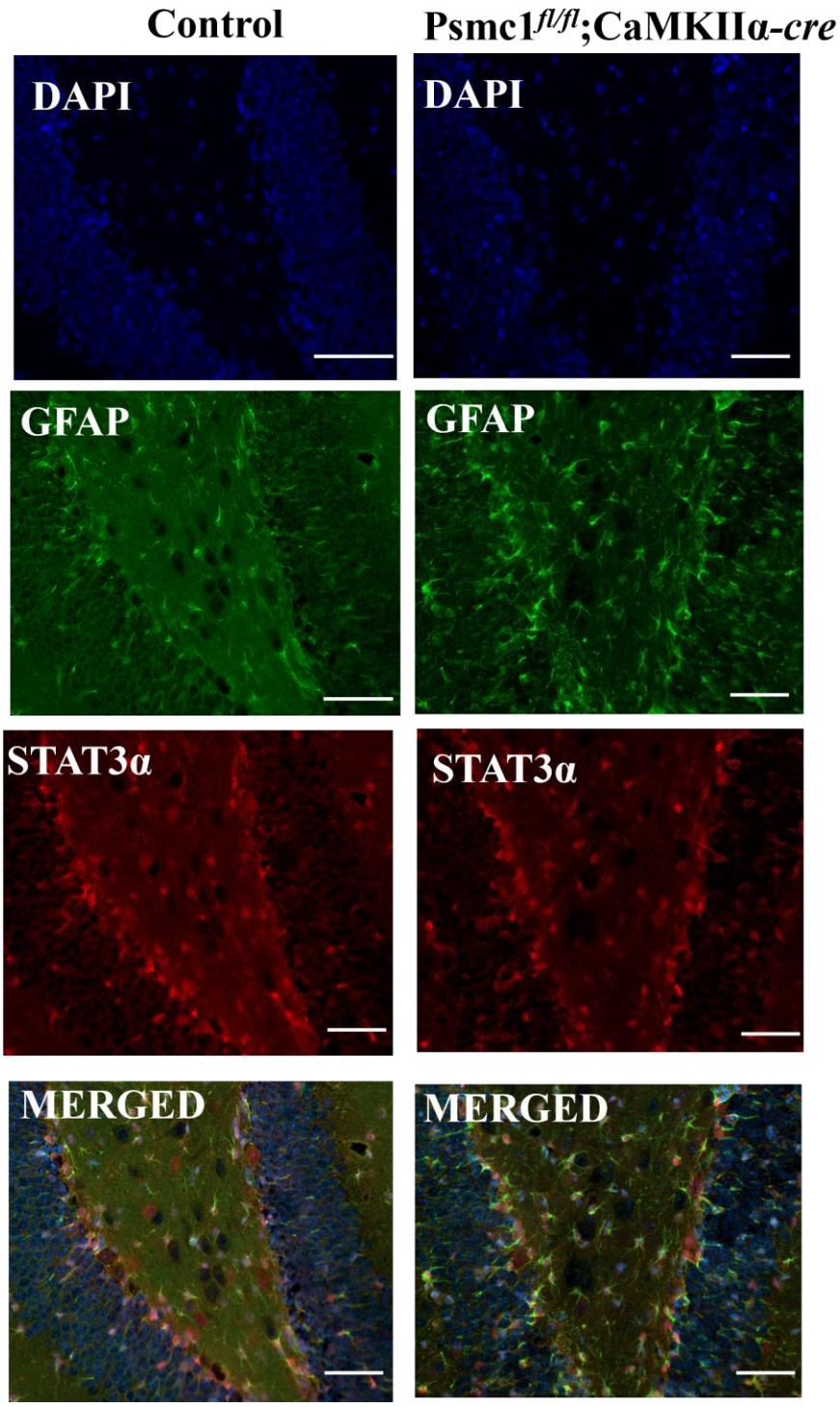

Figure 4. 22:DAPI, GFAP and STAT3α staining in 4-week old DG region in control and Psmc1 *fl/fl*;CaMKIIα-*cre* mice. 20x images of DAPI (blue),GFAP (green) and STAT3α (red) –scale bar:100µm

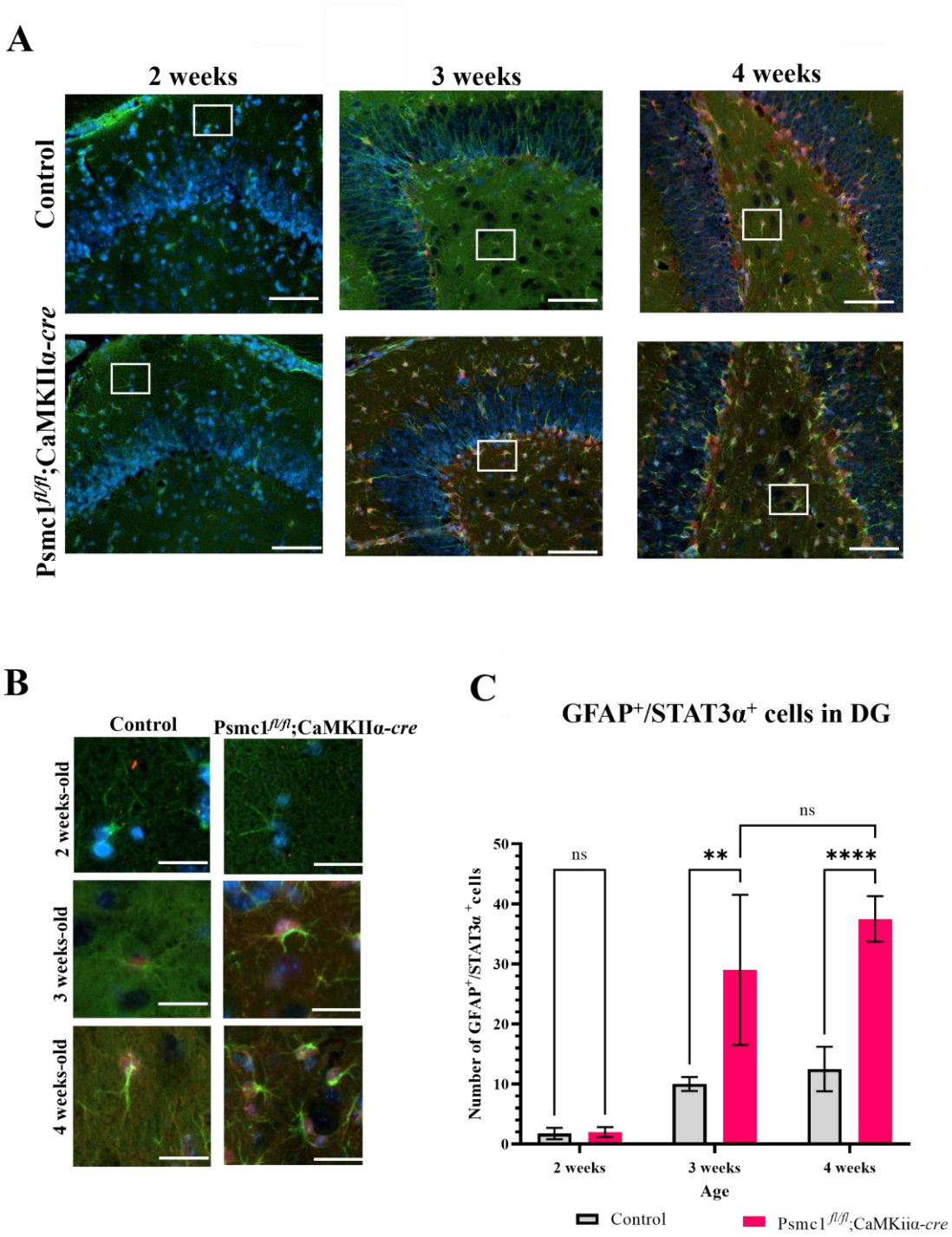

Figure 4.23:GFAP$^+$/STAT3α^+ cells are significantly increased in 3 and 4-week Psmc1$^{fl/fl}$;CaMKIIα-*cre* mice in the DG region. 4.23A)20 x images of STAT3α, GFAP and DAPI (merged) in 2,3,4 week Psmc1$^{fl/fl}$;CaMKIIα-*cre* mice and aged-matched control, scale bar: 100µm. The white box indicates the region of interest (3 x 3) which was used for GFAP area analysis. 4.23B) ROI identified, scale bar 25 µm. 4.23C) Post-hoc Tukeys multiple comparison reported a significant difference in the number of GFAP$^+$/STAT3α$^+$ cells between 3 and 4 week Psmc1 $^{fl/fl}$;CaMKIIα-*cre* mice and their age-matched litter mates (****p =<0.0001, ** p = <0.01).

4.3.6 Astrocytic-STAT3 is significantly increased in the CA3 and DG in 3- and 4-week old Psmc1 $^{fl/fl}$;CaMKIIα-cre mice

ROI images featuring GFAP^{+}/STAT3α^{+} cells were used to investigate the Astrocytic-STAT3α area as a measure of the total STAT3 positive astrocytic compartment in the different regions.

Images channels were split into DAPI, FITC and TRITC then the TRITC channel (STAT3α) was thresholded to create a binary image. The selection tool was used to select astrocytes which were then measured to identify the area of astrocytic-STAT3.

A two-way ANOVA was performed to analyse the effect of age and genotype on the number of Astrocytic-STAT3 area. Four separate two-way ANOVAs were conducted for each region of interest (Cortex, CA1, CA3, DG).

In the cortex, the two-way ANOVA revealed that there was no statistically significant interaction between the effects of age and genotype ($F(2,18=1.357)$, $p=0.2826$) of Astrocytic-STAT3 area. Tukeys multiple comparison analysis reported a non-significant difference at 2 weeks (3.9 vs 4.5, $P > 0.05$), 3 weeks (9.4 vs 16.3 $P > 0.05$) or 4 weeks (14.53 vs 16.49 $P > 0.05$) in the cerebral cortex (figure 4.24A). There is no significant difference in Astrocytic-STAT3 area between 3 and 4 week Psmc1$^{fl/fl}$;CaMKIIα-*cre* mice (-0.18, $p>0.05$) (figure 4.24A).

In the CA1 region, the two-way ANOVA revealed that there was no statistically significant interaction between the effects of age and genotype ($F(2,18=2.811)$, $p=0.086$) of Astrocytic-STAT3 area. Tukeys multiple comparison analysis reported a non-significant difference at 2 weeks (4.02 vs 3.53, $P > 0.05$), 3 weeks (5.69 vs 13.04, $p > 0.05$) or 4 weeks (7.16 vs 12.33, $p > 0.05$). There is no significant difference in Astrocytic-STAT3 area between 3 and 4 week Psmc1$^{fl/fl}$;CaMKIIα-*cre* mice (-0.71, $p>0.05$) (figure 4.24B).

In the CA3 region, the two-way ANOVA revealed that there was a statistically significant interaction between the effects of age and genotype ($F(2,18=5.456)$, $p=0.0140$) of Astrocytic-STAT3 area. Tukeys multiple comparison analysis reported a significant difference in the astrocytic -STAT3 area in the CA3 region at 3 weeks (6.6 vs 16.31, $p<0.001$) and 4 weeks (5.8 vs 12.6, $p <0.5$). There is no significant difference in Astrocytic-STAT3 area between 3 and 4 week Psmc1$^{fl/fl}$;CaMKIIα-*cre* mice (3.75, $p>0.05$) (figure 4.24C).

In the DG region, the two-way ANOVA revealed that there was a statistically significant interaction between the effects of age and genotype (F (2,18=14.77), p = 0.0002) of Astrocytic-STAT3 area. Tukeys multiple comparison analysis reported a significant difference significant increase in astrocytic-STAT3 in the DG area at 3-weeks old (7.17 vs 19.40, p <0.0001) and 4-week old (5.19 vs 15.98, p <0.001. There is no significant difference in Astrocytic-STAT3 area between 3 and 4 week Psmc1$^{fl/fl}$;CaMKIIα-*cre* mice (3.42, p>0.05) (figure 4.24D).

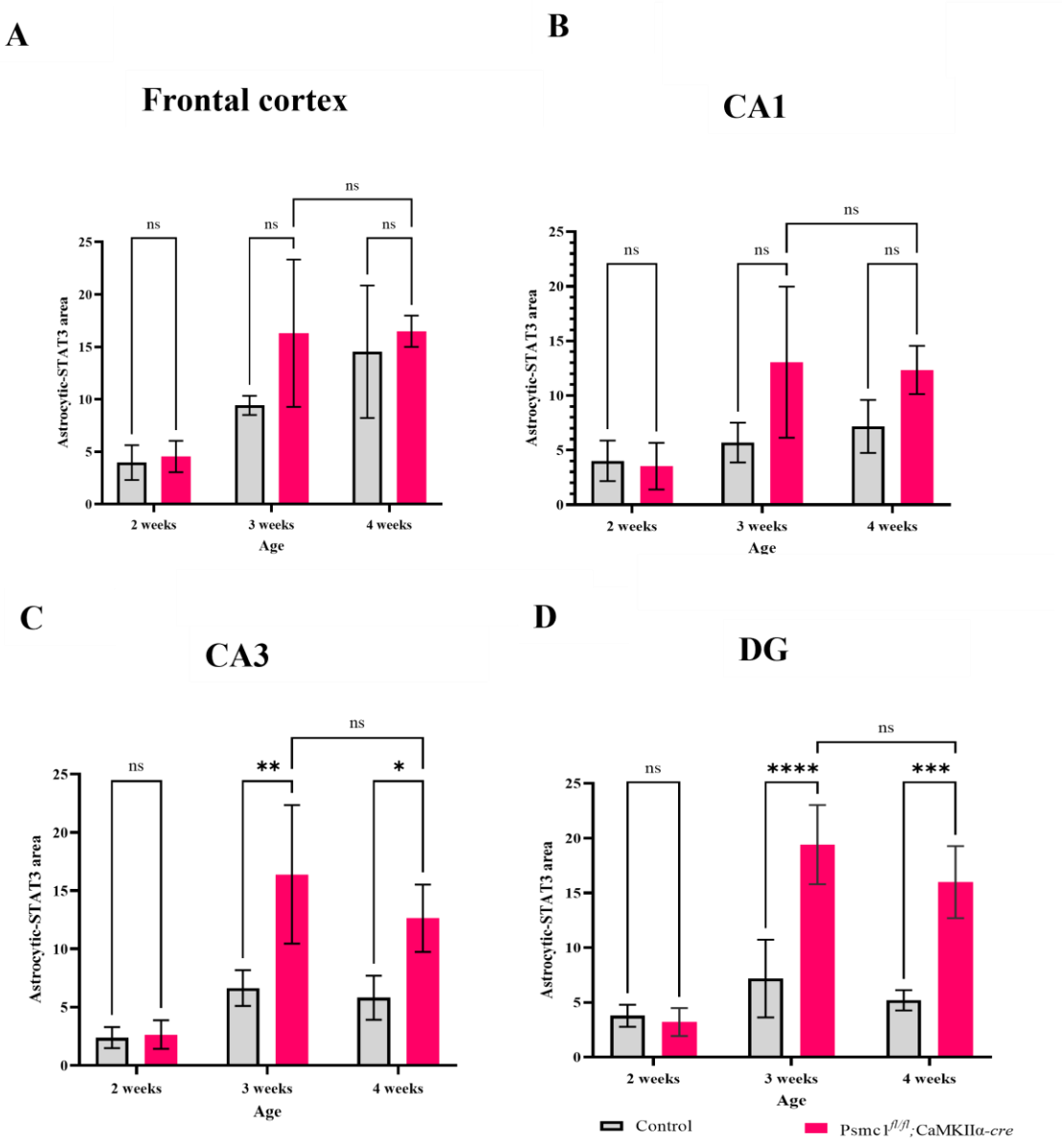

Figure 4.24:Astrocytic-STAT3 area is significantly increased the CA3 and DG region in 3 and 4-week Psmc1$^{fl/fl}$;CaMKIIα-*cre* mice versus age-matched litter mates. 4.24A) Cerebral cortex, 4.24B) CA1 region, 4.24C) CA3 region, 4.24D) DG region Significance details post-hoc tukey test results (**** =P<0.0001 ,**=P<0.01,*=P<0.05).

4.4 Discussion

Protein expression profiling using SWATH-MS in Psmc1$^{fl/fl}$;CaMKIIα-*cre* mice highlighted GFAP, a major intermediate filament protein in astrocytes, to be consistently upregulated in line with disease progression. This chapter aimed to further validate this marker, using western blot and immunofluorescence techniques to identify protein upregulation and map its location in the Psmc1$^{fl/fl}$;CaMKIIα-*cre* cortex. We found that GFAP expression in astrocytes increases with disease progression and correlates with STAT3 and phosphorylated-STAT3 expression and localisation in astrocytes. This provides evidence that astrocyte reactivity is associated with JAK/STAT3 activation in this mouse model.

Western blot results supported SWATH-MS data, reporting no significant fold change at two weeks before the loss of Psmc1, but a significant fold change of at 3 weeks old, increasing to 2.18 at 4 weeks old compared to age-matched control littermates. Through western blot, it is also visible that unique additional bands were detected in the Psmc1$^{fl/fl}$;CaMKIIα-*cre* mice at 3 and 4 weeks old. Speculatively, it can be attributed that these bands represent differential GFAP isoforms. To date, 6 different GFAP isoforms are shared between the mice and the human nervous system (GFAP α, β, δ, ζ, κ, Δ exon 7), which are detectable with the GFAP antibody used in this study (Meli et al., 2014; Yang et al., 2017). In support of this, Alzheimer's and Parkinson's disease models show an increase in GFAP isoforms associated with chronic pathology (Clairembault et al., 2014; Hol & Pekny, 2015; Kamphuis et al., 2012; Sullivan, 2014). However, these isoform roles in their contribution to neuroinflammation remain elusive.

After confirmation of GFAP upregulation via western blot, we decided to assess STAT3 levels via western blot also. Western blots probing for STAT3α in Psmc1$^{fl/fl}$;CaMKIIα-*cre* mice demonstrated no significant fold change at two weeks,to a significant fold change at 3 weeks old, further increasing at 4 weeks old compared to age-matched control littermates. In line with this, detection of phosphorylated STAT3 tyrosine 705 showed a significant fold change at 3 weeks and at 4 weeks old in Psmc1$^{fl/fl}$;CaMKIIα-*cre* mice compared to age-matched control littermates. This upregulation in STAT3α coincides with a significant increase in STAT3 Tyrosine 705 phosphorylation. This phenomenon is supported by literature in the field which reports that STAT3 undergoes a positive autoregulatory loop, where STAT3 tyrosine 705 binds to the promoter of STAT3α, therefore leading to an overall increase in protein expression (Ichiba et al., 1998; He et al., 2005).

To assess if astrocytes were the source of JAK/STAT signaling, immunofluorescence labelling of STAT3 Tyrosine 705 on paraffin-embedded slices was attempted. However, the use of this was unsuccessful, displaying no specific staining. It is noted in the literature that detection of phosphorylated-STAT3 is difficult in paraffin-embedded slices due to low levels and reduction of epitope availability due to fixation methods (Mueller et al., 2011). In addition to this, a comparative study performed by O' Callaghan and Sriram reported traditional methods of culling, such decapitation, reduced the preservation of the phosphorylation states of proteins (O'Callaghan and Sriram, 2004). Therefore, an alternative approach was needed. It was decided to use STAT3α colocalization with DAPI as a marker of STAT3-phosphorylation, as used and published by other groups (Haim et al., 2015).

Firstly, we assessed if there were any significant changes in the number of STAT3α+/DAPI+ cells compared to age-matched control mice. The cerebral cortex and dentate gyrus showed a significant increase compared to control at both 3 and 4 weeks of age. The CA3 region showed no significant increase at 3 weeks old but reached significance at 4 weeks old. These results support that there is an increase in STAT3 phosphorylation associated with an increase in disease pathology. However, the CA1 region showed a significant increase at 3 weeks old but failed to reach significance at 4 weeks. One reason for this may be that STAT3 expression in the brain increases at P28, therefore masking potential disease related STAT3 changes (Sadok et al., 2021).

To clarify these findings, we dual-stained for $GFAP^{+}/STAT3\alpha^{+}$ cells and reported that all regions examined across all weeks reported a significant increase in the number of $GFAP^{+}/STAT3\alpha^{+}$ cells compared to the age-matched control. A two-way ANOVA reported that there was a significant increase in the number of $GFAP^{+}/STAT3\alpha^{+}$ in the CA3 region between 3-week and 4-week-old $Psmc1^{fl/fl}$;CaMKIIα-*cre* mice (+9, $p<0.05$).

As STAT3 has been linked with neurite outgrowth in neurons, and as neuroinflammation is associated with a reduction in healthy neuronal physiology, a decline in $STAT3\alpha^{+}./DAPI^{+}$ only cells could be attributed to the effects of reactive gliosis (Park, Nozell and Benveniste, 2012; Leibinger et al., 2013; Su et al., 2020).Neuronal STAT3 inhibition has been cited in neurodegenerative disease models, citing intracellular crowding of aggregate prone proteins in neurons as a cause of neuronal death (He et al., 2020; Hong et al., 2020; Zhang et al., 2021).

This hypothesis would need to be confirmed with further studies, such as dual staining of neurons (e.g. with MAP2) and STAT3α. In addition to this, mitochondrial dysfunction has been cited at 3 weeks old in this model, which has a strong relation to STAT3. It is possible to speculate that STAT3 dysfunction in neurons may have a role in activating JAK/STAT signaling in astrocytes.

We then decided to undertake an analysis of the GFAP area in hippocampal regions and the cerebral cortex. We used the GFAP area as a measure of astrocyte hypertrophy, thereby indicating reactivity. At 3-weeks of age, GFAP area reported a significant increase in the cerebral cortex (+8% ,$p < 0.01$), CA3 region (+12%, $p < 0.01$) and Dentate Gyrus (+18%, $p < 0.0001$), however not in the CA1 region (+2%, $p > 0.5$). At 4-weeks of age, all areas demonstrated a significant increase in GFAP area, cerebral cortex (+9%, $p<0.01$), CA3 (+28%, $p < 0.0001$), CA1 (+11%, $p < 0.01$) and DG (+28%, $p < 0.0001$).

Two-way ANOVA also demonstrated a significant increase in astrocyte hypertrophy in the cerebral cortex and CA3 between 3 and 4 week Psmc1$^{fl/fl}$;CaMKIIα-*cre* mice, but not in the dentate gyrus and the CA1 region. This data suggests that astrocyte reactivity in this model is a heterogeneous phenomenon, potentially attributed to the localisation of CaMKIIα neurons. What is of most interest, is that although hypertrophy in the CA1 region did not significantly increase at 3 weeks old, the number of GFAP$^+$/STAT3α$^+$ cells significantly increased. As CA1 hypertrophy is increased at 4 weeks old, this previous increase in the number of GFAP$^+$/STAT3α$^+$ cells supports the notion that STAT3 drives GFAP hypertrophy as it precedes GFAP hypertrophy, therefore potentially offering therapeutic avenues that have already been used in previous neurodegenerative disease models (Abjean et al., 2022; Ceyzériat et al., 2016; Guillemaud et al., 2020).For future work, the use of a STAT3 antibody in chromatin immunoprecipitation would validate this notion.

The astrocytic-STAT3 area was also investigated by measuring the area of STAT3 localised in Astrocytes, marked by the GFAP area. Astrocytic-STAT3 area showed a significant increase in 3-week and 4-week old Psmc1$^{fl/fl}$;CaMKIIα-*cre* mice compared to age-matched littermates, showing statistical significance in the CA3 and DG regions (3 weeks, 4 weeks). An increase in STAT3 protein via western blot, followed by detected phosphorylated-STAT3 tyrosine, an increase in the GFAP$^+$/STAT3α$^+$ positive cells as well as an increase in astrocytic-STAT3 area

strongly supports STAT3 positive autoregulatory loop, driving reactive gliosis (Ichiba et al., 1998; Narimatsu et al., 2001; Tyzack et al., 2014).

Overall, there are many limitations to this work. Although STAT3 colocalization with nuclei is used by other groups, this does not indicate what type of STAT3 phosphorylation is undertaken in the astrocyte. It must also be noted that other groups expressed their results as 'high expressing' STAT3 astrocytes versus 'low expressing' STAT3 astrocytes, a differentiation which was not made in this model. To truly understand if STAT3 is responsible for driving astrogliosis, an *in-vivo* intervention experiment should be conducted, where expression and phosphorylation of STAT3 are regulated exogenously, through stereotactic injections of viral vectors specific for transgene expression in astrocytes which are specific for JAK2 or STAT-induced inhibitor, SOCS3 (Ceyzériat, ben Haim, Denizot, Pommier, Matos, Guillemaud, M.-A. Palomares, et al., 2018).

Despite this, there is good evidence for the role of the JAK/STAT3 pathway in the cellular response to proteasome loss in the Psmc1$^{fl/fl}$;CaMKIIα-*cre* model. As a possible link between proteostasis and STAT3, transcriptomic analysis of acutely sorted astrocytes from Huntington disease mice shows that JAK/STAT3 astrocyte signaling is associated with an increase in UPS and lysosomal degradation proteins, thereby indicating a phagocytosis role for astrocytes in neurodegeneration (Abjean et al., 2022). As this model is a disruption of neuronal proteolysis, this is a key hypothesis that could be utilised for further testing.

4.5 Conclusions and further work

In conclusion, this data chapter provides evidence of an increase in GFAP hypertrophy that is coupled with STAT3-signaling. We demonstrate a significant increase in the number of GFAP$^+$/STAT3α$^+$ cells, alongside a significant fold change in total STAT3 and STAT3-phosphorylated Tyrosine 705, indicating a positive-feedback loop of reactive gliosis. The next chapter serves to investigate the initiator of STAT3-driven astrogliosis.

Chapter 5 Pharmacological treatment of acute slices to investigate initiators of STAT3 reactivity in astrocytes

5.1 Introduction

5.1.1 Initiators of STAT3 reactivity in astrocytes

The last two chapters of this thesis showed a clear signaling pathway in the response to 26S proteasome depleted neurons. Firstly, we identified an upregulation in GFAP, a major cytoskeletal protein in astrocytes which was correlated with a downregulation in neuronal structure and projection across disease progression. Secondly, immunofluorescence staining and western blot analysis confirmed this upregulation. Thirdly, we found that total astrocytic-STAT3 was rapidly upregulated from 3 weeks of age in the hippocampus of Psmc1 $^{fl/fl}$;CaMKIIα-*cre* mice and this was confirmed by the increase in phosphorylated- STAT3 tyrosine 705 levels in the whole brain.

This current collection of results indicates that astrocytes can detect and respond to some cue in the brain of Psmc1 deficient mice, thereby leading to STAT3 activation prior to intraneuronal inclusion formation. It is therefore important to identify the molecular initiator of this signaling pathway, to better understand what is triggering the early gliosis response that precedes neurodegenerative pathology.

One major feasible molecular mechanism is the direct release of proinflammatory cytokines, CXCL10, TNF-α and IL-6, all of which have been cited to be released from proteotoxic neurons (Fattori et al., 1995; Israelsson et al., 2010) (figure 5.1a). However, it has been previously reported that 3-week-old Psmc1$^{fl/fl}$;CaMKIIα-*cre* mice exhibit paranuclear accumulation of mitochondria, alongside an increase in Cytochrome oxidase IV and Parkin protein (Elkharaz et al., 2013; Ugun-Klusek et al., 2017). Given this background, mitochondrial damage in response to 26S proteasome depletion is a reasonable hypothesis for an initiator of gliosis, especially as mitochondrial DAMPS, such as ADP and ATP, have been shown to cause STAT3-phosphorylation in astrocytes(figure 5.1b). These ligands have been shown to interact with astrocyte-specific receptors, as outlined in figure 1.5c (Breder et al., 1993; Washburn and Neary, 2006; Vinet et al., 2010; Gandelman et al., 2010; Probert, 2015; Liu et al., 2018; Ali, Biswas and Pal, 2019; Zhou et al., 2019; Davidson et al., 2022).

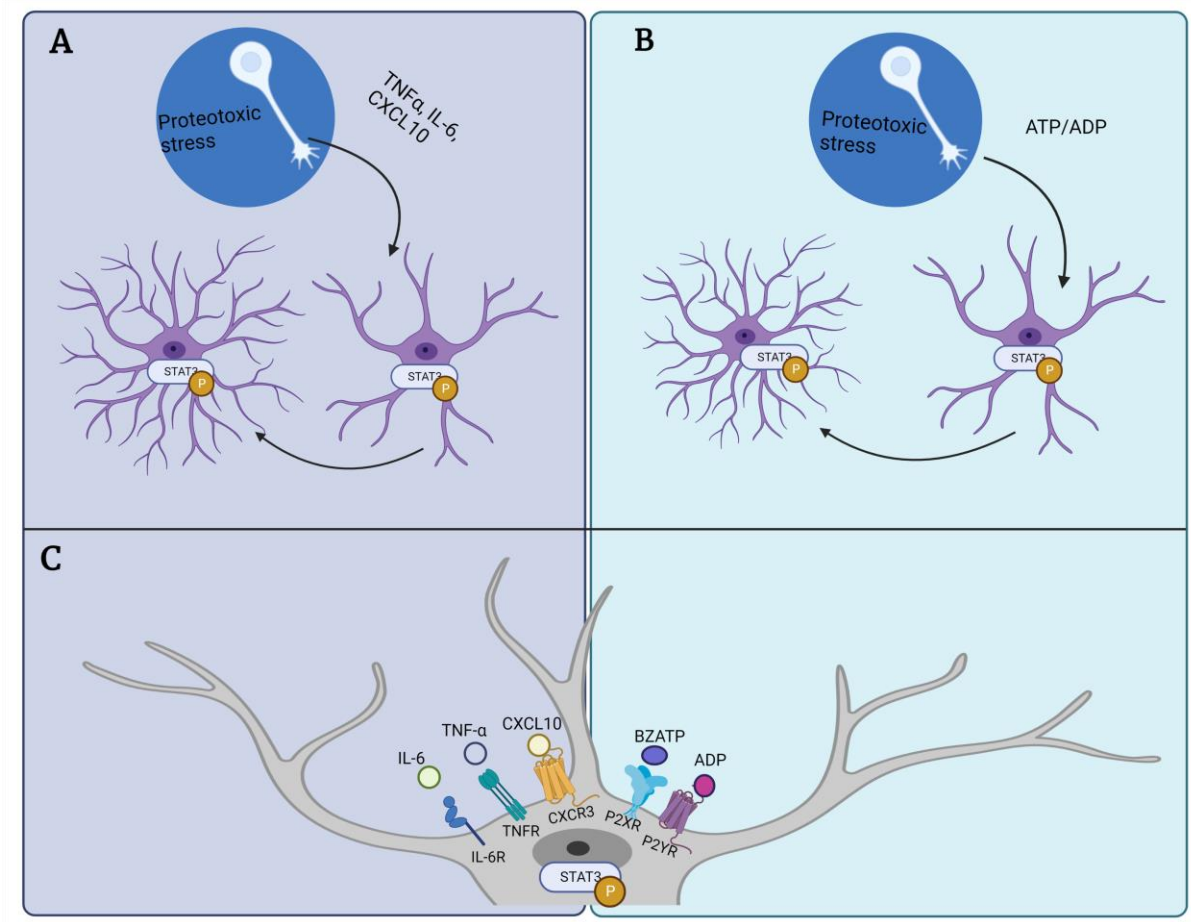

Figure 5.1:Hypothesized initiators of STAT3 Tyrosine 705 phosphorylation from Psmc1 $^{fl/fl}$;CaMKIIα-*cre* neurons. 5.1A) The release of proinflammatory cytokines can activate Astrocytic STAT3 tyrosine 705 phosphorylation, leading to increased hypertrophy. 5.1B) The release of DAMPS can activate Astrocytic-STAT3 tyrosine 705. 5.1C) A schematic diagram of potential receptor-ligand interaction in astrocytes. Abbreviations: Interleukin-6 (IL-6), Interleukin-6 Receptor (IL-6R), Tumour Necrosis Factor Alpha (TNF-α), Tumour Necrosis Factor Receptor (TNFR), C-X-C motif chemokine ligand 10 (CXCL10), C-X-C motif chemokine receptor 3, (CXCR3), 2′(3′)-O-(4-Benzoylbenzoyl)adenosine 5′-triphosphate (BZATP), P2X receptor (P2XR), Adenosine Diphosphate(ADP), P2Y receptor (P2YR) *Image made with biorender.com*

5.1.2 Aims of this chapter

This chapter aims to identify which of these potential upstream signaling networks could be contributing to STAT3 activation in astrocytes, and so may account for the early-stage gliosis observed at 3-week Psmc1$^{fl/fl}$;CaMKIIα-*cre* mice.

Firstly, we will screen samples from 3, 4 and 5-week-old control and Psmc1$^{fl/fl;}$CaMKIIα-*cre* mice for the expression of pro-inflammatory mediators, alongside GFAP and STAT3α, via quantitative-real time PCR. Secondly, we will use acutely isolated cerebral cortex and hippocampal slices to test the ability of known agonists (CXCL10, IL-6, TNF-α, BzATP, ADP) to initiate STAT3 tyrosine 705 phosphorylation, using STATTIC inhibitor of STAT3 phosphorylation as a negative control. Thirdly and finally, we will immunolabel these areas to quantify the number of STAT3α^{+} astrocytes in each condition to assess if there is a significant difference between experimental conditions

5.2 Materials & Methods

5.2.1 qRT-PCR

Snap frozen hippocampi from 3,4 and 5 weeks-old Psmc1$^{fl/fl}$;CaMKIIα-*cre* mice (n =3) and age-matched control littermates (n=3) underwent RNA-extraction using the RNeasy Plus Mini Kit (Qiagen.# 74134). cDNA synthesis was undertaken and qRT-PCR was carried out using 10/25ng of cDNA depending on the chosen target. Log fold change was normalised to GAPDH expression. An unpaired students t-test was undertaken to assess statistical significance between each age group. Please see section 2.5 for full details.

5.2.2 Acute slice preparation and experimental procedure

3-week-old C57BL mice were sacrificed by cervical dislocation, the brain was rapidly removed and placed in ice-cold cutting buffer (126 mM NaCl, 3 mM KCl, 1.2 mM NaH_2PO_4, 25 mM $NaHCO_3$, 15 mM glucose, 3mM $MgSO_4$, 2mM Ca^{2+}). The occipital lobe and cerebellum were removed then hemispheres were separated. Each hemisphere was mounted on the vibratome stage with the sagittal plane uppermost and cut sagittal 400µm slices. Slices were transferred to the recovery chamber in a water bath set at 32 ºC and left for 1 hour to recover. 3-4 slices were transferred from the recovery chamber to the experimental chambers. A pharmacological agent at the desired concentration in the recovery buffer was added via direct pipetting over the slice and left for 30 minutes. Slices for western blotting were snap frozen in liquid nitrogen and slices for immunofluorescence were fixed in 4% PFA w/v PBS for 3 hours, then submerged in 20% sucrose overnight at 4 ºC. Slices were washed thrice in PBS for 10 minutes then submerged in OCT in cryomolds. A cryostat was used to cut 10µm slices which were then mounted on superfrost slides. Slides were kept at -20 ºC until needed. Please see section 2.6 for full details.

5.2.3 Western blotting

Snap frozen slices were lysed using a similar protocol to brain homogenisation, however using a smaller volume of RIPA buffer (100 µL). Protein quantification was estimated using a BCA assay and 100 µg of protein was loaded to 10% SDS-page gels and transferred to nitrocellulose membranes overnight. Membranes were blocked with 5% NFDM in TBS-T and incubated with primary antibody pSTAT3-tyrosine 705 (1:250) overnight. After several washes of TBS-T, membranes were either incubated with HRP-Rabbit antibody (1:1000) or Licor 800 anti-rabbit

(1:1000) for one hour. Results were viewed using appropriate detection methods specific to the secondary antibody used. Please see section 2.4 for full details.

5.2.4 Immunofluorescence

Superfrost slides were returned to room temperature and washed in PBS for 5 min. Slides were treated with 0.1% sodium borohydride for 10mins thrice, then washed with 0.9% (w/v) NaCl for 40 minutes then washed with PBS for 40 minutes. The non-specific background was blocked using a 10% goat v/v M.O.M blocking agent (as directed) for one hour at room temperature. The blocking agent was removed, and primary antibodies (pSTAT3: 1:50; GFAP 1:200) in 10% goat serum and 10% M.O.M concentrate were added and incubated for 48 hours at 4ºC. Slides were washed with PBS for one hour, then second antibody (1:500 AF568 Rabbit, 1;500 AF488 Mouse) in 10% goat serum and 10% MOM concentrate for one hour in the dark. Slides were washed in PBS then DAPI (1:1000) was applied for 5 mins. Slides were washed in PBS and then mounted with DAKO media. Please see section 2.6.5 for full details.

5.3 Results

5.3.1 qRT-PCR indicates a significant upregulation of key initiators and markers of reactive gliosis

To assess potential chemokine and cytokine initiators of STAT3 activation in astrocytes, quantitative PCR was undertaken in 3,4- and 5-week-old Psmc1 $^{fl/fl}$;CaMKIIα-*cre* mice cortices and their age-matched controls. IL-6 showed no significant difference at 3-weeks (1.00 vs 3.04, $p > 0.05$) and 4-weeks old (1.00 vs 4.33, $p > 0.05$), however showed a significant difference at 5-weeks old (1.00 vs 7.33, $p < 0.05$) (figure 5.2A). TNF-α showed a significant increase at 3-weeks (1.03 vs 1.21, $p < 0.05$) 4-weeks (1.01 vs 2.58, $p < 0.0001$) and 5-week old (1.00 vs 3.14) in Psmc1$^{fl/fl}$;CaMKIIα-*cre* mice vs age-matched littermates (figure 5.2B). CXCL10 showed no significant difference at 3-weeks old (1.00 vs 0.78, $p > 0.05$), 4-weeks old (1.00 vs 12.78, $p > 0.05$) and 5-weeks old (1.00 vs 17.81, $p > 0.05$)(figure 5.2C). In this last case, there were large changes in mean fold change, but also large variance between samples.

To compare qRT-PCR results to previous data, STAT3α and GFAP expression were also investigated. STAT3α expression showed no significant upregulation at 3-weeks old (1.00 vs 1.21, $p > 0.05$), however did reach statistical significance at 4-weeks old (1.00 vs 2.58, $p < 0.01$) and 5-weeks old (1.00 vs 3.13, $p < 0.01$) (Figure 5.3A). GFAP also showed no significant upregulation at 3 weeks old (1.00 vs 1.48, $p > 0.05$), however also reached statistical significance at 4 weeks old (1.00 vs 13.13, $p < 0.05$) and 5 weeks old (1.00 vs 41.18, $p < 0.01$) (Figure 5.3B). This contrasts with previous SWATH-MS data and western bot, demonstrating a significant increase at 3 weeks of age.

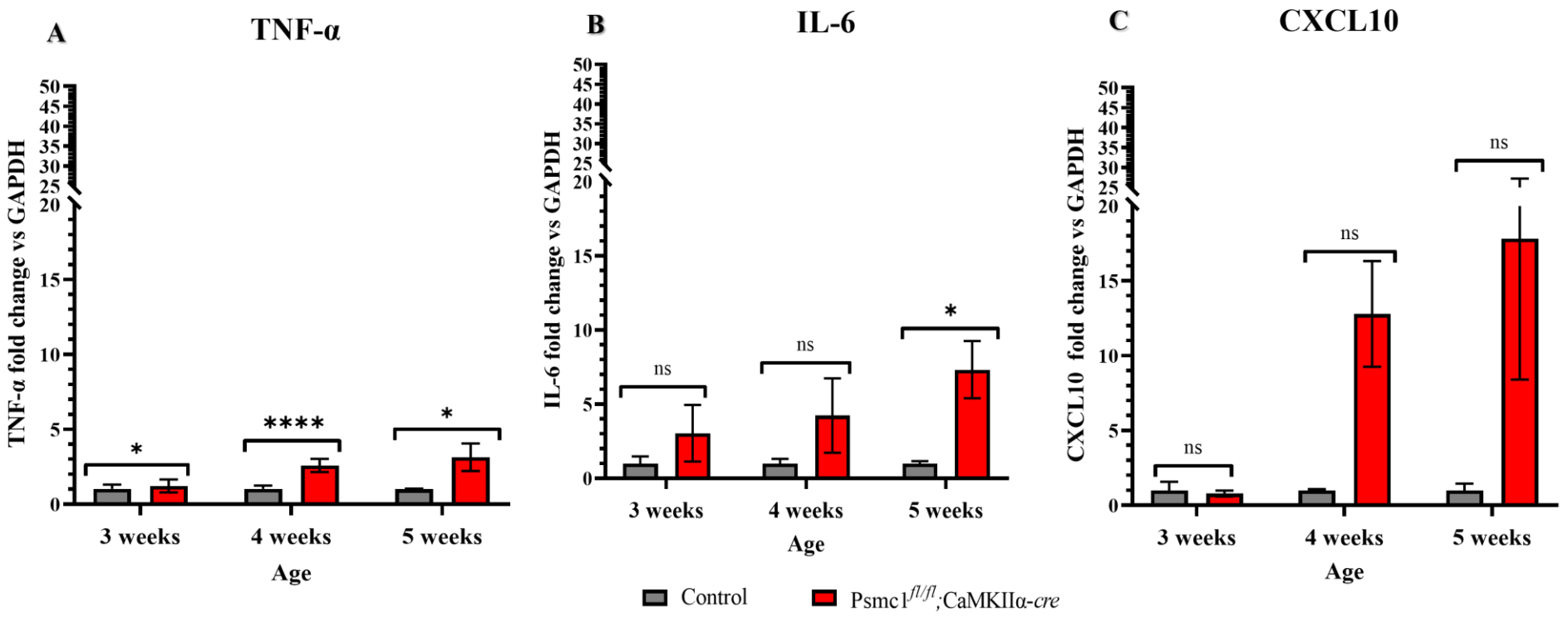

Figure 5.2:qRT-PCR demonstrates an upregulation in possible initiators (TNF-α, IL-6 and CXCL10) in 3-week, 4-week and 5-week old Psmc1$^{fl/fl}$;CaMKIIα-*cre* mice compared to age-matched control littermates .5.2A) IL-6, 5.2B) TNF- α, 5.2C) CXCL10, students t-test conducted – n=3 of each genotype, significance values: ns = non significant (p>0.05), * = p<0.05, ** = p <0.01, *** = p<0.01, ****= p <0.0001)

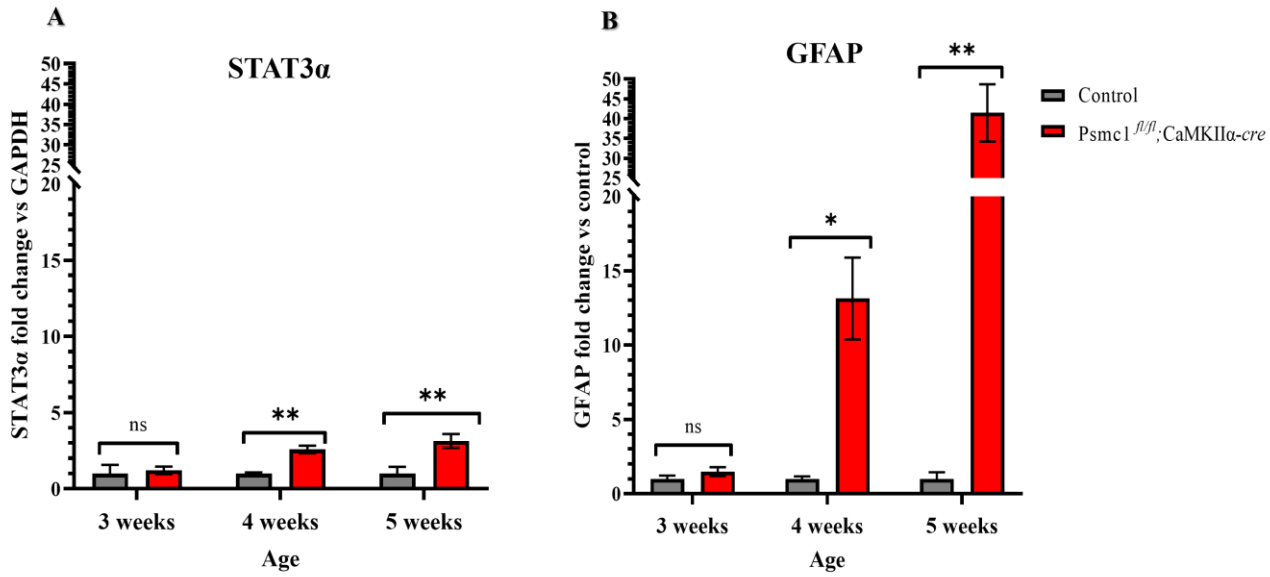

Figure 5.3:qRT-PCR demonstrates an upregulation in possible in Astrocytic-STAT3 in 3-week, 4-week and 5-week old Psmc1$^{fl/fl}$;CaMKIIα-*cre* mice compared to age-matched control littermates 5.3A) STAT3α, 5.3B) GFAP..Students t-test conducted - significance values: ns = non significant (p>0.05), * = p<0.05, ** = p <0.01, *** = p<0.01, ****= p <0.0001)

5.3.2 Significance increase in GFAP and CXCL10 mRNA is in association with disease pathology.

To assess if there was a significant difference between agonists and markers of gliosis across disease stages (3,4 and 5-week old), a two-way ANOVA per sample group (control and Psmc1$^{fl/fl}$;CaMKIIα-*cre*) was conducted to assess the effect of age (IV) and gene targets (IV) on mRNA expression (DV).

Firstly, chemokines and cytokines were investigated for developmental changes in control mice between 3,4 and 5 weeks of age. A two-way ANOVA reported no significant interaction between age, gene targets and their relative mRNA expression ($F(4,18) = 0.03775$, $P=0.9970$). Post hoc Tukey tests reported there was no significant change across 3,4 and 5 weeks for CXCL10 (1.22, 1.00, 1.15), IL-6 (1.16,1.05, 1.02) and TNF-α (1.06, 1.10, 1.11), all reporting a probability of $p>0.05$ (Figure 5.4A).

A two-way ANOVA reported no significant interaction between age, gene targets and their relative mRNA expression ($F(4,18) = 0.9840$, $P=0.4410$) in Psmc1$^{fl/fl}$;CaMKIIα-*cre* mice. CXCL10 displayed a fold change increase in 3, 4 and 5 weeks of age (0.78, 12.78, 22.97), with

post hoc tukey tests indicating a significant fold change in CXCL10 between 3- and 5-week-old mice (+22.22, $p<0.5$) however no significance was detected between 3 -, 4 -week and 4-, 5-week old mice (+12, $p>0.05$, +10.19, $p>0.05$). TNF-α also displayed an increase in mean fold change with disease progression across 3,4-and 5-week Psmc1$^{fl/fl}$;CaMKIIα-*cre* mice (1.81,8.21,15.78), but this did not reach statistical significance ($p>0.05$). IL-6 followed in this progression (3 weeks:3.04, 4 weeks:4.23, 5 weeks: 8.75), however again did not reach statistical significance ($p>0.05$) (Figure 5.4B).

Next, GFAP and STAT3 were investigated for changes in control mice across 3,4 and 5 weeks of age. A two-way ANOVA reported no significant interaction between age, gene targets and their relative mRNA expression ($F(2,12) = 0.08215$ $P=0.9216$). Post hoc tukey tests reported there was no significant change across 3,4 and 5 weeks for GFAP (3 weeks: 1.05, 4 weeks: 1.02, 5 weeks: 1.18) or STAT3 (1.03,1.02, 1.00) all reporting a probability of $p>0.05$ (Figure 5.5A).

GFAP and STAT3 were investigated for changes in Psmc1$^{fl/fl}$;CaMKIIα-*cre* mice across 3,4 and 5 weeks of age. A two-way ANOVA reported a significant interaction between age, gene targets and their relative mRNA expression ($F(2,12) = 24.74$ $P=<0.001$). GFAP displayed a fold change increase at 3, 4 and 5 weeks of age (3 weeks: 1.48, 4 weeks: 13.13, 5 weeks: 46.58), and Post hoc tukey tests reported there was a significant fold change between 4 and 5-week old mice (ca 33 fold, $p<0.0001$) and between 3 and 5-week old mice (ca 45 fold, $p<0.0001$) however no significance was detected between 3 - 4 week old mice (ca 12 fold, $p>0.05$). STAT3α also displayed an increase in fold change with disease progression across 3,4- and 5-week Psmc1 fl/fl;CaMKIIα-cre mice (3weeks: 1.21, 4 weeks: 2.59,5 weeks: 3.54) however did not reach statistical significance ($p>0.05$) (Figure 5.5B).

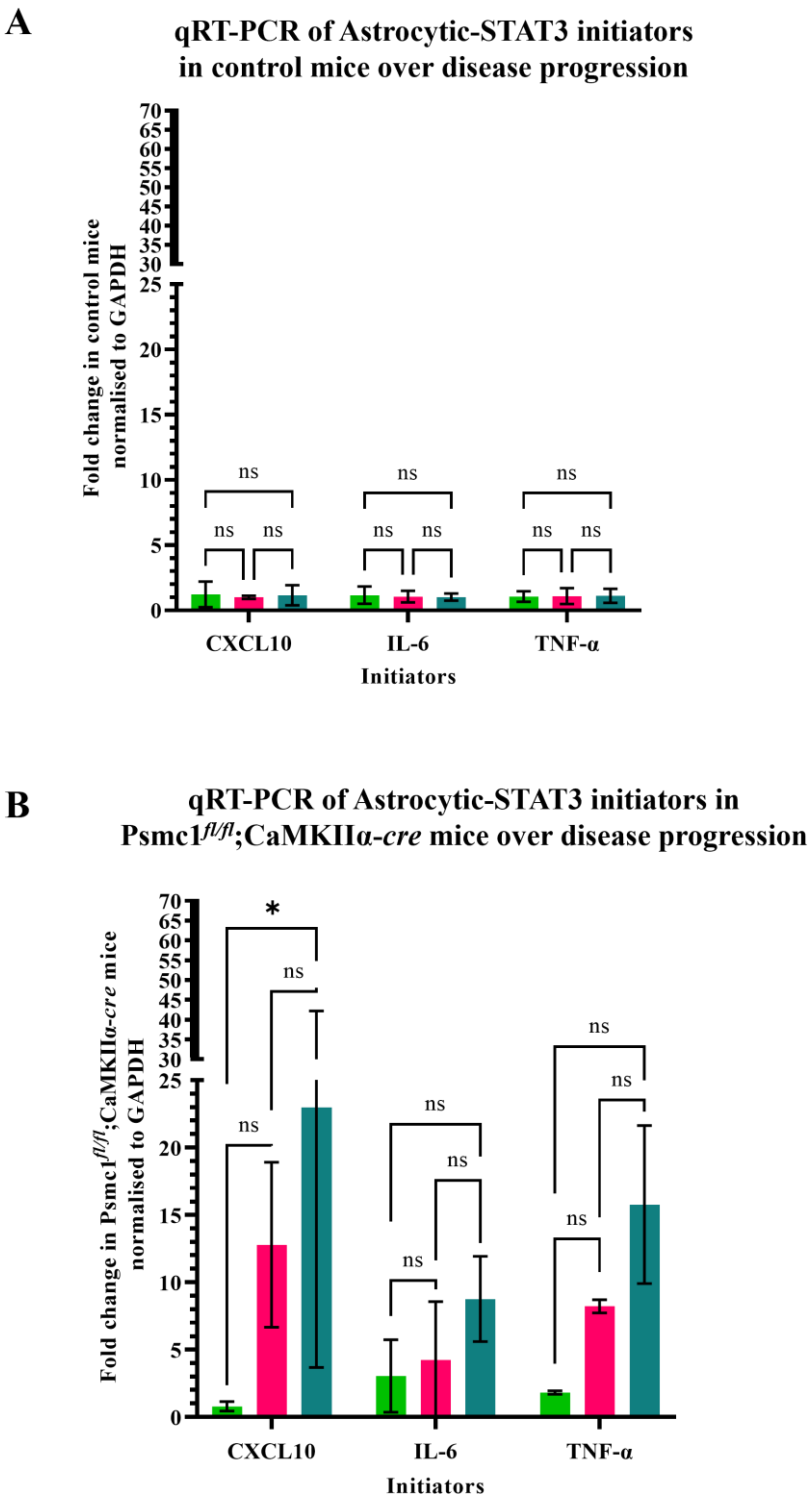

Figure 5.4:Two-way ANOVA of qRT-PCR demonstrating STAT3-agonists fold change over disease progression period (3, 4 and 5-weeks old) in control and Psmc1$^{fl/fl}$;CaMKIIα-*cre* mice. 5.4A) Agonist change in control mice over disease progression period. 5.4B) Agonist change in Psmc1$^{fl/fl}$;CaMKIIα-*cre* mice over disease progression. Post-Hoc Tukey Test values plotted - Significance values: ns = non-significant ($p>0.05$), * = $p<0.05$

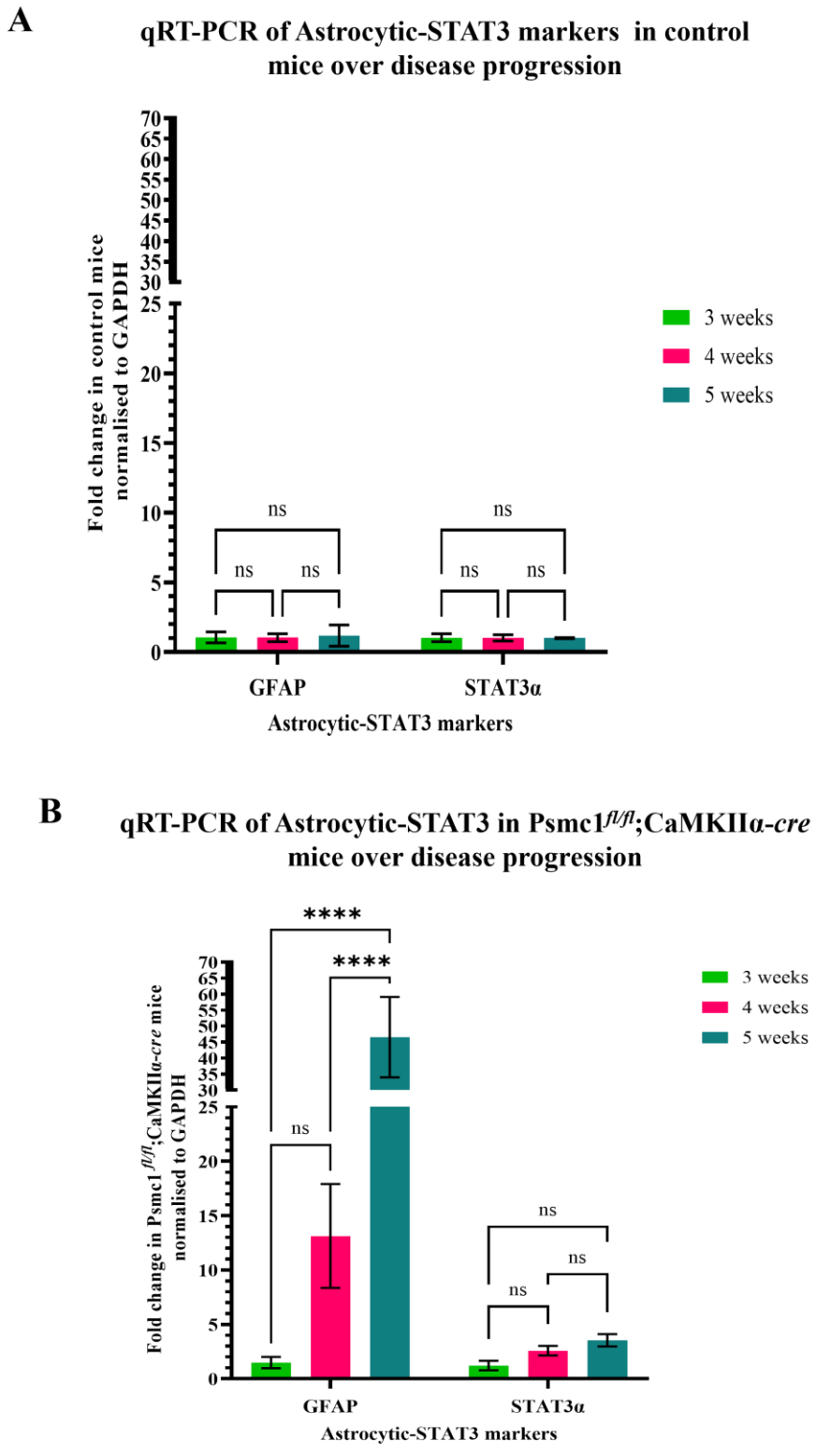

Figure 5.5:Two-way ANOVA of qRT-PCR demonstrating the increase in fold change of markers of gliosis at 4 and 5-week old in Psmc1$^{fl/fl}$;CaMKIIα-*cre* mice. 5.5A) No fold change was present across age groups in control mice 5.5B) GFAP demonstrated a significant fold change across 4 and 5-week-old Psmc1$^{fl/fl}$;CaMKIIα-*cre* mice. . Post-Hoc Tukey Test values plotted - Significance values: ns = non-significant ($p>0.05$), **** = $p<0.0001$.

Collectively these results confirm the increase in STAT3 and GFAP reported in previous chapters and identify several significant changes in chemokine and cytokine levels, but with limits on the reliability of detecting consistent changes accurately.

5.3.3 pSTAT3 astrocyte localisation present at cut-edge in acute slices

Immunofluorescence staining was undertaken in control slices to optimise the staining procedure before moving on to treated slices. It is demonstrated that p-STAT3 Tyrosine 705 positive astrocytes are localised at the edge of the tissue, speculated to be due to astroglia activation after the physical damage of slicing (figure 5.5A-B). There is also evidence that p-STAT3 Tyrosine 705 positive astrocytes activation within the control slice, however, it must be noted this is in a small quantity compared to the cut edge (figure 5.6A-B).

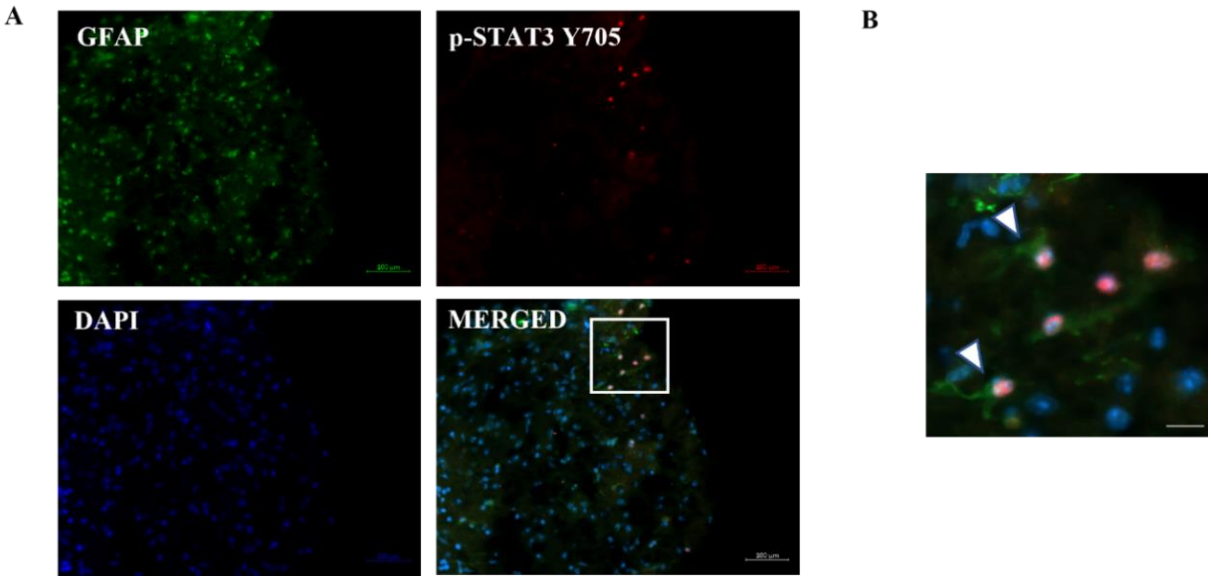

Figure 5.6:STAT3 Tyrosine 705 specific phosphorylation in Astrocytes in control slice shows localisation towards cut-edge of slice 5.6A) GFAP (green), p-STAT3 Y705 (red), and DAPI (blue) as a nuclear stain alongside merged image – scale bar 25µm (images taken at 10x magnification) 5.6B) Close up region of interest with arrows pointing to p-STAT3 Y705 positive astrocytes on the cut slice of the edge – scale bar = 25µm..

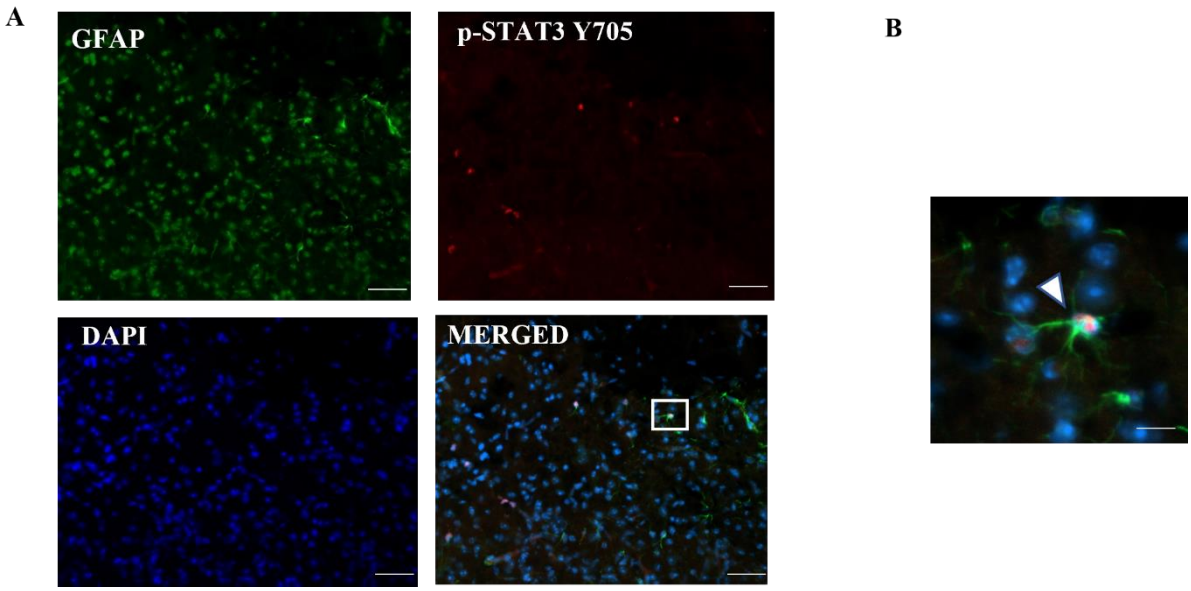

Figure 5.7:STAT3 Tyrosine 705 specific phosphorylation in Astrocytes in control slice 5.7A)GFAP (green), p-STAT3 Y705 (red), and DAPI (blue) as a nuclear stain alongside merged image, images taken at x20 magnification). 5.7B) Close up region of interest with arrows pointing to p-STAT3 Y705 positive astrocytes– scale bar = 25µm

5.3.4 Western blot demonstrates that CXCL10, TNF-α and IL-6 report a significant upregulation in pSTAT3 Tyrosine 705

As control slices showed p-STAT3 Tyrosine 705 astroglia specific activation towards the cut edge, it was decided that the control slice would be used as a normalisation control for western blotting densitometry analysis. As reported in chapter 4, phosphorylated-STAT3 Tyrosine 705 expression is difficult to obtain due to low levels, therefore two methods of immunoblotting were conducted: LICOR (the use of a secondary fluorescence probe) and HRP (the use of a HRP-conjugated secondary antibody increasing sensitivity of signal).

Immunoblotting using LICOR demonstrated a visible presence in phosphorylated-STAT3 Tyrosine 705 expression in control slices, and slices incubated with CXCL10, IL-6 and TNF-α (figure 5.7A). One sample t-test demonstrated a significant increase in p-STAT3 levels in TNF-α treated slices (1.13, $p<0.05$), but did not reach statistical significance for CXCL10 (1.25, $p>0.5$) or IL-6 (1.40, $p>0.5$) (figure 5.7B). It must be noted that no p-STAT3 signal was detected in slices treated with BZ-ATP or ADP, therefore we decided to move on to a more sensitive method of detection using HRP-conjugated antibodies.

Immunoblotting using the more sensitive HRP-conjugated antibody methods again demonstrated a visible presence in phosphorylated-STAT3 Tyrosine 705 expression in control, CXCL10, IL-6 and TNF-α treated slices (figure 5.9A). One sample t-test demonstrated a significant upregulation in TNF- α treated slices when all three replicates were included (1.39, $p<0.05$) however did not reach statistical significance for CXCL10 (1.17, $p>0.5$) or IL-6 (1.26, $p>0.5$) (figure 5.9B)

Pooling all replicates from both detection methods, using their respective control as a comparison, demonstrated a significant upregulation in treated slices: CXCL10 (1.20, $p <0.01$), IL-6 (1.32, $p<0.05$) and TNF- α (1.27, $p<0.01$)(figure 5.10). In both detection methods, there was no detectable phosphorylated-STAT3 Tyrosine 705 in ADP, BZ-ATP or STATTIC treated slices.

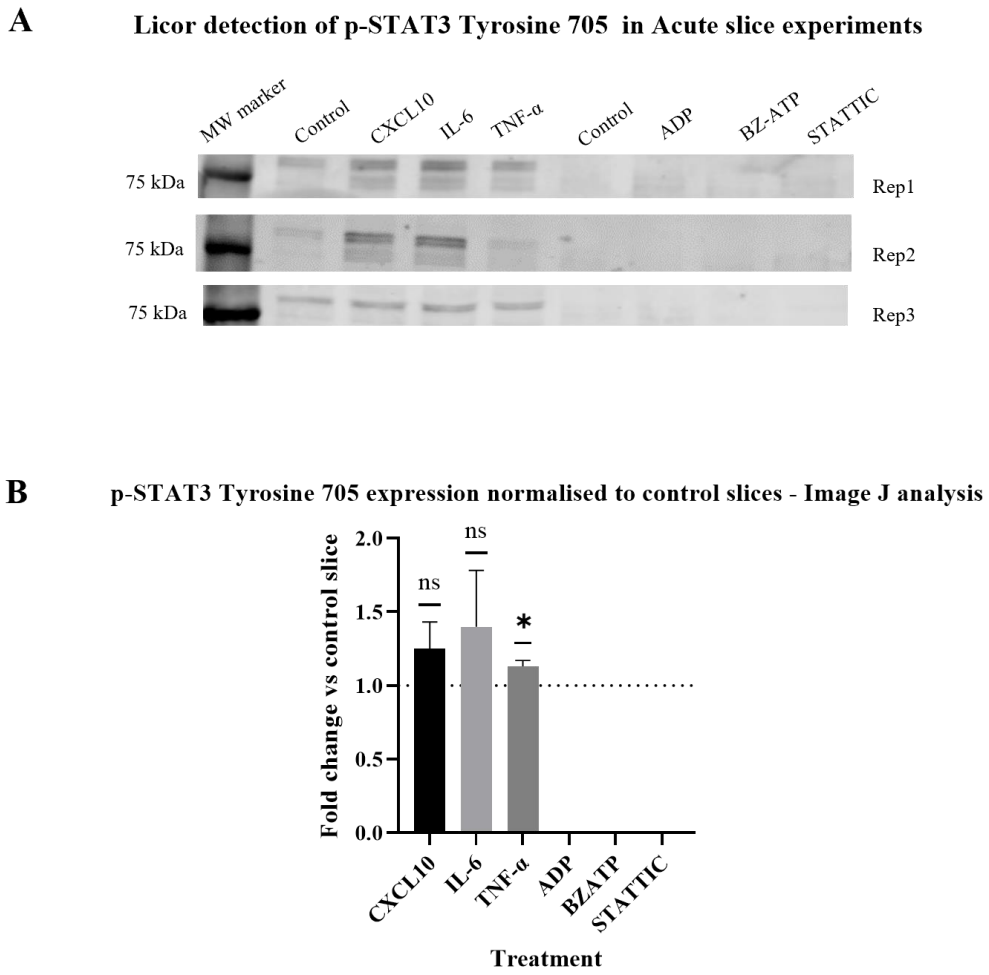

Figure 5.8:Immunoblotting shows p-STAT3 Tyrosine 705 activation in control, CXCL10, IL-6 and TNF-α treated slices via Licor Fluorescence detection. 5.8A) Western blot shows the positive signal in 3 individual replicates, 5.8B) One sample t-test illustrated TNF-α to be significant compared to control slice expression (* P = <0.05). *5D of control group used for normalization is 0.001*

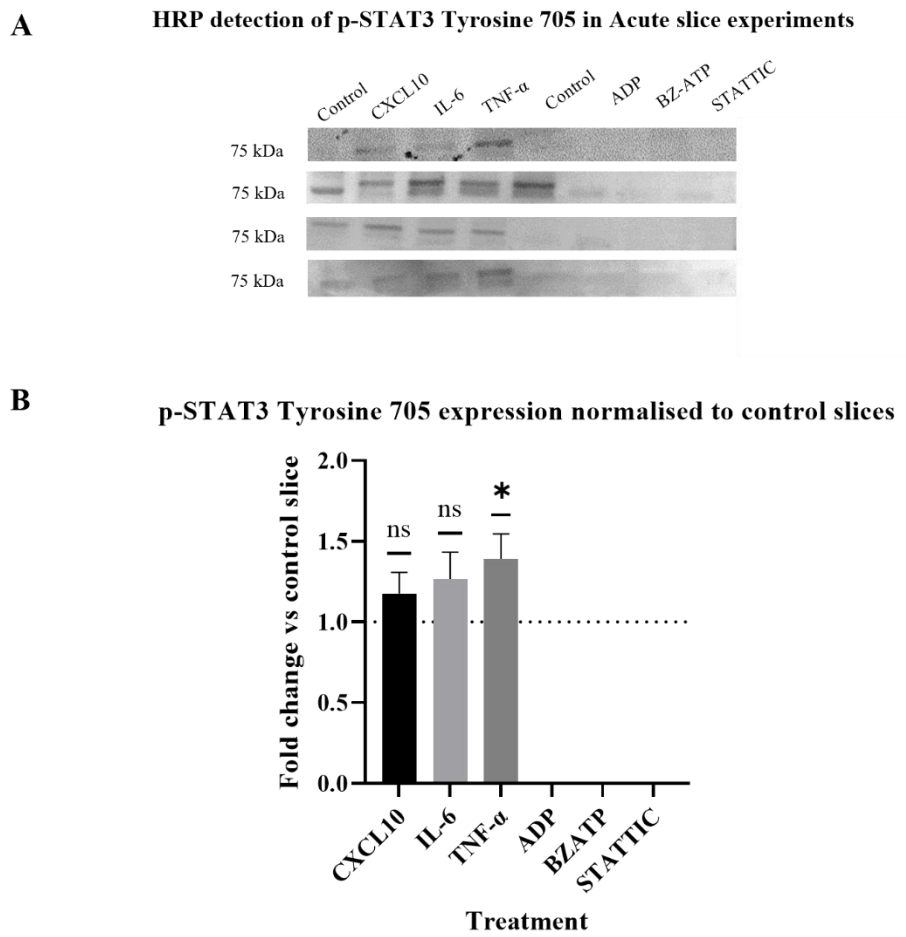

Figure 5.9:Immunoblotting shows p-STAT3 Tyrosine 705 activation in control, CXCL10, IL-6 and TNF-α treated slices via HRP-detection. 5.9A) Western blot shows a positive signal in 4 individual replicates, probed by HRP. 5.9B) One sample t-test illustrated TNF-α to be significant compared to control slice expression (* P = <0.05).

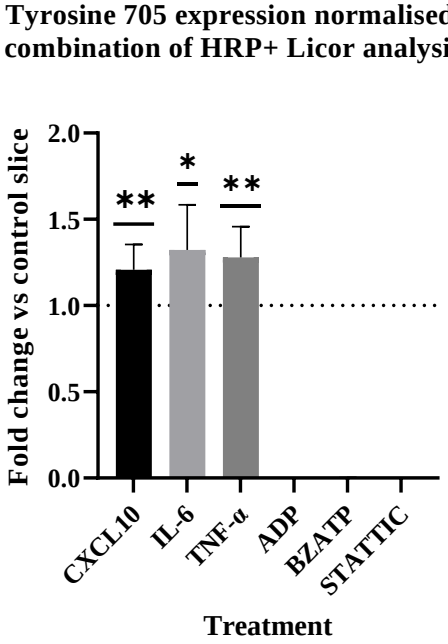

Figure 5.10:Pooled immunoblotting results show significant fold change in p-STAT3 Tyrosine 705 activation in CXCL10, IL-6 and TNF-α treated slices in one sample t-test. N= 4 significance * = p <0.5, ** = p<0.001

5.3.5 Slice sample deterioration prevented validation of western-blot data

Immunofluorescence was performed on treated acute slices to validate immunoblotting data, however, after multiple attempts, it became apparent that slice samples had deteriorated to such a point where there was no epitope availability (figure 5.10A, 5.10B). The plausible causes for this deterioration will be addressed in the discussion section.

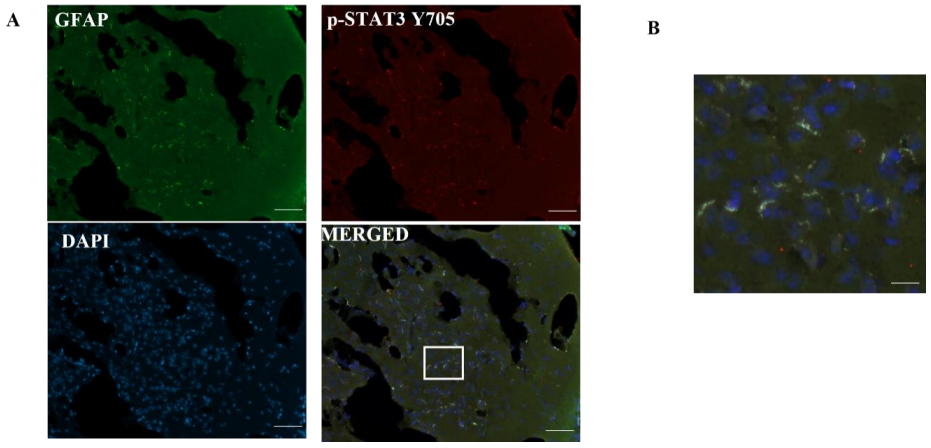

Figure 5.11:**Failure to successfully stain treated slices** 5.11A)GFAP (green), p-STAT3 Y705 (red), and DAPI as a nuclear stain alongside the merged image, images taken at x10 magnification. Scale bar is 100 µm 5.11B) Close-up region of interest showing non-specific staining of slices speculated to be due to the failure to antigen restoration. Scale bar = 25 µm.

5.4 Discussion

The overall aim of this chapter was to identify plausible candidates for the onset of STAT3 signaling in astrocytes, thereby initiating early-stage gliosis in the Psmc1$^{fl/fl}$;CaMKIIα-*cre* mice model at 3-weeks of age. As cited in the introduction, mitochondrial damage and increase in microglia soma area are key events in 3-week old Psmc1$^{fl/fl}$;CaMKIIα-*cre* mice, therefore mitochondrial DAMPS (ATP/ADP) and microglia released cytokines/chemokines (CXCL10, TNF-α, IL-6) were investigated as plausible initiators for STAT3 reactivity in astrocytes.

Quantitative-PCR screening of Psmc1$^{fl/fl}$;CaMKIIα-*cre* mice and their age-matched control littermates supported our immunohistochemical and western blot data indicating an upregulation of STAT3 and GFAP, displaying significant difference at 4 weeks old. GFAP mRNA also showed a significant difference between 4 and 5-week-old Psmc1$^{fl/fl}$;CaMKIIα-*cre* mice and between 3 and 5-week-old Psmc1$^{fl/fl}$;CaMKIIα-*cre* mice, thereby indicating a progression of reactive astrogliosis as a key feature in this neurodegenerative disease pathology.

Quantitative PCR results for potential initiators were less clear due to large variation. CXCL10 displayed no significant difference between Psmc1$^{fl/fl}$;CaMKIIα-*cre* mice and control mice across disease progression, however, a two-way ANOVA did show significant upregulation between 3 and 5-week old Psmc1$^{fl/fl}$;CaMKIIα-*cre* mice. The significant increase in CXCL10 mRNA in Psmc1$^{fl/fl}$;CaMKIIα-*cre* mice could be attributed to an additional reactive astrogliosis feedback loop, CXCL10 reporting recruitment of peripheral immune cells such as $CD4^+$ and $CD8^+$ cells (Roberts et al., 2015).

IL-6 showed a significant difference at 5 weeks old in Psmc1$^{fl/fl}$;CaMKIIα-*cre* mice, however, no significant difference was found at any other stage or between age groups. Once again, IL-6 has also reported a self-regulatory loop and thereby significant escalation could be the result of reactive astrogliosis (Camporeale and Poli, 2011).

TNF-α mRNA demonstrated a significant increase in association with disease pathology in the Psmc1$^{fl/fl}$;CaMKIIα-*cre* model with no significant differences demonstrated between age-matched control mice.

Initial immunostaining of control acute slices highlighted STAT3α^{+} astrocytes localised towards the cut edge of the tissue slice. As there was only a small number of STAT3α^{+} astrocytes present in the center of the acute slice, it was deemed that this was due to the methodological consequence of acute slice preparation. As this cut-edge effect had the potential to confound immunoblotting analysis, immunoblots were normalised to the expression of pStat3 Tyrosine 705 control slice for statistical analysis.

Immunoblotting also demonstrated that CXCL10, TNF-α and IL-6 could upregulate p-STAT3 Tyrosine 705 phosphorylation, however, there was a high variance in the detectable signal. To remedy this, two detection methods were used, with HRP being favoured due to its increased sensitivity. Samples were pooled and normalised to control slice to get to the result, which demonstrates a significant upregulation in STAT3 Tyrosine 705 phosphorylation. In principle, this confirms that all pro-inflammatory cytokines tested can increase STAT3 Tyrosine 705 phosphorylation, and so could be contributing to the early gliosis response.

In contrast, slices treated with Bz-ATP or ADP did not show any STAT3-tyrosine 705 phosphorylation in any experiments. This can be simply attributed that these DAMPS do not initiate this effect, but it is also concerning that p-STAT3 was also undetectable in control slices in these experiments. Another issue, upon looking at the literature, is that it may be due to the aspect that we only incubated the slices for 30 minutes when other studies have used a minimum of 2 hours and a higher concentration of agonists (Eyo et al., 2013; Munoz et al., 2017). We must also take into consideration the potential molecular signaling pathways of these DAMPs; for example, it may first activate microglia via purinergic receptors. This is supported by previous research indicating that microglia soma size is significantly increased in 3-week-old Psmc1$^{fl/fl}$;CaMKIIα-*cre* mice (Geiszler et al., 2018). Literature suggests that microglia activation of P2X7/P2X4 receptors increases the resting calcium status, and this increase in calcium has been attributed to microglia phagocytosis and the release of chemokines/cytokines, including IL-6, CXCL10 and TNF-α (Hoffmann et al., 2003)(figure 5.11).

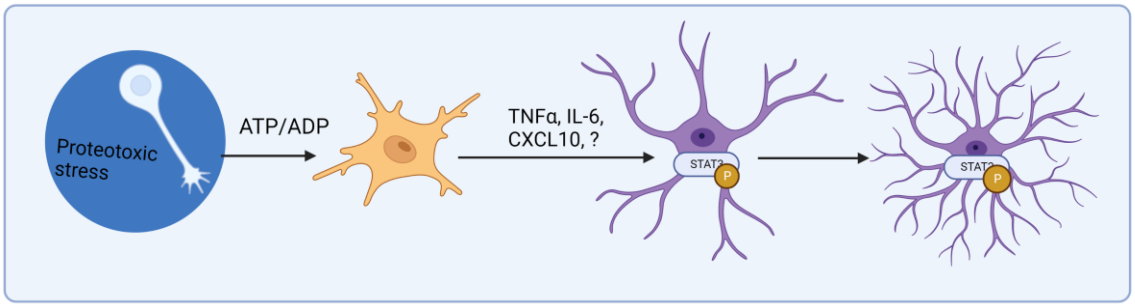

Figure 5.12:DAMP-driven activation of microglia may lead to the release of proinflammatory cytokines that lead to astrocytic-STAT3 phosphorylation. ADP/ATP can activate microglia purinoreceptors, thereby leading to an increase in proinflammatory cytokines that lead to STAT3-phosphorylation in astrocytes. *Figure made using biorad.com.*

If this is the originator of the pro-inflammatory cytokines that do initiate STAT3α^{+} astrocytes in the Psmc1$^{fl/fl}$;CaMKIIα-*cre* model, the microglia priming process can take a matter of hours and if this is the case, direct ATP/ADP stimulation of astrocytes would not show an increase in phosphor-STAT3 tyrosine 705 in this experiment.

Immunofluorescence of treated slices was planned to validate that phospho-STAT3 Tyrosine 705 activation was localised to astrocytes. Unfortunately, reliable fixation and sectioning of slices proved difficult, with many experiments showing little to no positive immunostaining. This can be attributed to the technical difficulty of working with the small size of the tissue slice, thereby making intact slices difficult to fix, process and cut reliably. The fixation process of 4% PFA for 3 hours may not have been long enough to preserve epitope availability.

In addition to this, it is important to note that there was a substantial delay between initial control experiments where slices were cut, stained and imaged before the onset of the COVID-19 pandemic, whereas other cutting, staining and images were performed after 4 months of sample storage. Poor fixation, thin torn slices and prolonged storage were obstacles to testing this hypothesis. To remedy this, free-floating slices paired with confocal imaging could be used in future studies to assess STAT3α^{+} astrocytic activation in response to pharmacological treatment.

Overall, the outcome of this chapter is mixed. We have demonstrated an increase in the expression of pro-inflammatory cytokines in Psmc1$^{fl/fl}$;CaMKIIα-cre mice. Although ATP and

ADP did not show tyrosine-705 phosphorylation in these pharmacological studies, the increased microglia soma at 3 weeks of age in association with mitochondrial damage represents a possibility of DAMP signaling at microglia, but not astrocytes. TNF-α is a key candidate in the possible initiators, however, the source of this TNF-α (neuronal/microglia) is to be decided by future work. Immunoblotting confirmed that all initiators do have the possibility to upregulate STAT3 tyrosine 705 phosphorylation, however with the lack of immunofluorescence data to support it we cannot definitively say that it is astrocyte-specific. However, in support of this, previous students in the Bellamy lab have shown that TNF-α treatment of primary cultures of astrocytes leads to STAT3 Tyrosine 705 phosphorylation (paper in progress), thereby suggesting TNFα as the molecular initiator to be worthy of further investigation.

Chapter 6 Discussion

6.1 Background and aims of the project

Defects in proteolytic systems are a key feature in neurodegeneration and are exemplified by the appearance of protein inclusions and aggregates in disease state. There is great uncertainty in the literature about how these typical features cause neuronal damage, and if these aggregates are related to relieving or exacerbating the burden of neurodegenerative disease. In this thesis, we used the Psmc1$^{fl/fl}$;CaMKIIα-*cre* mouse model, which selectively depletes the 26S proteasome complex in CaMKIIα-*cre* neurons over 3 weeks, therefore providing a valuable tool for investigating neurodegenerative mechanisms. Despite a documented evidence base regarding progressive gliosis (see table 1.5, introduction) there are important unanswered questions about the detailed progression from neuronal-proteolytic dysfunction to neurodegeneration and how glial cell reactivity influences disease pathology. This thesis aimed to examine glial responses in this mouse model during the onset of neuronal dysfunction and neuroinflammation to elucidate the potential mechanisms, signaling pathways and initiators at play. A summary of the key results can be found in figure 6.1.

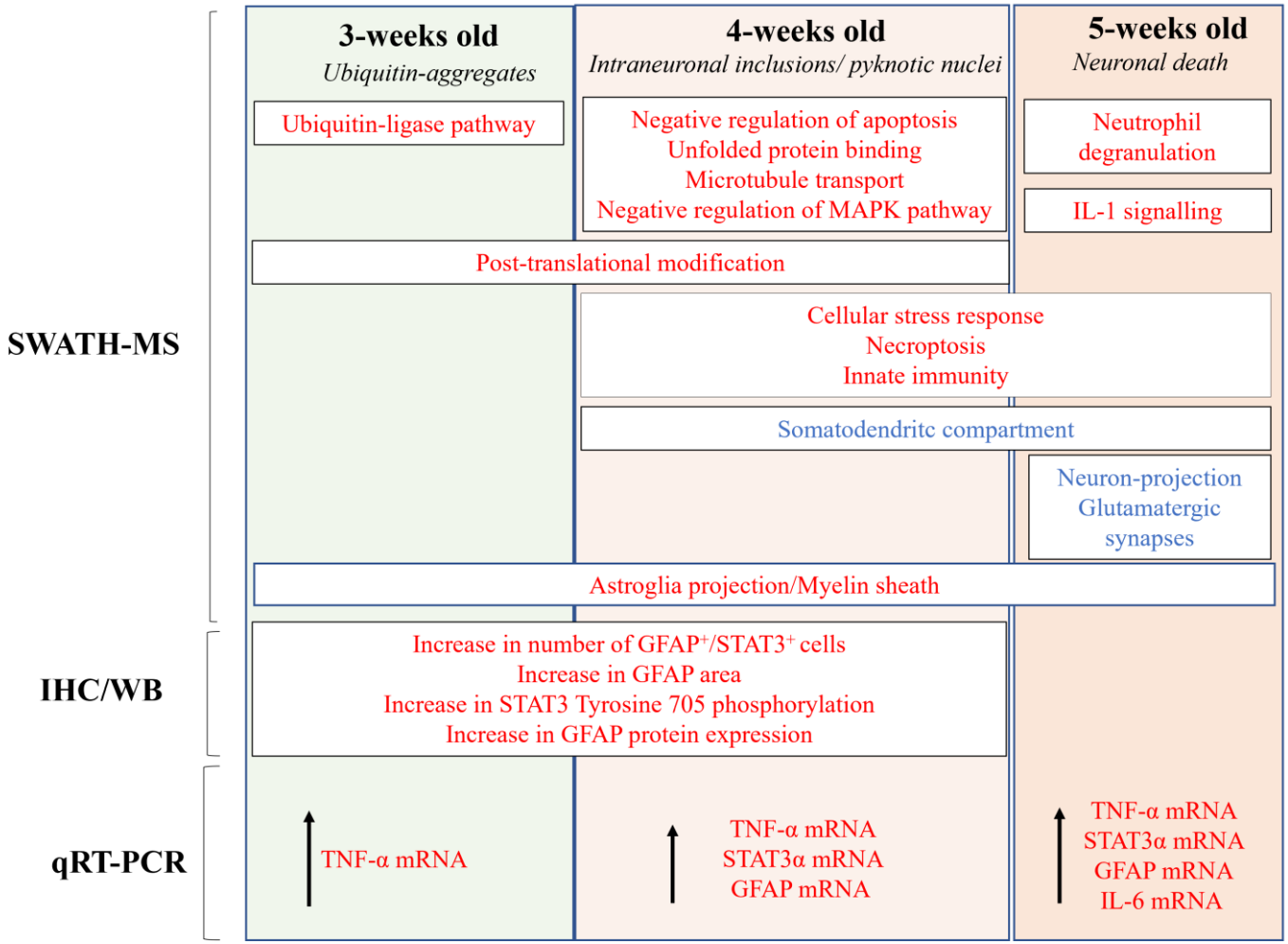

Figure 6.1:Schematic representation of the summary of the results and how they map onto proteasome depleted neurons Writing in italics is representative of neurodegenerative stages in the mouse model and results are separated by technique. Red text symbolises upregulated processes compared to age-matched control; blue text symbolises downregulated components compared to age-matched controls.

6.2 Molecular analysis of the progression of neurodegeneration

The aim of chapter 3 was to identify key changes during progressive neurodegeneration using SWATH-MS to perform protein-expression profiling of 2-,3-,4- and 5-week old Psmc1$^{fl/fl}$;CaMKIIα-*cre* mice compared to their age-matched littermates. Significant protein-protein interactions and pathway analyses of these proteins were performed using STRING software. A range of pathways and cellular components showed enrichment or downregulation particular to disease state; all of which were supported by external literature citing common pathways in neuroinflammation and neurodegeneration.

3-week-old Psmc1$^{fl/fl;}$CaMKIIα-*cre* mice demonstrated an upregulation of the ubiquitin-ligase pathway, which has been previously evidenced in this model and speculated to be due to compensation for 26S proteasome loss (Bedford et al., 2008; Geiszler et al., 2018). This was important confirmation that the proteomic approach was able to successfully detect known changes in the mouse phenotype, but with additional detail in the network of related proteins involved. The upregulation of pathways associated with unfolded-protein binding and negative regulation of apoptosis coincides with intraneuronal inclusions in CaMKIIα neurons at 4-weeks of age, further supporting the argument that inclusions are protective in neurodegeneration (Shankar et al., 2007). 4- and 5-week-old Psmc1$^{fl/fl}$;CaMKIIα-*cre* mice share overlapping pathways in necroptosis, cellular stress response and innate immunity. 4-week neurons also evidence pyknotic nuclei, therefore supporting necroptosis to be a pathway of neuronal death. In addition to this, neuronal death has previously been shown by our lab to be present at 5 weeks old, supporting STRING-pathway reports of downregulation of cellular components in neuron-projection, somatodendritic compartment and glutamatergic synapses (Geiszler et al., 2018).

Of most importance, GFAP was shown to be consistently upregulated from an early stage, with increasing levels observed throughout disease progression, supporting the key role of reactive astrogliosis in this mouse model. In addition to this, SWATH-MS supported previous astroglia-centered peer-reviewed data reported, such as upregulation in PRDX6 (Elkharaz et al., 2013). SWATH-MS corroborated a lot of existing results, but importantly, it added a quantitative analysis of protein levels, and it increased the understanding of the connectivity of molecular signaling networks implicated in the progression of the disease. While previous work identified individual target proteins, SWATH provides broader coverage of protein networks and can

identify clusters of functionally connected proteins at the systems level. That helps map the key processes occurring, rather than scattershot coverage of individual markers. Furthermore, SWATH analysis is relatively unbiased and so identified previously unrecognised changes that might not have been predicted from existing knowledge.

Although SWATH-MS overall supported previous research on this mouse model, there are disadvantages to this method and the subsequent STRING analysis. Firstly, immunohistochemical staining using microglia marker Iba1 has shown an increase in soma size and area associated with disease progression. However, Iba1 was not detected in SWATH-MS data of 2,3-,4- or 5-week-old mice, even at 0% confidence levels. One argument for this could be due to the small molecular weight of Iba1 at 17 kDa, and thus it was therefore impossible to detect Iba-1 by mass spectrometry. However, this argument falls flat with evidence that alpha-synuclein, a 14 kDa molecular weight protein, was detected and quantified in 5-week data sets.

An alternative explanation for this inconsistent result could lie in sample preparation. Trypsin, the enzyme used for peptide cleavage before mass spectrometry, cleaves peptides at the lysine(K) and arginine (R) residue. An examination of the amino acid sequence of both proteins demonstrates that alpha-synuclein does not contain arginine residues, whilst Iba1 does. Hypothetically, the number of peptides generated by trypsin cleavage has been mapped in figure 6.2. As shown below, Iba1 produces a multitude of peptides under 6-7 amino acids long, which are not recognised by the mass spectrometer, whereas alpha-synuclein cleaved results in longer peptide sequences. The probability of these peptides being exclusive to Iba1 is also a factor, and as there are so few of them, would reduce confidence also. Overall, it can be concluded that factors in the preparation process may cause some proteins to be missed in the analysis.

In addition, single polypeptides detected by SWATH-MS were removed from the data set, therefore reducing the likelihood that Iba1 would be reported. This is not a unique problem, with one study citing that only 26% of the proteome is surveyed by using trypsin-digested samples, therefore significantly restricting the area of the proteome covered (Simpson, 2006; Tsiatsiani et al., 2015). Overall, it appears that SWATH-MS only gives us ¼ of the story, leaving 75% unknown.

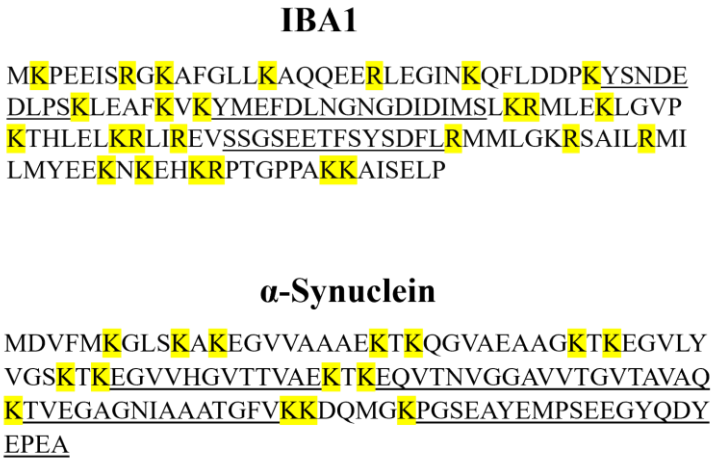

Figure 6.2:Hypothetical trypsin cleavage of IBA1 and alpha-synuclein show potential amino acids for detection by mass spectrometry. K – lysine residue, R – Arginine residue

Secondly, SWATH-MS was performed in the brain cortex, with a mixed range of cells present. Although some proteins are cell-specific (e.g. GFAP), other proteins localisation needs to be confirmed through alternative techniques such as immunohistochemistry. In addition to this, it has been argued that results using whole brain tissue are driven by cell abundance and therefore do not represent the accurate cellular signaling pathways of all cell types (Srinivasan et al., 2016). Finally, STRING analysis indicates but does not validate the pathway, and more so does not consider the fold change in SWATH-MS data.

Despite these caveats, this data chapter builds on and extended previous work on this model. The most striking result in this chapter is the predominance of GFAP which arises prior to intraneuronal inclusions and neuronal death, which progressively increases in line with disease progression. The initial cause of astrocyte activation was decided to be the focus of the subsequent chapter.

6.3 Mechanism of early onset astrogliosis

The aim of chapter 4 was to extend the results from SWATH-MS data which indicated that GFAP, a marker of astrocytes, increased with disease progression. STAT3 has been cited as a key early regulator of astrogliosis, with downstream effector genes showing roles in astroglial hypertrophy and glial scar formation (Acarin, González and Castellano, 2000; O'Callaghan et al., 2014a; Renault-Mihara and Okano, 2017).

Western blotting supported SWATH-MS data, displaying a significant increase in GFAP protein expression from 2,3-4 weeks old. Immunofluorescence corroborated this, showing a distinct increase in astrocyte hypertrophy correlating with disease progression that varied in brain regions. The number of $GFAP^{+}/STAT3\alpha^{+}$ cells significantly increased over time, however, this also varied in the different brain regions studied. This could potentially be attributed to the distribution of CaMKIIα neurons, which are more concentrated in the CA3 and DG areas (Wang, Zhang, Szábo and Q. Q. Sun, 2013). Support for this hypothesis comes from additional data in this chapter, which demonstrated a significant increase in astrocytic-STAT3 in the CA3 and DG area at 3 and 4 weeks old. Western blotting demonstrated a significant increase in STAT3 and STAT3 phosphorylated tyrosine 705 at 3 and 4 weeks old, therefore suggesting that STAT3 upregulation may be due to its subsequent phosphorylation, providing a positive feedback loop (Narimatsu et al., 2001; Tyzack et al., 2014).

Albeit our results display an increase in $GFAP^{+}/STAT3\alpha^{+}$ astrocytes, we are unable to conclude if this serves as beneficial or detrimental in the progression of neurodegeneration in our mouse model. Using the SWATH-MS data as an indicator, we found astrocytic proteins functionally associated with neurotoxic astrocytes to be upregulated at 4 weeks old (i.e., Connexin 43, NDRG2). In addition to this, support comes from other studies in neurodegenerative mouse models which also report an increase in $GFAP^{+}/STAT3\alpha^{+}$ cells and demonstrates that STAT3 inhibition reduces disease burden (Ceyzériat et al., 2016; Ceyzériat, ben Haim, Denizot, Pommier, Matos, Guillemaud, M. A. Palomares, et al., 2018). On the other hand, there are also 3-week SWATH-MS data which indicates that these astrocytes may be protective, reporting an enrichment in Glutathione S-transferase A4, which has neuroprotective roles in neurodegenerative disease models (Jewett, Jimenez-Ferrer and Swanberg, 2017; Jewett et al., 2018; McGann and Mandel, 2018). In addition to this, $GFAP^{+}/STAT3\alpha^{+}$ astrocytes have also

shown beneficial roles in promoting proteostasis in neurodegenerative disease. Astrocytic-STAT3 has been cited to be A1, A2 and even pan reactive through previous literature in a range of neurodegenerative models, therefore reinforcing the questioning of whether these astrocytes are friend or foe in disease state (Das et al., 2020; Fan and Huo, 2021).

STAT3 has been cited to be translocated to the mitochondria where it has established roles in regulating energy production and the synthesis of antioxidant genes through Serine 727 phosphorylation (Joo et al., 2009). In support of this, cultured astrocytes from the STAT3 $^{fl/fl}$;GFAP-*cre* mouse model report a decrease in ATP production and a reduction in mitochondrial membrane potential and mass compared to their control counterparts (Sarafian et al., 2010). In addition to this, astrocyte cultures in a disease model of neurodegenerative report a decrease in phospho-serine 727 phosphorylation, leading to a loss in astrocytic protective phenotype. Of most interest, this was not reflected in the total STAT3 protein (Muñoz, Paula-Lima and Núñez, 2018). It may be reasonable to assume that these astrocytes are at first neuroprotective, then move to neurotoxicity, however, further experiments will be needed to address this hypothesis.

Another limitation of this work is the use of formalin-fixed paraffin-embedded tissues, therefore only providing a 'snapshot' of the cellular state, therefore potentially minimizing the true reflection of Astrocytic-STAT3 phosphorylation. Despite STAT3 localization to the nucleus being used as a measurement of STAT3 phosphorylation by other groups, this does not accurately address whether the STAT3 Tyrosine 705 phosphorylation detected in western blot originated from astrocytes. We reason that the increase in GFAP$^+$/STAT3α^+ cells is reflected in the elevation of tyrosine 705 phosphorylation. Another caveat that was not addressed was the intensity of STAT3 staining in astrocytes, other published work has addressed this and sorted their data by the intensity of expression. This level of data analysis may provide clearer answers in comparing astrocytes across disease progression.

The results from this chapter show for the first time that the earliest stages of neuronal stress caused by Psmc1 loss trigger activation of STAT3 in astrocytes, and the initiation of the classic astrogliosis response. This indicates that astrocytes can detect and respond to a stimulus linked to STAT3 signaling networks very soon after proteolysis in neurons is compromised. It seems

reasonable to speculate that an active process causes this stimulation of astrocytes, as the initiation of STAT3 signaling precedes any overt damage or apoptotic or necrotic death of neurons, which would be expected to cause gliosis in a more responsive manner. The next question was to address the unknown triggers that could lead to astrogliosis as a result of neuronal proteasomal depletion.

6.4 Triggers for STAT3 activation in astrocytes

The aim of chapter 5 was to assess potential agonists of astrocytic-STAT3, as candidates for the stimulus that triggers gliosis in the early period after Psmc1 deletion. Agonists were chosen based on their perceived feasibility as mediators in relation to neuronal proteasomal depletion. There are two main feasible mechanisms for STAT3 activation and phosphorylation in astrocytes: the release of cytoplasmic DAMPS (ATP/ADP) and the active release of pro-inflammatory cytokines.

Quantitative PCR of hippocampi tissue of the Psmc1$^{fl/fl}$;CaMKIIα-*cre* model reported a significant increase in TNF-α throughout disease progression, displaying significant upregulation at 3, 4 and 5 weeks of age. IL-6 also reported a significant increase at 5 weeks of age. CXCL10 displayed a significant fold change from 3-week old to 5-week old Psmc1$^{fl/fl}$;CaMKIIα-*cre* model. This is of interest, as neutrophil degranulation, a pathway indicated in SWATH-MS data in chapter 3, releases CXCL10 (Benigni et al., 2017; Rawat, Syeda and Shrivastava, 2021).

It must be noted that real-time quantitative PCR (RT-qPCR) data must be treated with caution. In addition to analyzing potential agonists, markers of gliosis GFAP and STAT3α were also assessed by RT-qPCR. Despite GFAP and STAT3α displaying a significant upregulation in immunohistochemistry and western blotting at 3 weeks old, this significance was not matched by RT-qPCR data. One of the reasons for this may be due to RT-qPCR primers mapping to isoforms that were overlooked in the immunohistochemistry and western blotting data and can also be explained due to the large standard error of the mean, which may be remedied by the addition of extra samples.

Acute slice experiments reported an increase in astrocytic-STAT3 tyrosine 705 phosphorylation at the cut edge, and western-blot supported that TNF-α, IL-6 and CXCL10 also could produce STAT3 tyrosine 705 phosphorylation, however, the localisation of this response to astrocytes could not be validated due to slice deterioration, technical difficulty, and time limitations. This, therefore, limited the conclusions that could have been drawn from this work. However, colleagues in the lab have demonstrated treatment of cortical astrocytes with TNF-α does lead to tyrosine 705 phosphorylation (Hareeri, 2021 – manuscript under review).

TNF-α is known to be released from proteasome-compromised neurons and has been evidenced in a range of neurodegenerative diseases such as Alzheimer's disease and Parkinson's disease (Sriram et al., 2002; Chang, Yee and Sumbria, 2017; Amin et al., 2022). Secondly, TNF-α is a potent activator of astrogliosis and thirdly, SWATH-MS pathways that are triggered for cell death, such as necroptosis, are initiated by TNF-α signaling (Gavillet, Allaman and Magistretti, 2008; Zhang et al., 2009; Alé et al., 2014; Habbas et al., 2015; Abd-El-Basset et al., 2021; Zhao et al., 2022). In conclusion, the data of this chapter suggests TNF-α to be a credible agonist of STAT3-driven astrogliosis in this model.

6.5 Limitations and future plans

The validation of TNF-α as the initiator of STAT3-driven astrogliosis needs further validation. This could potentially be done by transfecting organotypic hippocampal slices of the Psmc1$^{fl/fl}$;CaMKIIα-*cre* mice with SiRNA for TNF-α to assess if this improves disease progression. Additionally, the characterisation of STAT3 expressing astrocytes needs to be developed, potentially through studying astrocytic-phagocytosis markers. For the progression of this research to be truly translational, *in-vivo* experiments will need to be performed to assess the consequence of astrocytic-STAT3 phosphorylation on disease pathology within this mouse model.

6.6 Conclusion

Overall, this thesis has demonstrated the utility of SWATH as a way of increasing detail of molecular changes at a network level, identified activation of astrocyte STAT3 as the origin of early astrogliosis in the model, and identified a plausible candidate for the upstream stimulus that astrocytes detect as a first indicator that neuronal protein handling is compromised. Filling in the details further will help understand the sequence of events that leads from protein dysregulation to neurotoxic death.

Chapter 7 References

ABD-EL-BASSET, E.M. et al. (2021) Tumor necrosis factor (TNF) induces astrogliosis, microgliosis and promotes survival of cortical neurons. *AIMS Neuroscience*, 8(4), p. 558.

ABJEAN, L. et al. (2022) Reactive astrocytes promote proteostasis in Huntington's disease through the JAK2-STAT3 pathway. *Brain : a journal of neurology*, [Online] Available from: doi.org/10.1093/BRAIN/AWAC068 [Accessed 07/05/2022].

ABJEAN, L. et al. (2021) The JAK2-STAT3 pathway controls a beneficial proteostasis response of reactive astrocytes in Huntington's disease. *bioRxiv*, p. 2021.04.29.441924.

ACARIN, L., GONZÁLEZ, B. and CASTELLANO, B. (2000) STAT3 and NFκB Activation Precedes Glial Reactivity in the Excitotoxically Injured Young Cortex but not in the Corresponding Distal Thalamic Nuclei. *Journal of Neuropathology & Experimental Neurology*, 59(2), pp. 151–163.

ADAMS, D.E., BLISKA, J.B. and COZZARELLI, N.R. (1992) Cre-lox recombination in Escherichia coli cells mechanistic differences from the in Vitro reaction. *Journal of Molecular Biology*, 226(3), pp. 661–673.

AHMED, T. and FREY, J.U. (2005) Plasticity-specific phosphorylation of CaMKII, MAP-kinases and CREB during late-LTP in rat hippocampal slices in vitro. *Neuropharmacology*, 49(4), pp. 477–492.

AIMONE, J.B. et al. (2014) Regulation and function of adult neurogenesis: from genes to cognition. *Physiological reviews*, 94(4), pp. 991–1026.

AIZENSTEIN, H.J. et al. (2008) Frequent Amyloid Deposition Without Significant Cognitive Impairment Among the Elderly. *Archives of Neurology*, 65(11), pp. 1509–1517.

ALBERT-GASCÓ, H. et al. (2020) MAP/ERK Signaling in Developing Cognitive and Emotional Function and Its Effect on Pathological and Neurodegenerative Processes. *International Journal of Molecular Sciences 2020, Vol. 21, Page 4471*, 21(12), p. 4471.

ALÉ, A. et al. (2014) Treatment with anti-TNF alpha protects against the neuropathy induced by the proteasome inhibitor bortezomib in a mouse model. *Experimental Neurology*, 253, pp. 165–173.

ALI, A., BISWAS, A. and PAL, M. (2019) HSF1 mediated TNF-α production during proteotoxic stress response pioneers proinflammatory signal in human cells. *FASEB Journal*, 33(2), pp. 2621–2635.

AMIN, R. et al. (2022) The role of Tumour Necrosis Factor in neuroinflammation associated with Parkinson's disease and targeted therapies. *Neurochemistry International*, 158, p. 105376.

ARANDA-ANZALDO, A. (2012) The post-mitotic state in neurons correlates with a stable nuclear higher-order structure. *Communicative & Integrative Biology*, 5(2), p. 134.

ARRASATE, M. et al. (2004) Inclusion body formation reduces levels of mutant huntingtin and the risk of neuronal death. *Nature*, 431(7010), pp. 805–810.

ASHFORD, T.P. and PORTER, K.R. (1962) Cytoplasmic components in hepatic cell lysosomes . *The Journal of Cell Biology*, 12(1), p. 198.

ASUNI, A.A. et al. (2007) Immunotherapy targeting pathological tau conformers in a tangle mouse model reduces brain pathology with associated functional improvements. *The Journal of neuroscience : the official journal of the Society for Neuroscience*, 27(34), pp. 9115–9129.

BANDEIRA, F., LENT, R. and HERCULANO-HOUZEL, S. (2009) Changing numbers of neuronal and non-neuronal cells underlie postnatal brain growth in the rat. *Proceedings of the National Academy of Sciences of the United States of America*, 106(33), p. 14108.

BEASON-HELD, L.L. et al. (2013) Changes in Brain Function Occur Years before the Onset of Cognitive Impairment. *The Journal of Neuroscience*, 33(46), p. 18008.

BEDFORD, L. et al. (2010) Assembly, Structure and Function of the 26S proteasome. *Trends in cell biology*, 20(7), p. 391.

BEDFORD, L. et al. (2008) Depletion of 26S proteasomes in mouse brain neurons causes neurodegeneration and Lewy-like inclusions resembling human pale bodies. *The Journal of neuroscience : the official journal of the Society for Neuroscience*, 28(33), pp. 8189–8198.

BEGLOPOULOS, V. and SHEN, J. (2004) Gene-targeting technologies for the study of neurological disorders. *NeuroMolecular Medicine*, 6(1), pp. 13–30.

BELLE, A.M. et al. (2018) Evaluation of in vitro neuronal platforms as surrogates for in vivo whole brain systems. *Scientific Reports 2018 8:1*, 8(1), pp. 1–9.

BENGOA-VERGNIORY, N. et al. (2017) Alpha-synuclein oligomers: a new hope. *Acta neuropathologica*, 134(6), pp. 819–838.

BENIGNI, G. et al. (2017) CXCR3/CXCL10 Axis Regulates Neutrophil–NK Cell Cross-Talk Determining the Severity of Experimental Osteoarthritis. *The Journal of Immunology*, 198(5), pp. 2115–2124.

BENTEA, E., VERBRUGGEN, L. and MASSIE, A. (2017) The Proteasome Inhibition Model of Parkinson's Disease. *Journal of Parkinson's Disease*, 7(1), p. 31.

BHEDA, A. et al. (2010) Ubiquitin editing enzyme UCH L1 and microtubule dynamics: Implication in mitosis. *Cell cycle (Georgetown, Tex.)*, 9(5), p. 980.

BILLINGHAM, R.E. and BOSWELL, T. (1953) Studies on the problem of corneal homografts. *Proceedings of the Royal Society of London. Series B - Biological Sciences*, 141(904), pp. 392–406.

BIRAN, A. et al. (2017) A 20S proteasome receptor for degradation of intrinsically disordered proteins. *bioRxiv*, p. 210898.

BISHOP, P., ROCCA, D. and HENLEY, J.M. (2016) Ubiquitin C-terminal hydrolase L1 (UCH-L1): structure, distribution and roles in brain function and dysfunction. *Biochemical Journal*, 473(16), p. 2453.

BOOTH, H.D.E., HIRST, W.D. and WADE-MARTINS, R. (2017) The Role of Astrocyte Dysfunction in Parkinson's Disease Pathogenesis. *Trends in neurosciences*, 40(6), pp. 358–370.

BOVÉ, J. et al. (2006) Proteasome inhibition and Parkinson's disease modeling. *Annals of Neurology*, 60(2), pp. 260–264.

BRADL, M. and LASSMANN, H. (2010) Oligodendrocytes: biology and pathology. *Acta Neuropathologica*, 119(1), p. 37.

BREDER, C.D. et al. (1993) Distribution and characterization of tumor necrosis factor-α-like immunoreactivity in the murine central nervous system. *Journal of Comparative Neurology*, 337(4), pp. 543–567.

BREUNIG, J.J. et al. (2012) Rapid genetic targeting of pial surface neural progenitors and immature neurons by neonatal electroporation. *Neural Development*, 7(1), pp. 1–13.

BUNK, J. et al. (2021) Cathepsin D Variants Associated With Neurodegenerative Diseases Show Dysregulated Functionality and Modified α-Synuclein Degradation Properties. *Frontiers in Cell and Developmental Biology*, 9, [Online] Available from: doi.org/10.3389/FCELL.2021.581805/FULL [Accessed 03/06/2022].

BUOSI, A.S. et al. (2018) Heterogeneity in Synaptogenic Profile of Astrocytes from Different Brain Regions. *Molecular Neurobiology*, 55(1), pp. 751–762.

BURGIN, K.E. et al. (1990) In situ hybridization histochemistry of Ca2+/calmodulin-dependent protein kinase in developing rat brain. *The Journal of neuroscience : the official journal of the Society for Neuroscience*, 10(6), pp. 1788–1798.

BUSH, K.T., GOLDBERG, A.L. and NIGAM, S.K. (1997) Proteasome Inhibition Leads to a Heat-shock Response, Induction of Endoplasmic Reticulum Chaperones, and Thermotolerance *. *Journal of Biological Chemistry*, 272(14), pp. 9086–9092.

BUSH, T.G. et al. (1999) Leukocyte infiltration, neuronal degeneration, and neurite outgrowth after ablation of scar-forming, reactive astrocytes in adult transgenic mice. *Neuron*, 23(2), pp. 297–308.

BUSHONG, E.A., MARTONE, M.E. and ELLISMAN, M.H. (2004) Maturation of astrocyte morphology and the establishment of astrocyte domains during postnatal hippocampal development. *International journal of developmental neuroscience : the official journal of the International Society for Developmental Neuroscience*, 22(2), pp. 73–86.

BUTOVSKY, O. et al. (2014) Identification of a unique TGF-β-dependent molecular and functional signature in microglia. *Nature neuroscience*, 17(1), pp. 131–143.

BUYLOVA GOLA, A. et al. (2020) Healthcare utilization and monetary costs associated with agitation in UK care home residents with advanced dementia: a prospective cohort study. *International Psychogeriatrics*, 32(3), pp. 359–370.

CAHOY, J.D. et al. (2008) A Transcriptome Database for Astrocytes, Neurons, and Oligodendrocytes: A New Resource for Understanding Brain Development and Function. *The Journal of Neuroscience*, 28(1), p. 264.

CAMPOREALE, A. and POLI, V. (2011) IL-6, IL-17 and STAT3: A holy trinity in auto-immunity? *Frontiers in Bioscience*, 17(6), pp. 2306–2326.

CAPECCHI, M.R. (1989) The new mouse genetics: altering the genome by gene targeting. *Trends in genetics : TIG*, 5(3), pp. 70–76.

CARLYLE, B.C., TROMBETTA, B.A. and ARNOLD, S.E. (2018a) Proteomic Approaches for the Discovery of Biofluid Biomarkers of Neurodegenerative Dementias. *Proteomes 2018, Vol. 6, Page 32*, 6(3), p. 32.

CARLYLE, B.C., TROMBETTA, B.A. and ARNOLD, S.E. (2018b) Proteomic Approaches for the Discovery of Biofluid Biomarkers of Neurodegenerative Dementias. *Proteomes 2018, Vol. 6, Page 32*, 6(3), p. 32.

CASANOVA, E. et al. (2001) A CamKIIalpha iCre BAC allows brain-specific gene inactivation. *Genesis (New York, N.Y. : 2000)*, 31(1), pp. 37–42.

CEYZÉRIAT, K., BEN HAIM, L., DENIZOT, A., POMMIER, D., MATOS, M., GUILLEMAUD, O., PALOMARES, M.A., et al. (2018) Modulation of astrocyte reactivity improves functional deficits in mouse models of Alzheimer's disease. *Acta neuropathologica communications*, 6(1), p. 104.

CEYZÉRIAT, K., BEN HAIM, L., DENIZOT, A., POMMIER, D., MATOS, M., GUILLEMAUD, O., PALOMARES, M.-A., et al. (2018) Modulation of astrocyte reactivity improves functional deficits in mouse models of Alzheimer's disease. *Acta Neuropathologica Communications 2018 6:1*, 6(1), pp. 1–23.

CEYZÉRIAT, K. et al. (2016) The complex STATes of astrocyte reactivity: How are they controlled by the JAK-STAT3 pathway? *Neuroscience*, 330, pp. 205–218.

CHANG, R., YEE, K.-L. and SUMBRIA, R.K. (2017) Tumor necrosis factor α Inhibition for Alzheimer's Disease. *Journal of Central Nervous System Disease*, 9, p. 117957351770927.

CHARLES, V. et al. (2000) Alpha-synuclein immunoreactivity of huntingtin polyglutamine aggregates in striatum and cortex of Huntington's disease patients and transgenic mouse models. *Neuroscience letters*, 289(1), pp. 29–32.

CHAUDHURI, A.D. et al. (2018) TNFα and IL-1β modify the miRNA cargo of astrocyte shed extracellular vesicles to regulate neurotrophic signaling in neurons. *Cell death & disease*, 9(3), [Online] Available from: doi.org/10.1038/S41419-018-0369-4 [Accessed 15/07/2022].

CHEN, Z. et al. (2021) Necroptotic astrocytes induced neuronal apoptosis partially through EVs-derived pro-BDNF. *Brain Research Bulletin*, 177, pp. 73–80.

CHO, S. et al. (2004) Spatiotemporal evidence of apoptosis-mediated ischemic injury in organotypic hippocampal slice cultures. *Neurochemistry international*, 45(1), pp. 117–127.

CHO, S., WOOD, A. and BOWLBY, M.R. (2007) Brain Slices as Models for Neurodegenerative Disease and Screening Platforms to Identify Novel Therapeutics. *Current Neuropharmacology*, 5(1), p. 19.

CHOI, M. et al. (2020) Inhibition of STAT3 phosphorylation attenuates impairments in learning and memory in 5XFAD mice, an animal model of Alzheimer's disease. *Journal of pharmacological sciences*, 143(4), pp. 290–299.

CHONG, S.H., IM, H. and HAM, S. (2019) Explicit Characterization of the Free Energy Landscape of pKID-KIX Coupled Folding and Binding. *ACS Central Science*, 5(8), pp. 1342–1351.

CHRISTIAN REINHARDT, H. and YAFFE, M.B. (2013) Phospho-Ser/Thr-binding domains: navigating the cell cycle and DNA damage response. *Nature Reviews Molecular Cell Biology 2013 14:9*, 14(9), pp. 563–580.

CIBOROWSKI, P. and SILBERRING, J. (2013) Proteomic Profiling and Analytical Chemistry. *Proteomic Profiling and Analytical Chemistry*, pp. 1–245.

CIBOROWSKI, P. and SILBERRING, J. (2016) Proteomic profiling and analytical chemistry : the crossroads.

CIECHANOVER, A. et al. (1981) Activation of the heat-stable polypeptide of the ATP-dependent proteolytic system. *Proceedings of the National Academy of Sciences of the United States of America*, 78(2 II), pp. 761–765.

CIECHANOVER, A. and SCHWARTZ, A.L. (1998) The ubiquitin-proteasome pathway: The complexity and myriad functions of proteins death. *Proceedings of the National Academy of Sciences of the United States of America*, 95(6), p. 2727.

CLAIREMBAULT, T. et al. (2014) Enteric GFAP expression and phosphorylation in Parkinson's disease. *Journal of Neurochemistry*, 130(6), pp. 805–815.

CLARKE, L.E. and BARRES, B.A. (2013) Emerging roles of astrocytes in neural circuit development. *Nature reviews. Neuroscience*, 14(5), p. 311.

COLOMBO, E. and FARINA, C. (2016) Astrocytes: Key Regulators of Neuroinflammation. *Trends in immunology*, 37(9), pp. 608–620.

COLOM-CADENA, M. et al. (2013) Confluence of α-synuclein, tau, and β-amyloid pathologies in dementia with Lewy bodies. *Journal of neuropathology and experimental neurology*, 72(12), pp. 1203–1212.

COX, D., CARVER, J.A. and ECROYD, H. (2014) Preventing α-synuclein aggregation: The role of the small heat-shock molecular chaperone proteins. *Biochimica et Biophysica Acta (BBA) - Molecular Basis of Disease*, 1842(9), pp. 1830–1843.

CRABBÉ, M. et al. (2019) Excitotoxic neurodegeneration is associated with a focal decrease in metabotropic glutamate receptor type 5 availability: an in vivo PET imaging study. *Scientific Reports 2019 9:1*, 9(1), pp. 1–10.

CROFT, C.L. et al. (2017) Inhibition of glycogen synthase kinase-3 by BTA-EG4 reduces tau abnormalities in an organotypic brain slice culture model of Alzheimer's disease. *Scientific Reports 2017 7:1*, 7(1), pp. 1–11.

CROFT, C.L. et al. (2019) rAAV-based brain slice culture models of Alzheimer's and Parkinson's disease inclusion pathologies. *Journal of Experimental Medicine*, 216(3), pp. 539–555.

CUMMING, R.C. et al. (2007) Increase in expression levels and resistance to sulfhydryl oxidation of peroxiredoxin isoforms in amyloid beta-resistant nerve cells. *The Journal of biological chemistry*, 282(42), pp. 30523–30534.

CURRAIS, A. et al. (2017) Intraneuronal protein aggregation as a trigger for inflammation and neurodegeneration in the aging brain. *The FASEB Journal*, 31(1), pp. 5–10.

DANIELE, S.G. et al. (2015) Activation of MyD88-dependent TLR1/2 signaling by misfolded α-synuclein, a protein linked to neurodegenerative disorders. *Science signaling*, 8(376), [Online] Available from: doi.org/10.1126/SCISIGNAL.2005965 [Accessed 15/07/2022].

DAS, S. et al. (2020a) Meta-analysis of mouse transcriptomic studies supports a context-dependent astrocyte reaction in acute CNS injury versus neurodegeneration. *Journal of Neuroinflammation 2020 17:1*, 17(1), pp. 1–17.

DAS, S. et al. (2020b) Meta-analysis of mouse transcriptomic studies supports a context-dependent astrocyte reaction in acute CNS injury versus neurodegeneration. *Journal of Neuroinflammation 2020 17:1*, 17(1), pp. 1–17.

DAS, S. et al. (2020c) Meta-analysis of mouse transcriptomic studies supports a context-dependent astrocyte reaction in acute CNS injury versus neurodegeneration. *Journal of Neuroinflammation 2020 17:1*, 17(1), pp. 1–17.

DATTA CHAUDHURI, A. et al. (2020) Stimulus-dependent modifications in astrocyte-derived extracellular vesicle cargo regulate neuronal excitability. *Glia*, 68(1), pp. 128–144.

DAVID, D.C. et al. (2010) Widespread Protein Aggregation as an Inherent Part of Aging in C. elegans. *PLOS Biology*, 8(8), p. e1000450.

DAVIDSON, S. et al. (2022) Protein kinase R is an innate immune sensor of proteotoxic stress via accumulation of cytoplasmic IL-24. *Science Immunology*, 7(68), [Online] Available from: doi.org/10.1126/SCIIMMUNOL.ABI6763 [Accessed 31/07/2022].

DAWSON, T.M. and DAWSON, V.L. (2010) The Role of Parkin in Familial and Sporadic Parkinson's Disease. *Movement disorders : official journal of the Movement Disorder Society*, 25(0 1), p. S32.

DAY, I.N.M. and THOMPSON, R.J. (2010) UCHL1 (PGP 9.5): neuronal biomarker and ubiquitin system protein. *Progress in neurobiology*, 90(3), pp. 327–362.

DEIANA, A. et al. (2019) Intrinsically disordered proteins and structured proteins with intrinsically disordered regions have different functional roles in the cell. *PLoS ONE*, 14(8), [Online] Available from: doi.org/10.1371/JOURNAL.PONE.0217889 [Accessed 09/07/2022].

DETURE, M.A. and DICKSON, D.W. (2019) The neuropathological diagnosis of Alzheimer's disease. *Molecular Neurodegeneration 2019 14:1*, 14(1), pp. 1–18.

DHURIYA, Y.K. and SHARMA, D. (2018) Necroptosis: a regulated inflammatory mode of cell death. *Journal of Neuroinflammation 2018 15:1*, 15(1), pp. 1–9.

DIAMANDIS, E.P. (2004) Mass Spectrometry as a Diagnostic and a Cancer Biomarker Discovery Tool: Opportunities and Potential Limitations *. *Molecular & Cellular Proteomics*, 3(4), pp. 367–378.

DIBATTISTA, A.M., SIERRA, F. and MASLIAH, E. (2020) NIA workshop on senescence in brain aging and Alzheimer's disease and its related dementias. *GeroScience 2020 42:2*, 42(2), pp. 389–396.

DICKSON, D.W. et al. (1994) Immunoreactivity profile of hippocampal CA2/3 neurites in diffuse Lewy body disease. *Acta neuropathologica*, 87(3), pp. 269–276.

DJAKOVIC, S.N. et al. (2009) Regulation of the Proteasome by Neuronal Activity and Calcium/Calmodulin-dependent Protein Kinase II. *The Journal of Biological Chemistry*, 284(39), p. 26655.

DODART, J.C. et al. (2002) Immunization reverses memory deficits without reducing brain Abeta burden in Alzheimer's disease model. *Nature neuroscience*, 5(5), pp. 452–457.

DOMERCQ, M., VAZQUEZ-VILLOLDO, N. and MATUTE, C. (2013) Neurotransmitter signaling in the pathophysiology of microglia. *Frontiers in Cellular Neuroscience*, 0(APR), p. 49.

DOORN, K.J. et al. (2014) Microglial phenotypes and toll-like receptor 2 in the substantia nigra and hippocampus of incidental Lewy body disease cases and Parkinson's disease patients. *Acta Neuropathologica Communications*, 2(1), [Online] Available from: doi.org/10.1186/s40478-014-0090-1 [Accessed 15/07/2022].

DOUGHERTY, S.E. et al. (2020) Expanding Role of Ubiquitin in Translational Control. *International Journal of Molecular Sciences 2020, Vol. 21, Page 1151*, 21(3), p. 1151.

DE DUVE, C. (1963) The lysosome. *Scientific American*, 208, pp. 64–72.

DE DUVE, C. and WATTIAUX, R. (1966) Functions of lysosomes. *Annual review of physiology*, 28, pp. 435–492.

ELKHARAZ, J. et al. (2013a) Implications for oxidative stress and astrocytes following 26S proteasomal depletion in mouse forebrain neurones. *Biochimica et Biophysica Acta - Molecular Basis of Disease*, 1832(12), pp. 1930–1938.

ELKHARAZ, J. et al. (2013b) Implications for oxidative stress and astrocytes following 26S proteasomal depletion in mouse forebrain neurones. *Biochimica et Biophysica Acta (BBA) - Molecular Basis of Disease*, 1832(12), pp. 1930–1938.

ETLINGER, J.D. and GOLDBERG, A.L. (1977) A soluble ATP-dependent proteolytic system responsible for the degradation of abnormal proteins in reticulocytes. *Proceedings of the National Academy of Sciences of the United States of America*, 74(1), pp. 54–58.

EYO, U.B. et al. (2013) "P2X7 Receptor Activation Regulates Microglial Cell Death During Oxygen-Glucose Deprivation". *Neuropharmacology*, 73, p. 311.

FAN, Y., XIE, L. and CHUNG, C.Y. (2017) Signaling Pathways Controlling Microglia Chemotaxis. *Molecules and Cells*, 40(3), p. 163.

FAN, Y.Y. and HUO, J. (2021) A1/A2 astrocytes in central nervous system injuries and diseases: Angels or devils? *Neurochemistry International*, 148, p. 105080.

FARRELL, M.E. et al. (2017) Association of Longitudinal Cognitive Decline With Amyloid Burden in Middle-aged and Older Adults: Evidence for a Dose-Response Relationship. *JAMA Neurology*, 74(7), p. 830.

FATTORI, E. et al. (1995) IL-6 Expression in Neurons of Transgenic Mice Causes Reactive Astrocytosis and Increase in Ramified Microglial Cells but no Neuronal Damage. *European Journal of Neuroscience*, 7(12), pp. 2441–2449.

FELLNER, L. et al. (2013) Toll-like receptor 4 is required for α-synuclein dependent activation of microglia and astroglia. *Glia*, 61(3), p. 349.

FERNÁNDEZ-CRUZ, I. and REYNAUD, E. (2021) Proteasome Subunits Involved in Neurodegenerative Diseases. *Archives of Medical Research*, 52(1), pp. 1–14.

FIESEL, F.C. et al. (2015) Structural and Functional Impact of Parkinson Disease-Associated Mutations in the E3 Ubiquitin Ligase Parkin. *Human mutation*, 36(8), pp. 774–786.

FINLEY, D. (2009) Recognition and processing of ubiquitin-protein conjugates by the proteasome. *Annual review of biochemistry*, 78, pp. 477–513.

FITTING, S. et al. (2010) Regional Heterogeneity and Diversity in Cytokine and Chemokine Production by Astroglia: Differential Responses to HIV-1 Tat, gp120 and Morphine Revealed by Multiplex Analysis. *Journal of proteome research*, 9(4), p. 1795.

FLÜGGE, G. et al. (2014) NDRG2 as a marker protein for brain astrocytes. *Cell and Tissue Research*, 357(1), pp. 31–41.

FORNAI, F. et al. (2003) Fine Structure and Biochemical Mechanisms Underlying Nigrostriatal Inclusions and Cell Death after Proteasome Inhibition. *The Journal of Neuroscience*, 23(26), p. 8955.

FOSTER, L. (2017) Active Ageing, Pensions and Retirement in the UK. *Journal of Population Ageing 2017 11:2*, 11(2), pp. 117–132.

FRANKLIN, K. and PAXINOS, G. (2008) The mouse brain atlas. *The Spinal Cord: A Christopher and Dana Reeve Foundation Text and Atlas*, p. 2007.

FUJII, T., BAUMGÄRTL, H. and LÜBBERS, D.W. (1982) Limiting section thickness of guinea pig olfactory cortical slices studied from tissue pO2 values and electrical activities. *Pflugers Archiv : European journal of physiology*, 393(1), pp. 83–87.

GANDELMAN, M. et al. (2010) Extracellular ATP and the P2X7 receptor in astrocyte-mediated motor neuron death: implications for amyotrophic lateral sclerosis. *Journal of Neuroinflammation*, 7, p. 33.

GANGULY, A. et al. (2017) Hsc70 chaperone activity is required for the cytosolic slow axonal transport of synapsin. *Journal of Cell Biology*, 216(7), pp. 2059–2074.

GAO, H. et al. (2021) Isoform-Specific Effects of Apolipoprotein E on Hydrogen Peroxide-Induced Apoptosis in Human Induced Pluripotent Stem Cell (iPSC)-Derived Cortical Neurons. *International Journal of Molecular Sciences 2021, Vol. 22, Page 11582*, 22(21), p. 11582.

GARWOOD, C. et al. (2013) Calcium dysregulation in relation to Alzheimer-type pathology in the ageing brain. *Neuropathology and Applied Neurobiology*, 39(7), pp. 788–799.

GARWOOD, C.J. et al. (2011) Astrocytes are important mediators of Aβ-induced neurotoxicity and tau phosphorylation in primary culture. *Cell Death & Disease 2011 2:6*, 2(6), pp. e167–e167.

GAVILLET, M., ALLAMAN, I. and MAGISTRETTI, P.J. (2008) Modulation of astrocytic metabolic phenotype by proinflammatory cytokines. *Glia*, 56(9), pp. 975–989.

GE, W.P. et al. (2012) Local generation of glia is a major astrocyte source in postnatal cortex. *Nature*, 484(7394), p. 376.

GEISZLER, P.C. et al. (2018a) Dynamic metabolic patterns tracking neurodegeneration and gliosis following 26S proteasome dysfunction in mouse forebrain neurons. *Scientific reports*, 8(1), [Online] Available from: doi.org/10.1038/S41598-018-23155-2 [Accessed 03/06/2022].

GEISZLER, P.C. et al. (2018b) Dynamic metabolic patterns tracking neurodegeneration and gliosis following 26S proteasome dysfunction in mouse forebrain neurons. *Scientific reports*, 8(1), [Online] Available from: doi.org/10.1038/S41598-018-23155-2 [Accessed 21/07/2022].

GENGATHARAN, A., BAMMANN, R.R. and SAGHATELYAN, A. (2016) The Role of Astrocytes in the Generation, Migration, and Integration of New Neurons in the Adult Olfactory Bulb. *Frontiers in Neuroscience*, 10(APR), p. 149.

GHOSH, M., XU, Y. and PEARSE, D.D. (2016) Cyclic AMP is a key regulator of M1 to M2a phenotypic conversion of microglia in the presence of Th2 cytokines. *Journal of Neuroinflammation*, 13(1), [Online] Available from: doi.org/10.1186/S12974-015-0463-9 [Accessed 14/07/2022].

GIANNAKI, M. et al. (2021) STAT3-dependent regulation of the electrogenic Na +/ HCO 3 - cotransporter 1 (NBCe1) functional expression in cortical astrocytes. *Journal of cellular physiology*, 236(3), pp. 2036–2050.

GIDALEVITZ, T., PRAHLAD, V. and MORIMOTO, R.I. (2011) The Stress of Protein Misfolding: From Single Cells to Multicellular Organisms. *Cold Spring Harbor Perspectives in Biology*, 3(6), pp. 1–18.

GILLET, L.C. et al. (2012) Targeted data extraction of the MS/MS spectra generated by data-independent acquisition: a new concept for consistent and accurate proteome analysis.

Molecular & cellular proteomics : MCP, 11(6), [Online] Available from: doi.org/10.1074/MCP.O111.016717 [Accessed 16/07/2022].

GILMAN, S. et al. (2005) Clinical effects of Aβ immunization (AN1792) in patients with AD in an interrupted trial. *Neurology*, 64(9), pp. 1553–1562.

GOETZL, E.J. et al. (2016) Cargo proteins of plasma astrocyte-derived exosomes in Alzheimer's disease. *FASEB journal : official publication of the Federation of American Societies for Experimental Biology*, 30(11), pp. 3853–3859.

GOMES, A. V. (2013) Genetics of Proteasome Diseases. *Scientifica*, 2013, pp. 1–30.

GORDON, S. (2003) Alternative activation of macrophages. *Nature Reviews Immunology 2003 3:1*, 3(1), pp. 23–35.

GROH, N. et al. (2017) Age-dependent protein aggregation initiates amyloid-β aggregation. *Frontiers in Aging Neuroscience*, 9(MAY), p. 138.

GU, X.L. et al. (2010) Astrocytic expression of Parkinson's disease-related A53T α-synuclein causes neurodegeneration in mice. *Molecular Brain*, 3(1), p. 12.

GUILLEMAUD, O. et al. (2020) Complex roles for reactive astrocytes in the triple transgenic mouse model of Alzheimer disease. *Neurobiology of Aging*, 90, pp. 135–146.

GUO, M. et al. (2020) Fasudil inhibits the activation of microglia and astrocytes of transgenic Alzheimer's disease mice via the downregulation of TLR4/Myd88/NF-κB pathway. *Journal of neuroimmunology*, 346, p. 577284.

GUO, S., WANG, H. and YIN, Y. (2022) Microglia Polarization From M1 to M2 in Neurodegenerative Diseases. *Frontiers in Aging Neuroscience*, 14, [Online] Available from: doi.org/10.3389/FNAGI.2022.815347/FULL [Accessed 15/07/2022].

GUO, W., STOKLUND DITTLAU, K. and VAN DEN BOSCH, L. (2020) Axonal transport defects and neurodegeneration: Molecular mechanisms and therapeutic implications. *Seminars in cell & developmental biology*, 99, pp. 133–150.

HABBAS, S. et al. (2015) Neuroinflammatory TNFα Impairs Memory via Astrocyte Signaling. *Cell*, 163(7), pp. 1730–1741.

HABCHI, J. et al. (2014) Introducing protein intrinsic disorder. *Chemical Reviews*, 114(13), pp. 6561–6588.

HAIM, L. BEN et al. (2015) The JAK/STAT3 Pathway Is a Common Inducer of Astrocyte Reactivity in Alzheimer's and Huntington's Diseases. *Journal of Neuroscience*, 35(6), pp. 2817–2829.

HALASSA, M.M. et al. (2007) Synaptic Islands Defined by the Territory of a Single Astrocyte. *Journal of Neuroscience*, 27(24), pp. 6473–6477.

HAN, R.T. et al. (2021) Astrocyte-immune cell interactions in physiology and pathology. *Immunity*, 54(2), pp. 211–224.

HANZEL, C.E. et al. (2014) Neuronal driven pre-plaque inflammation in a transgenic rat model of Alzheimer's disease. *Neurobiology of aging*, 35(10), pp. 2249–2262.

HARRISON, E.M. (2013) Understanding suffering: Utermohlen's self-portraits and Alzheimer's disease. *Nurse educator*, 38(1), pp. 20–25.

HARTL, F.U., BRACHER, A. and HAYER-HARTL, M. (2011) Molecular chaperones in protein folding and proteostasis. *Nature 2011 475:7356*, 475(7356), pp. 324–332.

HAYASHI, H. et al. (2007) Apolipoprotein E-Containing Lipoproteins Protect Neurons from Apoptosis via a Signaling Pathway Involving Low-Density Lipoprotein Receptor-Related Protein-1. *The Journal of Neuroscience*, 27(8), p. 1933.

HE, D. et al. (2020) Bisdemethoxycurcumin exerts a cell-protective effect via JAK2/STAT3 signaling in a rotenone-induced Parkinson's disease model in vitro. *Folia histochemica et cytobiologica*, 58(2), pp. 127–134.

HE, F. et al. (2005) A positive autoregulatory loop of Jak-STAT signaling controls the onset of astrogliogenesis. *Nature Neuroscience 2005 8:5*, 8(5), pp. 616–625.

HENEKA, M.T. (2017) Inflammasome activation and innate immunity in Alzheimer's disease. *Brain Pathology*, 27(2), pp. 220–222.

HERCULANO-HOUZEL, S. (2009) The Human Brain in Numbers: A Linearly Scaled-up Primate Brain. *Frontiers in Human Neuroscience*, 3(NOV), [Online] Available from: doi.org/10.3389/NEURO.09.031.2009 [Accessed 09/07/2022].

HERSHKO, A. et al. (1983) Components of ubiquitin-protein ligase system. Resolution, affinity purification, and role in protein breakdown. *Journal of Biological Chemistry*, 258(13), pp. 8206–8214.

HICKMAN, S.E., ALLISON, E.K. and EL KHOURY, J. (2008) Microglial dysfunction and defective beta-amyloid clearance pathways in aging Alzheimer's disease mice. *The Journal of neuroscience : the official journal of the Society for Neuroscience*, 28(33), pp. 8354–8360.

HIGASHI, S. et al. (2007) Concurrence of TDP-43, tau and alpha-synuclein pathology in brains of Alzheimer's disease and dementia with Lewy bodies. *Brain research*, 1184(1), pp. 284–294.

HOFFMANN, A. et al. (2003) Elevation of basal intracellular calcium as a central element in the activation of brain macrophages (microglia): suppression of receptor-evoked calcium signaling and control of release function. *The Journal of neuroscience : the official journal of the Society for Neuroscience*, 23(11), pp. 4410–4419.

HOL, E.M. and PEKNY, M. (2015) Glial fibrillary acidic protein (GFAP) and the astrocyte intermediate filament system in diseases of the central nervous system. *Current Opinion in Cell Biology*, 32, pp. 121–130.

HOLMES, C. et al. (2008) Long-term effects of Aβ42 immunisation in Alzheimer's disease: follow-up of a randomised, placebo-controlled phase I trial. *The Lancet*, 372(9634), pp. 216–223.

HOLTMAN, I.R. et al. (2015) Induction of a common microglia gene expression signature by aging and neurodegenerative conditions: a co-expression meta-analysis. *Acta neuropathologica communications*, 3(1), p. 31.

HONG, S. and SONG, M.R. (2014) STAT3 but not STAT1 is required for astrocyte differentiation. *PloS one*, 9(1), [Online] Available from: doi.org/10.1371/JOURNAL.PONE.0086851 [Accessed 07/05/2022].

HONG, X.Y. et al. (2020) STAT3 ameliorates cognitive deficits by positively regulating the expression of NMDARs in a mouse model of FTDP-17. *Signal Transduction and Targeted Therapy 2020 5:1*, 5(1), pp. 1–13.

HONG, Y. et al. (2018) Progesterone suppresses Aβ42-induced neuroinflammation by enhancing autophagy in astrocytes. *International Immunopharmacology*, 54, pp. 336–343.

HOSHINO, T. et al. (2011) Suppression of Alzheimer's disease-related phenotypes by expression of heat shock protein 70 in mice. *The Journal of neuroscience : the official journal of the Society for Neuroscience*, 31(14), pp. 5225–5234.

HUANG, H. et al. (2020) The Active Constituent From Gynostemma Pentaphyllum Prevents Liver Fibrosis Through Regulation of the TGF-β1/NDRG2/MAPK Axis. *Frontiers in Genetics*, 11, p. 1395.

HUDMON, A. and SCHULMAN, H. (2002) Neuronal Ca2+/calmodulin-dependent protein kinase II: The role of structure and autoregulation in cellular function. *Annual Review of Biochemistry*, 71, pp. 473–510.

HUMPEL, C. (2015) Organotypic brain slice cultures: A review. *Neuroscience*, 305, pp. 86–98.

ICHIBA, M. et al. (1998) Autoregulation of the Stat3 Gene through Cooperation with a cAMP-responsive Element-binding Protein *. *Journal of Biological Chemistry*, 273(11), pp. 6132–6138.

ISHII, T., HAGA, S. and SHIMIZU, F. (1975) Identification of components of immunoglobulins in senile plaques by means of fluorescent antibody technique. *Acta Neuropathologica 1975 32:2*, 32(2), pp. 157–162.

ISRAELSSON, C. et al. (2010) Appearance of Cxcl10-expressing cell clusters is common for traumatic brain injury and neurodegenerative disorders. *European Journal of Neuroscience*, 31(5), pp. 852–863.

JAMES MURPHY, B.B. and STURM, E. CONDITIONS D E T E R M I N I N G THE TRANSPLANTABILITY OF TISSUES IN THE BRAIN.

JAYARAJ, R.L. et al. (2019) Neuroinflammation: friend and foe for ischemic stroke. *Journal of Neuroinflammation 2019 16:1*, 16(1), pp. 1–24.

JELLINGER, K.A. and POPESCU, B. (2012) Interaction between pathogenic proteins in neurodegenerative disorders. *Journal of Cellular and Molecular Medicine*, 16(6), p. 1166.

JEWETT, M. et al. (2018) Glutathione S-Transferase Alpha 4 Prevents Dopamine Neurodegeneration in a Rat Alpha-Synuclein Model of Parkinson's Disease. *Frontiers in Neurology*, 9(APR), p. 6.

JEWETT, M., JIMENEZ-FERRER, I. and SWANBERG, M. (2017) Astrocytic Expression of GSTA4 Is Associated to Dopaminergic Neuroprotection in a Rat 6-OHDA Model of Parkinson's Disease. *Brain Sciences*, 7(7), [Online] Available from: doi.org/10.3390/BRAINSCI7070073 [Accessed 22/07/2022].

JIANG, Y. et al. (2013) N-Acetyl cysteine blunts proteotoxicity in a heat shock protein-dependent manner. *Neuroscience*, 255, pp. 19–32.

JO, S. et al. (2014) GABA from reactive astrocytes impairs memory in mouse models of Alzheimer's disease. *Nature medicine*, 20(8), p. 886.

JOE, E.H. et al. (2018) Astrocytes, Microglia, and Parkinson's Disease. *Experimental Neurobiology*, 27(2), pp. 77–87.

JOHN LIN, C.C. et al. (2017) Identification of diverse astrocyte populations and their malignant analogs. *Nature neuroscience*, 20(3), p. 396.

JOHNSON, D. et al. (2013) Optimization of Data-Dependent Acquisition Parameters for Coupling High-Speed Separations with LC-MS/MS for Protein Identifications. *Journal of Biomolecular Techniques : JBT*, 24(2), p. 62.

JONES, R.S. et al. (2013) Amyloid-β-induced astrocytic phagocytosis is mediated by CD36, CD47 and RAGE. *Journal of neuroimmune pharmacology : the official journal of the Society on NeuroImmune Pharmacology*, 8(1), pp. 301–311.

JOO, E.J. et al. (2009) Regulation of Mn-Superoxide Dismutase Activity and Neuroprotection by STAT3 in Mice after Cerebral Ischemia. *The Journal of Neuroscience*, 29(21), p. 7003.

JULIO-CÉSAR, G. and ROSA-HELENA, B. (2018) The Genetic Diagnosis of Neurodegenerative Diseases and Therapeutic Perspectives. *Brain sciences*, 8(12), [Online] Available from: doi.org/10.3390/BRAINSCI8120222 [Accessed 31/05/2022].

JYLHÄ, A. et al. (2018) Comparison of itraq and swath in a clinical study with multiple time points. *Clinical Proteomics*, 15(1), pp. 1–11.

KAJIWARA, Y. et al. (2018) GJA1 (connexin43) is a key regulator of Alzheimer's disease pathogenesis. *Acta Neuropathologica Communications 2018 6:1*, 6(1), pp. 1–20.

KAKLAMANOS, G., APREA, E. and THEODORIDIS, G. (2016) Mass spectrometry: principles and instrumentation. *Encyclopedia of Food and Health*, pp. 661–668.

KASHON, M.L. et al. (2004) Associations of cortical astrogliosis with cognitive performance and dementia status. *Journal of Alzheimer's disease : JAD*, 6(6), pp. 595–604.

KECK, S. et al. (2003) Proteasome inhibition by paired helical filament-tau in brains of patients with Alzheimer's disease. *Journal of neurochemistry*, 85(1), pp. 115–122.

KELLER, A. et al. (2002) Empirical statistical model to estimate the accuracy of peptide identifications made by MS/MS and database search. *Analytical chemistry*, 74(20), pp. 5383–5392.

KELLY, P.T. and VERNON, P. (1985) Changes in the subcellular distribution of calmodulin-kinase II during brain development. *Brain research*, 350(1–2), pp. 211–224.

KEREKES, N., SANCHÉZ-PÉREZ, A.M. and LANDRY, M. (2021) Neuroinflammation as a possible link between attention-deficit/hyperactivity disorder (ADHD) and pain. *Medical Hypotheses*, 157, p. 110717.

KHAKH, B.S. and DENEEN, B. (2019) The Emerging Nature of Astrocyte Diversity. *Annual review of neuroscience*, 42, pp. 187–207.

KHAKH, B.S. and SOFRONIEW, M. V. (2015) Diversity of astrocyte functions and phenotypes in neural circuits. *Nature Neuroscience 2015 18:7*, 18(7), pp. 942–952.

KIM, C. et al. (2013) Neuron-released oligomeric α-synuclein is an endogenous agonist of TLR2 for paracrine activation of microglia. *Nature communications*, 4, [Online] Available from: doi.org/10.1038/NCOMMS2534 [Accessed 15/07/2022].

KLAIPS, C.L., JAYARAJ, G.G. and HARTL, F.U. (2018) Pathways of cellular proteostasis in aging and disease. *The Journal of cell biology*, 217(1), pp. 51–63.

KLEIN, C. and WESTENBERGER, A. (2012) Genetics of Parkinson's Disease. *Cold Spring Harbor Perspectives in Medicine*, 2(1), [Online] Available from: doi.org/10.1101/CSHPERSPECT.A008888 [Accessed 10/07/2022].

KO, I.G. (2020) Therapeutic Strategies Against Apoptosis and Gliosis. *International Neurourology Journal*, 24(Suppl 2), p. 65.

KORDOWER, J.H. et al. (2006) Failure of proteasome inhibitor administration to provide a model of Parkinson's disease in rats and monkeys. *Annals of Neurology*, 60(2), pp. 264–268.

KOZAK, M. (2007) Lessons (not) learned from mistakes about translation. *Gene*, 403(1–2), pp. 194–203.

LANG, B.J. et al. (2021) The functions and regulation of heat shock proteins; key orchestrators of proteostasis and the heat shock response. *Archives of Toxicology*, 95(6), pp. 1943–1970.

LANJAKORNSIRIPAN, D. et al. (2018) Layer-specific morphological and molecular differences in neocortical astrocytes and their dependence on neuronal layers. *Nature Communications 2018 9:1*, 9(1), pp. 1–15.

LECKER, S.H., GOLDBERG, A.L. and MITCH, W.E. (2006) Protein degradation by the ubiquitin-proteasome pathway in normal and disease states. *Journal of the American Society of Nephrology : JASN*, 17(7), pp. 1807–1819.

LEE, Y.B., NAGAI, A. and KIM, S.U. (2002) Cytokines, chemokines, and cytokine receptors in human microglia. *Journal of Neuroscience Research*, 69(1), pp. 94–103.

LEIBINGER, M. et al. (2013) Neuronal STAT3 activation is essential for CNTF- and inflammatory stimulation-induced CNS axon regeneration. *Cell Death & Disease 2013 4:9*, 4(9), pp. e805–e805.

LEONG, S. -K and LING, E. -A (1992) Amoeboid and ramified microglia: Their interrelationship and response to brain injury. *Glia*, 6(1), pp. 39–47.

LEVINE, J. et al. (2016) Traumatically injured astrocytes release a proteomic signature modulated by STAT3-dependent cell survival. *Glia*, 64(5), pp. 668–694.

LEVISON, S.W. et al. (1993) The migrational patterns and developmental fates of glial precursors in the rat subventricular zone are temporally regulated. *Development (Cambridge, England)*, 119(3), pp. 611–622.

LEVY, D.E. et al. (1988) Interferon-induced nuclear factors that bind a shared promoter element correlate with positive and negative transcriptional control. *Genes & development*, 2(4), pp. 383–393.

LI, C. et al. (2011) Astrocytes: implications for neuroinflammatory pathogenesis of Alzheimer's disease. *Current Alzheimer research*, 8(1), pp. 67–80.

LI, C.L. and MCILWAIN, H. (1957) Maintenance of resting membrane potentials in slices of mammalian cerebral cortex and other tissues in vitro. *The Journal of Physiology*, 139(2), p. 178.

LI, K. et al. (2019) Reactive Astrocytes in Neurodegenerative Diseases. *Aging and Disease*, 10(3), p. 664.

LI, L. et al. (2021) Role of astroglial toll-like receptors (TLRs) in central nervous system infections, injury and neurodegenerative diseases. *Brain, Behavior, and Immunity*, 91, p. 740.

LIN, K. et al. (2015) N-myc downstream-regulated gene 2 in the nervous system: from expression pattern to function. [Online] Available from: doi.org/10.1093/abbs/gmv082.

LINDEBERG, O., MATTSSON, R. and EBENDAL, T. (2002) Timing the doxycycline yields different patterns of genomic recombination in brain neurons with a new inducible Cre transgene. *Journal of neuroscience research*, 68(2), pp. 248–253.

LIU, C.W. and JACOBSON, A.D. (2013) Functions of the 19S complex in proteasomal degradation. *Trends in Biochemical Sciences*, 38(2), pp. 103–110.

LIU, H., LEAK, R.K. and HU, X. (2016) Neurotransmitter receptors on microglia. *Stroke and Vascular Neurology*, 1(2), p. 52.

LIU, S. et al. (2012) TLR2 Is a Primary Receptor for Alzheimer's Amyloid β Peptide To Trigger Neuroinflammatory Activation. *The Journal of Immunology*, 188(3), pp. 1098–1107.

LIU, Y. et al. (2018) Anticonvulsant agent DPP4 inhibitor sitagliptin downregulates CXCR3/RAGE pathway on seizure models. *Experimental Neurology*, 307, pp. 90–98.

ŁOBOCKA, M.B. et al. (2004) Genome of Bacteriophage P1. *Journal of Bacteriology*, 186(21), p. 7032.

LOGIACCO, F. et al. (2021) Microglia sense neuronal activity via GABA in the early postnatal hippocampus. *Cell Reports*, 37(13), p. 110128.

LOIZEAU, A.J. et al. (2019) Physician and Surrogate Agreement with Assisted Dying and Continuous Deep Sedation in Advanced Dementia in Switzerland. *Neurodegenerative Diseases*, 19(1), pp. 4–11.

LOPEZ-SALON, M. et al. (2001) The ubiquitin-proteasome cascade is required for mammalian long-term memory formation. *European Journal of Neuroscience*, 14(11), pp. 1820–1826.

LOWE, J. et al. (1988) Ubiquitin is a common factor in intermediate filament inclusion bodies of diverse type in man, including those of Parkinson's disease, Pick's disease, and Alzheimer's disease, as well as Rosenthal fibres in cerebellar astrocytomas, cytoplasmic bodies in muscle, and mallory bodies in alcoholic liver disease. *The Journal of Pathology*, 155(1), pp. 9–15.

LOWE, J., HAND, N. and MAYER, R.J. (2005) Application of ubiquitin immunohistochemistry to the diagnosis of disease. *Methods in enzymology*, 399, pp. 86–119.

LUCAS, X.; and CIULLI, A. (2016) Recognition of substrate degrons by E3 ubiquitin ligases and modulation by small-molecule mimicry strategies. *Current Opinion in Structural Biology*, 44, pp. 101–110.

DI LUCENTE, J. et al. (2018) The voltage-gated potassium channel Kv1.3 is required for microglial pro-inflammatory activation in vivo. *Glia*, 66(9), pp. 1881–1895.

LUCILE, X. et al. (2015) Development/Plasticity/Repair The JAK/STAT3 Pathway Is a Common Inducer of Astrocyte Reactivity in Alzheimer's and Huntington's Diseases. [Online] Available from: doi.org/10.1523/JNEUROSCI.3516-14.2015.

LULL, M.E. and BLOCK, M.L. (2010) Microglial Activation and Chronic Neurodegeneration. *Neurotherapeutics*, 7(4), pp. 354–365.

LYON, M.S. and MILLIGAN, C. (2019) Extracellular heat shock proteins in neurodegenerative diseases: New perspectives. *Neuroscience Letters*, 711, p. 134462.

MAHMOUD, S. et al. (2019) Astrocytes Maintain Glutamate Homeostasis in the CNS by Controlling the Balance between Glutamate Uptake and Release. *Cells 2019, Vol. 8, Page 184*, 8(2), p. 184.

MAK, T.W. (2007) Gene targeting in embryonic stem cells scores a knockout in Stockholm. *Cell*, 131(6), pp. 1027–1031.

MALLA, B. et al. (2022) Teriflunomide Preserves Neuronal Activity and Protects Mitochondria in Brain Slices Exposed to Oxidative Stress. *International Journal of Molecular Sciences*, 23(3), [Online] Available from: doi.org/10.3390/IJMS23031538/S1 [Accessed 16/07/2022].

MANDA-HANDZLIK, A. and DEMKOW, U. (2019) The Brain Entangled: The Contribution of Neutrophil Extracellular Traps to the Diseases of the Central Nervous System. *Cells 2019, Vol. 8, Page 1477*, 8(12), p. 1477.

MANNING-BOĞ, A.B. et al. (2006) Lack of nigrostriatal pathology in a rat model of proteasome inhibition. *Annals of Neurology*, 60(2), pp. 256–260.

MARTIN, S.W. et al. (2006) Phosphorylation sites on calcium channel α1 and β subunits regulate ERK-dependent modulation of neuronal N-type calcium channels. *Cell Calcium*, 39(3), pp. 275–292.

MASLIAH, E. et al. (2005) Effects of alpha-synuclein immunization in a mouse model of Parkinson's disease. *Neuron*, 46(6), pp. 857–868.

MASLIAH, E. et al. (2011) Passive immunization reduces behavioral and neuropathological deficits in an alpha-synuclein transgenic model of Lewy body disease. *PloS one*, 6(4), [Online] Available from: doi.org/10.1371/JOURNAL.PONE.0019338 [Accessed 10/07/2022].

MATEJUK, A. and RANSOHOFF, R.M. (2020) Crosstalk Between Astrocytes and Microglia: An Overview. *Frontiers in Immunology*, 11, p. 1416.

MAYFORD, M. et al. (1996) Control of memory formation through regulated expression of a CaMKII transgene. *Science (New York, N.Y.)*, 274(5293), pp. 1678–1683.

MCGANN, J.C. and MANDEL, G. (2018) Neuronal activity induces glutathione metabolism gene expression in astrocytes. *Glia*, 66(9), pp. 2024–2039.

MCGEER, P.L. et al. (1988) Reactive microglia are positive for HLA-DR in the substantia nigra of Parkinson's and Alzheimer's disease brains. *Neurology*, 38(8), pp. 1285–1291.

MCGUINNESS, T.L., LAI, Y. and GREENGARD, P. (1985) Ca2+/calmodulin-dependent protein kinase II. Isozymic forms from rat forebrain and cerebellum. *The Journal of biological chemistry*, 260(3), pp. 1696–1704.

MCHUGH, T.J. et al. (1996a) Impaired hippocampal representation of space in CA1-specific NMDAR1 knockout mice. *Cell*, 87(7), pp. 1339–1349.

MCHUGH, T.J. et al. (1996b) Impaired hippocampal representation of space in CA1-specific NMDAR1 knockout mice. *Cell*, 87(7), pp. 1339–1349.

MCKENZIE, A.T. et al. (2017) Multiscale network modeling of oligodendrocytes reveals molecular components of myelin dysregulation in Alzheimer's disease. *Molecular Neurodegeneration*, 12(1), pp. 1–20.

MCNAUGHT, K.S.P., MYTILIN, C., et al. (2002) Impairment of the ubiquitin-proteasome system causes dopaminergic cell death and inclusion body formation in ventral mesencephalic cultures. *Journal of neurochemistry*, 81(2), pp. 301–306.

MCNAUGHT, K.S.P., BJÖRKLUND, L.M., et al. (2002) Proteasome inhibition causes nigral degeneration with inclusion bodies in rats. *Neuroreport*, 13(11), pp. 1437–1441.

MCNAUGHT, K.S.P. et al. (2004) Systemic exposure to proteasome inhibitors causes a progressive model of Parkinson's disease. *Annals of neurology*, 56(1), pp. 149–162.

MEDAWAR, P.B. (1948) Immunity to Homologous Grafted Skin. III. The Fate of Skin Homographs Transplanted to the Brain, to Subcutaneous Tissue, and to the Anterior Chamber of the Eye. *British Journal of Experimental Pathology*, 29(1), p. 58.

MELI, L. et al. (2014) Three dimensional cellular microarray platform for human neural stem cell differentiation and toxicology ScienceDirect. *Stem Cell Research*, 13, pp. 36–47.

MENZIES, F.M. et al. (2017) Autophagy and Neurodegeneration: Pathogenic Mechanisms and Therapeutic Opportunities. *Neuron*, 93(5), pp. 1015–1034.

MERRILL, M. et al. (2005) Activity-driven postsynaptic translocation of CaMKII. *Trends in pharmacological sciences*, 26(12), pp. 645–653.

MEYER, J.G. and SCHILLING, B. (2017) Clinical applications of quantitative proteomics using targeted and untargeted data-independent acquisition techniques. *http://dx.doi.org/10.1080/14789450.2017.1322904*, 14(5), pp. 419–429.

MILLER, A.R., LIANG, Y. and VAN ZANT, G. (2005) Stem Cell Aging Studies Reveal Changes in the Proteasome. *Blood*, 106(11), pp. 4207–4207.

MILLER, S.G. and KENNEDY, M.B. (1985) Distinct forebrain and cerebellar isozymes of type II Ca2+/calmodulin-dependent protein kinase associate differently with the postsynaptic density fraction. *The Journal of biological chemistry*, 260(15), pp. 9039–9046.

MITCHELL, T.J. and JOHN, S. (2005) Signal transducer and activator of transcription (STAT) signaling and T-cell lymphomas. *Immunology*, 114(3), p. 301.

MORFINI, G.A. et al. (2009) Pathogenic Huntingtin Inhibits Fast Axonal Transport by Activating JNK3 and Phosphorylating Kinesin. *Nature neuroscience*, 12(7), p. 864.

MOTORI, E. et al. (2013) Inflammation-Induced Alteration of Astrocyte Mitochondrial Dynamics Requires Autophagy for Mitochondrial Network Maintenance. *Cell Metabolism*, 18(6), pp. 844–859.

MUELLER, C. et al. (2011) One-Step Preservation of Phosphoproteins and Tissue Morphology at Room Temperature for Diagnostic and Research Specimens. *PLoS ONE*, 6(8), [Online] Available from: doi.org/10.1371/JOURNAL.PONE.0023780 [Accessed 08/05/2022].

MULDER, G.J. (1838) Sur la composition de quelques substances animales. *Bulletin des sciences physiques et naturelles en Neerlande*, pp. 9–9.

MULDOON, L.L. et al. (2013) Immunologic privilege in the central nervous system and the blood–brain barrier. *Journal of Cerebral Blood Flow & Metabolism*, 33(1), p. 13.

MUNOZ, F.M. et al. (2017) Neuronal P2X7 receptor-induced reactive oxygen species production contributes to nociceptive behavior in mice. *Scientific Reports*, 7(1), [Online] Available from: doi.org/10.1038/S41598-017-03813-7 [Accessed 10/06/2022].

MYEKU, N. and DUFF, K.E. (2018) Targeting the 26S Proteasome To Protect Against Proteotoxic Diseases. *Trends in molecular medicine*, 24(1), p. 18.

NAGANATHAN, A.N. et al. (2006) Dynamics, Energetics and Structure in Protein Folding. *Biochemistry*, 45(28), p. 8466.

NAKAGAWA, Y. and CHIBA, K. (2014) Role of Microglial M1/M2 Polarization in Relapse and Remission of Psychiatric Disorders and Diseases. *Pharmaceuticals 2014, Vol. 7, Pages 1028-1048*, 7(12), pp. 1028–1048.

NARIMATSU, M. et al. (2001) Tissue-Specific Autoregulation of the stat3 Gene and Its Role in Interleukin-6-Induced Survival Signals in T Cells. *Molecular and Cellular Biology*, 21(19), p. 6615.

NIELSEN, H.M. et al. (2010) Astrocytic Aβ1-42 uptake is determined by Aβ-aggregation state and the presence of amyloid-associated proteins. *Glia*, 58(10), pp. 1235–1246.

NIKODEMOVA, M. et al. (2015) Microglial numbers attain adult levels after undergoing a rapid decrease in cell number in the third postnatal week. *Journal of neuroimmunology*, 0, p. 280.

NIMMERJAHN, A., KIRCHHOFF, F. and HELMCHEN, F. (2005) Neuroscience: Resting microglial cells are highly dynamic surveillants of brain parenchyma in vivo. *Science*, 308(5726), pp. 1314–1318.

VAN NOORT, J.M., BUGIANI, M. and AMOR, S. (2017) Heat Shock Proteins: Old and Novel Roles in Neurodegenerative Diseases in the Central Nervous System. *CNS and Neurological Disorders. Drug Targets*, 16(3), pp. 244–256.

NOVIKOFF, A., BEAUFAY, H. and DE DUVE, C. (1956) Electron microscopy of lysosome-rich fractions from Rat Liver. *Journal of Biophysics and Biochemistry*, 2(4), pp. 179–184.

NUEBLING, G.S., BUTZHAMMER, E. and LORENZL, S. (2021) Assisted Suicide in Parkinsonian Disorders. *Frontiers in Neurology*, 12, p. 331.

O'CALLAGHAN, J.P. et al. (2014a) Early Activation of STAT3 Regulates Reactive Astrogliosis Induced by Diverse Forms of Neurotoxicity. *PLOS ONE*, 9(7), p. e102003.

O'CALLAGHAN, J.P. et al. (2014b) Early Activation of STAT3 Regulates Reactive Astrogliosis Induced by Diverse Forms of Neurotoxicity. *PLOS ONE*, 9(7), p. e102003.

O'CALLAGHAN, J.P. and SRIRAM, K. (2004) Focused microwave irradiation of the brain preserves in vivo protein phosphorylation: comparison with other methods of sacrifice and analysis of multiple phosphoproteins. *Journal of neuroscience methods*, 135(1–2), pp. 159–168.

OKOYE, C.N. et al. (2022) Counting Degrons: Lessons From Multivalent Substrates for Targeted Protein Degradation. *Frontiers in Physiology*, 0, p. 1292.

OKUDA, T., KOKAME, K. and MIYATA, T. (2008) Differential Expression Patterns of NDRG Family Proteins in the Central Nervous System. *Journal of Histochemistry and Cytochemistry*, 56(2), p. 175.

ORIHUELA, R., MCPHERSON, C.A. and HARRY, G.J. (2016) Microglial M1/M2 polarization and metabolic states. *British Journal of Pharmacology*, 173(4), pp. 649–665.

OUIMET, C.C., MCGUINNESS, T.L. and GREENGARD, P. (1984) Immunocytochemical localization of calcium/calmodulin-dependent protein kinase II in rat brain. *Proceedings of the National Academy of Sciences of the United States of America*, 81(17), pp. 5604–5608.

PAL, G.K. (2021) *Textbook of Medical Physiology*. 4th ed. India: Elsevier Health Sciences.

PANKIEWICZ, J.E. et al. (2020) Peroxiredoxin 6 mediates protective function of astrocytes in Aβ proteostasis. *Molecular Neurodegeneration*, 15(1), pp. 1–22.

PAOLICELLI, R.C. et al. (2011) Synaptic pruning by microglia is necessary for normal brain development. *Science*, 333(6048), pp. 1456–1458.

PARK, K.W., NOZELL, S.E. and BENVENISTE, E.N. (2012) Protective Role of STAT3 in NMDA and Glutamate-Induced Neuronal Death: Negative Regulatory Effect of SOCS3. *PLOS ONE*, 7(11), p. e50874.

PARK, S.A. et al. (2020) SWATH-MS analysis of cerebrospinal fluid to generate a robust battery of biomarkers for Alzheimer's disease. *Scientific Reports*, 10(1), [Online] Available from: doi.org/10.1038/S41598-020-64461-Y [Accessed 16/07/2022].

PARVIAINEN, L. et al. (2017) Glial cells are functionally impaired in juvenile neuronal ceroid lipofuscinosis and detrimental to neurons. *Acta neuropathologica communications*, 5(1), p. 74.

PAUDEL, Y.N. et al. (2018) HMGB1: A common biomarker and potential target for TBI, neuroinflammation, epilepsy, and cognitive dysfunction. *Frontiers in Neuroscience*, 12(SEP), p. 628.

PHATNANI, H. and MANIATIS, T. (2015) Astrocytes in Neurodegenerative Disease. *Cold Spring Harbor Perspectives in Biology*, 7(6), pp. 1–18.

PIETRONIGRO, E.C. et al. (2017) NETosis in Alzheimer's disease. *Frontiers in Immunology*, 8(MAR), p. 211.

PIHLAJA, R. et al. (2011) Multiple cellular and molecular mechanisms are involved in human Aβ clearance by transplanted adult astrocytes. *Glia*, 59(11), pp. 1643–1657.

PODDAR, M.K., CHAKRABORTY, A. and BANERJEE, S. (2021) Neurodegeneration: Diagnosis, Prevention, and Therapy. *Oxidoreductase*, [Online] Available from: doi.org/10.5772/INTECHOPEN.94950 [Accessed 10/07/2022].

POEWE, W. et al. (2010) Levodopa in the treatment of Parkinson's disease: an old drug still going strong. *Clinical Interventions in Aging*, 5, p. 229.

PRACUCCI, E. et al. (2021) Neuroinflammation: A Signature or a Cause of Epilepsy? *International Journal of Molecular Sciences*, 22(13), [Online] Available from: doi.org/10.3390/IJMS22136981 [Accessed 13/07/2022].

PROBERT, L. (2015) TNF and its receptors in the CNS: The essential, the desirable and the deleterious effects. *Neuroscience*, 302, pp. 2–22.

QIAO, P. et al. (2020) Curcumin Prevents Neuroinflammation by Inducing Microglia to Transform into the M2-phenotype via CaMKKβ-dependent Activation of the AMP-

Activated Protein Kinase Signal Pathway. *Current Alzheimer Research*, 17(8), pp. 735–752.

RAGHUNATH, A. et al. (2018) Heat Shock Proteins and Endoplasmic Reticulum Stress. pp. 39–78.

RANSOHOFF, R.M. and PERRY, V.H. (2009) Microglial Physiology: Unique Stimuli, Specialized Responses. *http://dx.doi.org/10.1146/annurev.immunol.021908.132528*, 27, pp. 119–145.

RAWAT, K., SYEDA, S. and SHRIVASTAVA, A. (2021) Neutrophil-derived granule cargoes: paving the way for tumor growth and progression. *Cancer and Metastasis Reviews*, 40(1), pp. 221–244.

RAYNES, R., POMATTO, L.C.D. and DAVIES, K.J.A. (2016) Degradation of oxidized proteins by the proteasome: Distinguishing between the 20S, 26S, and immunoproteasome proteolytic pathways. *Molecular aspects of medicine*, 50, pp. 41–55.

RE, D.B. et al. (2014) Necroptosis drives motor neuron death in models of both sporadic and familial ALS. *Neuron*, 81(5), p. 1001.

REEMST, K. et al. (2016) The indispensable roles of microglia and astrocytes during brain development. *Frontiers in Human Neuroscience*, 10(NOV2016), p. 566.

REES, T.M. and BRIMIJOIN, S. (2003) The role of acetylcholinesterase in the pathogenesis of Alzheimer's disease. *Drugs of today (Barcelona, Spain : 1998)*, 39(1), pp. 75–83.

REID, K.H. et al. (1988) Pitfalls in the use of brain slices. *Progress in Neurobiology*, 31(1), pp. 1–18.

REINICKE, A.T. et al. (2019) Ubiquitin C-terminal hydrolase L1 (UCH-L1) loss causes neurodegeneration by altering protein turnover in the first postnatal weeks. *Proceedings of the National Academy of Sciences of the United States of America*, 116(16), pp. 7963–7972.

RENAULT-MIHARA, F. and OKANO, H. (2017) STAT3-regulated RhoA drives reactive astrocyte dynamics. *https://doi.org/10.1080/15384101.2017.1377032*, 16(21), pp. 1995–1996.

RENOM-GUITERAS, A. et al. (2018) Potentially inappropriate medication among people with dementia in eight European countries. *Age and Ageing*, 47(1), pp. 68–74.

RIEGLER, A.N. et al. (2019) Necroptotic cell death promotes adaptive immunity against colonizing pneumococci. *Frontiers in Immunology*, 10(APR), [Online] Available from: doi.org/10.3389/FIMMU.2019.00615/FULL [Accessed 25/06/2022].

RILEY, B.E. et al. (2013) Structure and function of Parkin E3 ubiquitin ligase reveals aspects of RING and HECT ligases. *Nature Communications*, 4, [Online] Available from: doi.org/10.1038/NCOMMS2982 [Accessed 20/10/2022].

ROBERTS, W.K. et al. (2015) A destructive feedback loop mediated by CXCL10 in central nervous system inflammatory disease. *Annals of Neurology*, 78(4), p. 619.

ROBINSON, M.B. et al. (2005) Extracellular Heat Shock Protein 70: A Critical Component for Motoneuron Survival. *Journal of Neuroscience*, 25(42), pp. 9735–9745.

ROSENZWEIG, R. et al. (2012) Rpn1 and Rpn2 coordinate ubiquitin processing factors at proteasome. *The Journal of biological chemistry*, 287(18), pp. 14659–14671.

RUANGRITCHANKUL, S. et al. (2020) Drug related problems in older adults living with dementia. *PLoS ONE*, 15(7), [Online] Available from: doi.org/10.1371/JOURNAL.PONE.0236830 [Accessed 20/10/2022].

SACRAMENTO, E.K. et al. (2020) Reduced proteasome activity in the aging brain results in ribosome stoichiometry loss and aggregation. *Molecular Systems Biology*, 16(6), p. e9596.

SADOK, S.H. et al. (2021) News and Views on STAT3 Psychopathology. *Frontiers in Genetics*, 12, p. 2401.

SADOWSKI, M. et al. (2012) Protein monoubiquitination and polyubiquitination generate structural diversity to control distinct biological processes. *IUBMB Life*, 64(2), pp. 136–142.

SAEZ, I. and VILCHEZ, D. (2014) The Mechanistic Links Between Proteasome Activity, Aging and Age-related Diseases. *Current Genomics*, 15(1), p. 38.

SALVI, V. et al. (2017) Role of atypical chemokine receptors in microglial activation and polarization. *Frontiers in Aging Neuroscience*, 9(MAY), p. 148.

SAMUEL, F. et al. (2016) Effects of Serine 129 Phosphorylation on α-Synuclein Aggregation, Membrane Association, and Internalization *. *Journal of Biological Chemistry*, 291(9), pp. 4374–4385.

SANDER, H. et al. (2019) Ponceau S Waste: Ponceau S Staining for Total Protein Normalization. *Analytical biochemistry*, 575, p. 44.

SARAFIAN, T.A. et al. (2010) Disruption of Astrocyte STAT3 Signaling Decreases Mitochondrial Function and Increases Oxidative Stress In Vitro. *PLOS ONE*, 5(3), p. e9532.

SARLUS, H. and HENEKA, M.T. (2017) Microglia in Alzheimer's disease. *The Journal of Clinical Investigation*, 127(9), pp. 3240–3249.

SAUER, B. and HENDERSON, N. (1988) Site-specific DNA recombination in mammalian cells by the Cre recombinase of bacteriophage P1. *Proceedings of the National Academy of Sciences of the United States of America*, 85(14), pp. 5166–5170.

SCHAFFERT, L.N. and CARTER, W.G. (2020) Do Post-Translational Modifications Influence Protein Aggregation in Neurodegenerative Diseases: A Systematic Review. *Brain Sciences 2020, Vol. 10, Page 232*, 10(4), p. 232.

SCHIMMEL, S.J., ACOSTA, S. and LOZANO, D. (2017) Neuroinflammation in traumatic brain injury: A chronic response to an acute injury. *Brain Circulation*, 3(3), p. 135.

SCHOENHEIMER, R. et al. (1938) The application of the nitrogen isotope n15 for the study of protein metabolism. *Science*, 88(2295), pp. 599–600.

SCHOLZ, W.K. et al. (1988) Developmental changes in Ca2+/calmodulin-dependent protein kinase II in cultures of hippocampal pyramidal neurons and astrocytes. *Journal of Neuroscience*, 8(3), pp. 1039–1051.

SCHULZ, C. et al. (2012) A lineage of myeloid cells independent of Myb and hematopoietic stem cells. *Science (New York, N.Y.)*, 336(6077), pp. 86–90.

SEMPLE, C.A.M. et al. (2003) The comparative proteomics of ubiquitination in mouse. *Genome research*, 13(6B), pp. 1389–1394.

SERRANO-POZO, A. et al. (2011) Neuropathological Alterations in Alzheimer Disease. *Cold Spring Harbor Perspectives in Medicine*, 1(1), p. a006189.

SHANBHAG, N.M. et al. (2019) Early neuronal accumulation of DNA double strand breaks in Alzheimer's disease. *Acta Neuropathologica Communications 2019 7:1*, 7(1), pp. 1–18.

SHANKAR, G.M. et al. (2007) Natural oligomers of the Alzheimer amyloid-beta protein induce reversible synapse loss by modulating an NMDA-type glutamate receptor-dependent signaling pathway. *The Journal of neuroscience : the official journal of the Society for Neuroscience*, 27(11), pp. 2866–2875.

SHEARMAN, M.S. (1999) [45] Toxicity of protein aggregates in PC12 cells: 3-(4,5-dimethylthiazol-2-yl)-2,5-diphenyltetrazolium bromide assay. *Methods in Enzymology*, 309, pp. 716–723.

SHELDON, A.L. and ROBINSON, M.B. (2007) The role of glutamate transporters in neurodegenerative diseases and potential opportunities for intervention. *Neurochemistry international*, 51(6–7), pp. 333–355.

SHEMIN, D. and RITTENBERG, D. (1946) The Biological Utilization of Glycine for the synthesis of the protoporphyrin of Hemoglobin. *Journal of Biological chemistry*, 166(2), pp. 621–625.

SHERER, T.B. et al. (2003) Mechanism of Toxicity in Rotenone Models of Parkinson's Disease. *The Journal of Neuroscience*, 23(34), p. 10756.

SHLOMOVITZ, I. et al. (2021) Proteomic analysis of necroptotic extracellular vesicles. *Cell Death & Disease 2021 12:11*, 12(11), pp. 1–13.

SHONESY, B.C. et al. (2014) CaMKII: a molecular substrate for synaptic plasticity and memory. *Progress in molecular biology and translational science*, 122, pp. 61–87.

SIMPSON, R.J. (2006) Fragmentation of protein using trypsin. *CSH protocols*, 2006(5), p. pdb.prot4550.

SOBUE, A. et al. (2021) Microglial gene signature reveals loss of homeostatic microglia associated with neurodegeneration of Alzheimer's disease. *Acta Neuropathologica Communications*, 9(1), pp. 1–17.

SOFRONIEW, M. V. (2015a) Astrogliosis. *Cold Spring Harbor Perspectives in Biology*, 7(2), [Online] Available from: doi.org/10.1101/CSHPERSPECT.A020420 [Accessed 15/07/2022].

SOFRONIEW, M. V. (2015b) Astrogliosis. *Cold Spring Harbor Perspectives in Biology*, 7(2), [Online] Available from: doi.org/10.1101/CSHPERSPECT.A020420 [Accessed 15/07/2022].

SOFRONIEW, M. V. and VINTERS, H. V. (2010) Astrocytes: biology and pathology. *Acta neuropathologica*, 119(1), pp. 7–35.

SOMJEN, G.G. (1988) Nervenkitt: Notes on the history of the concept of neuroglia. *Glia*, 1(1), pp. 2–9.

SONG, C.Q. et al. (2017) Genome-wide CRISPR Screen Identifies Regulators of MAPK as Suppressors of Liver Tumors in Mice. *Gastroenterology*, 152(5), p. 1161.

SPITALE, F.M. et al. (2020) Increased expression of connexin 43 in a mouse model of spinal motoneuronal loss. *Aging (Albany NY)*, 12(13), p. 12598.

SRINIVASAN, K. et al. (2016) Untangling the brain's neuroinflammatory and neurodegenerative transcriptional responses. *Nature Communications 2016 7:1*, 7(1), pp. 1–16.

SRIRAM, K. et al. (2002) Mice deficient in TNF receptors are protected against dopaminergic neurotoxicity: Implications for Parkinson's disease. *The FASEB Journal*, 16(11), pp. 1474–1476.

SRIRAM, S.M., KIM, B.Y. and KWON, Y.T. (2011) The N-end rule pathway: emerging functions and molecular principles of substrate recognition. *Nature Reviews Molecular Cell Biology 2011 12:11*, 12(11), pp. 735–747.

STELZMA, R.A., NORMAN SCHNITZLEIN, H. and MURLLAGH, F.R. (1995) An English I'ranslation of Alzheimer's 1907 Paper, 'ijber eine eigenartige Erlranliung der Hirnrinde'. *Clinical Anatomy*, 8, pp. 429–472.

STEWART, M.D. et al. (2016) E2 enzymes: more than just middle men. *Cell Research 2016 26:4*, 26(4), pp. 423–440.

STRICHER, F. et al. (2013) HSPA8/HSC70 chaperone protein: structure, function, and chemical targeting. *Autophagy*, 9(12), pp. 1937–1954.

SU, Y. et al. (2020) STAT3 Regulates Mouse Neural Progenitor Proliferation and Differentiation by Promoting Mitochondrial Metabolism. *Frontiers in Cell and Developmental Biology*, 8, p. 362.

SUIRE, C.N. et al. (2020) Cathepsin D regulates cerebral Aβ42/40 ratios via differential degradation of Aβ42 and Aβ40. *Alzheimer's Research and Therapy*, 12(1), pp. 1–13.

SULLIVAN, S.M. (2014) GFAP variants in health and disease: stars of the brain… and gut. *Journal of Neurochemistry*, 130(6), pp. 729–732.

SUN, P.D., FOSTER, C.E. and BOYINGTON, J.C. (2004) Overview of Protein Structural and Functional Folds. *Current Protocols in Protein Science*, 35(1), p. 1711.

SZELIGA, M. (2020) Peroxiredoxins in Neurodegenerative Diseases. *Antioxidants 2020, Vol. 9, Page 1203*, 9(12), p. 1203.

SZKLARCZYK, D. et al. (2019) STRING v11: protein–protein association networks with increased coverage, supporting functional discovery in genome-wide experimental datasets. *Nucleic Acids Research*, 47(D1), pp. D607–D613.

TAFT, J.R., VERTES, R.P. and PERRY, G.W. (2005) Distribution of GFAP+ astrocytes in adult and neonatal rat brain. *The International journal of neuroscience*, 115(9), pp. 1333–1343.

TAI, H.C. et al. (2010a) Characterization of the brain 26S proteasome and its interacting proteins. *Frontiers in Molecular Neuroscience*, 3, p. 12.

TAI, H.C. et al. (2010b) Characterization of the brain 26S proteasome and its interacting proteins. *Frontiers in Molecular Neuroscience*, 3, [Online] Available from: doi.org/10.3389/FNMOL.2010.00012 [Accessed 10/07/2022].

TAKEICHI, T. et al. (2011) The effect of Ndrg2 expression on astroglial activation. *Neurochemistry International*, 59(1), pp. 21–27.

TANAKA, K. (2009) The proteasome: Overview of structure and functions. *Proceedings of the Japan Academy. Series B, Physical and Biological Sciences*, 85(1), p. 12.

TANZI, R.E. (2015) TREM2 and Risk of Alzheimer's Disease — Friend or Foe? *New England Journal of Medicine*, 372(26), pp. 2564–2565.

TEYLER, T.J. (1980) Brain slice preparation: Hippocampus. *Brain Research Bulletin*, 5(4), pp. 391–403.

THIBAUDEAU, T.A., ANDERSON, R.T. and SMITH, D.M. (2018) A common mechanism of proteasome impairment by neurodegenerative disease-associated oligomers. *Nature Communications*, 9(1), [Online] Available from: doi.org/10.1038/S41467-018-03509-0 [Accessed 10/07/2022].

THOMPSON, D., HAKALA, K. and DEMARTINO, G.N. (2009) Subcomplexes of PA700, the 19 S regulator of the 26 S proteasome, reveal relative roles of AAA subunits in 26 S proteasome assembly and activation and ATPase activity. *Journal of Biological Chemistry*, 284(37), pp. 24891–24903.

TOHID, H. (2016) Robin Williams' suicide: a case study. *Trends in Psychiatry and Psychotherapy*, 38(3), pp. 178–182.

TONOKI, A. et al. (2009) Genetic evidence linking age-dependent attenuation of the 26S proteasome with the aging process. *Molecular and cellular biology*, 29(4), pp. 1095–1106.

TORAL-RIOS, D. et al. (2020a) Activation of STAT3 Regulates Reactive Astrogliosis and Neuronal Death Induced by AβO Neurotoxicity. *International Journal of Molecular Sciences 2020, Vol. 21, Page 7458*, 21(20), p. 7458.

TORAL-RIOS, D. et al. (2020b) Activation of STAT3 Regulates Reactive Astrogliosis and Neuronal Death Induced by AβO Neurotoxicity. *International Journal of Molecular Sciences 2020, Vol. 21, Page 7458*, 21(20), p. 7458.

TROUBAT, R. et al. (2021) Neuroinflammation and depression: A review. *European Journal of Neuroscience*, 53(1), pp. 151–171.

TSIATSIANI, L. et al. (2015) Proteomics beyond trypsin. *The FEBS Journal*, 282(14), pp. 2612–2626.

TSIEN, J.Z. (2016) Cre-Lox Neurogenetics: 20 Years of Versatile Applications in Brain Research and Counting…. *Frontiers in Genetics*, 7(FEB), [Online] Available from: doi.org/10.3389/FGENE.2016.00019 [Accessed 21/10/2021].

TYZACK, G.E. et al. (2014) Astrocyte response to motor neuron injury promotes structural synaptic plasticity via STAT3-regulated TSP-1 expression. *Nature Communications 2014 5:1*, 5(1), pp. 1–15.

UENO, M. et al. (2013) Layer V cortical neurons require microglial support for survival during postnatal development. *Nature neuroscience*, 16(5), pp. 543–551.

UGUN-KLUSEK, A. et al. (2017a) Continued 26S proteasome dysfunction in mouse brain cortical neurons impairs autophagy and the Keap1-Nrf2 oxidative defence pathway. *Cell Death & Disease*, 8(1), p. e2531.

UGUN-KLUSEK, A. et al. (2017b) Continued 26S proteasome dysfunction in mouse brain cortical neurons impairs autophagy and the Keap1-Nrf2 oxidative defence pathway. *Cell Death & Disease 2017 8:1*, 8(1), pp. e2531–e2531.

UPADHYA, R. et al. (2020) Astrocyte-derived extracellular vesicles: Neuroreparative properties and role in the pathogenesis of neurodegenerative disorders. *Journal of controlled release : official journal of the Controlled Release Society*, 323, pp. 225–239.

UPADHYA, S.C. et al. (2006) Differential regulation of proteasome activity in the nucleus and the synaptic terminals. *Neurochemistry International*, 48(4), pp. 296–305.

UVERSKY, V.N. (2019) Intrinsically disordered proteins and their 'Mysterious' (meta)physics. *Frontiers in Physics*, 7(FEB), p. 10.

VALLÉE, A. (2022) Neuroinflammation in Schizophrenia: The Key Role of the WNT/β-Catenin Pathway. *International Journal of Molecular Sciences*, 23(5), [Online] Available from: doi.org/10.3390/IJMS23052810 [Accessed 13/07/2022].

VANDENABEELE, P. et al. (2010) Molecular mechanisms of necroptosis: an ordered cellular explosion. *Nature reviews. Molecular cell biology*, 11(10), pp. 700–714.

VERKHRATSKY, A. et al. (2016) Astrocytes as secretory cells of the central nervous system: idiosyncrasies of vesicular secretion. *The EMBO journal*, 35(3), pp. 239–257.

VERKHRATSKY, A. et al. (2019) Physiology of Astroglia. *Advances in experimental medicine and biology*, 1175, p. 45.

VERKHRATSKY, A. and BUTT, A. (2013) Glial Physiology and Pathophysiology. *Glial Physiology and Pathophysiology*, [Online] Available from: doi.org/10.1002/9781118402061 [Accessed 30/07/2022].

VERNACE, V.A., SCHMIDT-GLENEWINKEL, T. and FIGUEIREDO-PEREIRA, M.E. (2007) Aging and regulated protein degradation: who has the UPPer hand? *Aging Cell*, 6(5), pp. 599–606.

VICKERY, H.B. (1950) The Origin of the Word Protein. *The Yale Journal of Biology and Medicine*, 22(5), p. 387.

VINET, J. et al. (2010) Expression of CXCL10 in cultured cortical neurons. *Journal of Neurochemistry*, 112(3), pp. 703–714.

VOLTERRA, A. and MELDOLESI, J. (2005) Astrocytes, from brain glue to communication elements: the revolution continues. *Nature reviews. Neuroscience*, 6(8), pp. 626–640.

WALSH, S. et al. (2021) Aducanumab for Alzheimer's disease? *BMJ*, 374, [Online] Available from: doi.org/10.1136/BMJ.N1682 [Accessed 20/10/2022].

WALTER, J. (2016) The Triggering Receptor Expressed on Myeloid Cells 2: A Molecular Link of Neuroinflammation and Neurodegenerative Diseases. *The Journal of biological chemistry*, 291(9), pp. 4334–4341.

WANG, F. et al. Electroacupuncture Attenuates Reference Memory Impairment Associated with Astrocytic NDRG2 Suppression in APP/PS1 Transgenic Mice. [Online] Available from: doi.org/10.1007/s12035-013-8609-1.

WANG, X., ZHANG, C., SZÁBO, G. and SUN, Q.Q. (2013) Distribution of CaMKIIα expression in the brain in vivo, studied by CaMKIIα-GFP mice. *Brain research*, 1518, p. 9.

WANG, X., ZHANG, C., SZÁBO, G. and SUN, Q.-Q. (2013) Distribution of CaMKIIα expression in the brain in vivo, studied by CaMKIIα-GFP mice. *Brain research*, 1518, p. 9.

WANG, X. et al. (2021) UBE2D3 contributes to myocardial ischemia-reperfusion injury by regulating autophagy in dependence of p62/SQSTM1. *Cellular Signaling*, 87, p. 110118.

WANG, Z. et al. (2021) Plasma Neurofilament Light Chain as a Predictive Biomarker for Post-stroke Cognitive Impairment: A Prospective Cohort Study. *Frontiers in Aging Neuroscience*, 13, [Online] Available from: doi.org/10.3389/FNAGI.2021.631738 [Accessed 02/06/2022].

WASHBURN, K.B. and NEARY, J.T. (2006) P2 purinergic receptors signal to STAT3 in astrocytes: Difference in STAT3 responses to P2Y and P2X receptor activation. *Neuroscience*, 142(2), pp. 411–423.

WELLBOURNE-WOOD, J. and CHATTON, J.Y. (2018) From Cultured Rodent Neurons to Human Brain Tissue: Model Systems for Pharmacological and Translational Neuroscience. *ACS chemical neuroscience*, 9(8), pp. 1975–1985.

WHITLOCK, J.R. et al. (2006) Learning induces long-term potentiation in the hippocampus. *Science (New York, N.Y.)*, 313(5790), pp. 1093–1097.

WILHELMSSON, U. et al. (2006) Redefining the concept of reactive astrocytes as cells that remain within their unique domains upon reaction to injury. *Proceedings of the National Academy of Sciences of the United States of America*, 103(46), pp. 17513–17518.

WINSTON, C.N. et al. (2019) Complement protein levels in plasma astrocyte-derived exosomes are abnormal in conversion from mild cognitive impairment to Alzheimer's disease dementia. *Alzheimer's & Dementia : Diagnosis, Assessment & Disease Monitoring*, 11, p. 61.

WRIGHT, P.E. and DYSON, H.J. (2014) Intrinsically disordered proteins in cellular signaling and regulation. *Nature Reviews Molecular Cell Biology 2015 16:1*, 16(1), pp. 18–29.

XIA, Y. et al. (2021) Reactive microglia enhance the transmission of exosomal α-synuclein via toll-like receptor 2. *Brain*, 144(7), pp. 2024–2037.

XIE, W. et al. (2010) Proteasome inhibition modeling nigral neuron degeneration in Parkinson's disease. *Journal of Neurochemistry*, 115(1), pp. 188–199.

YANG, Y. et al. (2017) Neuroprotective Effects and Mechanism of β-Asarone against A β 1-42-Induced Injury in Astrocytes. *Evidence-based complementary and alternative medicine : eCAM*, 2017, [Online] Available from: doi.org/10.1155/2017/8516518 [Accessed 26/07/2022].

YARMOLINSKY, M. and HOESS, R. (2015) The Legacy of Nat Sternberg: The Genesis of Cre-lox Technology. *Annual review of virology*, 2(1), pp. 25–40.

YEO, I.J. et al. (2019) PRDX6 Inhibits Neurogenesis through Downregulation of WDFY1-Mediated TLR4 Signal. *Molecular Neurobiology*, 56(5), pp. 3132–3144.

YI, C. et al. (2016) Astroglial connexin43 contributes to neuronal suffering in a mouse model of Alzheimer's disease. *Cell Death & Differentiation 2016 23:10*, 23(10), pp. 1691–1701.

YIANNOPOULOU, K.G. and PAPAGEORGIOU, S.G. (2020) Current and Future Treatments in Alzheimer Disease: An Update. *Journal of Central Nervous System Disease*, 12, p. 117957352090739.

YUN, H.M. et al. (2015) PRDX6 Exacerbates Dopaminergic Neurodegeneration in a MPTP Mouse Model of Parkinson's Disease. *Molecular Neurobiology*, 52(1), pp. 422–431.

ZALCMAN, G., FEDERMAN, N. and ROMANO, A. (2018a) CaMKII Isoforms in Learning and Memory: Localization and Function. *Frontiers in molecular neuroscience*, 11, [Online] Available from: doi.org/10.3389/FNMOL.2018.00445 [Accessed 02/07/2022].

ZALCMAN, G., FEDERMAN, N. and ROMANO, A. (2018b) CaMKII isoforms in learning and memory: Localization and function. *Frontiers in Molecular Neuroscience*, 11, p. 445.

ZARIFKAR, P. et al. (2022) Frequency of Neurological Diseases After COVID-19, Influenza A/B and Bacterial Pneumonia. *Frontiers in Neurology*, 0, p. 1276.

ZHANG, D.W. et al. (2009) RIP3, an energy metabolism regulator that switches TNF-induced cell death from apoptosis to necrosis. *Science*, 325(5938), pp. 332–336.

ZHANG, L. et al. (2021a) miR-204 silencing reduces mitochondrial autophagy and ROS production in a murine AD model via the TRPML1-activated STAT3 pathway. *Molecular Therapy - Nucleic Acids*, 24, pp. 822–831.

ZHANG, L. et al. (2021b) miR-204 silencing reduces mitochondrial autophagy and ROS production in a murine AD model via the TRPML1-activated STAT3 pathway. *Molecular Therapy - Nucleic Acids*, 24, pp. 822–831.

ZHANG, Q. et al. (2017) Activation of the α7 nicotinic receptor promotes lipopolysaccharide-induced conversion of M1 microglia to M2. *American Journal of Translational Research*, 9(3), p. 971.

ZHANG, YOUWEN et al. (2018) TREM2 modulates microglia phenotypes in the neuroinflammation of Parkinson's disease. *Biochemical and biophysical research communications*, 499(4), pp. 797–802.

ZHAO, W. et al. (2022) Targeting Necroptosis as a Promising Therapy for Alzheimer's Disease. *ACS chemical neuroscience*, 13(12), pp. 1697–1713.

ZHENG, H. et al. (2018) TREM2 in Alzheimer's Disease: Microglial Survival and Energy Metabolism. *Frontiers in Aging Neuroscience*, 10, [Online] Available from: doi.org/10.3389/FNAGI.2018.00395 [Accessed 29/10/2022].

ZHENG, N. and SHABEK, N. (2017) Ubiquitin Ligases: Structure, Function, and Regulation. *https://doi.org/10.1146/annurev-biochem-060815-014922*, 86, pp. 129–157.

ZHOU, Y., ULLAND, T.K. and COLONNA, M. (2018) TREM2-Dependent Effects on Microglia in Alzheimer's Disease. *Frontiers in Aging Neuroscience*, 10(JUL), [Online] Available from: doi.org/10.3389/FNAGI.2018.00202 [Accessed 15/07/2022].

ZHOU, Y.-Q. et al. (2019) The Role of CXCR3 in Neurological Diseases. *Current Neuropharmacology*, 17(2), pp. 142–150.

ZHU, J. et al. (2020) NDRG2 attenuates ischemia-induced astrocyte necroptosis via the repression of RIPK1. *Molecular Medicine Reports*, 22(4), pp. 3103–3110.

ZHU, Y.M. et al. (2021) The Key Regulator of Necroptosis, RIP1 Kinase, Contributes to the Formation of Astrogliosis and Glial Scar in Ischemic Stroke. *Translational Stroke Research*, 12(6), pp. 991–1017.

ZUIN, A., ISASA, M. and CROSAS, B. (2014) Ubiquitin signaling: extreme conservation as a source of diversity. *Cells*, 3(3), pp. 690–701.